

AD-A032 079

GENERAL ELECTRIC CO CINCINNATI OHIO AIRCRAFT ENGINE GROUP F/G 1/3
DYNAMIC DIGITAL BLADE ROW COMPRESSION COMPONENT STABILITY MODEL--ETC(U)
AUG 76 G G REYNOLDS, W G STEENKEN F33615-75-C-2029

UNCLASSIFIED

R76AEG299

AFAPL-TR-76-76

NL

1 of 4
ADA032079



AD A032079

AFAPL-TR-76-76

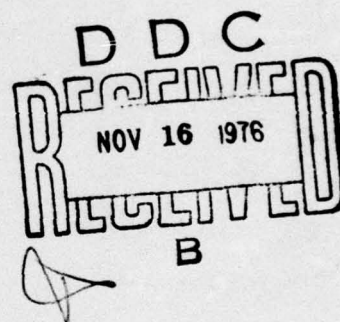
12 FG

**DYNAMIC DIGITAL BLADE ROW COMPRESSION
COMPONENT STABILITY MODEL
MODEL VALIDATION AND ANALYSIS OF PLANAR
PRESSURE PULSE GENERATOR AND TWO-STAGE FAN
TEST DATA**

*GENERAL ELECTRIC COMPANY
AIRCRAFT ENGINE GROUP
CINCINNATI, OHIO 45215*

AUGUST 1976

TECHNICAL REPORT AFAPL-TR-76-76
FINAL REPORT FOR PERIOD 1 APRIL 1975 - 31 MAY 1976



Approved for public release; distribution unlimited

AIR FORCE AERO-PROPULSION LABORATORY
AIR FORCE WRIGHT AERONAUTICAL LABORATORIES
AIR FORCE SYSTEMS COMMAND
WRIGHT-PATTERSON AIR FORCE BASE, OHIO 45433


NOTICE

When Government drawings, specifications, or other data are used for any purpose other than in connection with a definitely related Government procurement operation, the United States Government thereby incurs no responsibility nor any obligation whatsoever; and the fact that the government may have formulated, furnished, or in any way supplied the said drawings, specifications, or other data, is not to be regarded by implication or otherwise as in any manner licensing the holder or any other person or corporation, or conveying any rights or permission to manufacture, use, or sell any patented invention that may in any way be related thereto.

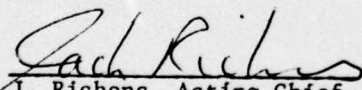
This final report was submitted by the General Electric Company Aircraft Engine Group, under Contract F33615-75-C-2029. The effort was sponsored by the Air Force Aero Propulsion Laboratory, Air Force Systems Command, Wright-Patterson AFB, Ohio under Project 3066, Task II, Work Unit 17 with Mr. S.J. Przybylko/AFAPL/TBA as Project Engineer. This program was initiated with FY 75 Aero Propulsion Laboratory Director's Funds. Dr. William G. Steenken of the General Electric Company was technically responsible for the work. The General Electric Program Manager was Mr. V.L. Reed; the Principle investigator was Mr. G.G. Reynolds. The expertise provided by Mr. W.A. Tesch in modifying the computer program is gratefully acknowledged.

This report has been reviewed by the Information Office, (ASD/OIP) and is releasable to the National Technical Information Service (NTIS). At NTIS, it will be available to the general public, including foreign nations.

This technical report has been reviewed and is approved for publication.


S.J. Przybylko
Project Manager

FOR THE COMMANDER


J. Richens, Acting Chief
Performance Branch

ACCESSION for	
NTIS	White Section <input checked="" type="checkbox"/>
DDC	Ref Section <input type="checkbox"/>
UNANNOUNCED	<input type="checkbox"/>
JUSTIFICATION	
BY	
DISTRIBUTION/AVAILABILITY CODES	
Dist.	AVAIL. and/or SPECIAL
A	

Copies of this report should not be returned unless return is required by security considerations, contractual obligations, or notice on a specific document.

Unclassified

SECURITY CLASSIFICATION OF THIS PAGE (When Data Entered)

REPORT DOCUMENTATION PAGE		READ INSTRUCTIONS BEFORE COMPLETING FORM
1. REPORT NUMBER AFAPL TR-76-76	2. GOVT ACCESSION NO.	3. RECIPIENT'S CATALOG NUMBER
4. TITLE (and Subtitle) DYNAMIC DIGITAL BLADE ROW COMPRESSION COMPONENT STABILITY MODEL Model Validation and Analysis of Planar Pressure Pulse Generation and Two-Stage Fan Test Data	5. TYPE OF REPORT & PERIOD COVERED Final Technical Report, 1 Apr 1975 - 31 May 1976	
7. AUTHOR G.G./Reynolds W.G./Steenken	6. PERFORMING ORG. REPORT NUMBER R76AEG299	
9. PERFORMING ORGANIZATION NAME AND ADDRESS General Electric Company Aircraft Engine Group, AE&TPD Cincinnati, Ohio 45215	8. CONTRACT OR GRANT NUMBER(s) F33615-75-C-2629 NEW	
11. CONTROLLING OFFICE NAME AND ADDRESS Air Force Aero Propulsion Laboratory (AFAPL/TB) Air Force Wright Aeronautical Laboratories Wright-Patterson AFB, Ohio 45433	10. PROGRAM ELEMENT, PROJECT, TASK AREA & WORK UNIT NUMBERS Project 3966 Task 11 Work Unit 17	
14. MONITORING AGENCY NAME & ADDRESS (if different from Controlling Office)	12. REPORT DATE August 1976	
	13. NUMBER OF PAGES 280 12 294p	
	15. SECURITY CLASS. (of this report) Unclassified	
15a. DECLASSIFICATION/DOWNGRADING SCHEDULE		
16. DISTRIBUTION STATEMENT (of this Report) Approved for Public Release; Distribution Unlimited		
17. DISTRIBUTION STATEMENT (of the abstract entered in Block 20, if different from Report) ---		
18. SUPPLEMENTARY NOTES		
19. KEY WORDS (Continue on reverse side if necessary and identify by block number) Two-Stage Fan Dynamic Distortion Sensitivity Fan and Compressor Stability Fan Transmission Characteristics Analytical Simulation Technique Turbomachinery Unsteady Flows Planar Wave Simulation		
20. ABSTRACT (Continue on reverse side if necessary and identify by block number) The objectives of this study were to determine the range of validity of a Dynamic Digital Blade Row Compression Component Stability Computer Model by comparing the results of model simulations with previously obtained test data and to determine the manner in which a fan component responded to imposed unsteady aerodynamics by examining calculated parameters. Validation of the modeling technique was obtained by simulating a facility and test conditions where the response of a two-stage fan to planar waves was deter-		

DD FORM 1 JAN 73 1473

EDITION OF 1 NOV 65 IS OBSOLETE

Unclassified
SECURITY CLASSIFICATION OF THIS PAGE (When Data Entered)

403468

[Signature]

Next page →

Unclassified

SECURITY CLASSIFICATION OF THIS PAGE(When Data Entered)

20. ABSTRACT

mined. The simulation of the two-stage fan component was carried out using a quasi one-dimensional, pitch line, blade-row by blade-row model which used blade-row loss coefficients and deviation angles determined from analysis of clean-inlet-flow test data. This model was ideally suited for studying the fan response to the planar waves produced by the Planar Pressure Pulse Generator, a device which produced highly planar waves with peak-to-peak fluctuations of 10-30 percent of the mean total pressure over a frequency range of 42 to 800 Hz.

The results of the simulations showed that the model accurately reproduced the waveshape, amplitude, and phase of the experimentally determined fan inlet and exit pressures and the fan inlet flow up to 75 Hz where the need for including unsteady blade circulation effects on blade characteristics began to become apparent. Further, the blade row model showed accurate simulation of the pressures in the interconnecting ducts by reproducing the wave and its harmonics up to approximately 118 Hz where the length of the volumes becomes too large to provide proper spatial definition of the harmonics of the standing waves although the fundamental frequency is properly reproduced. In addition, the model accurately predicted the trends and approximately predicts the level of fan dynamic distortion sensitivity and transfer.

A method for including the unsteady blade circulation effects in the fan simulation has been investigated and appears to improve the phase relationships between predicted and test values at higher frequencies. Further refinement of this method is required. ←

Unclassified

SECURITY CLASSIFICATION OF THIS PAGE(When Data Entered)

TABLE OF CONTENTS

<u>Section</u>		<u>Page</u>
1.0	SUMMARY	1
2.0	INTRODUCTION	3
3.0	PLANAR PRESSURE PULSE GENERATOR AND TWO-STAGE FAN TEST AND RESULTS	6
3.1	Test Description	6
3.2	Results of Test Data Analysis	9
3.3	Data Enhancement Analysis	13
4.0	DESCRIPTION OF DYNAMIC DIGITAL MODEL	20
4.1	Overview of Model Techniques	20
4.2	Digital Compression Component Model Refinements	29
4.2.1	Free-Volume Mean Pressure	30
4.2.2	Tangential Blade Force in Unsteady Flows	33
4.2.3	Unsteady Blade Characteristics	35
4.3	Digital Model of Planar Pressure Pulse Generator	41
4.4	Digital Model of Test Installation	42
4.4.1	System Geometry	42
4.4.2	Two-Stage Fan Characteristics	50
4.4.3	Boundary Conditions	51
4.5	Method of Model Operation	53
4.6	Instability Identification	53
5.0	RESULTS OF DIGITAL SIMULATIONS AND COMPARISONS WITH TEST DATA	55
5.1	Clean Inlet Flow	55
5.2	Validation of Model Dynamic Characteristics	55

TABLE OF CONTENTS (Concluded)

<u>Section</u>	<u>Page</u>
5.2.1 Waveform Fidelity	55
5.2.1.1 Simulation of Rdg. 71, 100% $N/\sqrt{\theta}$, 42 Hz	65
5.2.1.2 Simulation of Rdg. 82, 80% $N/\sqrt{\theta}$, 42 Hz	65
5.2.1.3 Simulation of Rdg. 69, 100% $N/\sqrt{\theta}$, 80 Hz	65
5.2.1.4 Simulation of Rdg. 77, 80% $N/\sqrt{\theta}$, 75 Hz	69
5.2.1.5 Simulation of Rdg. 64, 100% $N/\sqrt{\theta}$, 118 Hz	69
5.2.1.6 Simulation of Rdg. 61, 80% $N/\sqrt{\theta}$, 118 Hz	69
5.2.1.7 Simulation of Rdg. 41, 100% $N/\sqrt{\theta}$, 220 Hz and Rdg. 57, 80% $N/\sqrt{\theta}$, 240 Hz	73
5.2.1.8 Simulation of Rdg. 43, 100% $N/\sqrt{\theta}$, 350 Hz and Rdg. 53, 80% $N/\sqrt{\theta}$, 350 Hz	73
5.2.2 Sample Plotted Results	73
5.3 Fan Planar Wave Distortion Transfer	85
5.4 Instability Analysis	97
5.4.1 General Observations	97
5.4.2 Discussion of Instability Point Data	97
5.4.3 Surge Pressure Ratio Sensitivity	109
5.4.4 Sample Plotted Results	111
5.4.5 Stage Initiating Instability	117
5.5 Effect of Unsteady Blade Characteristics	118
6.0 CONCLUSIONS AND RECOMMENDATIONS	122
 <u>APPENDICES</u>	
A. Data Enhancement of Corrected Airflow and Pressure Ratio	125
B. Loss Coefficients, Deviation Angles, and Lift Direction Angles as a Function of Incidence Angle	130
C. Plot Data from Stationary Model Operation	144
D. Amplitude Transmission Characteristics	229
E. Instability Identification Parameters	242
REFERENCES	273
GLOSSARY	275
NOMENCLATURE	276

LIST OF ILLUSTRATIONS

<u>Figure</u>		<u>Page</u>
1.	Clean-Inlet-Flow Two-Stage Fan Map.	7
2.	Scaled Installation Layout and Instrumentation Locations.	8
3.	Planar Wave Distortion Sensitivity, $N/\sqrt{\theta} = 80\%$.	11
4.	Planar Wave Distortion Sensitivity, $N/\sqrt{\theta} = 100\%$.	12
5.	Fan Hub Planar Wave Distortion Transfer.	14
6.	Fan Tip Planar Wave Distortion Transfer.	15
7.	Posttest Steady-State Surge Margin Check.	16
8.	Data Enhancement, Rdg. 41 $N/\sqrt{\theta} = 100\%$, 220 Hz.	18
9.	Ensemble Averaged Waveforms, Rdg. 71, 100% $N/\sqrt{\theta}$, 42 Hz.	19
10.	Dynamic Model Block Diagram.	27
11.	Dyanmic Lift Coefficient in a Cascade.	37
12.	Dynamic Lift Coefficient in a Cascade Extrapolated For Higher Solidities.	39
13.	Time Constant Coefficient as a Function of Solidity.	40
14.	System Area Distribution.	43
15.	Loss Coefficient and Deviation Angle Polynomial Representation.	52
16.	Clean Inlet Two-Stage Fan Map.	56
17.	Airflow Ratio Vs. Time, 100% $N/\sqrt{\theta}$, Steady-State Surge.	57
18.	Airflow Ratio Vs. Time, 80% $N/\sqrt{\theta}$, Steady-State Surge.	58
19.	Amplitude Comparison of Model and Test Results, 80% $N/\sqrt{\theta}$.	61
20.	Amplitude Comparison of Model and Test Results, 100% $N/\sqrt{\theta}$.	62
21.	Phase Angle Comparison of Model and Test Results, 80% $N/\sqrt{\theta}$.	63
22.	Phase Angle Comparison of Model and Test Results, 100% $N/\sqrt{\theta}$.	64
23.	Simulation of Rdg. 71, 100% $N/\sqrt{\theta}$, 42 Hz.	66
24.	Simulation of Rdg. 82, 80% $N/\sqrt{\theta}$, 42 Hz.	67
25.	Simulation of Rdg. 69, 100% $N/\sqrt{\theta}$, 80 Hz.	68
26.	Simulation of Rdg. 77, 80% $N/\sqrt{\theta}$, 75 Hz..	70
27.	Simulation of Rdg. 64, 100% $N/\sqrt{\theta}$, 118 Hz.	71
28.	Simulation of Rdg. 61, 80% $N/\sqrt{\theta}$, 118 Hz.	72
29.	Simulation of Rdg. 41, 100% $N/\sqrt{\theta}$, 220 Hz.	74

LIST OF ILLUSTRATIONS (Continued)

<u>Figure</u>		<u>Page</u>
30.	Simulation of Rdg. 57, 80% $N/\sqrt{\theta}$, 240 Hz.	75
31.	Simulation of Rdg. 43, 100% $N/\sqrt{\theta}$, 350 Hz.	76
32.	Simulation of Rdg. 53, 80% $N/\sqrt{\theta}$, 350 Hz.	77
33.	Physical Airflow Vs. Time, 100% $N/\sqrt{\theta}$, 42 Hz.	78
34.	Tangent of Incidence Angle Vs. Time, 100% $N/\sqrt{\theta}$, 42 Hz.	79
35.	Loss Coefficient Vs. Time, 100% $N/\sqrt{\theta}$, 42 Hz.	80
36.	Tangent of Deviation Angle Vs. Time, 100% $N/\sqrt{\theta}$, 42 Hz.	81
37.	Blade Row Total-Pressure Ratio Vs. Time, 100% $N/\sqrt{\theta}$, 42 Hz.	82
38.	Blade Row Static-Pressure Ratio Vs. Time, 100% $N/\sqrt{\theta}$, 42 Hz.	83
39.	Blade Row Total-Temperature Ratio Vs. Time, 100% $N/\sqrt{\theta}$, 42 Hz.	84
40.	Amplitude Transmission Characteristics, 100% $N/\sqrt{\theta}$, 42 Hz.	86
41.	Amplitude Transmission Characteristics, 100% $N/\sqrt{\theta}$, IGV.	88
42.	Amplitude Transmission Characteristics, 100% $N/\sqrt{\theta}$, Stage 1.	89
43.	Amplitude Transmission Characteristics, 100% $N/\sqrt{\theta}$, Stage 2.	90
44.	Amplitude Transmission Characteristics, 80% $N/\sqrt{\theta}$, IGV.	91
45.	Amplitude Transmission Characteristics, 80% $N/\sqrt{\theta}$, Stage 1.	92
46.	Amplitude Transmission Characteristics, 80% $N/\sqrt{\theta}$, Stage 2.	93
47.	Fan Planar Wave Transfer, 100% $N/\sqrt{\theta}$.	94
48.	Fan Planar Wave Transfer, 80% $N/\sqrt{\theta}$.	96
49.	Airflow Ratio Vs. Time, 100% $N/\sqrt{\theta}$, 80 Hz, Surge.	99
50.	Unsteady Blade Force Vs. Time, 100% $N/\sqrt{\theta}$, 80 Hz, Surge.	100
51.	Path of Model Mean Operating Point, 80% $N/\sqrt{\theta}$, 240 Hz, Surge.	101
52.	Amplification Function Vs. Time, 80% $N/\sqrt{\theta}$, 240 Hz, Surge.	102
53.	Amplification Function Vs. Time, 100% $N/\sqrt{\theta}$, 350 Hz, Stationary.	103
54.	Comparison of Model Vs. Test, Mean Operating Point Path, 100% $N/\sqrt{\theta}$, 350 Hz.	105
55.	Unsteady Blade Force Vs. Time, 80% $N/\sqrt{\theta}$, 350 Hz, Surge.	106
56.	Fan Map Representation of Model Instability Characteristics.	107
57.	Model Interstage Instability Characteristics.	108
58.	Planar Wave Distortion Sensitivity, 100% $N/\sqrt{\theta}$.	110
59.	Planar Wave Distortion Sensitivity, 80% $N/\sqrt{\theta}$.	112

LIST OF ILLUSTRATIONS (Continued)

<u>Figure</u>		<u>Page</u>
60.	Unsteady Blade Force Vs. Time, 100% $N/\sqrt{\theta}$, 118 Hz.	114
61.	Amplification Function Vs. Time, 100% $N/\sqrt{\theta}$, 118 Hz.	115
62.	Tangent of Incidence Angle Vs. Time, 100% $N/\sqrt{\theta}$, 118 Hz.	116
63.	Circulation Readjustment, 100% $N/\sqrt{\theta}$, 80 Hz.	119
64.	Circulation Readjustment, 100% $N/\sqrt{\theta}$, 118 Hz.	120
65.	Enhancement of Rdg. 71 Data, 100% $N/\sqrt{\theta}$, 42 Hz.	126
66.	Enhancement of Rdg. 69 Data, 100% $N/\sqrt{\theta}$, 80 Hz.	127
67.	Enhancement of Rdg. 43 Data, 100% $N/\sqrt{\theta}$, 350 Hz.	128
68.	Enhancement of Rdg. 77 Data, 80% $N/\sqrt{\theta}$, 75 Hz.	129
69.	Two-Stage Fan Rotor 1 Total-Pressure Loss Coefficients, 100% $N/\sqrt{\theta}$.	131
70.	Two-Stage Fan Rotor 1 Deviation Angles, 100% $N/\sqrt{\theta}$.	132
71.	Two-Stage Fan Rotor 2 Total-Pressure Loss Coefficients, 100% $N/\sqrt{\theta}$.	133
72.	Two-Stage Fan Rotor 2 Deviation Angles, 100% $N/\sqrt{\theta}$.	134
73.	Two-Stage Fan Rotor 1 Total-Pressure Loss Coefficients, 80% $N/\sqrt{\theta}$.	135
74.	Two-Stage Fan Rotor 1 Deviation Angles, 80% $N/\sqrt{\theta}$.	136
75.	Two-Stage Fan Rotor 2 Total-Pressure Loss Coefficients, 80% $N/\sqrt{\theta}$.	137
76.	Two-Stage Fan Rotor 2 Deviation Angles, 80% $N/\sqrt{\theta}$.	138
77.	Two-Stage Fan Lift Direction Correction Angles, 100% $N/\sqrt{\theta}$.	141
78.	Two-Stage Fan Lift Direction Correction Angles, 80% $N/\sqrt{\theta}$.	142
79.	Physical Airflow Vs. Time, 100% $N/\sqrt{\theta}$, 25 Hz.	145
80.	Tangent of Incidence Angle Vs. Time, 100% $N/\sqrt{\theta}$, 25 Hz.	146
81.	Loss Coefficient Vs. Time, 100% $N/\sqrt{\theta}$, 25 Hz.	147
82.	Tangent of Deviation Angle Vs. Time, 100% $N/\sqrt{\theta}$, 25 Hz.	148
83.	Blade Row Total-Pressure Ratio Vs. Time, 100% $N/\sqrt{\theta}$, 25 Hz.	149
84.	Blade Row Static-Pressure Ratio Vs. Time, 100% $N/\sqrt{\theta}$, 25 Hz.	150
85.	Blade Row Total-Temperature Ratio Vs. Time, 100% $N/\sqrt{\theta}$, 25 Hz.	151
86.	Physical Airflow Vs. Time, 100% $N/\sqrt{\theta}$, 42 Hz.	152
87.	Tangent of Incidence Angle Vs. Time, 100% $N/\sqrt{\theta}$, 42 Hz.	153

LIST OF ILLUSTRATIONS (Continued)

<u>Figure</u>		<u>Page</u>
88.	Loss Coefficient Vs. Time, 100% $N/\sqrt{\theta}$, 42 Hz.	154
89.	Tangent of Deviation Angle Vs. Time, 100% $N/\sqrt{\theta}$, 42 Hz.	155
90.	Blade Row Total-Pressure Ratio Vs. Time, 100% $N/\sqrt{\theta}$, 42 Hz.	156
91.	Blade Row Static-Pressure Ratio Vs. Time, 100% $N/\sqrt{\theta}$, 42 Hz.	157
92.	Blade Row Total-Temperature Ratio Vs. Time, 100% $N/\sqrt{\theta}$, 42 Hz.	158
93.	Physical Airflow Vs. Time, 100% $N/\sqrt{\theta}$, 60 Hz.	159
94.	Tangent of Incidence Angle Vs. Time, 100% $N/\sqrt{\theta}$, 60 Hz.	160
95.	Loss Coefficient Vs. Time, 100% $N/\sqrt{\theta}$, 60 Hz.	161
96.	Tangent of Deviation Angle Vs. Time, 100% $N/\sqrt{\theta}$, 60 Hz.	162
97.	Blade Row Total-Pressure Ratio Vs. Time, 100% $N/\sqrt{\theta}$, 60 Hz.	163
98.	Blade Row Static-Pressure Ratio Time, 100% $N/\sqrt{\theta}$, 60 Hz.	164
99.	Blade Row Total-Temperature Ratio Vs. Time, 100% $N/\sqrt{\theta}$, 60 Hz.	165
100.	Physical Airflow Vs. Time, 100% $N/\sqrt{\theta}$, 80 Hz.	166
101.	Tangent of Incidence Angle Vs. Time, 100% $N/\sqrt{\theta}$, 80 Hz.	167
102.	Loss Coefficient Vs. Time, 100% $N/\sqrt{\theta}$, 80 Hz.	168
103.	Tangent of Deviation Angle Vs. Time, 100% $N/\sqrt{\theta}$, 80 Hz.	169
104.	Blade Row Total-Pressure Ratio Vs. Time, 100% $N/\sqrt{\theta}$, 80 Hz.	170
105.	Blade Row Static-Pressure Ratio Vs. Time, 100% $N/\sqrt{\theta}$, 80 Hz.	171
106.	Blade Row Total-Temperature Ratio Vs. Time, 100% $N/\sqrt{\theta}$, 80 Hz.	172
107.	Physical Airflow Vs. Time, 100% $N/\sqrt{\theta}$, 118 Hz.	173
108.	Tangent of Incidence Angle Vs. Time, 100% $N/\sqrt{\theta}$, 118 Hz.	174
109.	Loss Coefficient Vs. Time, 100% $N/\sqrt{\theta}$, 118 Hz.	175
110.	Tangent of Deviation Angle Vs. Time, 100% $N/\sqrt{\theta}$, 118 Hz.	176
111.	Blade Row Total-Pressure Ratio Vs. Time, 100% $N/\sqrt{\theta}$, 118 Hz.	177
112.	Blade Row Static-Pressure Ratio Vs. Time, 100% $N/\sqrt{\theta}$ 118 Hz.	178
113.	Blade Row Total-Temperature Ratio Vs. Time, 100% $N/\sqrt{\theta}$, 118 Hz.	179
114.	Physical Airflow Vs. Time, 100% $N/\sqrt{\theta}$, 220 Hz.	180
115.	Tangent of Incidence Angle Vs. Time, 100% $N/\sqrt{\theta}$, 220 Hz.	181
116.	Loss Coefficient Vs. Time, 100% $N/\sqrt{\theta}$, 220 Hz.	182
117.	Tangent of Deviation Angle Vs. Time, 100% $N/\sqrt{\theta}$, 220 Hz.	183

LIST OF ILLUSTRATIONS (Continued)

<u>Figure</u>		<u>Page</u>
118.	Blade Row Total-Pressure Ratio Vs. Time, 100% $N/\sqrt{\theta}$, 220 Hz.	184
119.	Blade Row Static-Pressure Ratio Vs. Time, 100% $N/\sqrt{\theta}$, 220 Hz.	185
120.	Blade Row Total-Temperature Ratio Vs. Time, 100% $N/\sqrt{\theta}$, 220 Hz.	186
121.	Physical Airflow Vs. Time, 100% $N/\sqrt{\theta}$, 350 Hz.	187
122.	Tangent of Incidence Angle Vs. Time, 100% $N/\sqrt{\theta}$, 350 Hz.	188
123.	Loss Coefficient Vs. Time, 100% $N/\sqrt{\theta}$, 350 Hz.	189
124.	Tangent of Deviation Angle Vs. Time, 100% $N/\sqrt{\theta}$, 350 Hz.	190
125.	Blade Row Total-Pressure Ratio Vs. Time, 100% $N/\sqrt{\theta}$, 350 Hz.	191
126.	Blade Row Static-Pressure Ratio Vs. Time, 100% $N/\sqrt{\theta}$, 350 Hz.	192
127.	Blade Row Total-Temperature Ratio Vs. Time, 100% $N/\sqrt{\theta}$, 350 Hz.	193
128.	Physical Airflow Vs. Time, 80% $N/\sqrt{\theta}$, 42 Hz.	194
129.	Tangent of Incidence Angle Vs. Time, 80% $N/\sqrt{\theta}$, 42 Hz.	195
130.	Loss Coefficient Vs. Time, 80% $N/\sqrt{\theta}$, 42 Hz.	196
131.	Tangent of Deviation Angle Vs. Time, 80% $N/\sqrt{\theta}$, 42 Hz.	197
132.	Blade Row Total-Pressure Ratio Vs. Time, 80% $N/\sqrt{\theta}$, 42 Hz.	198
133.	Blade Row Static-Pressure Ratio Vs. Time, 80% $N/\sqrt{\theta}$, 42 Hz.	199
134.	Blade Row Total-Temperature Ratio Vs. Time, 80% $N/\sqrt{\theta}$, 42 Hz.	200
135.	Physical Airflow Vs. Time, 80% $N/\sqrt{\theta}$, 75 Hz.	201
136.	Tangent of Incidence Angle Vs. Time, 80% $N/\sqrt{\theta}$, 75 Hz.	202
137.	Loss Coefficient Vs. Time, 80% $N/\sqrt{\theta}$, 75 Hz.	203
138.	Tangent of Deviation Angle Vs. Time, 80% $N/\sqrt{\theta}$, 75 Hz.	204
139.	Blade Row Total-Pressure Ratio Vs. Time, 80% $N/\sqrt{\theta}$, 75 Hz.	205
140.	Blade Row Static-Pressure Ratio Vs. Time, 80% $N/\sqrt{\theta}$, 75 Hz.	206
141.	Blade Row Total-Temperature Ratio Vs. Time, 80% $N/\sqrt{\theta}$, 75 Hz.	207
142.	Physical Airflow Vs. Time, 80% $N/\sqrt{\theta}$, 118 Hz.	208
143.	Tangent of Incidence Angle Vs. Time, 80% $N/\sqrt{\theta}$, 118 Hz.	209
144.	Loss Coefficient Vs. Time, 80% $N/\sqrt{\theta}$, 118 Hz.	210
145.	Tangent of Deviation Angle Vs. Time, 80% $N/\sqrt{\theta}$, 118 Hz.	211
146.	Blade Row Total-Pressure Ratio Vs. Time, 80% $N/\sqrt{\theta}$, 118 Hz.	212
147.	Blade Row Static-Pressure Ratio Vs. Time, 80% $N/\sqrt{\theta}$, 118 Hz.	213
148.	Blade Row Total-Temperature Ratio Vs. Time, 80% $N/\sqrt{\theta}$, 118 Hz.	214

LIST OF ILLUSTRATIONS (Continued)

<u>Figure</u>		<u>Page</u>
149.	Physical Airflow Vs. Time, 80% $N/\sqrt{\theta}$, 240 Hz.	215
150.	Tangent of Incidence Angle Vs. Time, 80% $N/\sqrt{\theta}$, 240 Hz.	216
151.	Loss Coefficient Vs. Time, 80% $N/\sqrt{\theta}$, 240 Hz.	217
152.	Tangent of Deviation Angle Vs. Time, 80% $N/\sqrt{\theta}$, 240 Hz.	218
153.	Blade Row Total-Pressure Ratio Vs. Time, 80% $N/\sqrt{\theta}$, 240 Hz.	219
154.	Blade Row Static-Pressure Ratio Vs. Time, 80% $N/\sqrt{\theta}$, 240 Hz.	220
155.	Blade Row Total-Temperature Ratio Vs. Time, 80% $N/\sqrt{\theta}$, 240 Hz.	221
156.	Physical Airflow Vs. Time, 80% $N/\sqrt{\theta}$, 350 Hz.	222
157.	Tangent of Incidence Angle Vs. Time, 80% $N/\sqrt{\theta}$, 350 Hz.	223
158.	Loss Coefficient Vs. Time, 100% $N/\sqrt{\theta}$, 350 Hz.	224
159.	Tangent of Deviation Angle Vs. Time, 80% $N/\sqrt{\theta}$, 350 Hz.	225
160.	Blade Row Total-Pressure Ratio Vs. Time, 80% $N/\sqrt{\theta}$, 350 Hz.	226
161.	Blade Row Static-Pressure Ratio Vs. Time, 80% $N/\sqrt{\theta}$, 350 Hz.	227
162.	Blade Row Total-Temperature Ratio Vs. Time, 80% $N/\sqrt{\theta}$, 350 Hz.	228
163.	Amplitude Transmission Characteristics, 100% $N/\sqrt{\theta}$, 25 Hz.	230
164.	Amplitude Transmission Characteristics, 100% $N/\sqrt{\theta}$, 42 Hz.	231
165.	Amplitude Transmission Characteristics, 100% $N/\sqrt{\theta}$, 60 Hz.	232
166.	Amplitude Transmission Characteristics, 100% $N/\sqrt{\theta}$, 80 Hz.	233
167.	Amplitude Transmission Characteristics, 100% $N/\sqrt{\theta}$, 118 Hz.	234
168.	Amplitude Transmission Characteristics, 100% $N/\sqrt{\theta}$, 220 Hz.	235
169.	Amplitude Transmission Characteristics, 100% $N/\sqrt{\theta}$, 350 Hz.	236
170.	Amplitude Transmission Characteristics, 80% $N/\sqrt{\theta}$, 42 Hz.	237
171.	Amplitude Transmission Characteristics, 80% $N/\sqrt{\theta}$, 75 Hz.	238
172.	Amplitude Transmission Characteristics, 80% $N/\sqrt{\theta}$, 118 Hz.	239
173.	Amplitude Transmission Characteristics, 80% $N/\sqrt{\theta}$, 240 Hz.	240
174.	Amplitude Transmission Characteristics, 80% $N/\sqrt{\theta}$, 350 Hz.	241
175.	Unsteady Blade Force Vs. Time, 100% $N/\sqrt{\theta}$, 25 Hz.	243
176.	Amplification Function Vs. Time, 100% $N/\sqrt{\theta}$, 25 Hz.	244
177.	Tangent of Incidence Angle Vs. Time, 100% $N/\sqrt{\theta}$, 25 Hz.	245
178.	Unsteady Blade Force Vs. Time, 100% $N/\sqrt{\theta}$, 60 Hz.	246

LIST OF ILLUSTRATIONS (Concluded)

<u>Figure</u>		<u>Page</u>
179.	Amplification Function Vs. Time, 100% $N/\sqrt{\theta}$, 60 Hz.	247
180.	Tangent of Incidence Angle Vs. Time, 100% $N/\sqrt{\theta}$, 60 Hz.	248
181.	Unsteady Blade Force Vs. Time, 100% $N/\sqrt{\theta}$, 118 Hz.	249
182.	Amplification Function Vs. Time, 100% $N/\sqrt{\theta}$, 118 Hz.	250
183.	Tangent of Incidence Angle Vs. Time, 100% $N/\sqrt{\theta}$, 118 Hz.	251
184.	Unsteady Blade Force Vs. Time, 100% $N/\sqrt{\theta}$, 220 Hz.	252
185.	Amplification Function Vs. Time, 100% $N/\sqrt{\theta}$, 220 Hz.	253
186.	Tangent of Incidence Angle Vs. Time, 100% $N/\sqrt{\theta}$, 220 Hz.	254
187.	Unsteady Blade Force Vs. Time, 100% $N/\sqrt{\theta}$, 350 Hz.	255
188.	Amplification Function Vs. Time, 100% $N/\sqrt{\theta}$, 350 Hz.	256
189.	Tangent of Incidence Angle Vs. Time, 100% $N/\sqrt{\theta}$, 350 Hz.	257
190.	Unsteady Blade Force Vs. Time, 80% $N/\sqrt{\theta}$, 42 Hz.	258
191.	Amplification Function Vs. Time, 80% $N/\sqrt{\theta}$, 42 Hz.	259
192.	Tangent of Incidence Angle Vs. Time, 80% $N/\sqrt{\theta}$, 42 Hz.	260
193.	Unsteady Blade Force Vs. Time, 80% $N/\sqrt{\theta}$, 75 Hz.	261
194.	Amplification Function Vs. Time, 80% $N/\sqrt{\theta}$, 75 Hz.	262
195.	Tangent of Incidence Angle Vs. Time, 80% $N/\sqrt{\theta}$, 75 Hz.	263
196.	Unsteady Blade Force Vs. Time, 80% $N/\sqrt{\theta}$, 118 Hz.	264
197.	Amplification Function Vs. Time, 80% $N/\sqrt{\theta}$, 118 Hz.	265
198.	Tangent of Incidence Angle Vs. Time, 80% $N/\sqrt{\theta}$, 118 Hz.	266
199.	Unsteady Blade Force Vs. Time, 80% $N/\sqrt{\theta}$, 240 Hz.	267
200.	Amplification Function Vs. Time, 80% $N/\sqrt{\theta}$, 240 Hz.	268
201.	Tangent of Incidence Angle Vs. Time, 80% $N/\sqrt{\theta}$, 240 Hz.	269
202.	Unsteady Blade Force Vs. Time, 80% $N/\sqrt{\theta}$, 350 Hz.	270
203.	Amplification Function Vs. Time, 80% $N/\sqrt{\theta}$, 350 Hz.	271
204.	Tangent of Incidence Angle Vs. Time, 80% $N/\sqrt{\theta}$, 350 Hz.	272

LIST OF TABLES

<u>Table</u>	<u>Page</u>
1. Summary of Surge Points.	10
2. Isentropic Relationships Polynomial Coefficients.	31
3. System Geometry.	45
4. IGV Schedule.	49
5. Model Parameters Used in Validation Study.	49
6. Summary of Model and Test Planar Wave Distortion Transfer Results.	95
7. Model and Test Planar Wave Distortion Sensitivities.	113
8. Model Stage Initiating Instability.	117
9. Polynomial Representation of Two-Stage Fan Characteristics, 100% $N/\sqrt{\theta}$.	139
10. Polynomial Representation of Two-Stage Fan Characteristics, 80% $N/\sqrt{\theta}$.	140
11. Lift Direction Correction Angle Coefficients.	143

1.0 SUMMARY

The objectives of this program were to demonstrate that a one-dimensional pitch-line Dynamic Digital Blade Row Compression Component Stability Model could provide an accurate simulation of a fan component when the fan was subjected to planar wave oscillations and to show the manner in which the fan aerodynamics responded to the unsteady flows.

The capability of the model to provide accurate simulations was demonstrated by conducting simulations of test points obtained during testing of a two-stage fan component and the Planar Pressure Pulse Generator used to generate an unsteady-planar-wave fan inflow. The capability of the model to handle unsteady flows was improved by introducing an analytical expression for the mean pressure acting on the lateral surfaces of a blade free volume, by including the tangential force resulting from the storage of angular momentum within a blade row volume, and by developing a method for handling the unsteady effects upon blade circulation.

The two-stage fan map was accurately simulated at 80% and 100% corrected speeds. Accurate prediction of the surge line was made through use of a previously established technique which is based upon the ratio of the flow leaving a blade row volume to the flow entering the volume.

Simulations of the Planar Pressure Pulse Generator test data were made over the 42 Hz to 350 Hz frequency range. These simulations gave accurate replication of the measured waveforms throughout the model over the 42 Hz to 80 Hz frequency range at both 80- and 100-percent corrected speeds. At higher frequencies the model had increasing difficulty in duplicating the harmonics in the waveforms such that at 220 Hz, the waveform harmonics are completely washed out, although the fundamental frequency appears to be adequately reproduced. The lack of reproduction of the harmonics is attributed to the presence of standing waves and the lack of spatial resolution; that is, the selected volume lengths are not sufficiently small compared to the wavelengths associated with the harmonic frequencies that are present. Planar wave distortion transfer was calculated from the model results and its value was found to fall between the hub and tip test values as should be the case for a pitch line model. In fact, the model predicted the anomalous amplification that was present in the test data at 118 Hz, 80% corrected speed.

Analysis of the stationary data prior to throttling to surge showed that at frequencies greater than 80 Hz ($\omega^* \approx 0.25$), the model-calculated-parameters downstream of the fan were out of phase with the measured variables with the former leading. The phase angle also appeared to be a function of frequency. This behavior was anticipated since the basic model formulation assumed that the blade characteristics adjusted instantaneously to the new incidence angle. Inclusion of an effective incidence angle based upon a blade-row time constant led to results which produced a lag in the calculated downstream parameters. However, further refinement of the time constant is needed.

Prior to discussing the results obtained by throttling the model to surge, it should be noted that the surge line results are based upon blade characteristics which have been extrapolated beyond values associated with the steady-state surge line. Such extrapolations are necessary if the model is to function in the presence of unsteady flows. The model was throttled to surge with the planar-wave inlet conditions and several interesting findings emerged. It was found that the planar-wave distortion-sensitivity trends and magnitudes were essentially reproduced out to 75 Hz, but at 118 Hz and above, especially, for 100% corrected speed, the magnitude of the sensitivity deviated considerably from test values. Further, it was interesting to note that at the experimentally determined surge points, the model exhibited behavior that appeared to duplicate the actual fan response; that is, at 100% corrected speed, the model instability developed extremely rapidly and computation ceased abruptly while at the 80% corrected speed, the model exhibited a much slower developing instability marked by erratic behavior of the fan internal aerodynamics. One parameter of particular interest was the tangential blade force associated with the storage of angular momentum within a blade-row volume. This parameter was very sensitive to developing instabilities and its increasingly time dependent and erratic behavior was the first evidence that an aerodynamic instability was developing, although all basic flow parameters were well behaved. It is possible that this force could provide an important analytic link between the aerodynamic and aeroelastic responses of a compression component.

The results of this study are most encouraging with respect to demonstrating the validity of the Dynamic Digital Blade Row Compression Component Stability Model. Improvements to this model can be made in three areas: 1) Volume-length selection with respect to increasing the frequency response of the model, 2) Improvement of the post-surge extrapolated blade-row characteristics and, 3) Refinement of the technique for including the finite time needed for the blade circulations to readjust.

2.0 INTRODUCTION

The time-varying characteristics of total-pressure distortion lead to documented losses in surge pressure ratio (References 1 and 2). In these studies, the loss in surge pressure ratio can be viewed as resulting from an imposed steady-state distortion and a random time-varying distortion fluctuating about the steady-state level. While these studies provide gross information concerning the effect of the flow unsteadiness characteristic of that produced by aircraft inlets, its random nature precludes deterministic analysis of the unsteady aerodynamic processes which take place within a compression component and the manner in which they induce surge. Compression component response to total-pressure fluctuations as a function of frequency was determined by subjecting a two-stage fan to inlet planar-wave total-pressure fluctuations, that is, deterministic time-varying oscillations. This effort has been reported upon by Reynolds, Vier, and Collins (Reference 3).

Experimental aerodynamic stability investigations such as those reported in References 1-3 involve considerable expense considering the costs associated with fabricating an unsteady-flow generator, installing a test vehicle in a cell, fully instrumenting a test vehicle, and running the test vehicle over a wide range of test conditions. Even if there are no facility limitations, the investigator is faced with instrumentation accuracy limitations which often make proper data interpretation a difficult or impossible task. Clearly, it would be desirable if an approach could be found which would supplant or at least complement such testing, and remain an economically viable alternative.

One alternative that is being developed by the Aircraft Engine Group of the General Electric Company is called the Dynamic Digital Blade Row Compression Component Stability Model. This procedure models the compression component on a quasi one-dimensional, pitch line, blade-row by blade-row, time dependent basis. The capabilities of this model offer an unique approach for studying the effect of planar wave flows upon the aerodynamic stability of compression system components.

In quoting from another work (Reference 4) "... if such models are to achieve their ultimate capability as a design and evaluation tool, it is necessary to develop and validate the capability of the models against existing bodies of test data. This step establishes confidence in the model, helps to define its range of validity, and insures that it is understood." The impact of this statement cannot be underestimated. Although a number of time-dependent computer models have been developed (References 5, 6, and 7), the investigators either did not possess or have access to large-amplitude, experimental data over a wide frequency range. Such data include the nonlinear aerodynamic interactions which occur within a compression component and provide the proper benchmark against which a dynamic model should be measured. General Electric acquired such data for a two-stage fan (Reference 3) under United States Air Force Aero Propulsion Laboratory Contract F33615-73-C-2001.

With these data in hand, General Electric was able to embark upon the effort documented in this report. The two main objectives to this program were: 1) To demonstrate that a one-dimensional, dynamic digital model, consisting of a Planar Pressure Pulse Generator (P^3G) model coupled to a two-stage fan model, would provide an accurate simulation of the previously acquired test data, thereby validating the dynamic modeling technique currently being utilized by the Aircraft Engine Group of General Electric and to determine the upper frequency limit of the model; and 2) To show the manner in which the aerodynamics of the fan responded to the unsteady flow created by the P^3G through detailed study of surge pressure ratio loss sensitivity, blade row and overall amplitude transmission coefficients, and other calculated parameters.

The objectives were accomplished by simulating the test conditions, analyzing the results, and by doing additional detailed analysis of some of the test data. Specifically, the one-dimensional digital P^3G and two-stage fan models were coupled so that the critical P^3G exit/fan-inlet-flow boundary conditions were self-established. The geometry (lengths and areas) of the entrance to, of the connecting and exit ducting of the P^3G , and of the two-stage fan were included in the model; that is, the test setup from the bellmouth entrance to the bypass discharge valve was simulated. The boundary conditions employed during this study assumed a constant total pressure and constant total temperature at the bellmouth entrance and a constant static pressure at the plane of the bypass discharge valve.

During the first phase of this program, the 80% and 100% corrected speed lines for the two-stage fan were simulated using steady, clean inlet flow conditions. This step was accomplished using the pitchline relative total-pressure loss coefficients and deviation angles for the rotors that were previously developed from clean-inlet-flow fan component data and a General Electric stage-stacking procedure. The clean surge line was established based upon the development of internally generated unsteady flows within the fan which lead to aerodynamic instability and was shown to accurately reproduce the experimentally determined surge line. Upon completion of this phase, the P^3G amplitudes and frequencies generated for surge points obtained during the February 1973 test of the P^3G and the two-stage fan were simulated (i.e., a baseline point which was a near-surge point and the ensuing throttling to surge). The validity of the model was demonstrated by comparing the amplitude, waveform shape, and phase of the calculated parameters at the fan entrance and exit. Additional checks upon the digital model are provided by pressures measured upstream of the P^3G , between the P^3G and fan entrance, and in the discharge system. Simulation of the pressures at these locations permitted determining whether a parameter was acting predominately as a standing wave or a traveling wave in the duct connecting the P^3G to the two-stage fan.

It was anticipated that comparison of some model results with test data would prove difficult if carried out directly. This was due to the presence in the test data of low-level electrical noise, aerodynamic noise (turbulence), and higher order harmonics of the impressed fundamental. The basic character of the waveforms was enhanced over the originally reported results (Reference 3) by filtering out high frequency content and employing a digital analysis technique - ensemble averaging - which essentially removed any random contributions to the waveform. This technique assumed that the data was statistically stationary. Favorable amplitude and phase angle comparisons of the model-produced signatures with the experimentally determined test signatures at each frequency and corrected speed combination provided a strong basis for considering the model validated. However, it was anticipated that the degree of simulation would necessarily begin to deteriorate for frequencies in the range of 100-200 Hz based upon analytical cascade results (Reference 8). This would be an indication that the loss coefficients and deviation angles derived from steady-state data could not be used to predict the "high-frequency" dynamic performance of the fan. This knowledge, for the first time, would give a realistic value on the upper limit of the frequency range for which these types of dynamic models are valid.

With the model essentially validated, each of the simulation cases was then dissected to provide detailed information as a function of frequency on:

- Overall fan dynamic transfer characteristics
- Stage transmission characteristics
- Overall fan surge pressure ratio loss per unit amplitude
- Range of incidence angles that each rotor encountered
- Estimation of the stage where instability initiated

Additionally, effort was expended towards developing a method for including the effect of the frequency dependency of the lift force, loss coefficients, deviation angles, etc.

This report provides a detailed account of the manner in which these objectives were approached and the results that were obtained.

3.0 PLANAR PRESSURE PULSE GENERATOR AND TWO-STAGE FAN TEST AND RESULTS

Because the information derived from USAF Aero Propulsion Laboratory Contract F33615-73-C-2001 (Reference 3) is such an integral part of the present effort, the test layout, instrumentation, and results are reviewed in this section to help provide perspective to the approach followed in this study and to obviate the need to refer to Reference 3 unless more specific details are required.

3.1 TEST DESCRIPTION

The fan component tested during February of 1973 in the Aircraft Engine Group's Large Fan Test Facility located in Lynn, Massachusetts was a two-stage fan of flight type design. This fan has a hub-to-tip radius ratio of 0.486 and a flapped IGV (Inlet Guide Vane) trailing edge which is positioned as a function of corrected speed. The fan flowpath is defined in Section 4.4.1. A clean inlet flow map for this fan is given in Figure 1.

The General Electric-developed Planar Pressure Pulse Generator (P^3G) was installed approximately one fan-face diameter upstream of the fan face and was used to produce the large amplitude planar waves used for evaluating the response of the fan to deterministic unsteady flows. The P^3G is a choked-flow device which uses a single-stage rotor and stator combination to sinusoidally modulate the minimum area. The frequency of the planar waves is governed by the rotor-to-stator spacing. The advantage of this device lies in its ability to produce highly planar waves with peak-to-peak amplitudes of 10-30% of the mean total-pressure over the 420-800 Hz frequency range.

A scaled installation layout is given in Figure 2 and shows the relationship of the bellmouth, the P^3G , the two-stage fan, the exit ducting, and the discharge valves to each other.

This fan was highly instrumented since the planar wave testing followed a performance test of the fan. In addition to the standard extensive array of steady-state instrumentation, the installation was instrumented with high-response wall-static pressure transducers, total-pressure probes, and a flow (ρV) probe. The locations of the instrumentation which provided useful data of interest to this study are also shown on the installation layout of Figure 2. The letters PS contained within a probe identifier designated wall-static-pressure transducers located upstream of the P^3G , between the P^3G and the fan IGV's, and in the fan discharge duct. Total-pressure transducers were designated by PT and were located at the IGV's as was the flow probe designated by WCA. The outputs of all high-response instrumentation were recorded on analog magnetic tape for permanency and subsequent analyses.

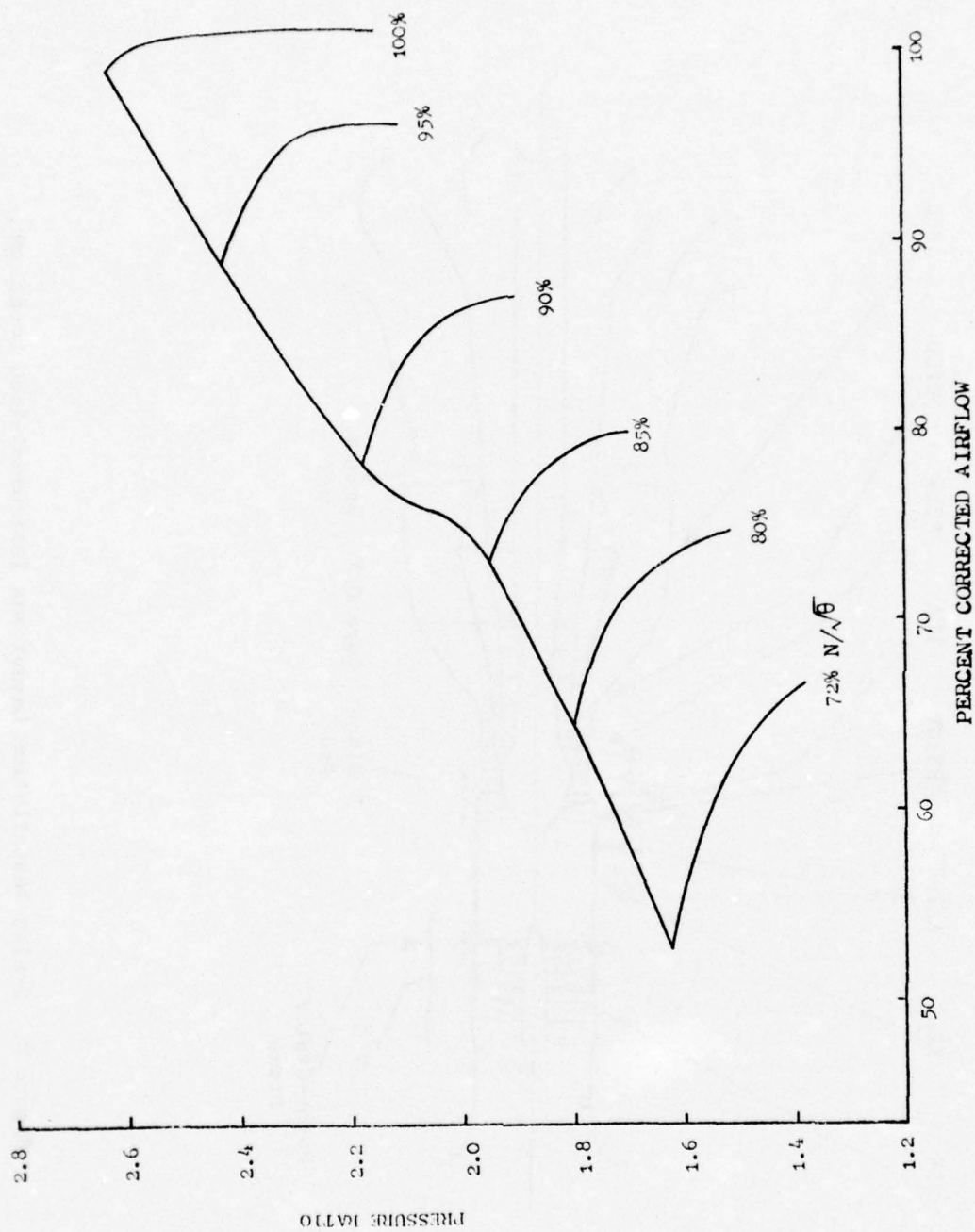


Figure 1. Clean-Inlet-Flow Two-Stage Fan Map.

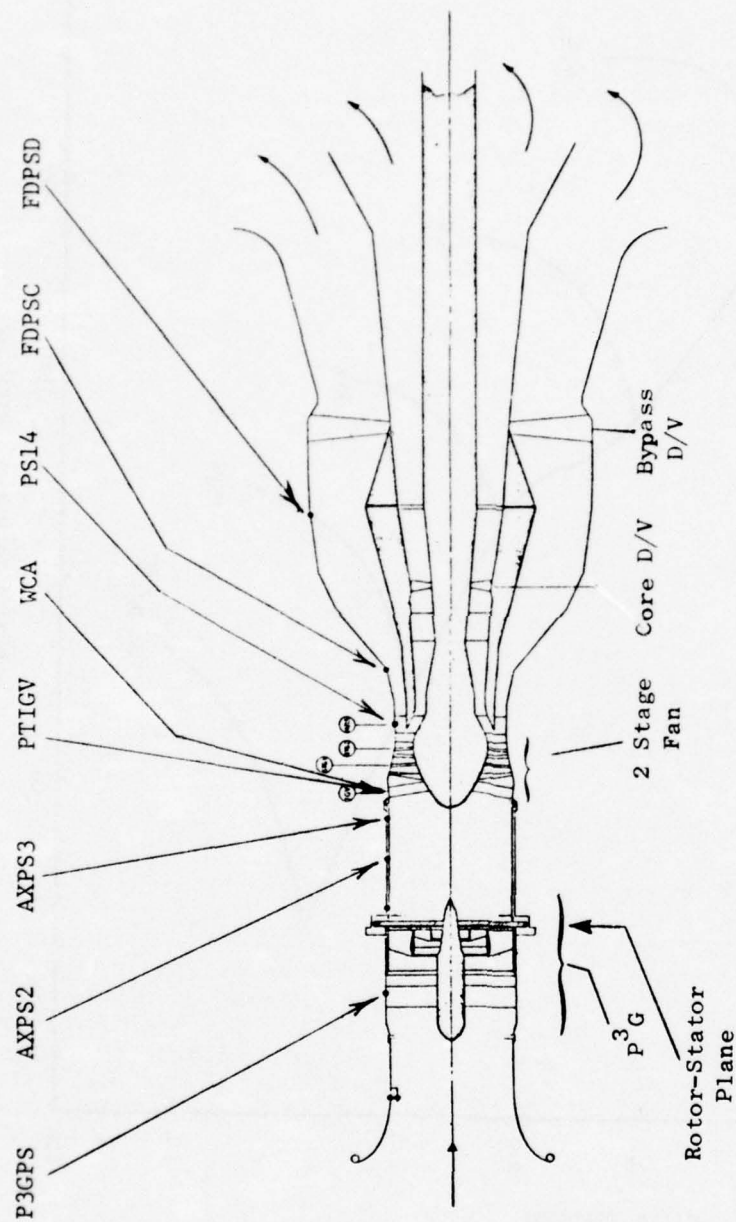


Figure 2. Scaled Installation Layout and Instrumentation Locations.

The procedure that was followed in operating the Planar Pressure Pulse Generator and fan system was to set the P³G rotor-to-stator spacing at its maximum value. The fan was brought to its proper speed and the pressure ratio for the baseline point was established by setting the bypass discharge valves. The P³G was then brought to the desired frequency and the desired planar wave amplitude was set by closing down the rotor-to-stator spacing. Baseline data were taken. The fan was then throttled to surge by slowly closing the bypass discharge valves; stationary data points were taken along the speed line in order to establish the influence of planar waves upon the pressure ratio flow relationship. Once the fan surged, the bypass discharge valves were opened to relieve the fan and to permit it to recover.

During this test, the dynamic characteristics of the fan were investigated at 80- and 100-percent corrected speeds. Twenty-four surges were induced as follows:

10 unsteady flow surges at 80% $N/\sqrt{\theta}$

13 unsteady flow surges at 100% $N/\sqrt{\theta}$

1 steady clean inlet flow posttest surge at 100% $N/\sqrt{\theta}$

The posttest surge was used as a check on fan deterioration. Of particular interest to the current study effort, are the sixteen surges given in Table 1 along with the baseline points that were to be used for waveform fidelity comparisons. The difference between the 16 surges with unsteady inlet flow conditions of Table 1 and the 23 surges obtained during the test represents repeated points. However, as will be noted by examining the 100% $N/\sqrt{\theta}$ points, there are two repeated points, one at 118 Hz and, the other 500 Hz. The purpose of this ostensible repetition is to determine if there is an effect of wave amplitude upon dynamic distortion sensitivity.

3.2 RESULTS OF TEST DATA ANALYSIS

The results which were obtained during the Planar Pressure Pulse Generator/two-stage fan test and which are particularly pertinent to the current study are discussed and reproduced in this section. The sensitivity of the fan to planar wave fluctuations is given in Figures 3 and 4 for 80% and 100% corrected speeds, respectively. The dynamic distortion sensitivity is defined as the loss in surge pressure ratio at constant flow measured between the clean surge line and the mean operating point with a planar wave amplitude of $[(P_{TMAX} - P_{TMIN})/2P_{TAVG}]$. Hence, the dynamic distortion sensitivity is the loss of surge pressure ratio per unit amplitude of the planar wave. This definition is in keeping with steady-state distortion sensitivity coefficients which are defined as the loss in surge pressure ratio per unit distortion (circumferential or radial). The data show that for frequencies up to approximately that equal to fan rotational speed, a loss in surge pressure ratio is produced. Above that frequency essentially no loss in surge pressure ratio is noted.

Table 1. Summary of Surge Points.

$\frac{\%N}{\sqrt{g}}$	f	Rotor to Stator Spacing	Surge Number	Baseline Reading Number
80	42	0.100	19	82
80	75	0.150	18	77
80	118	0.090	11	61
80	240	0.090	9	57
80	350	0.090	7	53
80	641	0.090	22	91
80	800	0.060	23	92
100	42	0.150	16	71
100	80	0.150	14	69
100	118	0.150	12	64
100	118	0.090	13	64
100	220	0.150	2	41
100	350	0.150	3	43
100	500	0.150	4	46
100	500	0.091	5	47
100	613	0.090	20	86

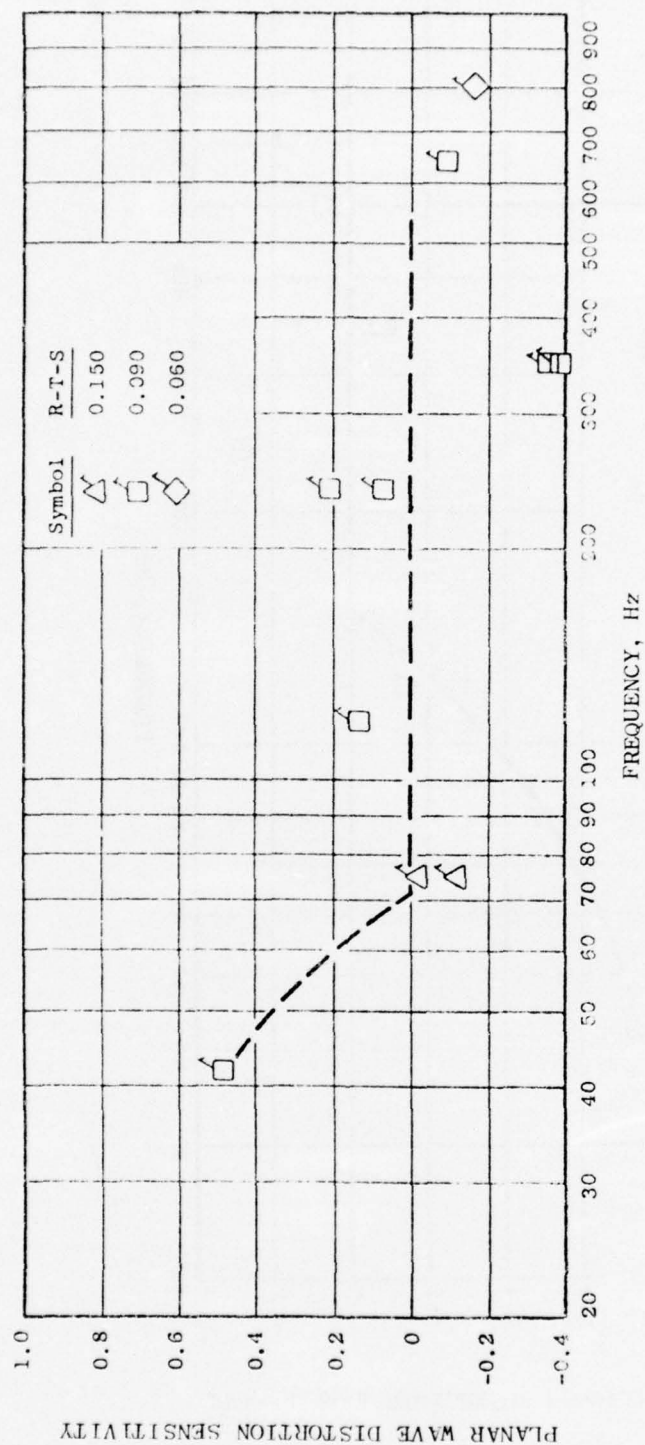


Figure 3. Planar Wave Distortion Sensitivity, $N/\bar{\theta} = 80\%$.

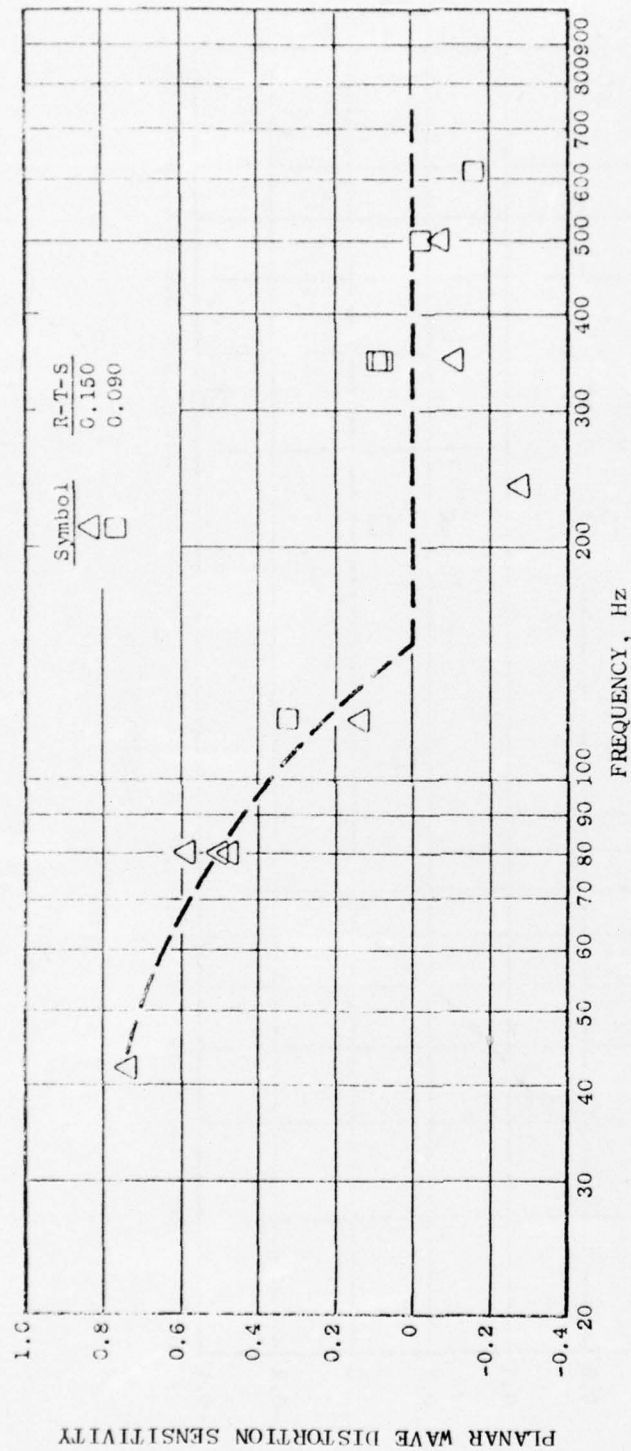


Figure 4. Planar Wave Distortion Sensitivity, $N/\sqrt{\theta} = 100\%$.

The manner in which the fan amplifies or attenuates the planar waves is described by the planar wave distortion transfer coefficient. This coefficient is the ratio of the nondimensionalized peak-to-peak total-pressure fluctuations at the fan exit divided by the nondimensionalized peak-to-peak total-pressure fluctuations at the fan inlet. Because the blade loadings are different at the hub and the tip, it is expected that the planar wave distortion transfer coefficient should show differences between values at the hub and tip. The hub transfer coefficient is shown in Figure 5 and the tip transfer coefficient is shown in Figure 6. It is interesting to note that, in general, both the hub and the tip of the fan attenuate planar waves with the hub showing pronounced attenuation. This is a beneficial effect for any compressor located downstream of the fan. However, it is worth noting that both the hub and the tip of the fan show an apparent amplification at 118 Hz. Although these points appeared to be out of place at the time the data analyses were performed, no justification could be found for deleting these points. Discussion later in this report will return to these data.

As a check on fan "health," a posttest clean-inlet-flow surge line determination check was performed at 100% $N/\sqrt{\theta}$. This check showed that due to deterioration, the fan lost approximately 1.2 percent in flow at surge and 0.017 in surge pressure ratio as shown in Figure 7 during the planar wave testing of the fan.

3.3 DATA ENHANCEMENT ANALYSIS

The results of the previous section were in part obtained by analysis of the analog data recorded on magnetic tape. The presence of electrical noise, turbulence, and other spurious disturbances which are random tend to distort the basic character of the waveform. Further, the higher harmonics associated with wave reflections within the test facility also distort the data. These disturbances do not compromise the validity of the results previously reported (Reference 3) or those reproduced in Section 3.2. However, since one of the primary objectives of this study is to validate the modeling technique by comparing computed waveforms with the test waveforms, it is necessary that the comparisons be carried out using comparable bases. The values calculated by the model are necessarily free from any random disturbances. Therefore, comparisons using these results should be made with test data which also are free of such disturbances. The operation upon test data to help reveal its basic character free from random or spurious disturbances is termed "Data Enhancement."

Detailed analysis of the instantaneous calculated airflow was undertaken since its behavior appeared to be most prejudiced by disturbances. A hard wired analog-to-digital computer (Time Data TDA-53P) was employed for digitizing and enhancing the airflow data by "ensemble averaging." The instantaneous airflow waveform was digitized over several cycles and each cycle overlaid on top of the next in such a manner that an average waveform is computed by the summation of all samples. Proper scaling was maintained by dividing by the number of samples. Thus, any disturbances which are random become smoothed and essentially eliminated from the resultant waveform when a sufficiently large number of data samples are taken.

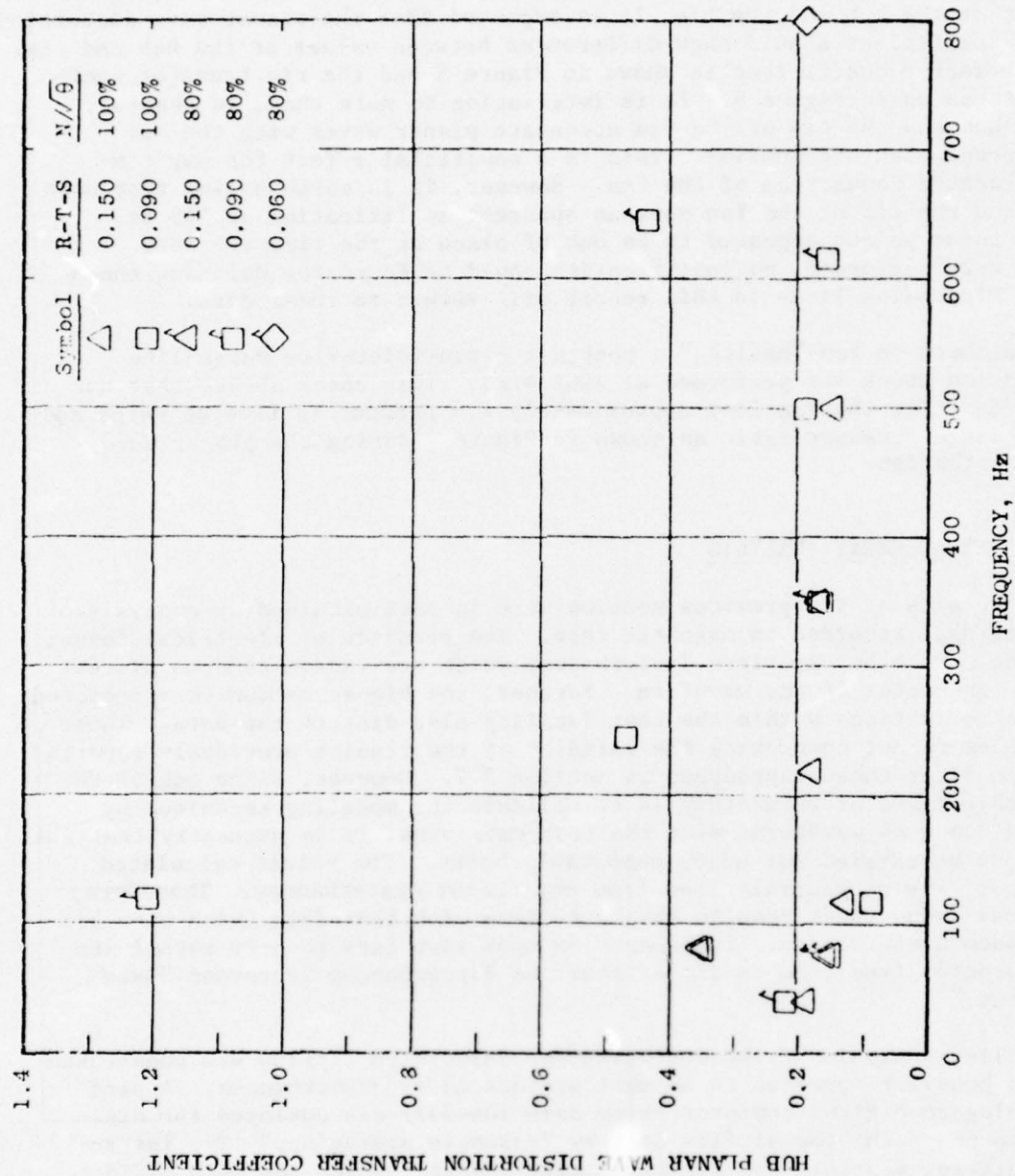


Figure 5. Fan Hub Planar Wave Distortion Transfer.

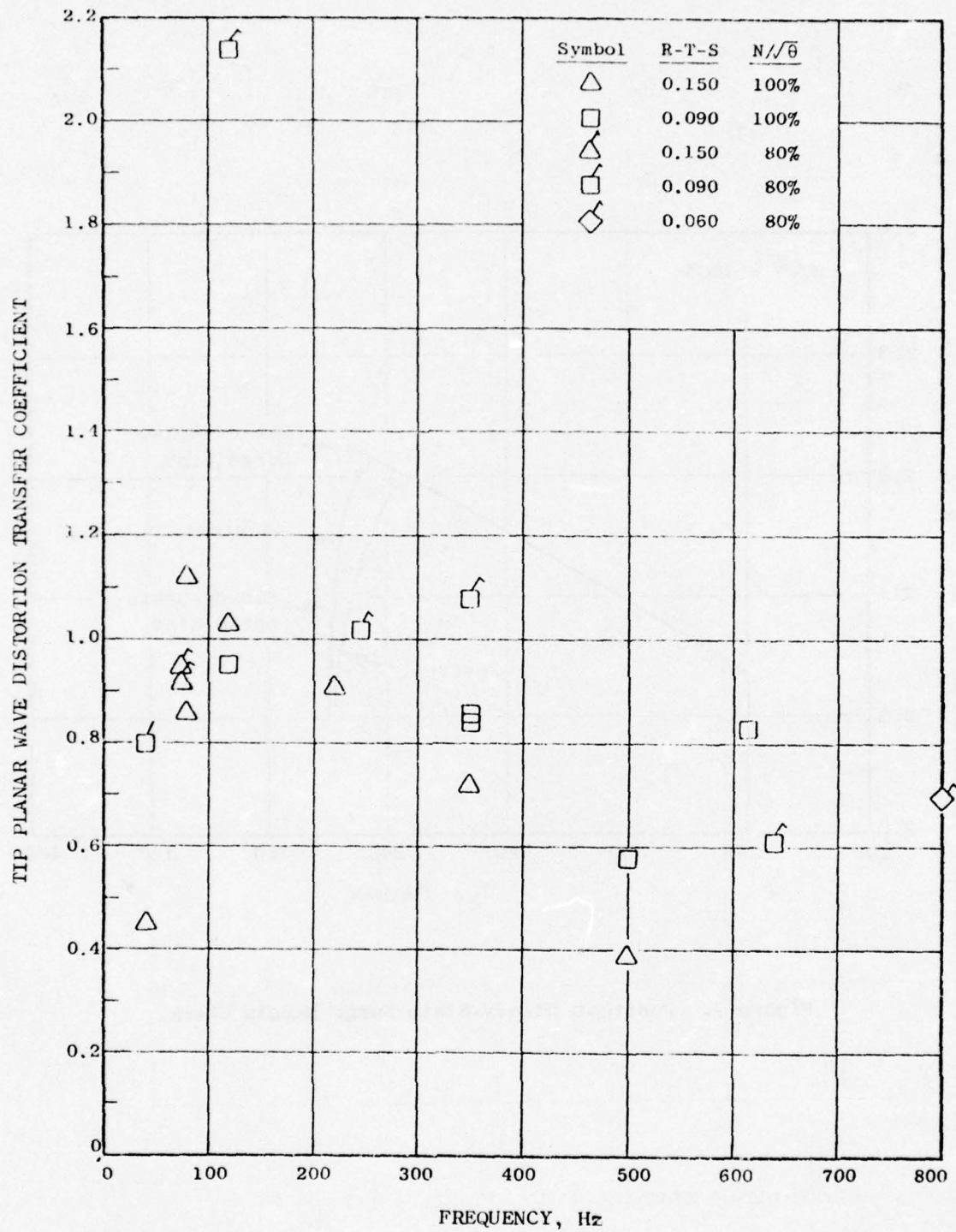


Figure 6. Fan Tip Planar Wave Distortion Transfer.

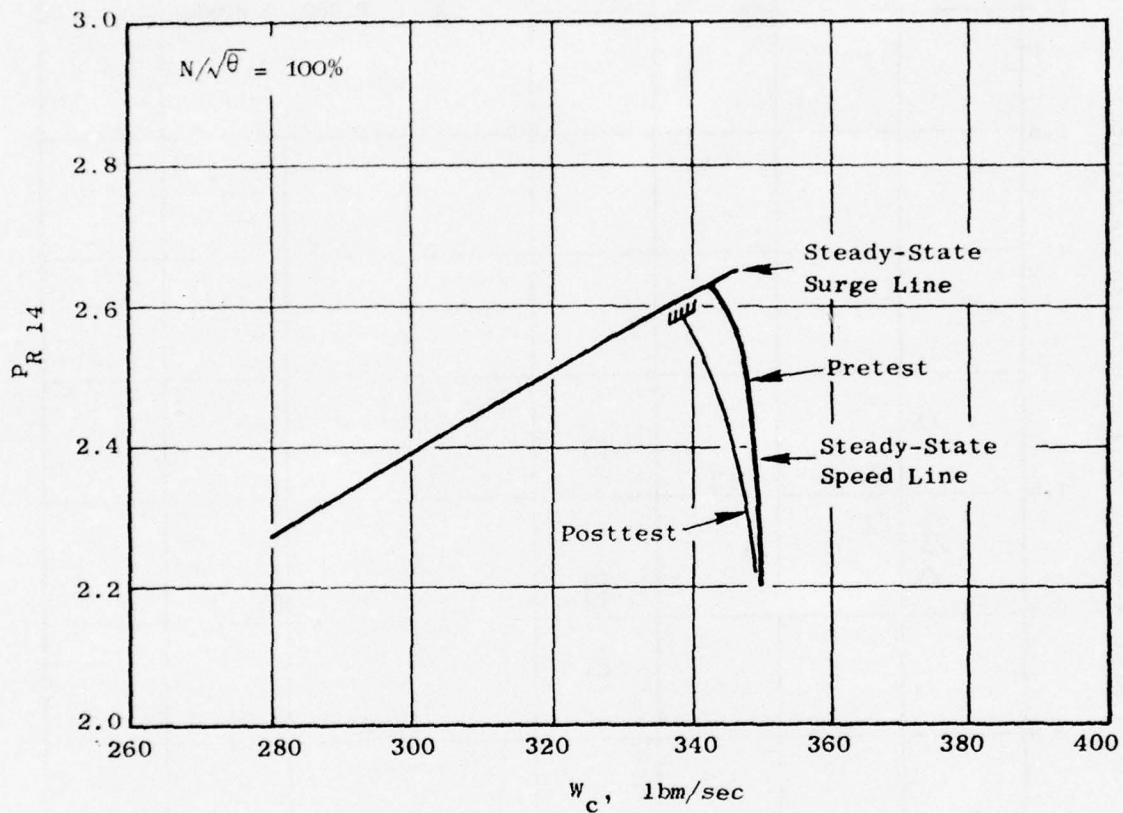


Figure 7. Posttest Steady-State Surge Margin Check.

Figure 8 shows a comparison of the raw data waveform for the calculated airflow in comparison to the enhanced data waveform. The ensemble averaged data indicate that the fundamental frequency and its first harmonic are the only significant contributors to the overall waveform and that all other contributors are either electronic noise or random aerodynamic events. This procedure verified that the primary events of interest were confined to the first two or three harmonics of the recorded data. Fluctuations occurring at frequencies above this limit did not contribute to the repetitive character of the waveform and could therefore be eliminated from the data analysis and comparisons. As a result of this finding and in view of the expense of this type of enhancement analysis, an alternate procedure was sought to permit enhancement of all variables for which comparisons between test and model results were to be made. It was determined that all data would be filtered at approximately 3 times its fundamental frequency thus eliminating the spurious noise contributions at the higher frequencies. Figure 8 also shows the result of the filtering procedure in comparison to the test data and enhancement results. Small-amplitude, random disturbances distort the wave shape locally, however, the basic nature of the waveform is clearly demonstrated. Therefore, the procedure adopted for data enhancement of all parameters used in the comparisons was to filter the raw data at a frequency commensurate with the third harmonic of the imposed fundamental P³G frequency.

As a point of information it should be noted that at the higher frequency test points ($f > 500$ Hz), this procedure did not always produce meaningful results with respect to the airflow measurement. Spurious signals from the experimental airflow probe were present and were not eliminated by the filtering process. Ensemble averaging of these data indicated that there was no periodic components for some readings. For these readings it was concluded that the probe was improperly functioning. The ensemble averaged airflow waveform is shown in Figure 9 relative to the instantaneous pressure ratio for 42 Hz at 100% corrected speed. Similarly enhanced waveforms for other test points are shown in Appendix A.

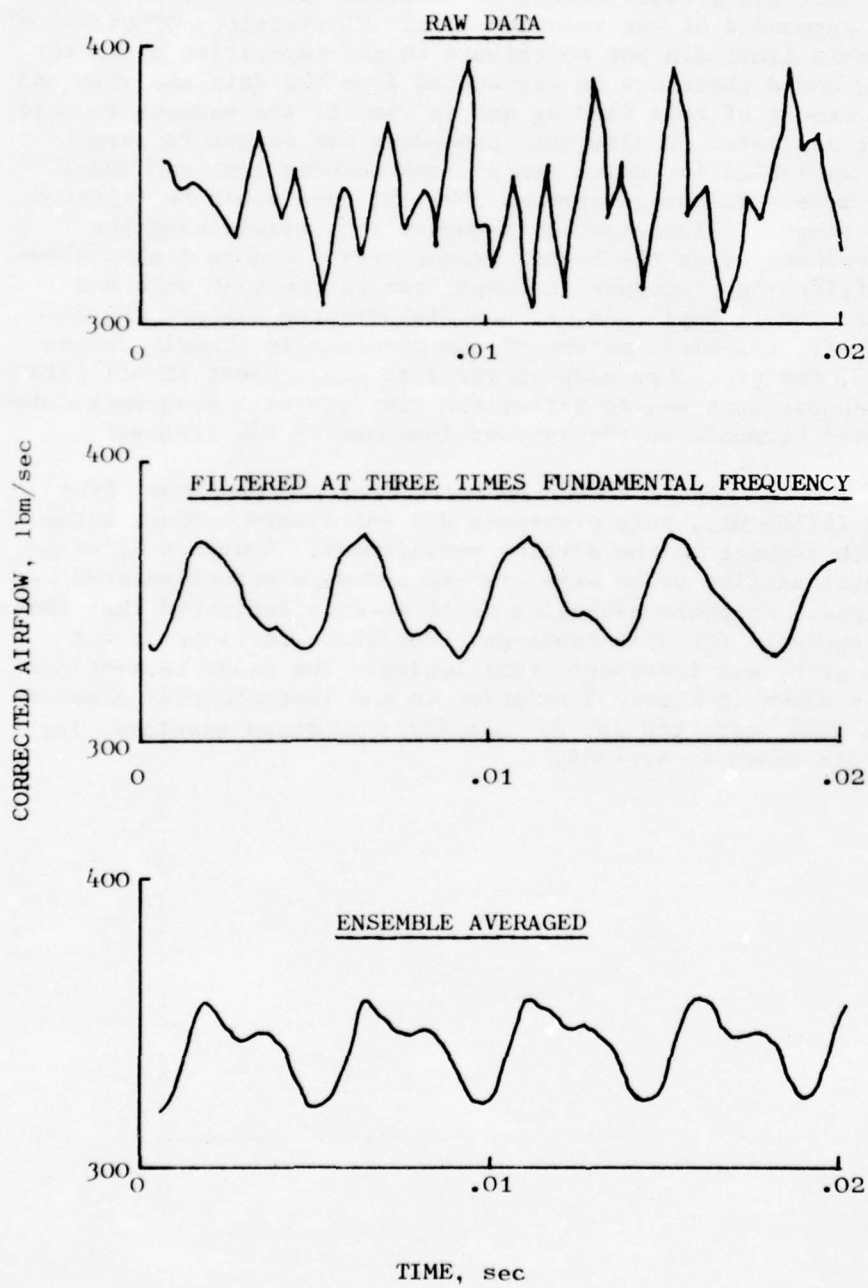


Figure 8. Data Enhancement, Rdg. 41, $N/\sqrt{\theta} = 100\%$, 220 Hz.

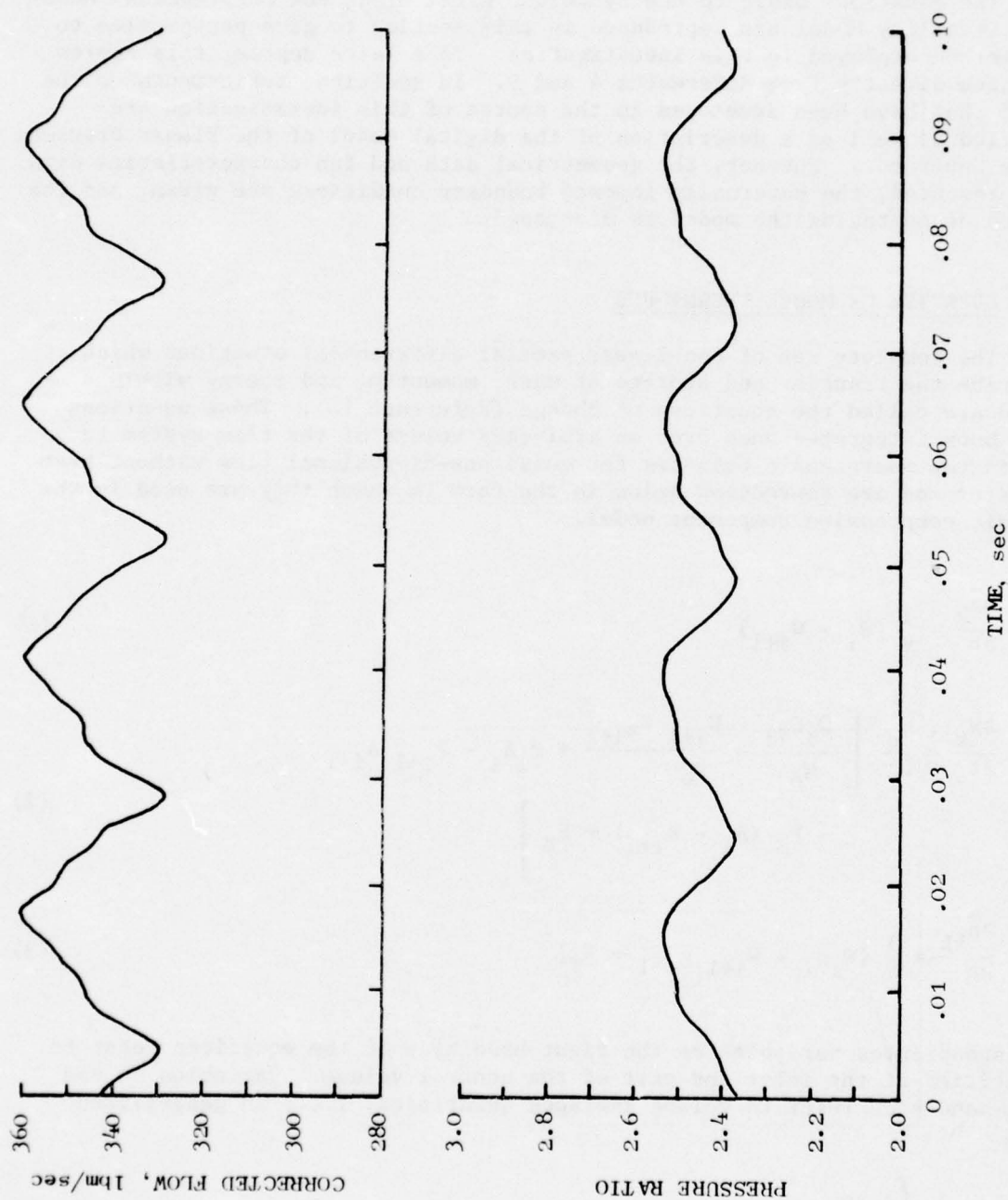


Figure 9. Ensemble Averaged Waveforms, Rdg. 71, 100% $N/\sqrt{\theta}$, 42 Hz.

4.0 DESCRIPTION OF DYNAMIC DIGITAL MODEL

The equations basic to the Dynamic Digital Blade Row Compression Component Stability Model are reproduced in this section to give perspective to the method employed in this investigation. To a large degree, this review is taken directly from References 4 and 9. In addition, refinements to the model that have been developed in the course of this investigation are detailed as well as a description of the digital model of the Planar Pressure Pulse Generator. Further, the geometrical data and fan characteristics data are presented, the externally imposed boundary conditions are given, and the method of operating the model is discussed.

4.1 OVERVIEW OF MODEL TECHNIQUES

The complete set of non-linear partial differential equations which describe the transfer and storage of mass, momentum, and energy within a fluid are called the equations of change (Reference 10). These equations have been integrated once over an arbitrary volume of the flow system to obtain the macroscopic balances for quasi one-dimensional flow without heat transfer and are reproduced below in the form in which they are used in the dynamic compression component model.

$$\frac{\partial \bar{\rho}_k}{\partial t} = \frac{1}{V} (W_i - W_{i+1}) \quad (1)$$

$$\frac{\partial \bar{W}_k}{\partial t} = \frac{g_o}{L} \left[\frac{W_i C_{zi}}{g_o} - \frac{W_{i+1} C_{zi+1}}{g_o} + P_i A_i - P_{i+1} A_{i+1} - P_M (A_i - A_{i+1}) + F_B \right] \quad (2)$$

$$\frac{\partial \bar{\rho}_{sk}}{\partial t} = \frac{1}{V} [W_i s_i - W_{i+1} s_{i+1} + S_F] \quad (3)$$

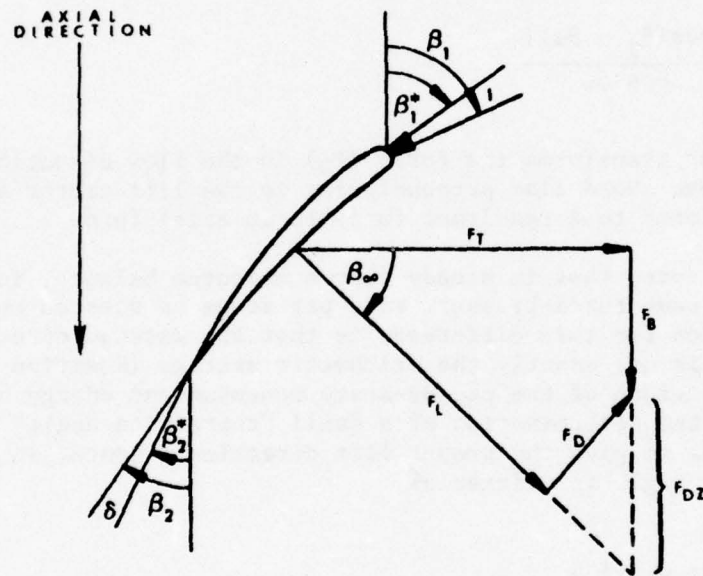
The subscripted variables on the right-hand side of the equations refer to quantities at the inlet and exit of the control volume. Variables on the left-hand side refer to volume averaged quantities, i.e., in generalized form

$$\bar{\xi} = \frac{\int \xi dV}{\int dV} \quad (4)$$

This set of equations (other than being applicable to quasi one-dimensional flows without heat transfer and to a finite, but small volume) properly and exactly describes the state of a fluid in motion. In order for a solution to Equations 1 to 3 be obtained, it is necessary to supply the caloric and thermal equations of state and expressions for F_B (Blade Force), P_M (Mean Pressure), and S_F (Entropy Production).

In the following paragraphs, the blade force and entropy production terms are discussed while discussion of the mean pressure is reserved for Section 4.2.1.

The blade force F_B of Equation 2 represents the blade force acting upon the fluid. The blade force can be determined through reference to the following sketch:



$$F_B = F_T \tan \beta_\infty - F_{DZ} \quad (5)$$

where

$$F_T = \frac{2}{g_o} \left(\frac{r_2 W_2 C_{U2} - r_1 W_1 C_{U1}}{r_1 + r_2} \right) \quad (6)$$

and is derived from the Euler Turbine Equation. There is an unsteady flow contribution to this equation which is discussed in Section 4.2.2. The direction of the lift vector is assumed to be

$$\beta_{\infty} = \frac{1}{2} (\beta_1 + \beta_2) \quad (7)$$

The drag force (F_D) is obtained from the following equation

$$F_D = \bar{\omega} \cdot \frac{P_1'}{P_{T1}'} \cdot \frac{P_{d1}'}{q_1'} (A_{1\beta} \cdot q_1') \quad (8)$$

which is based upon an analogy with the drag coefficient for duct flows. It is noted that the drag force acts in the direction of the inlet flow β_1 . The term F_{DZ} in Equation 5 is then obtained from the relation

$$F_{DZ} = F_D \frac{[\cos(\beta_1 - \beta_{\infty})]}{\cos \beta_{\infty}} \quad (9)$$

where the numerator transforms the force (F_D) in the flow direction to a force along the mean chord line perpendicular to the lift vector and the denominator transforms that resultant force to an axial force.

It should be noted that in steady flow a momentum balance, in general, will not give the same total-pressure rise per stage as does an energy balance. The reason for this difference is that the assumed direction of the blade lift vector is not exactly the arithmetic average (Equation 7) of the flow angles. Comparison of the steady-state momentum and energy balance solutions permits the determination of a small "correction angle" which can then be added to β_{∞} to give the proper lift direction. Hence, in actuality the lift direction angle is written as

$$\beta_{\infty} = 1/2 (\beta_1 + \beta_2) + \beta_c \quad (10)$$

Equation 7, then, is replaced by Equation 10.

The term S_F in Equation 3 represents the total rate of irreversible conversion of mechanical to internal energy and, in the case of this model, represents the entropy production due to blade row losses. It can be obtained from the expression:

$$S_F = \bar{W}R \ln \left(\frac{P_{T2}'/P_{T1}'}{P_{T2}'/P_{T1}'} \right)_{\text{ideal}}^{\text{actual}} \quad (11)$$

where the ideal relative total-pressure ratio which accounts for the change in pitch line radius from the entrance of a rotor blade row to its exit is written as

$$\left(\frac{P_{T2}}{P_{T1}} \right)_{\text{ideal}} = \left\{ 1 + \frac{\gamma - 1}{2} M_T^2 \left[1 - \left(\frac{r_1}{r_2} \right)^2 \right] \right\}^{\gamma/(\gamma - 1)} \quad (12)$$

M_T is equal to the ratio of the blade-row-exit pitch-line wheel speed to the inlet relative stagnation velocity of sound ($2\pi N r_2 / a_{T1}$). In the case of a stator, the ideal relative total-pressure ratio is equal to one. The actual relative total-pressure ratio requires knowledge of the relative total-pressure loss coefficient which is defined as

$$\bar{\omega} = \frac{P_{T2}^{\text{ideal}} - P_{T2}^{\text{actual}}}{P_{T1}^{\text{ideal}} - P_1} \quad (13)$$

Equation 13 can be rewritten in the form

$$\begin{aligned} \left(\frac{P_{T2}}{P_{T1}} \right)_{\text{actual}} &= \left(\frac{P_{T2}}{P_{T1}} \right)_{\text{ideal}} \\ &- \bar{\omega} \left\{ 1 - \left[\frac{1}{1 + \frac{\gamma - 1}{2} (M_1')^2} \right]^{\gamma/(\gamma - 1)} \right\} \end{aligned} \quad (14)$$

Hence, Equations 12 and 14 when substituted into Equation 11 provide complete definition of the entropy production term.

As might be expected, the input to the program, in addition to physical speed, inlet conditions and compressor geometry, requires the relative total-pressure loss coefficient ($\bar{\omega}$) for each blade row, the tangent of the deviation angle (δ) for the rotors, and the tangent of the correction angle (β_c) for both the rotors and stators. The relative total-pressure loss coefficient and the deviation angle are derived from stage-stacking results and are based upon clean-inlet-flow test data obtained by throttling at constant speed. The correction angle is obtained by comparing steady-flow force and energy balance solutions on a blade-row basis. These parameters can be represented as functions of incidence angle and are input to the program in this manner. These parameters, in conjunction with the velocity triangles and other ancillary relations, permit the determination of the thermodynamics of the fluid at

each station. Blade-free volumes are treated as lossless volumes with no imposed blade force; hence, the F_B and S_F terms of Equations 2 and 3 are identically zero.

Time dependent solution of the system of equations (Equations 1 through 3 and the relations for F_B , P_M , and S_F) that comprise the dynamic digital compression component model is effected through a Taylor series which establishes the values of the three independent volume-averaged variables at the next increment in time. In the case of this model and with references to the left hand side of Equations 1, 2, and 3, the variables $\bar{\rho}$, \bar{W} , and $\bar{\rho}_s$ are ones for which a solution is sought. Solution is now straight-forward and will be illustrated for one variable - the volume-averaged density. Considering that this method is applicable to any volume, the subscript "k", indicating the k-th volume will be dropped. The Taylor series for volume-averaged density correct to second order can be written as:

$$\bar{\rho}(t+\Delta t) = \bar{\rho}(t) + \frac{\partial \bar{\rho}(t)}{\partial t} \Delta t + \frac{\partial^2 \bar{\rho}(t)}{\partial t^2} \frac{(\Delta t)^2}{2} \quad (15)$$

where:

$\bar{\rho}(t)$ is established by the initial conditions or from the previous time step.

$$\frac{\partial \bar{\rho}(t)}{\partial t} = \frac{1}{V} (W_i - W_{i+1}) \text{ from Equation 1 and differentiating}$$

Equation 1 with respect to time yields:

$$\frac{\partial^2 \bar{\rho}(t)}{\partial t^2} = \frac{1}{V} \left(\frac{\partial W_i}{\partial t} - \frac{\partial W_{i+1}}{\partial t} \right) \quad (16)$$

Examination of Equation 16 reveals that the right-hand side is composed of derivatives of station values of flow with respect to time. Since Equation 2 will supply only the derivatives of the volume-averaged flow with respect to time, use of an interpolation scheme for obtaining station values from volume-averaged values will permit Equation 16 to be solved for the second partial derivative of volume-averaged density with respect to time. Equations 1 and 16 then can be substituted into Equation 15 to obtain the estimate of the volume averaged density correct to second order at the next increment in time. Equation 16 implies that first derivatives with respect to time of a large number of terms (e.g., F_B , P_M , and S_F) will be required. Although these expansions are lengthy, they can be derived in a straightforward manner and will not be reproduced here. Similarly, this technique can be used for the remaining two variables (\bar{W} and $\bar{\rho}_s$) and can be continued from one time step to the next for the desired number of time steps.

This calculational scheme is numerically stable, and (to date) anomalous behavior has occurred only when a physical aerodynamic instability in the flow would be expected to occur. There are two related aspects of the errors introduced by truncating the Taylor series: 1) error in estimation of a parameter at a given time and 2) buildup of error with time. The error in a parameter at a given time introduced by truncation is given in Lagrangian form (Reference 11) by

$$R_2 = \frac{(\Delta t)^3}{3!} \frac{\partial^3 \bar{p}(t)}{\partial t^3} \quad t \leq t \leq t + \Delta t \quad (17)$$

This error is negligibly small for typical time increments on the order of 10^{-4} to 10^{-5} seconds. The error introduced by truncating the Taylor series after second order does not appear to give rise to an error buildup in the calculated parameters as time increases. Rather these errors result in contributions to the time derivatives in the macrobalances which then act as restoring forces. This behavior has been noted during simulation of steady-state operating conditions.

Now the calculational technique utilized in the Dynamic Digital Blade Row Compression Component Stability Model can be discussed and is illustrated in Figure 10 in block diagram format. The use of the blade row building block concept allowed construction of a generalized model which is independent of the particular compression component being simulated.

Block I is a statement of the required dependent variable information, that is, volume-averaged density, flow, and entropy. These variables are available from either a steady-state (SS) initialization or a previous time step of a time-dependent (TD) analysis.

Block II presents the macrobalances in the form they are used in the analysis. The variables on the right-hand side of the equations are station-value properties. Knowledge of these parameters allows the first time derivatives of the volume-averaged properties to be calculated. However, as stated in Block I, only volume-averaged quantities are available at the beginning of each time step. Therefore, Block II illustrates that it is necessary to interpolate between volume-averaged parameters in order to obtain station-value properties.

In the case of blade-free volumes, where no blade forces act or entropy production takes place, it is only necessary to calculate station axial velocity in order to evaluate the macrobalances. As shown in the lower branch of Block IV, the assumption of constant absolute flow angle across the volume is made. Total pressure, total temperature and other desirable parameters are also calculated at this point. A special case of the blade free-volume calculations is the imposition of the boundary conditions. At the model inlet, constant total pressure and total temperature as well as constant entropy are maintained. At the exit of a model of a turbojet compressor and burner, a specified exit-flow-function boundary condition is

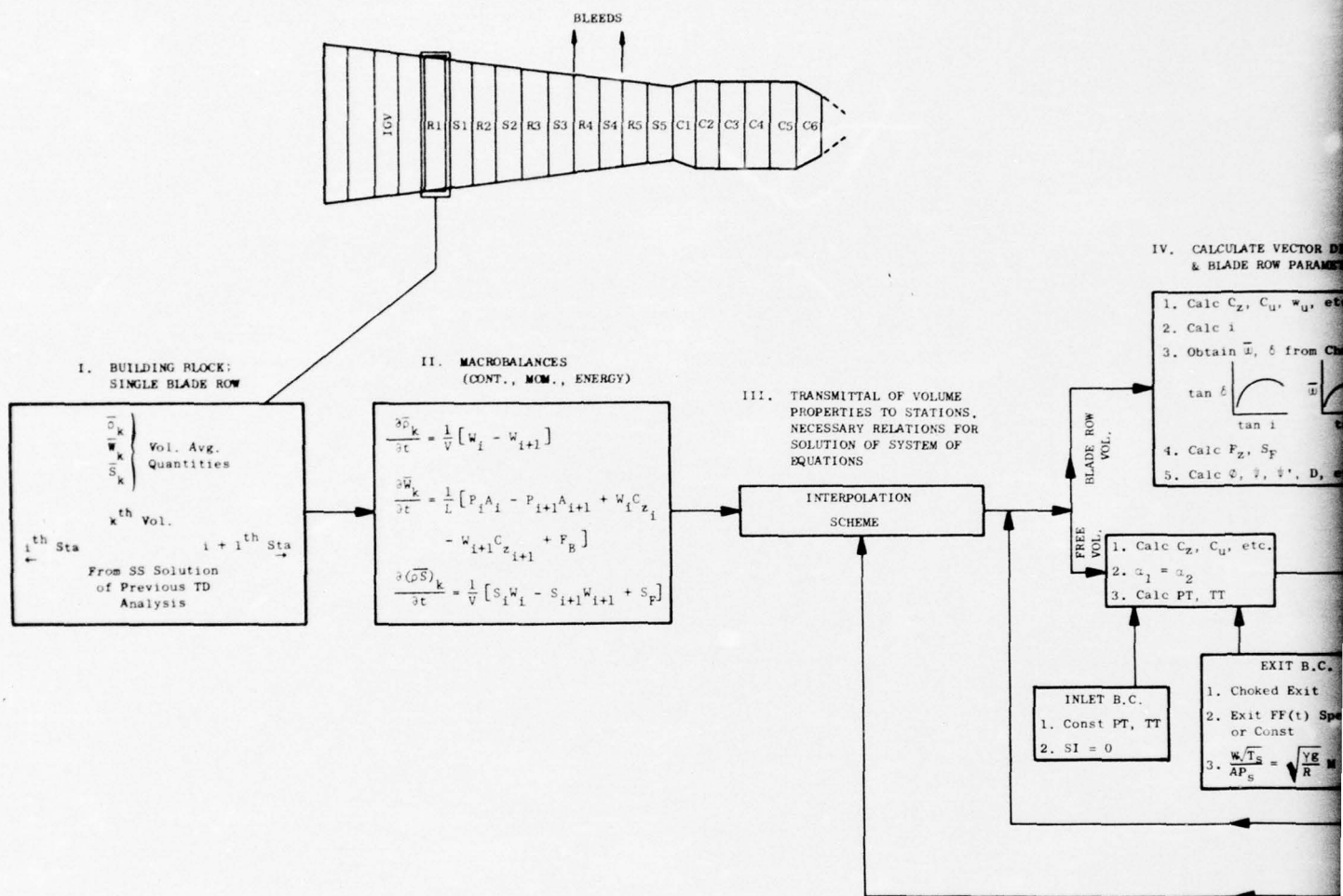


Figure 10. Dynamic Model Block

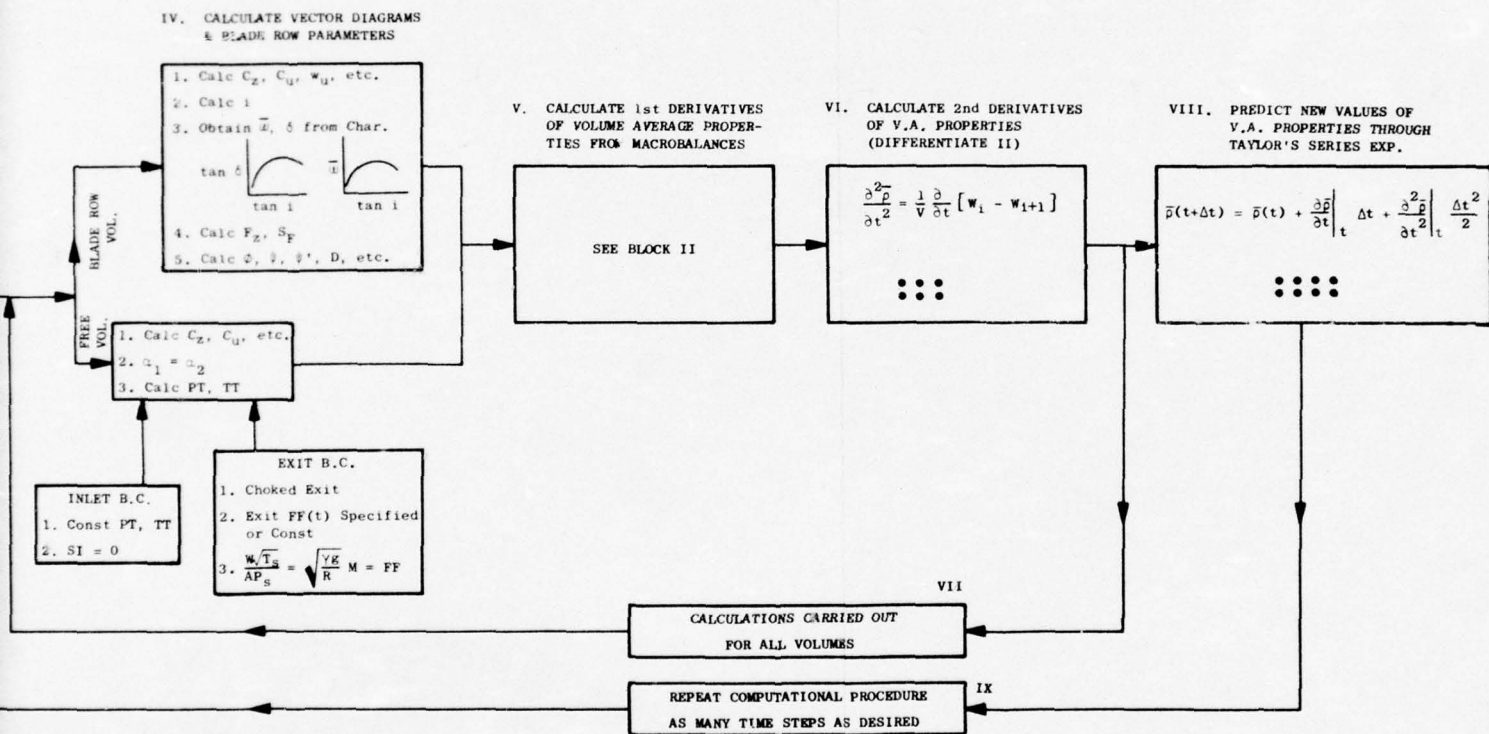


Figure 10. Dynamic Model Block Diagram.

imposed. This boundary condition was derived from the assumption that a fictitious, zero-length choked nozzle existed at the burner exit. The fictitious, zero-length choked exit condition implies the upstream flow function at the burner exit is specified and can be either held constant or changed at some rate to simulate a constant-speed throttling process.

As indicated in the upper branch of Block IV, the presence of a bladed volume requires the net axial blade force, entropy production, and station axial velocities to be calculated. Calculation of the net axial force and entropy production terms require knowledge of the loss coefficient and deviation angle. This information is available as polynomial representations which are functions of incidence angle. Stationary blade rows may be assumed to be lossless and are assumed to have constant deviation angles.

Once the flow conditions at the stations are completely described, various quantities of interest can be calculated such as stage coefficients, diffusion factors, etc. With all the necessary quantities on the right hand side of the macrobalances available, the first time derivatives of the volume-averaged properties can be calculated as indicated in Block V using the macrobalances of Block II.

Expressions for the second time derivatives of the volume averaged quantities are obtained from differentiating the macrobalances with respect to time. Analytical expressions for the time derivatives of the station properties can be evaluated by interpolating between volumes and through use of the macrobalances. Thus, as indicated in Block VI, the second time derivatives of volume-averaged properties can be calculated.

This procedure for calculating station properties and evaluating first and second time derivatives of the volume-averaged properties can be carried out for any number and types of volumes (Block VII) and is not dependent on the particular geometry being modeled. Once these calculations are carried out for all the volumes, the solution can be advanced to the next time step through use of the second-order Taylor's series approximations, Block VIII. As specified in Block IX, the technique can be repeated for as many time steps as required by the event being simulated.

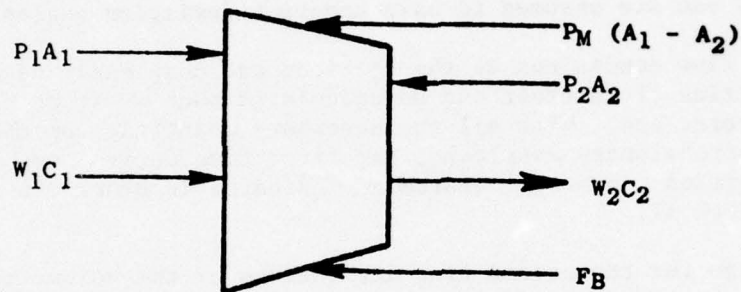
4.2 DIGITAL COMPRESSION COMPONENT MODEL REFINEMENTS

During this contractual effort, a number of refinements were introduced to the basic model as reviewed in the previous sections. These refinements were introduced to improve the generality of the model, its accuracy, and to handle inherently unsteady flows correctly, since prior to this study, the model had been exercised in detail only for slow throttling transients of a compressor. The following paragraphs detail a generalized method for handling the free-volume mean-pressure term. In addition, the formulation for the unsteady contribution to the tangential component of the blade force is given as well as a method for handling the lift force, loss coefficient, deviation angle, and lift direction correction angle in a way such that at high

frequencies it is not necessary to assume that these parameters adjust instantaneously to a new value of incidence angle.

4.2.1 Free-Volume Mean Pressure

The mean pressure P_M of Equation 2 represents the integral of the pressure distribution acting over the lateral surface area of a volume. Its relationship to the outer terms in the momentum equation is shown in the sketch below



where:

$$P_M = \frac{\int_1^2 P dA}{\int_1^2 dA} \quad (18)$$

The expression that was used for the free volume mean pressure in the Reference 4 study was based upon an empirical relationship involving a scale factor. For high Mach numbers or for large area changes across a volume, this expression was too inaccurate and led to numerical stability problems. Therefore, an effort was undertaken to improve the accuracy of P_M , its generality, and to provide it with some analytical basis. One aspect that must be considered in developing a relation for P_M is that it must be independent of the momentum equation (Reference 2) in order that redundancy is not encountered.

As a starting place for our derivation, we begin with Equation 18 written in the form

$$\frac{P_M}{P_T} = \frac{\int_1^2 P/P_T d(A/A^*)}{\int_1^2 d(A/A^*)} \quad (19)$$

which can be done if the total pressure and total temperature across a free volume are constant. During steady flow, the total pressure and total temperature across a lossless free volume will remain constant and hence, the flow will be isentropic. Therefore, the isentropic relations for P/P_T and A/A^* can be written as

$$P/P_T = (1 + \frac{\gamma-1}{2} M^2)^{-\frac{\gamma}{\gamma-1}} \quad (20)$$

$$A/A^* = \frac{1}{M} \left[\frac{2(1 + \frac{\gamma-1}{2} M^2)}{\gamma+1} \right]^{\frac{\gamma+1}{2(\gamma-1)}} \quad (21)$$

The differentiation and integration tasks implied by Equation 19 can be significantly reduced by curve fitting Equations 20 and 21 with polynomials as follows:

$$P/P_T = A_1 + B_1 M + C_1 M^2 + D_1 M^3 + E_1 M^4 \quad (22)$$

$$A/A^* = A_2 + B_2 M + C_2 M^2 + D_2 M^3 + E_2 M^4 \quad (23)$$

where the values of the coefficients are given in Table 2.

Table 2. Isentropic Relationships Polynomial Coefficients

<u>Coefficient</u>	<u>P/P_T</u>	<u>A/A[*]</u>
A	0.9999810	1.4648536
B	0.0018162	-1.0785448
C	-0.7229570	0.3238214
D	0.0967896	-0.0407312
E	0.1721226	0.0017179

Equation 23 can be differentiated and substituted into Equation 19 along with Equation 22. The integrations in Mach number can easily be carried out to give

$$P_M/P_T = \frac{A_3(M_2-M_1) + B_3(M_2^2-M_1^2)/2 + C_3(M_2^3-M_1^3)/3 + D_3(M_2^4-M_1^4)/4 + E_3(M_2^5-M_1^5)/5}{B_2(M_2-M_1) + C_2(M_2^2-M_1^2) + D_2(M_2^3-M_1^3) + E_2(M_2^4-M_1^4)} \quad (24)$$

where

$$A_3 = A_1 B_2 \quad (25)$$

$$B_3 = B_1 B_2 + 2A_1 C_2 \quad (26)$$

$$C_3 = C_1 B_2 + 2B_1 C_2 + 3A_1 D_2 \quad (27)$$

$$D_3 = D_1 B_2 + 2C_1 C_2 + 3B_1 D_2 + 4A_1 E_2 \quad (28)$$

$$E_3 = E_1 B_2 + 2D_1 C_2 + 3C_1 D_2 + 4B_1 E_2 \quad (29)$$

During the reported effort, an approximation to Equation 24 was used which can be derived from the relation

$$P_M/P_T = \frac{\int_1^2 P/P_T dM}{\int_1^2 dM} \quad (30)$$

Upon carrying out the integration of Equation 30, the following expression is obtained

$$P_M/P_T = \frac{A_1(M_2-M_1) + B_1(M_2^2-M_1^2)/2 + C_1(M_2^3-M_1^3)/3 + D_1(M_2^4-M_1^4)/4}{M_2-M_1} \quad (31)$$

which is seen to be the lead terms of Equation 24. Equation 31 matches Equation 24 within a few percent in the range of interest.

Although the relations given by Equations 24 and 31 were derived for steady flow, they are assumed to apply in unsteady flows where the wavelength

of the disturbance is considerably greater than the length of a volume. Further, since in unsteady flows the total pressure is not generally constant, it is necessary to assume that the total pressure P_T of Equations 24 and 31 is equal to the average of the inlet- and exit-total pressures.

4.2.2 Tangential Blade Force in Unsteady Flows

The tangential blade force is determined from a generalized expression for the conservation of angular momentum. As our starting point, we begin with the moment of linear momentum equation (Reference 12) for a stationary control volume in the form

$$\Sigma (\underline{F} \times \underline{r}) = \frac{1}{g_o} \left\{ \int_S \rho (\underline{C} \times \underline{r}) \underline{C} \cdot d\underline{S} + \frac{d}{dt} \int_R \rho \underline{C} \times \underline{r} dR \right\} \quad (32)$$

The first term of the right-hand side of Equation 32 represents the net change in flux of angular momentum across the control surface S and the second term represents the rate of change of angular momentum of the fluid within the region R . Only the angular momentum components which contribute to the net torque are considered. Hence, only tangential velocity components will contribute, since the radial velocity acts through the origin.

In steady flow, Equation 32 reduces to the well known Euler turbine relationship in the following manner. The fluid is assumed to be homogenous within the region and uniform at the boundaries of the surface at two geometrically defined locations. Then, the factor $\rho \underline{V} \cdot d\underline{S}$ is simply equal to the differential of flow rate dW . Hence, the integral

$$\int \rho (\underline{C} \times \underline{r}) \underline{C} \cdot d\underline{S} = \int_1^2 (\underline{C} \times \underline{r}) dW \quad (33)$$

Considering the tangential component of velocity, then

$$\int \rho (\underline{C} \times \underline{r}) \underline{C} \cdot d\underline{S} = r_2 C_{u_2} W_2 - r_1 C_{u_1} W_1 \quad (34)$$

and for steady flow Equation 32 becomes

$$F_T \bar{r} = \frac{1}{g_o} (r_2 C_{u_2} W_2 - r_1 C_{u_1} W_1) \quad (35)$$

or

$$F_T = (r_2 C_{u_2} W_2 - r_1 C_{u_1} W_1) / \left[g_o (r_1 + r_2) / 2 \right] \quad (36)$$

Now let us consider the second term on the right-hand side of Equation 32. The storage of tangential angular momentum can be written as

$$\frac{d}{dt} \int_R \rho \underline{C} \times \underline{r} dR = \frac{d}{dt} \int_R \rho C_u r dR = \frac{d}{dt} (\overline{\rho C_u} r V) \quad (37)$$

or

$$\frac{d}{dt} \int_R \rho \underline{C} \times \underline{r} dR = V \bar{r} \frac{d}{dt} (\overline{\rho C_u}) \quad (38)$$

Therefore, Equation 32 can now be written in the form

$$F_T \bar{r} = \frac{1}{g_o} \left[(r_2 C_{u_2} W_2 - r_1 C_{u_1} W_1) + V \bar{r} \frac{d}{dt} \overline{\rho C_u} \right] \quad (39)$$

or

$$F_T = \frac{1}{g_o} \left[\frac{2 (r_2 C_{u_2} W_2 - r_1 C_{u_1} W_1)}{r_1 + r_2} + V \frac{d(\overline{\rho C_u})}{dt} \right] \quad (40)$$

Note that

$$\begin{aligned} \frac{d(\overline{\rho C_u})}{dt} \approx \frac{d}{dt} \rho \frac{(C_{u_1} + C_{u_2})}{2} &\approx \frac{\bar{\rho}_k}{2} \left(\frac{dC_{u_1}}{dt} + \frac{dC_{u_2}}{dt} \right) \\ &+ \frac{C_{u_1} + C_{u_2}}{2} \frac{d\bar{\rho}_k}{dt} \end{aligned} \quad (41)$$

Inspection of Equation 41 with respect to the manner in which computations are carried out in the model shows that all terms on the right-hand side are known with the exception of dC_{u_2}/dt . Solution of the momentum equation given by Equation 2 for the time rate of change of the volume averaged flow in the k-th volume requires knowledge of the derivative with respect to time of the absolute tangential velocity at the exit of the volume. But, the time rate of change of the absolute tangential velocity at the exit cannot be determined unless the time rate of change of the volume averaged flow has been determined. This impasse which occurs within a time step can be avoided by using information from the previous time step in the following manner.

$$\text{At } t - \Delta t \quad C_{u_2} = C_{u_2}(t - \Delta t) \quad (42)$$

$$\text{At } t \quad C_{u_2} = C_{u_2}(t) \quad (43)$$

Since $C_{u_2}(t - \Delta t)$ and $C_{u_2}(t)$ are known values prior to making the calculation for the time rate of change of the absolute tangential velocity, the desired derivative can be approximated as follows:

$$\frac{d C_{u_2}(t)}{dt} \approx \left[C_{u_2}(t) - C_{u_2}(t - \Delta t) \right] / \Delta t \quad (44)$$

and is updated at each time step. Detailed calculations show that computation of the derivative in this manner provides an accurate approximation of the precise value of dC_{u_2}/dt .

4.2.3 Unsteady Blade Characteristics

The lift coefficient (Reference 13) for thin, non-fluttering, non-translating isolated airfoils immersed in an oscillating flow can be written as

$$\frac{L}{\rho U_\infty^2 c/2} = \pi C(k) \alpha + \frac{\pi}{U_\infty} \frac{c}{2} [1 + C(k)] \dot{\alpha} \quad (45)$$

where the term proportional to α gives the contribution of lift proportional to the mean angle of attack and the term proportional to $\dot{\alpha}$ gives the contribution of lift proportional to the change in circulation about the airfoil with time.

An equivalent expression for a cascade does not exist. But an approximation can be formulated which treats the essence of the problem. The work of Melick (Reference 14) suggested an approach which established a relationship between the instantaneous angle of attack of a blade in a cascade and an effective angle of attack of a blade which is associated with the actual values of the blade lift coefficients. This approach has subsequently been drawn upon by Kimzey (Reference 15) for treating the effect of varying angular extent 1/rev circumferential distortions.

It is postulated that the effective angle of attack of an airfoil in unsteady flow can be related to the instantaneous angle of attack of the airfoil through a differential equation of the following form:

$$\tau_n \frac{d(\alpha_E - \alpha_o)}{dt} + (\alpha_E - \alpha_o) = (\alpha_I - \alpha_o) \quad (46)$$

where α_E = effective angle of attack
 α_I = instantaneous angle of attack
 α_o = mean angle of attack
 τ_n = time constant for n-th blade row

It is noted that in the limit of steady flow, the effective angle of attack is equal to the instantaneous angle of attack. Given that the instantaneous angle of attack is known, it is possible to find the effective angle of attack if the time constant for each blade row is known.

The work of Schorr and Reddy (Reference 8) provides predictions for a cascade with oscillating, inviscid, incompressible inlet flow from which blade row time constants can be derived. Their results in terms of a nondimensional dynamic lift coefficient as a function of reduced frequency are reproduced with some slight changes in nomenclature in Figure 11. Further, their work shows that the dynamic lift coefficient is a stronger function of solidity than stagger angle in the region of interest ($\omega_* \leq 3.0$). Equation 46 can be solved for the Schorr and Reddy parameter by assuming $\alpha_I - \alpha_o = A\alpha_o \sin \omega t$. It then becomes necessary to choose the value of the time constant τ_n which causes the solution of Equation 47 and the results of Schorr and Reddy to match.

$$\tau_n \frac{d(\alpha_E - \alpha_o)}{dt} + (\alpha_E - \alpha_o) = A \alpha_o \sin \omega t \quad (47)$$

The particular solution to this equation can be written as

$$\alpha_E - \alpha_o = \frac{A\alpha_o}{\sqrt{1 + (\tau_1 \omega)^2}} \sin (\omega t - \phi) \quad (48)$$

and the absolute magnitude of the dynamic fluctuations can be written as

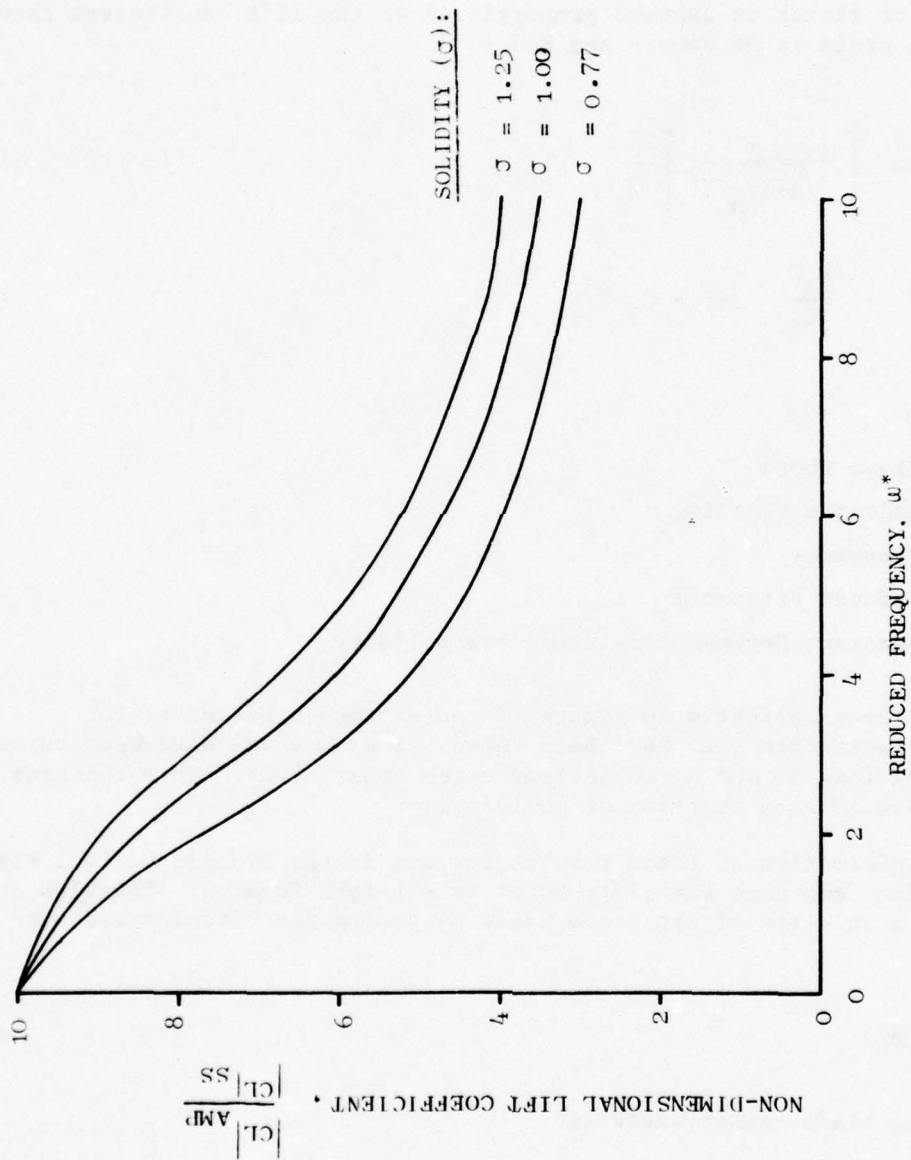


Figure 11. Dynamic Lift Coefficient in a Cascade.

$$\frac{|\alpha_E - \alpha_o|}{|A\alpha_o|} = \left| \frac{1}{\sqrt{1 + (\tau_n \omega)^2}} \right| \quad (49)$$

If the angle of attack is assumed proportional to the lift coefficient then we obtain the ordinate of Schorr and Reddy

$$\frac{|C_L|_{AMP}}{|C_L|_{SS}} \approx \left| \frac{1}{\sqrt{1 + (\tau_n \omega)^2}} \right| \quad (50)$$

$$\text{where } \tau_n \omega = \frac{C_3 C}{U_R} \quad 2\pi f = C_3 \omega^* \quad (51)$$

and

- C = Blade Chord
- U_R = Relative Velocity
- f = Frequency
- ω^* = Reduced Frequency
- C_3 = Constant Dependent on Blade Row Solidity

Figure 11 has been replotted in Figure 12 and extrapolated curves for solidities greater than 1.25 have been added. These curves have been curve fit using Equations 50 and 51 to determine the constant C_3 . This constant is shown in Figure 13 as a function of solidity.

The transformation of these results for use in the Dynamic Digital Blade Row Compression Component Stability Model is straight forward. Equation 46 can be written in terms of incidence angle by noting for circular arc airfoils

$$\alpha = 1 + \phi/2 \quad (52)$$

where ϕ is the blade camber angle as

$$\tau_n \frac{d(i_E - i_o)}{dt} + (i_E - i_o) = (i_I - i_o) \quad (53)$$

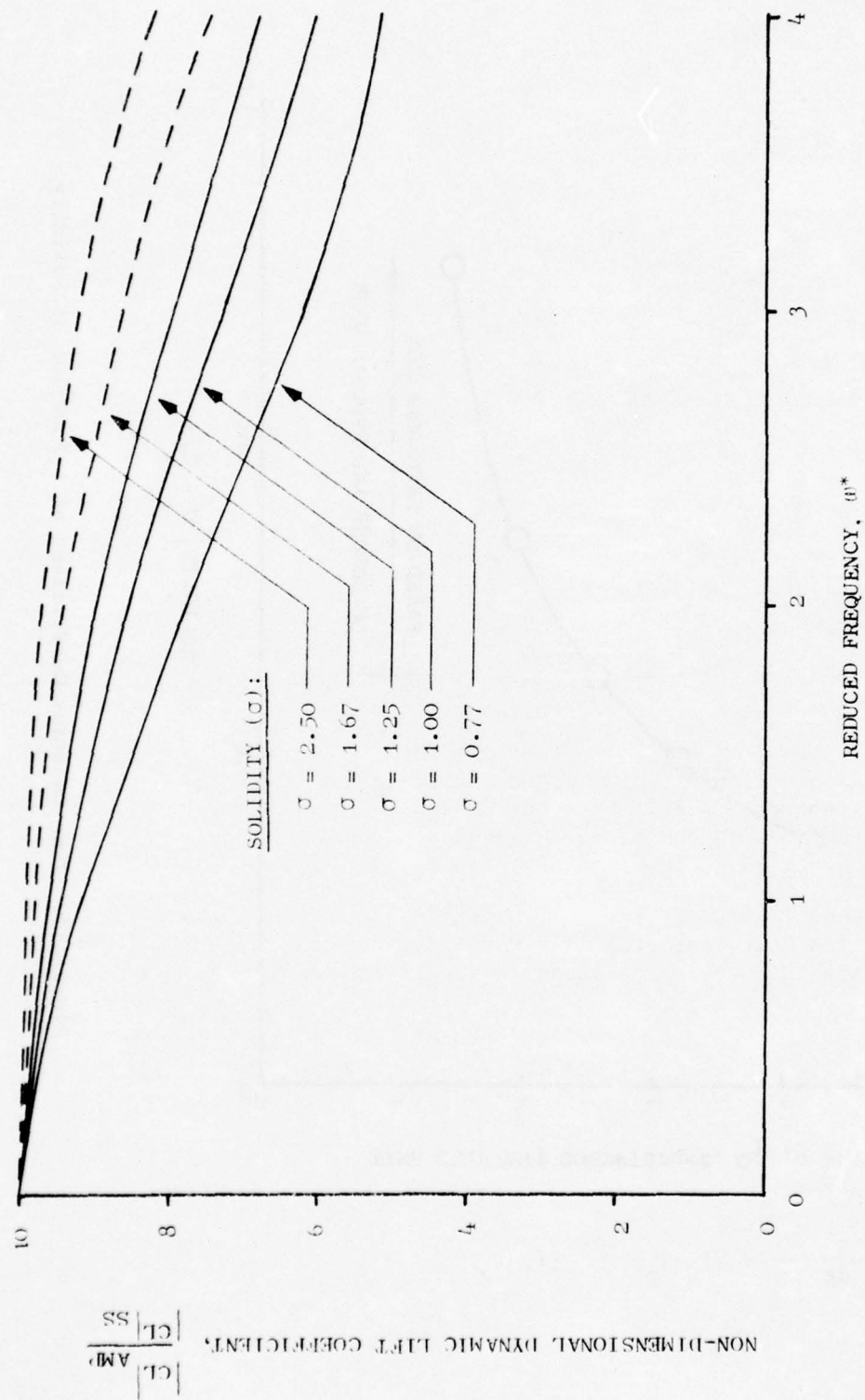


Figure 12. Dynamic Lift Coefficient in a Cascade Extrapolated for Higher Solidities.

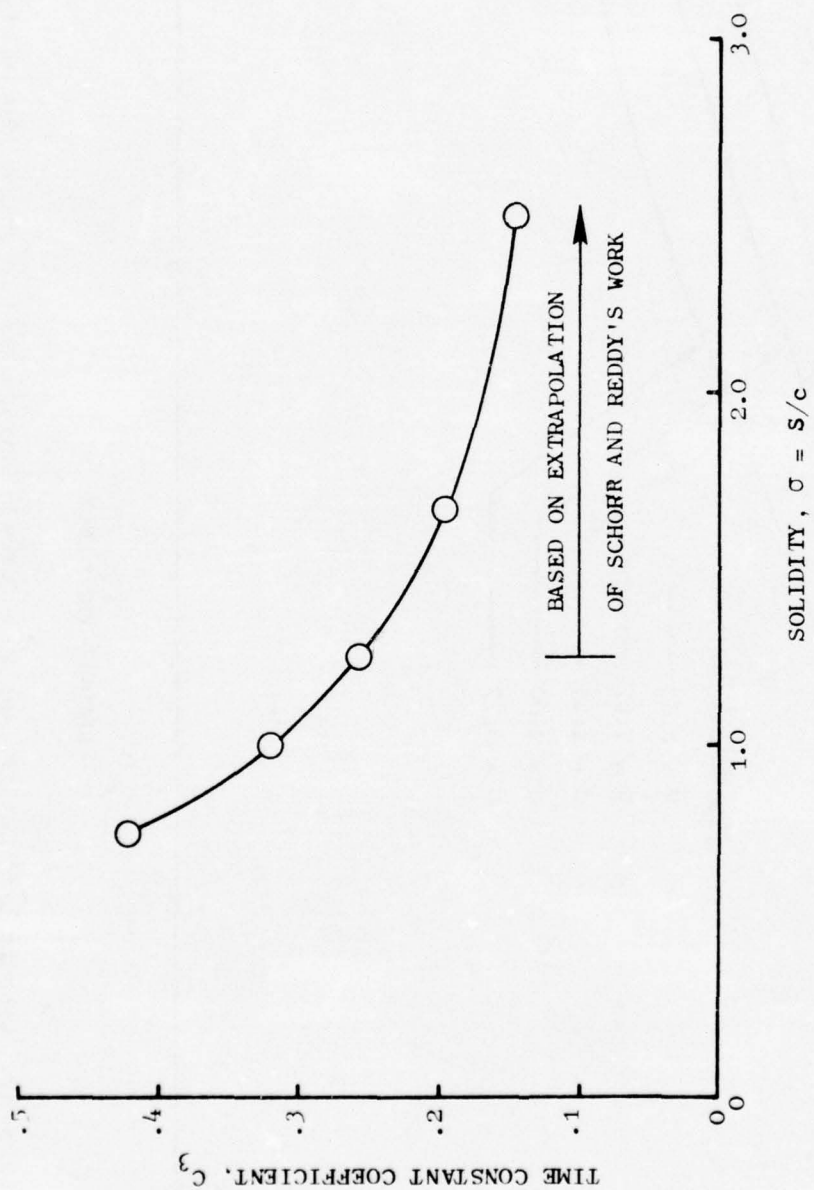


Figure 13. Time Constant Coefficient as a Function of Solidity.

$$\begin{aligned}
 i_E &= \text{Effective Incidence Angle} \\
 i_O &= \text{Mean Angle of Incidence Angle} \\
 i_I &= \text{Instantaneous Incidence Angle} \\
 \tau_n &= C_3 c/U_R
 \end{aligned}$$

Since the model computes the instantaneous incidence angle for each blade row, then given the solidity, blade chord, and relative velocity for a blade row, the blade-row time constant is defined and Equation 53 can be solved for the effective incidence angle through use of a second-order Taylor-series expansion. In effect, the relative total-pressure loss coefficients, deviation angles, lift direction, and lift direction correlation angles become functions of the effective incidence angle rather than the instantaneous incidence angle as was assumed in the original model formulation.

The assumption inherent to this approach is contained in assuming that Schorr and Reddy's work for incompressible flow is also applicable to compressible flow. In actuality, it is anticipated that detailed comparisons between model predictions and test data will result in the modification of the relationship between solidity and the constant C_3 of Figure 13. The effect of including the aspects of unsteady blade characteristics as embodied in Equation 53 is discussed in Section 5.5.

4.3 DIGITAL MODEL OF PLANAR PRESSURE PULSE GENERATOR

The planar pressure pulse generator is a siren-like device with a stator and rotor positioned in such a manner that the mean effective area is modulated as the rotor rotates producing variations in the total-pressure loss of the air drawn through the rotor-stator combination by a downstream energy source. In the case of the present study, the energy is supplied by a two-stage fan. The P³G area is essentially choked at all times and the total-pressure loss results primarily from shock losses as the air upstream of the P³G attempts to adjust to the downstream Mach number boundary condition. Some viscous losses are present, but for the flow rates and planar wave amplitudes of interest, the shock losses predominate. The amplitude of the pressure pulses are physically controlled by modulating the separation between the rotor and stator since the stator translates axially. This changes the effective area (both in the mean and at the extrema) and, therefore, varies the amplitude of the total-pressure loss.

The P³G simulation approximates the aerodynamics of the P³G operation as follows: A steady-state condition satisfying the "mean" conditions at the P³G during operation is established using the mean steady-state recovery across the P³G as measured during the test. This recovery implies an effective choked area at the P³G which can be computed. The mean area becomes the base for the amplitude of the area fluctuation. The amplitude is controlled by the parameter "amp" as shown in the following equation.

$$A_{P^3G_{choked}} = A_{P^3G_{base}} [1 + \text{amp} \cdot \sin(2\pi Nt/60)] \quad (54)$$

The choked area can be related to the upstream duct A^*/A_{duct} and provides a fundamental boundary condition to the P^3G problem. As much of the existing General Electric Dynamic Digital Blade Row Compression Component Stability Model logic was used as possible and the P^3G simulation was constructed primarily as a subroutine to the main program. With reference to the model as described in Section 4.1 and schematically described in the block diagram of Figure 10, the P^3G subroutine was treated as a block parallel to the free volume and blade row subroutines in Step IV. All necessary derivatives are computed as additions to the blocks of Steps V and VI.

4.4 DIGITAL MODEL OF TEST INSTALLATION

The system geometry, the two-stage fan-blade-row characteristics, and the boundary conditions imposed on the model are discussed in the following paragraphs.

4.4.1 System Geometry

The geometry of the test configuration was shown previously in Figure 2. The entire test set-up from the bellmouth entrance to the bypass discharge valve exit was simulated by the system model. Table 3 defines the individual characteristics of the 69 volumes used to model the overall facility and the area distribution of the test setup as used in the model is shown in Figure 14. Each blade row of the fan is represented by one volume such that the minimum volume length is 2.54 inches and is dictated by the axial length of the second stator. The maximum and most common volume length is 4 inches and is used to represent the blade-free volumes in the system. The IGV was represented by two distinct volumes; one for the forward-fixed portion of the vane and one for the movable trailing edge. This representation of the IGV was accomplished without compromising the blade row aerodynamics and permitted maintaining the length of all volumes equal to or less than 4 inches. If the IGV were not represented by two volumes, its length would have been 7.7 inches and the model frequency response would have been sacrificed. The total length of the modeled system was 266 inches.

The physical characteristics of the fan geometry, the metal angles, pitch-line radii, blockages, areas, and solidities, are also defined for each blade row in Table 3. In addition, the exit air angle for each stator is given. Table 4 shows the IGV exit metal and air angle schedules as a function of corrected speed ($100\% N/\sqrt{\theta} = 7556 \text{ rpm}$).

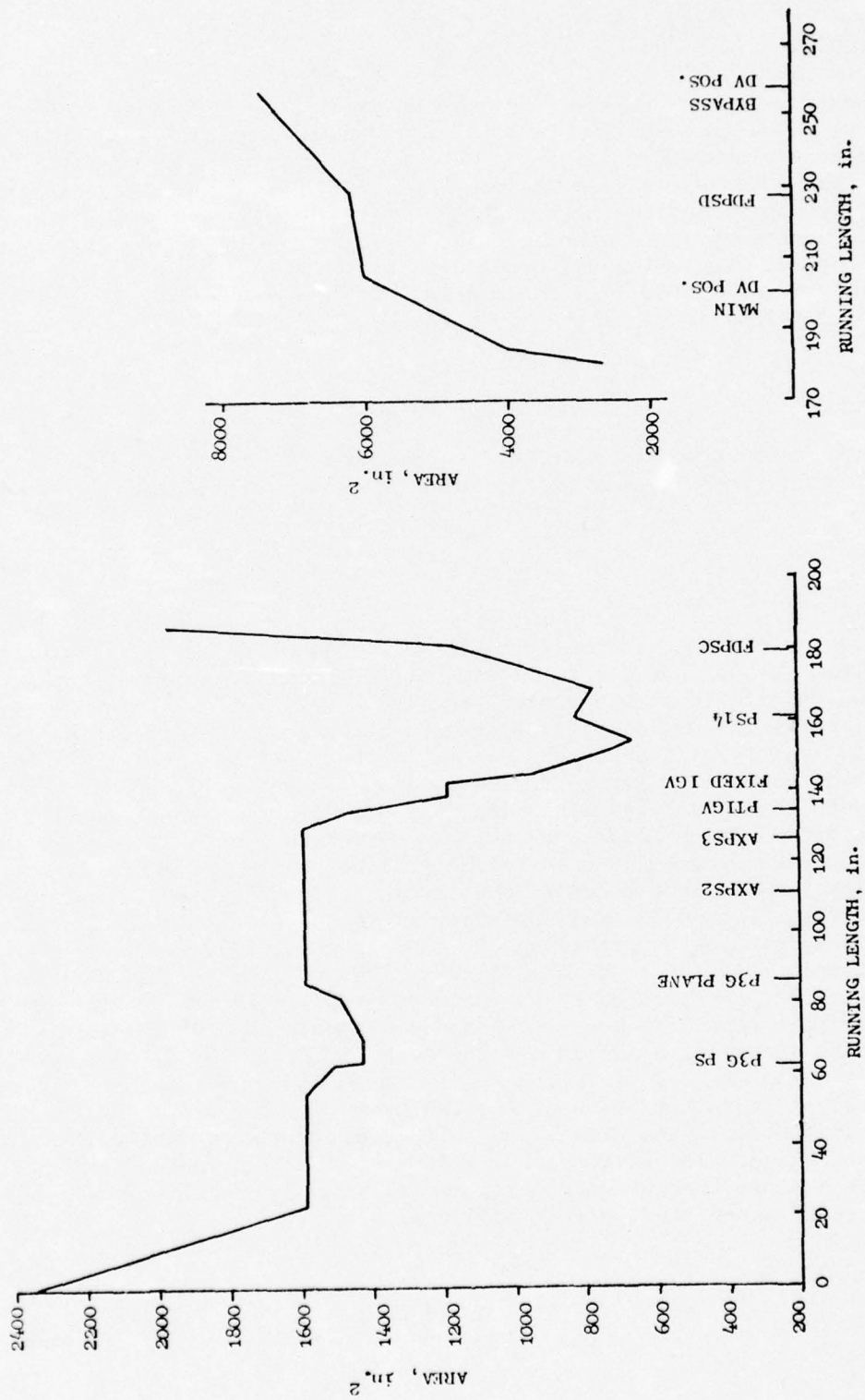


Figure 14. System Area Distribution.

Table 3. System

VOLUME DESCRIPTION	STATION NUMBER	INSTRUMENTATION	AREA (IN ²)		EFFECTIVE
			PHYSICAL	BLOCKAGE	
Bellmouth Entrance	1		2350	1.0	2350
Duct Ahead of P ³ G	2		2220	1.0	2220
	3		2090	1.0	2090
	4		1960	1.0	1960
	5		1825	1.0	1825
	6		1590	1.0	1590
	7	BMPT & BMPS	1590	1.0	1590
	8		1590	1.0	1590
	9		1590	1.0	1590
	10		1590	1.0	1590
	11		1590	1.0	1590
	12		1590	1.0	1590
	13		1590	1.0	1590
	14		1590	1.0	1590
	15		1590	1.0	1590
	16		1585	1.0	1585
	17	P ³ GPS	1538	1.0	1538
	18		1430	1.0	1430
	19		1415	1.0	1415
	20		1440	1.0	1440
	21		1460	1.0	1460
	22		1480	1.0	1480
	23		1590	1.0	1590
P ³ G Location	24		1590	1.0	1590
	25		1590	1.0	1590
	26	AXPS1	1590	1.0	1590
	27		1590	1.0	1590
	28		1590	1.0	1590
	29		1590	1.0	1590
	30	AXPS2	1590	1.0	1590

Table 3. System Geometry.

AREA (IN ²) AL	BLOCKAGE	EFFECTIVE	R _P	VOLUME NUMBER	α_1^* (DEG.)	α_2^* (DEG.)	α_2 (DEG.)	LENGTH (IN.)	SOLIDITY
1.0	2350	--	--	1	--	--	--	4	--
1.0	2220	--	--	2	--	--	--	4	--
1.0	2090	--	--	3	--	--	--	4	--
1.0	1960	--	--	4	--	--	--	4	--
1.0	1825	--	--	5	--	--	--	4	--
1.0	1590	--	--	6	--	--	--	4	--
1.0	1590	--	--	7	--	--	--	4	--
1.0	1590	--	--	8	--	--	--	4	--
1.0	1590	--	--	9	--	--	--	4	--
1.0	1590	--	--	10	--	--	--	4	--
1.0	1590	--	--	11	--	--	--	4	--
1.0	1590	--	--	12	--	--	--	4	--
1.0	1590	--	--	13	--	--	--	4	--
1.0	1590	--	--	14	--	--	--	4	--
1.0	1590	--	--	15	--	--	--	4	--
1.0	1585	--	--	16	--	--	--	4	--
1.0	1538	--	--	17	--	--	--	4	--
1.0	1430	--	--	18	--	--	--	4	--
1.0	1415	--	--	19	--	--	--	4	--
1.0	1440	--	--	20	--	--	--	4	--
1.0	1460	--	--	21	--	--	--	4	--
1.0	1480	--	--	22	--	--	--	4	--
1.0	1590	--	--	23	--	--	--	4	--
1.0	1590	--	--	24	--	--	--	4	--
1.0	1590	--	--	25	--	--	--	4	--
1.0	1590	--	--	26	--	--	--	4	--
1.0	1590	--	--	27	--	--	--	4	--
1.0	1590	--	--	28	--	--	--	4	--
1.0	1590	--	--	29	--	--	--	4	--
1.0	1590	--	--	30	--	--	--	4	--

Table 3. System Geometry (Con

<u>VOLUME DESCRIPTION</u>	<u>STATION NUMBER</u>	<u>INSTRUMENTATION</u>	<u>AREA (IN²)</u>		<u>EFFECTIVE</u>	<u>R_P</u>
			<u>PHYSICAL</u>	<u>BLOCKAGE</u>		
	31	AXPS3	1590	1.0	1590	--
	32		1590	1.0	1590	--
	33		1590	1.0	1590	--
	34		1590	1.0	1590	--
	35		1510	1.0	1510	--
IGV Leading Edge	36	PTIGV	1465	1.0	1465	16.76
IGV Trailing Flap	37		1242.06	.98	1217.21	17.68
Rotor 1	38		1242.06	.98	1217.21	17.67
Stator 1	39		1008.05	.965	972.76	17.60
Rotor 2	40		856.78	.965	826.79	17.50
Stator 2	41		777.33	.950	738.46	17.41
Stator 2 Trailing Edge	42		712.47	.945	673.28	17.20
Duct Behind Fan	43		770	1.0	770	--
	44	Plane 14/25	810	1.0	810	--
	45		805	1.0	805	--
	46		800	1.0	800	--
	47		915	1.0	915	--
	48	FDPSC	1035	1.0	1035	--
	49		1238	1.0	1238	--
	50		1825	1.0	1825	--
	51		2665	1.0	2665	--
	52		3880	1.0	3880	--
	53		4310	1.0	4310	--
	54		4635	1.0	4635	--
	55		5015	1.0	5015	--
	56		5440	1.0	5440	--
	57		5850	1.0	5850	--
	58		6040	1.0	6040	--
	59		6080	1.0	6080	--
	60		6110	1.0	6110	--

Table 3. System Geometry (Continued).

<u>BLOCKAGE</u>	<u>EFFECTIVE</u>	<u>R_P</u>	<u>VOLUME NUMBER</u>	<u>α₁[*] (DEG.)</u>	<u>α₂[*] (DEG.)</u>	<u>α₂ (DEG.)</u>	<u>LENGTH (IN.)</u>	<u>SOLIDITY</u>
1.0	1590	--	31	--	--	--	4	--
1.0	1590	--	32	--	--	--	4	--
1.0	1590	--	33	--	--	--	4	--
1.0	1590	--	34	--	--	--	4	--
1.0	1510	--	35	--	--	--	3.5	--
1.0	1465	16.76	36	--	--	--	3.31	1.5
.98	1217.21	17.68	37	0	See Schedule	--	3.90	1.5
.98	1217.21	17.675	38	57.23	45.40	--	3.84	1.61
.965	972.76	17.602	39	38.54	0.55	6.18	3.50	1.76
.965	826.79	17.507	40	57.24	47.97	--	3.50	1.751
.950	738.46	17.413	41	38.41	-7.76	0.00	2.56	1.845
.945	673.28	17.204	42	--	--	--	2.54	--
1.0	770	--	43	--	--	--	3.85	--
1.0	810	--	44	--	--	--	4	--
1.0	805	--	45	--	--	--	4	--
1.0	800	--	46	--	--	--	4	--
1.0	915	--	47	--	--	--	4	--
1.0	1035	--	48	--	--	--	4	--
1.0	1238	--	49	--	--	--	4	--
1.0	1825	--	50	--	--	--	4	--
1.0	2665	--	51	--	--	--	4	--
1.0	3880	--	52	--	--	--	4	--
1.0	4310	--	53	--	--	--	4	--
1.0	4635	--	54	--	--	--	4	--
1.0	5015	--	55	--	--	--	4	--
1.0	5440	--	56	--	--	--	4	--
1.0	5850	--	57	--	--	--	4	--
1.0	6040	--	58	--	--	--	4	--
1.0	6080	--	59	--	--	--	4	--
1.0	6110	--	60	--	--	--	4	--

2

Table 3. System Geometry (Conclu


<u>VOLUME DESCRIPTION</u>	<u>STATION NUMBER</u>	<u>INSTRUMENTATION</u>	<u>AREA (IN²)</u>		<u>EFFECTIVE</u>	<u>R_P</u>
			<u>PHYSICAL</u>	<u>BLOCKAGE</u>		
Duct Behind Fan 	61	FDPSD	6140	1.0	6140	--
	62		6170	1.0	6170	--
	63		6205	1.0	6205	--
	64		6330	1.0	6330	--
	65		6510	1.0	6510	--
	66		6690	1.0	6690	--
	67		6890	1.0	6890	--
	68		7045	1.0	7045	--
	69		7200	1.0	7200	--
Bypass DV Location	70		7400	1.0	7400	--

Table 3. System Geometry (Concluded).

<u>PACKAGE</u>	<u>EFFECTIVE</u>	<u>R_P</u>	<u>VOLUME NUMBER</u>	<u>α_1^* (DEG.)</u>	<u>α_2^* (DEG.)</u>	<u>α_2 (DEG.)</u>	<u>LENGTH (IN.)</u>	<u>SOLIDITY</u>
1.0	6140	--	61	--	--	--	4	--
1.0	6170	--	62	--	--	--	4	--
1.0	6205	--	63	--	--	--	4	--
1.0	6330	--	64	--	--	--	4	--
1.0	6510	--	65	--	--	--	4	--
1.0	6690	--	66	--	--	--	4	--
1.0	6890	--	67	--	--	--	4	--
1.0	7045	--	68	--	--	--	4	--
1.0	7200	--	69	--	--	--	4	--
1.0	7400	--	70	--	--	--	4	--

Table 4. IGV Schedule.

$\%N/\sqrt{\theta}$	Metal Angle	Air Angle
72	25	20.02
80	20	16.77
85	16	14.17
90	10	10.27
95	0	3.77
100	-10	-2.73
104	-14	-5.33

The location of instrumentation is shown also in Figure 2 and Table 3. Instrumentation locations that were used during the test were duplicated in the model setup to provide a direct comparison between model results and test data. The parameters chosen for this comparison are defined in Table 5 and were consistent with the objectives of verifying model fidelity as well as documenting the fan aerodynamic response.

Table 5. Model Parameters Used in Validation Study.

<u>Parameter</u>	<u>Description</u>
P3GPS	Static pressure between the forward boundary (bellmouth inlet) and the P ³ G plane.
AXPS2 } AXPS3 }	Static pressures in the duct between the P ³ G and the fan inlet.
PTIGV	Total pressure at the IGV plane.
WCA	Approximate calculated airflow at the IGV plane.
PS14	Static pressure at the fan exit.
FDPSC	Static pressure in the fan duct just down-stream of the splitter.
FDPSC	Static pressure close to the bypass discharge in the fan discharge duct.

The fan duct discharge area was divided at the core entrance plane in the physical test set-up. For the purposes of the model, the two flow areas (core duct and bypass duct) were summed together and represented by a single flow area.

4.4.2 Two-Stage Fan Characteristics

The performance characteristics of the two-stage fan were established during steady-state component testing. During this type of testing, inter-stage aerodynamic information was obtained from which the performance of the individual stages was established and the performance of the blade rows was inferred. Internal fan steady-state pressures and temperatures were measured as the fan was throttled from its lowest operating point until surge occurred. Based upon standard compressor design techniques, this data was represented in two different forms. The first was a non-dimensional representation of the stage characteristics, showing the pressure coefficient (ψ'), the work coefficient (ψ), and stage efficiency (η) as functions of flow coefficient (ϕ) for each stage. The positive feature of this format was that the form is amenable to generalization and that the behavior of a stage may be assessed with reference to stage characteristics established for other compression components. This form is useful for stage performance representation, but not for blade-row by blade-row characteristics which are the basic input to the model simulation. Blade-row performance characteristics take the form of blade-row relative total-pressure loss coefficients (\bar{w}') and deviation angles (δ) as a function of air incidence angle (i). In this program, all losses were assigned to the rotor and it was assumed that only lossless turning of the flow occurs in the stators. This assumption is necessary if high-quality test data are not obtained at each blade row or design stator loss coefficients are not available. Although, only the blade characteristics form of performance representation is directly applicable to the analytical model, the stage characteristics are useful in analyzing the credibility of the assumptions that go into the blade-row by blade-row results.

The rotor loss coefficients and the deviation angles as functions of incidence angle ($\tan i$) are tabulated in Appendix B for both rotors at the two test speeds of interest, 80 and 100%, respectively. These characteristics represent blade-row performance up to steady-state surge. However, due to the fundamental nature of the disturbances that were to be imposed on the model, it was known that the incidence angles encountered during model operation would instantaneously exceed the steady-state surge limit. Therefore, an analysis was conducted of the extrapolation of the steady-state data into the post steady-state surge regime. Numerous extrapolations were attempted and analyzed using the non-dimensional $\phi - \psi, \psi', \eta$ format to aid in the interpretation of results in this uncharted region. At the conclusion of this study, it was determined that the most simple of data extrapolations worked best, a straight line tangent to the data at the end points. Any other technique produced an unrealistic "folding back" of the characteristics that did not appear to be consistent with the aerodynamics of the compression component. Subsequent model results have shown the importance of the

extrapolated characteristics, but the detailed shape in the steady-state post-surge region still cannot be established with the existing model and existing test results.

The blade row performance characteristics are represented by a fourth order polynomial curve fit of the steady-state data with linear extrapolations at the end points. Figure 15 illustrates this technique showing the curve through the data and the end points of the polynomial representation beyond which a linear extrapolation of the curve at a slope tangent to the end point is used. Plots of the characteristics and tabulations of the polynomial coefficients as used in the model are contained in Appendix B.

It should be noted that all of the results obtained from the model during this study were obtained using blade characteristics that were obtained from undeteriorated performance test results. However, the test results against which the model results are being compared, include progressive amounts of deterioration which culminate in the deteriorated 100% corrected speed line as was shown in Figure 7.

One item of empirical information is used to represent the test data in the model, the lift direction correction angle. This parameter was discussed in Section 4.1 and the curves of this parameter and tabulations of the polynomial coefficients are given in Appendix B.

4.4.3 Boundary Conditions

The system model is bounded by two distinctly different conditions that are intended to approximate the physics of the environment at their respective locations.

The forward boundary position is geometrically coincident with the bellmouth inlet plane. Constant entrance total pressure and total temperature equal to the measured test values were assumed for the inlet plane aerodynamic boundary condition. Subsequent analysis of this assumption has indicated that the bellmouth entrance conditions are not exactly "plenum-like," but, are sufficiently close for all practical purposes. Other considerations which encouraged the use of this boundary condition were the sheer size of the system model in its basic state which necessarily restricts the construction of a larger plenum forward of the bellmouth and the fact that the P³G downstream of the inlet provides a very hard boundary condition of its own, decoupling the fan from the inlet representation.

The exit boundary condition was established at the bypass discharge valve location. A constant static pressure is established in the model at this point and is felt to be consistent with the actual test conditions since there are no choke points or even high Mach numbers downstream of the fan exit.

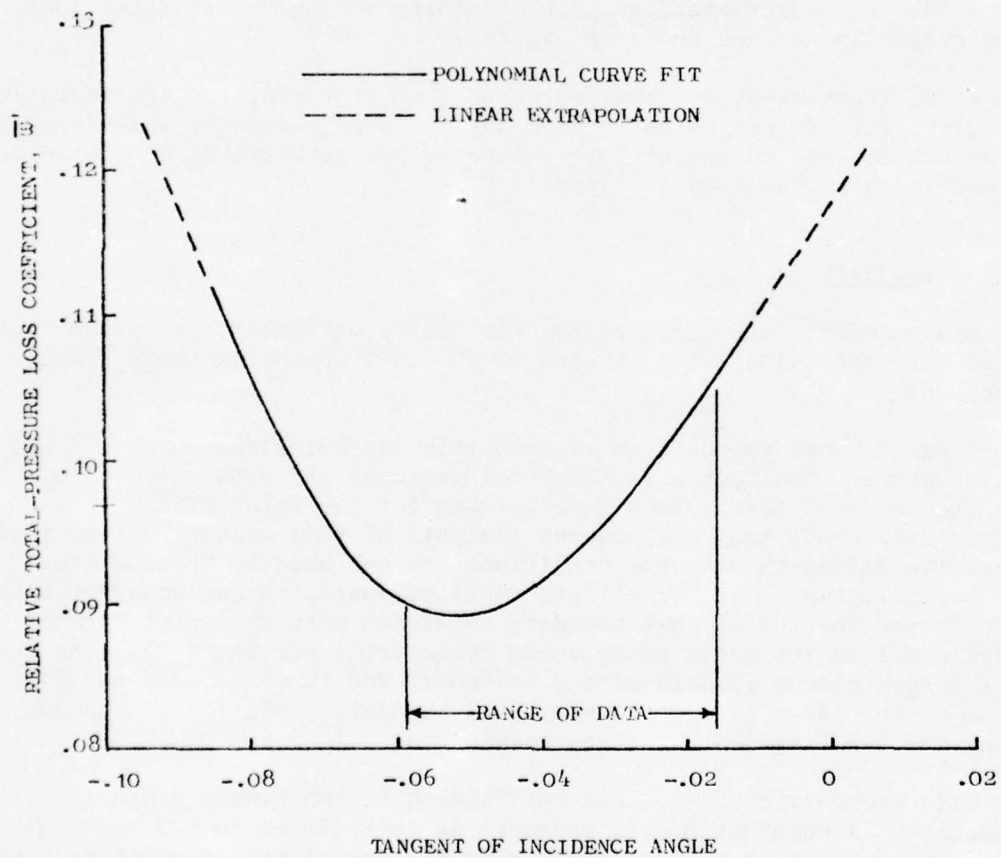


Figure 15. Loss Coefficient and Deviation Angle Polynomial Representation.

4.5 METHOD OF MODEL OPERATION

The procedure for establishing conditions in the dynamic model similar to test conditions evolved as the simulations were attempted until the model operational technique became remarkably similar to the test method. As previously described, the test procedure called for establishing the fan at a relatively low level operating point on the chosen speed line and then bringing the P³G to the appropriate frequency before decreasing the rotor-to-stator spacing to increase the planar wave amplitude. Similarly, the model enters the computation at the chosen fan speed and a near surge operating point. The initial operating point was not always commensurate with the test reading in the interests of conserving computation time and as a result, some dissimilarities in mean point behavior occurred between model and test results. However, a mean operating point was established on the model consistent with the mean total-pressure loss across the P³G at the desired rotor-to-stator (R-T-S) spacing. The area fluctuation about this mean condition was then increased slowly until the IGV total-pressure fluctuation of the model matched the measured value. Behavior of the model P³G representation with respect to amplitude versus frequency was not always predictable due to standing wave patterns. As a result, several attempts to match model and test amplitudes were required for some cases. The procedure of ramping the model from zero to maximum amplitude rather than starting the model with full amplitude at the outset was consistent with the slow closing procedure of the rotor-to-stator spacing during the actual test. In fact, attempting to start the model abruptly almost always resulted in violently unsteady conditions that produced a model computation abort very similar in nature to a surge.

The test procedure called for the fan and P³G oscillation to reach a stable operating condition and then the bypass discharge valve to be slowly closed until surge was induced. Closure of the discharge valve produced an increased blockage and, therefore, increased the back pressure on the fan. This caused the fan operating point to move up the speed line characteristic either to an operating condition that was in equilibrium with the downstream conditions or to a point of instability. The model performs precisely the same function. The static pressure at the discharge valve boundary is increased at a prescribed constant rate until aerodynamic instability is encountered. The speed of the model closure is necessarily faster than that of the test since model operation is conducted on a microscopic time scale in comparison with real time test conditions. It should be noted that the faster throttling rates used on the model are necessitated by computation costs and are justified by the fact that model rates of pressure increase of 0.00075 psi and 0.00025 psi per time step have been attempted without observing any large dissimilarities in results or causing deviation from the steady-state stage characteristics. A time step of 0.0001 sec was used throughout this program.

4.6 INSTABILITY IDENTIFICATION

It was beyond the scope of this program to determine if one unique parameter would be capable of identifying model instability and further, would correlate with the occurrence of physical aerodynamic surge. Only

individual flow parameters were examined as indications of instability rather than trying to form a unique combination of flow parameters. An effort to predict instability using analytical expressions developed by other investigators (References 16 and 17) did not yield either consistent or realistic results and is omitted from discussion.

Instability identification initially was completely based upon the flow ratio and amplification function parameters developed during the Reference 4 study. The flow ratio parameter, W_2/W_1 , is a measure of the storage of fluid within a volume since it is the ratio of the flow leaving the volume to the flow entering the volume. A decrease in the flow ratio indicates that the flow leaving a blade row is decreasing at a faster rate than the flow which enters the blade row and implies that the instability initiated in this blade row. Upstream blade rows tend to show the same response ($W_2/W_1 < 1$) and the downstream blade rows show a flow ratio response greater than one since these blade rows are being evacuated. The amplification function is the ratio of the derivative of the volume averaged flow with respect to time to the derivative of the flow with respect to time at the system exit where the throttling boundary condition is imposed. The amplification function is a measure of the rate at which internally generated disturbances grow with respect to the rate that the externally applied boundary condition is imposed.

During the course of the study, three other parameters were examined for gaining insight to aerodynamic instability development.

1. The unsteady blade force which is the component of the total blade force associated with the time rate of change of angular momentum within a blade row.
2. The incidence angle which gives some perspective to the stage mean-operating condition relative to the steady-state limit and the degree of oscillation into the post-steady-state surge region.
3. The mean overall operating point which describes the mean-overall-pressure ratio/mean-inlet-flow trajectory on the steady-state fan map.

Discussion of the specific use of these parameters and illustrative examples are given in Section 5.4.2.

5.0 RESULTS OF DIGITAL SIMULATIONS AND COMPARISONS WITH TEST DATA

The results obtained from the clean-inlet-flow throttling simulations and from the planar-wave-distortion inlet-flow throttling simulations are presented and discussed in detail in this section. More specifically, the stage amplitude transmission characteristics, the fan planar wave transfer, and stage initiating instability results have been examined and are presented here. Further, the simulation results obtained by including the unsteady blade characteristic effects are discussed.

5.1 CLEAN INLET FLOW

Simulation of the clean-inlet compression-unit steady-state performance and establishment of the stability limit are basic steps in the construction of a dynamic model. Simulation of the two-stage fan with clean inlet flow at 80% and 100% corrected speeds is shown in Figure 16 relative to the measured, non-deteriorated fan characteristics. The speed-line characteristics pass through the measured data points and the stability limits are coincident with the steady-state surge line as experimentally determined.

The stability limit of the steady-state simulation at 100% corrected speed is defined by the behavior of the blade row flow ratio W_2/W_1 . Figure 17 illustrates the blade-row flow ratio (W_2/W_1) across both rotors of the two-stage fan as a function of time. Applying the previously discussed logic with respect to flow ratio behavior at surge (Section 4.6), it is seen that rotor 1 appears to be the "initiating stage" that produces the fan instability. The rotor 1 exit flow is less than the entrance flow indicating that a breakdown in the flow pumping capability of the stage has occurred. Rotor 2 flow ratio reacts to the upstream disturbance by reflecting the loss of flow through rotor 1 as a decrease in W_1 relative to W_2 and, therefore, a rise in W_2/W_1 .

Figure 18 illustrates the behavior of the 80% corrected speed steady-state model instability characteristic. The initiating stage is not as clearly defined for this surge. Rotor 1 and rotor 2 appear to go unstable almost simultaneously. However, rotor 2 recovers while rotor 1 remains at a low value of W_2/W_1 which indicates a more pronounced instability.

5.2 VALIDATION OF MODEL DYNAMIC CHARACTERISTICS

5.2.1 Waveform Fidelity

A prime objective of this study was to demonstrate the ability to accurately simulate the Planar Pressure Pulse Generator Program data reported in Reference 3. To achieve that goal, certain test readings and measurement locations were selected for comparison of model results to test data (See Figures 2 and 14 and Tables 3 and 5).

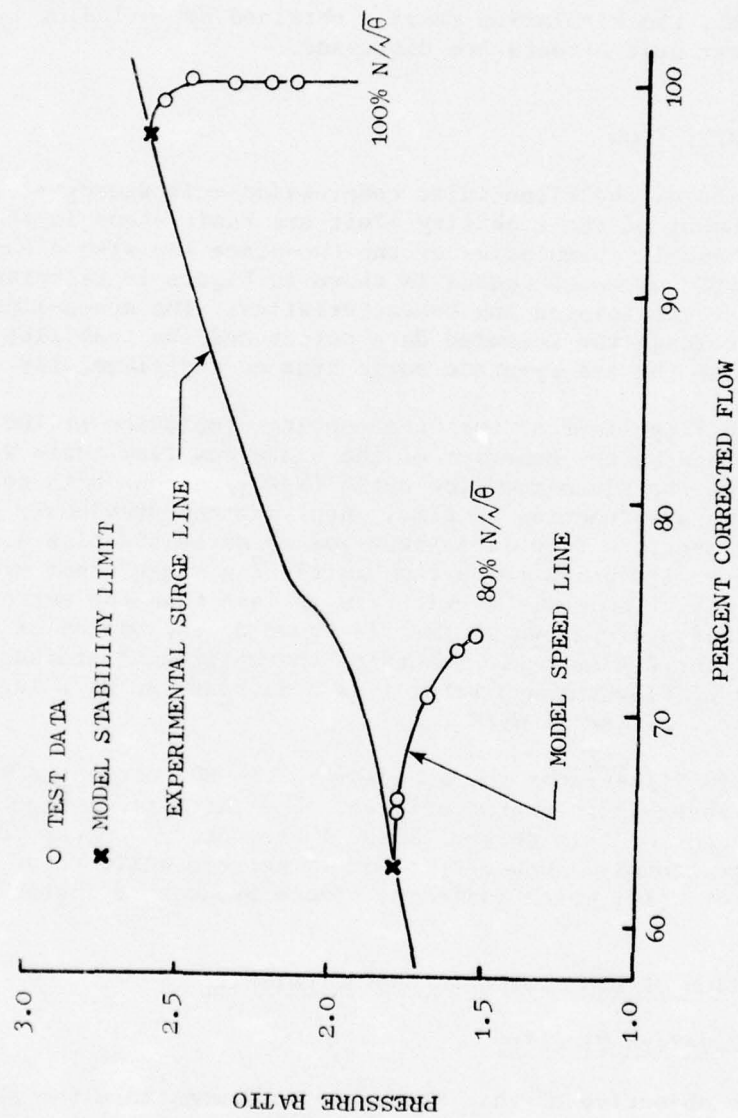


Figure 16. Clean Inlet Flow Two-Stage Fan Map.

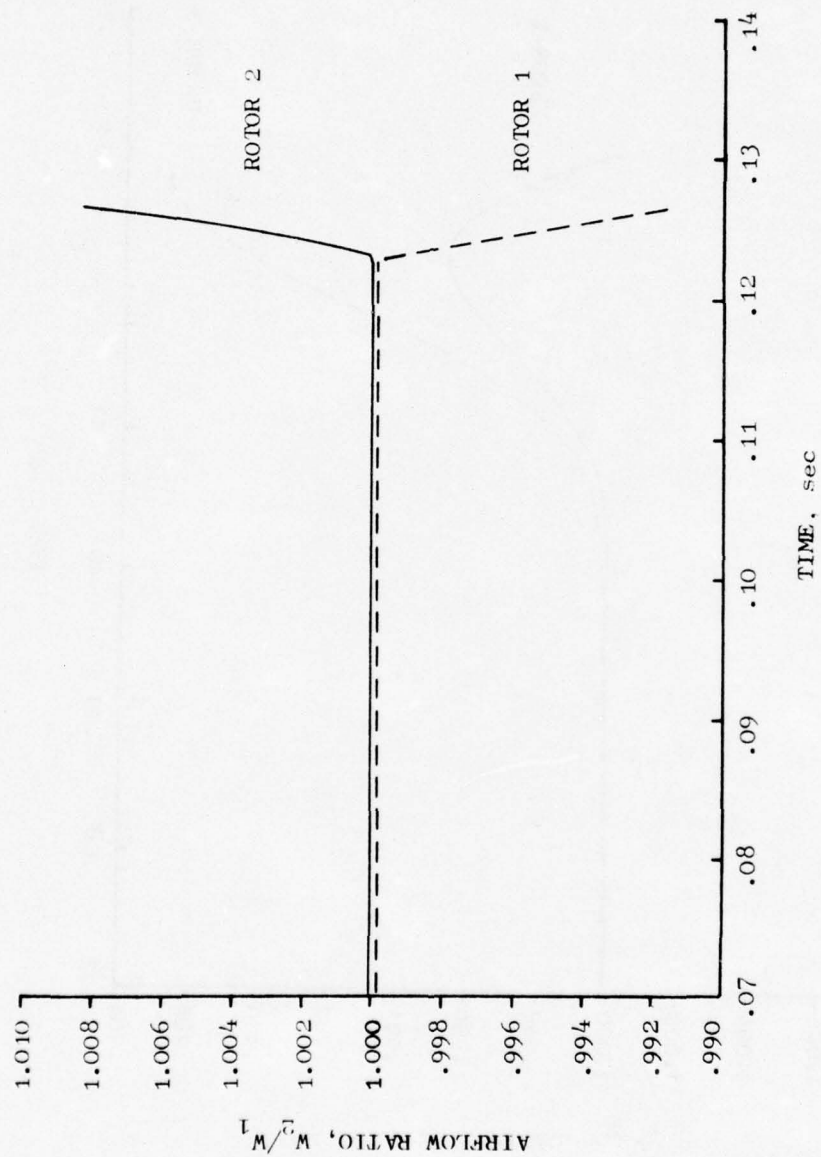


Figure 17. Airflow Ratio Vs. Time, 100% $N/\sqrt{\theta}$, Steady-State Surge.

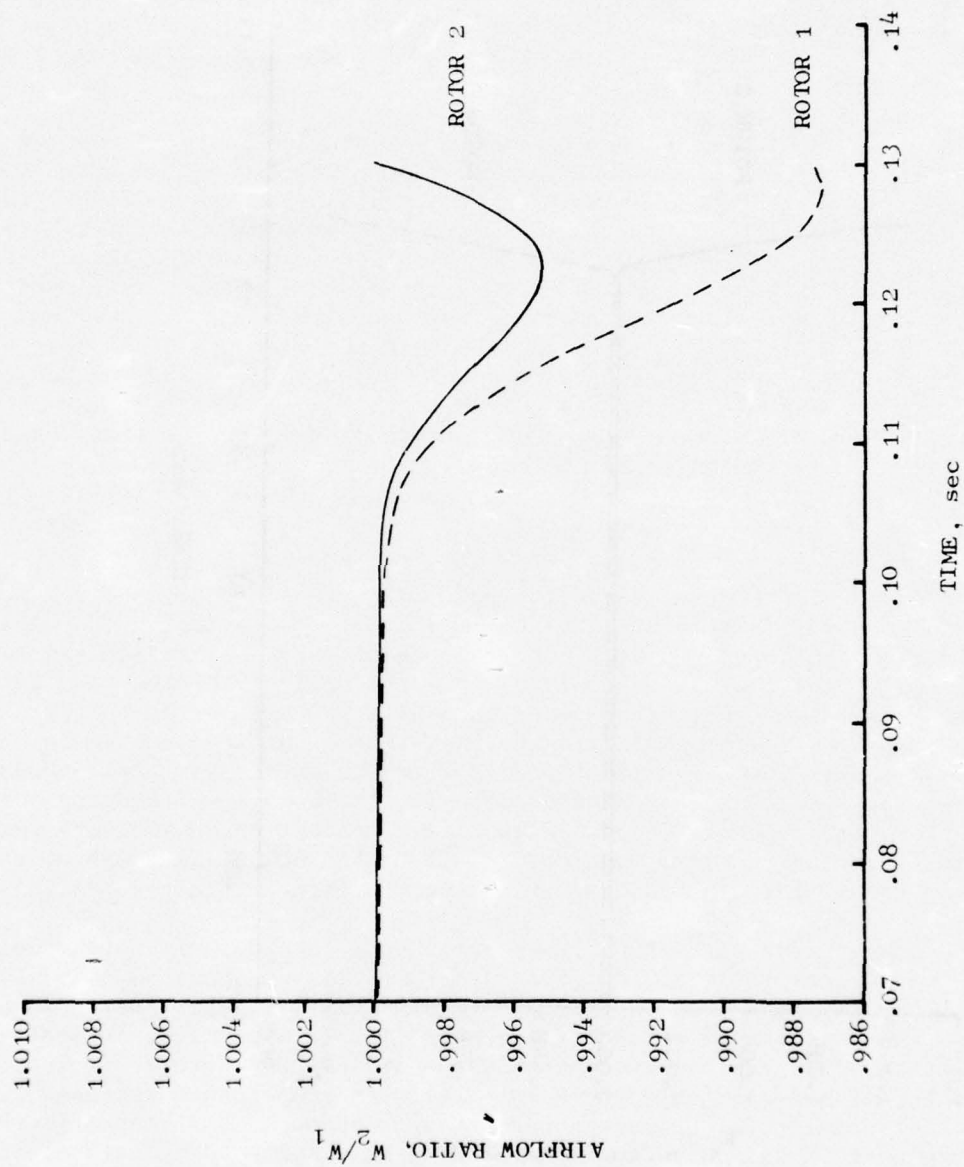


Figure 18. Airflow Ratio Vs. Time, **80%** $N/\sqrt{\theta}$, Steady-State Surge.

The test readings selected for simulation were originally chosen on the basis of being "operating-line" points. The term "operating-line" is somewhat nebulous since the test vehicle is a rig and not an engine. It became apparent during the modeling effort that a more convenient and cost-effective test point could be selected. The fan operating condition "near surge" was adopted as a more practical baseline point for comparison since its proximity to surge meant that considerably less computer time would be expended in throttling from the stationary, mean operating-point up to the region of instability.

A revision to the waveform replication scope (See Table 1) was made as modeling at the higher frequencies progressed. Analysis of the model waveform character for frequencies greater than one-per-rev (≈ 125 Hz) indicated that the model had limited capability to reproduce the higher harmonic components of the fundamental wave. At the higher frequencies, the waveform replication was affected by the structure of the wave pattern developed by the Planar Pressure Pulse Generator and the system boundary conditions. The major part of the wave amplitude is associated with standing waves rather than traveling waves in the ducting between the P³G and the fan IGv. The significant aspect of this type of unsteady flow is that the wavelength at a given frequency is much shorter for a standing wave (λ_S) than for a traveling wave (λ_T) as shown by the Equation 55.

$$\lambda_S = (1-M) \lambda_T \quad (55)$$

The smaller wavelength at a given frequency and the fixed "lumped volume" lengths of the model imply a reduction in spatial resolution of the waveform, especially for the higher harmonics. As a result of this finding and in recognition of the conclusions reached from the analysis of the test data indicating that stability losses were insignificant beyond the one-per-rev frequency, the proposed simulation matrix (Table 1) was restructured as follows: 1) All proposed simulations at frequencies greater than 350 Hz were deleted and, 2) Additional emphasis was placed on low frequency analysis in an effort to better define the Planar Wave Distortion Sensitivity characteristic. Simulations were conducted at 25 Hz and 60 Hz, although no test data were taken at these frequencies during the experimental program.

The measurement parameters that were chosen for comparison to model results have been previously defined (See Table 5). Special note should be taken of the fan-face airflow parameter WCA. This parameter, which is an approximation to the instantaneous corrected fan-face airflow, is based on the instantaneous physical airflow ρAV , the instantaneous total pressure P_T , and the mean total temperature \bar{T}_T . The mean temperature was used since the instantaneous total temperature was not measured. This "approximate" corrected airflow was computed from the test data. The identical set of parameters were used to calculate the same variable in the model. During the analysis of the airflow test data during this program it was determined that the original airflow data, as reported in Reference 3, were inverted. This inversion has been removed from the experimental data used in this report.

The model results that were used for establishing the fidelity of the model were obtained by allowing the model to compute through a sufficient number of cycles to insure that transients had settled out. This procedure insured that "essentially stationary" conditions were established and provided model results that were representative of the "near surge" stationary data point to which the model results would be compared. The use of the term "essentially stationary" should be noted. In some cases, both the model results and the test data showed evidence of low-frequency beat frequencies which led to slight deviations from waveform stationarity.

The results of the waveform simulations have been summarized in terms of amplitude and phase angle as a function of frequency. Where the model amplitudes (parameter maximum minus parameter minimum all divided by the average value of the parameter) of the PTIGV parameter did not quite match the test data, the model values of all parameters were scaled by the ratio of the test data PTIGV value to the model PTIGV value. Examination of Figures 19 and 20 illustrates some of the aspects of model fidelity. It is noted that at both 80% and 100% corrected speeds, there is good agreement between model and test amplitudes up to 118 Hz and lesser agreement above this frequency, although the trends in amplitude are generally the same. The parameter which shows the greatest spread in values is the P3GPS parameter. This probably is the result of the boundary condition which was specified at the bellmouth entrance and was previously discussed in Section 4.4.3.

The phase angles of both the model and test parameters are measured relative to the PTIGV parameter and are given in Figures 21 and 22 for 80% and 100% speeds, respectively. Good agreement in the phase angle results are noted up to approximately 80 Hz. Above this frequency, the trends are reproduced, but there is a wide discrepancy between model and test phase angles.

The phase angle plots of Figures 21 and 22 may raise questions as to how waves propagate, that is, at lower frequencies a parameter downstream of the PTIGV parameter may lag while at higher frequencies it may lead. Clarification of this situation is difficult because both standing wave and traveling wave components are present, but it suffices to say that the phase angle relative to PTIGV could lead or lag the given value by an integral multiple of cycles.

The data comparison presentations take the following form: Eight parameters are plotted on a page starting with the static pressure P3GPS and continue in a logical geometrical progression through the test set-up concluding with the fan duct pressure at the discharge valve FDPD. Only the unsteady portion of the waveform is shown since the mean value of the parameter has been removed. The PTIGV parameter was chosen as the reference parameter. The procedure for conducting waveform comparisons began by overlaying the model waveform of PTIGV on top of the test data PTIGV waveform, since all the model waveforms are time correlated with each other and all the test data waveforms are time correlated with each other. The P3G model amplitude was chosen in a manner that caused as close a match as practical between the PTIGV model amplitude and the PTIGV test data amplitude. Hence, the degree of waveform similitude between the model results and the test data can be assessed for the other parameters.

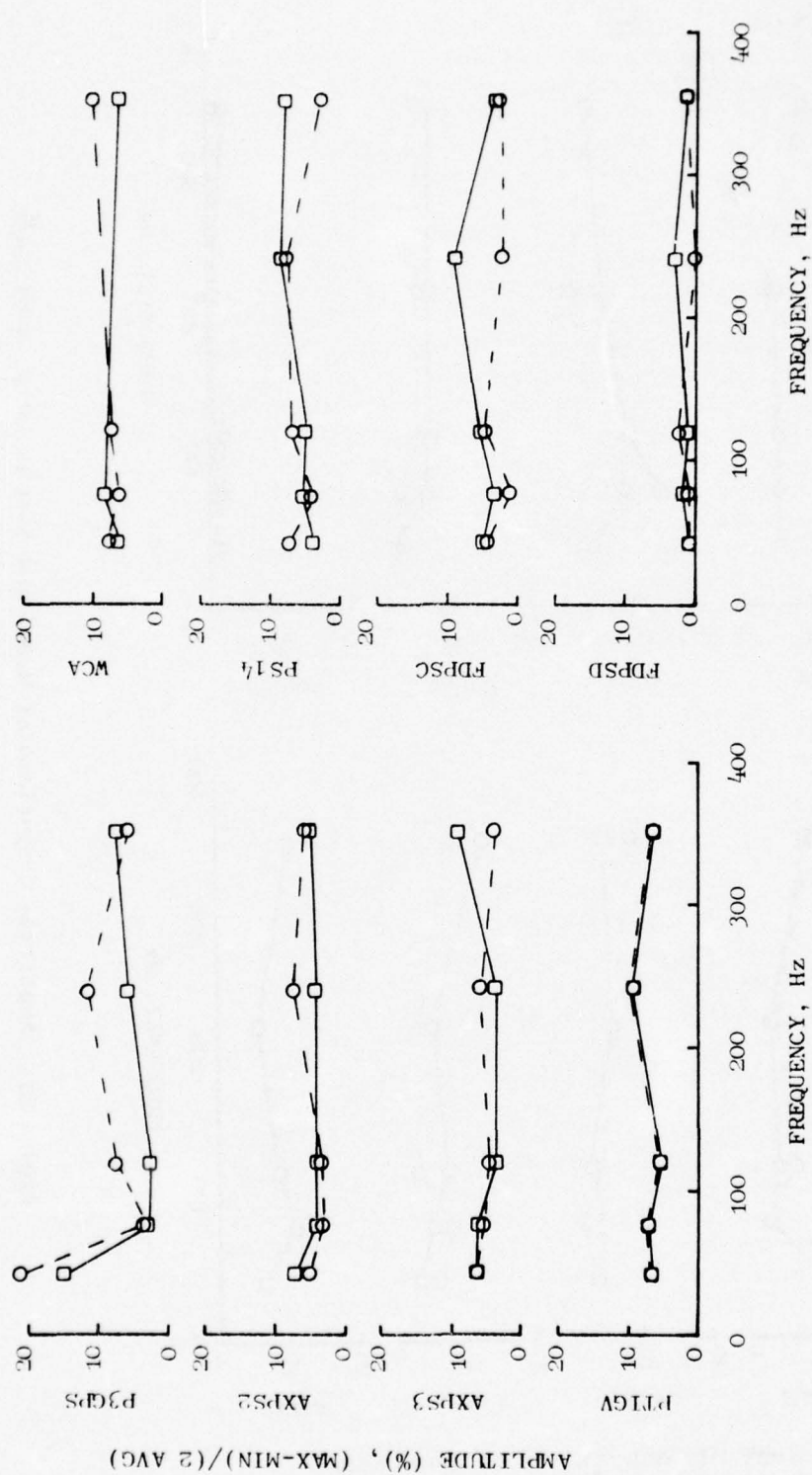


Figure 19. Amplitude Comparison of Model and Test Results, 80% N/\sqrt{g} .

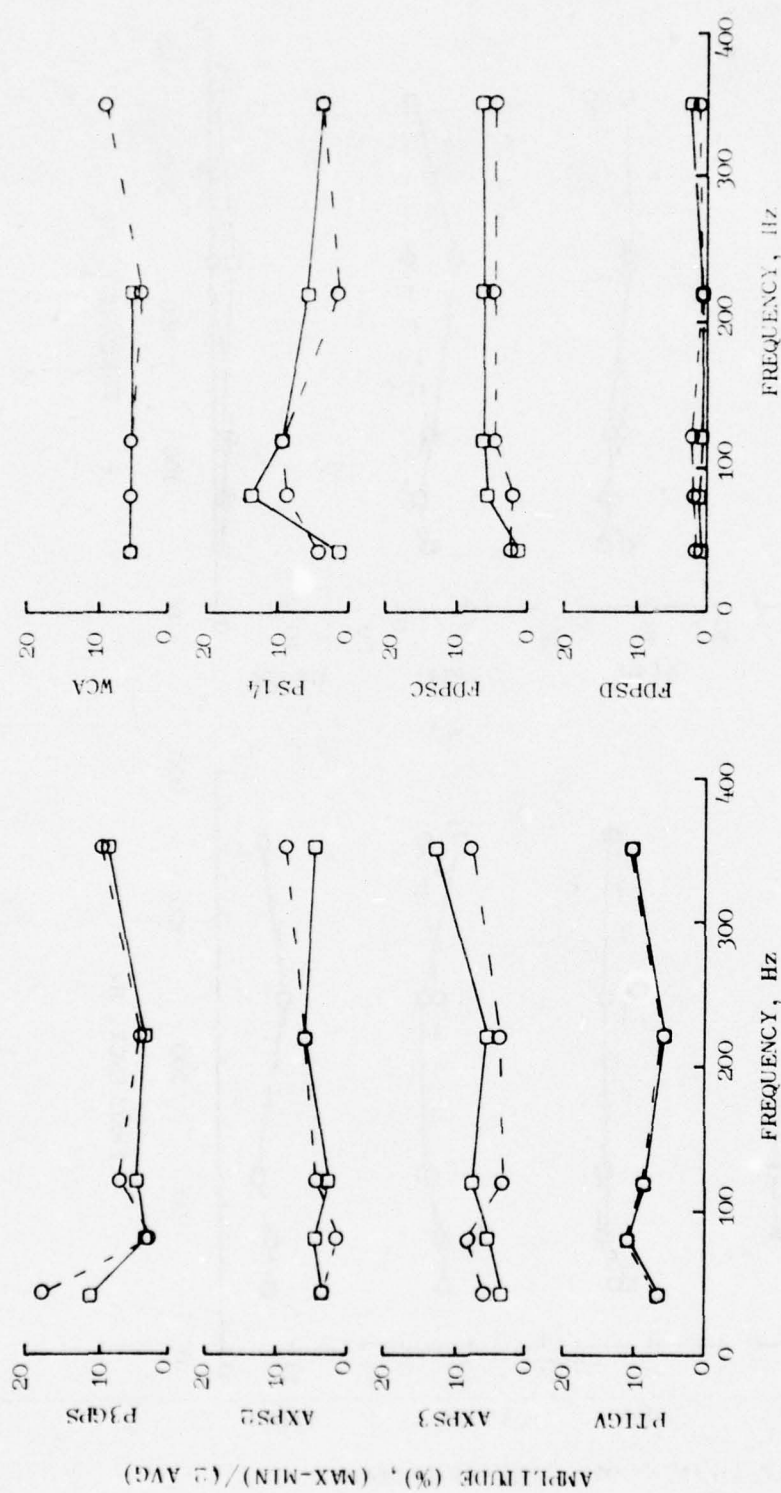


Figure 20. Amplitude Comparison of Model and Test Results, 100% $N/\sqrt{\theta}$.

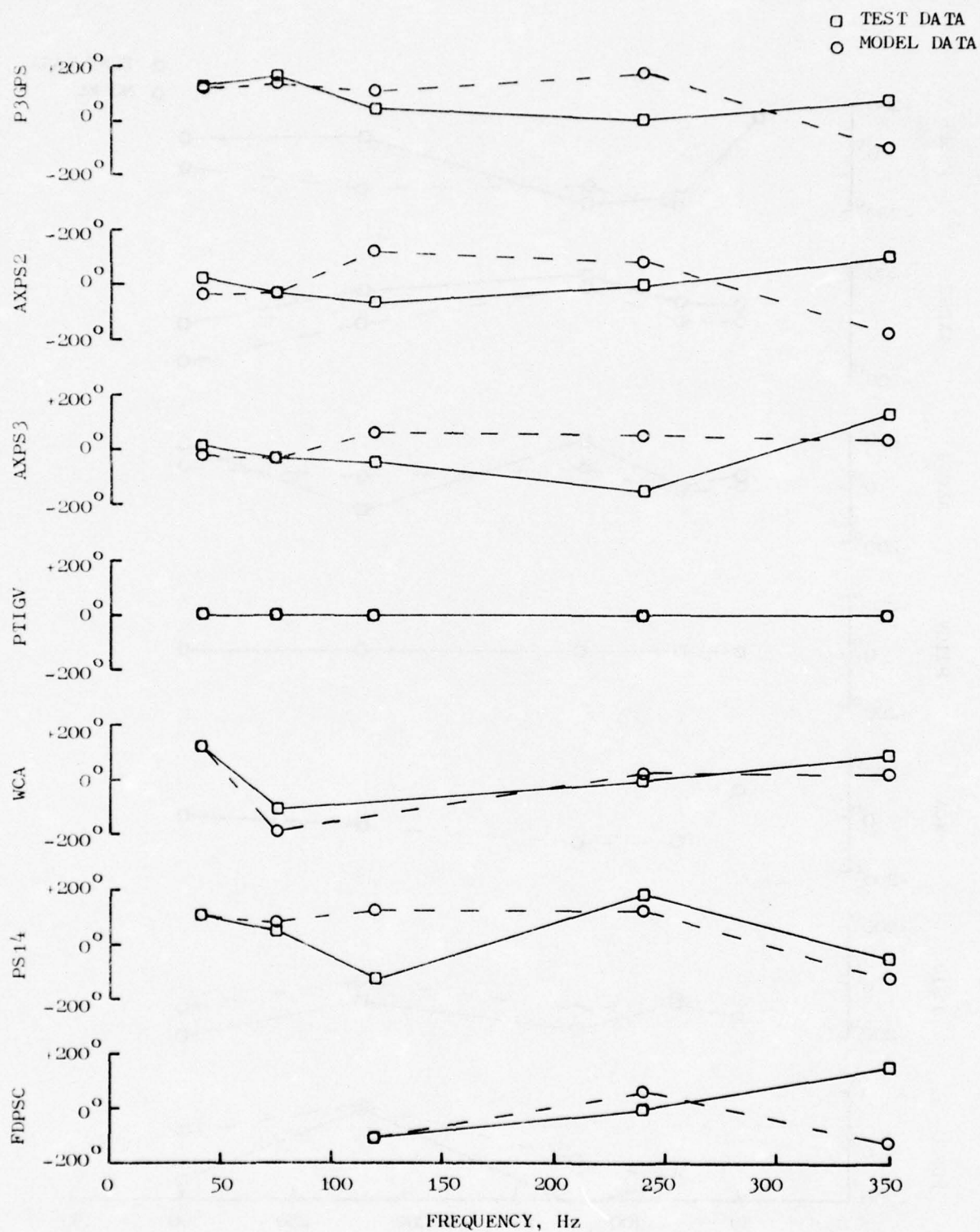


Figure 21. Phase Angle Comparison of Model and Test Results,
80% N/\sqrt{G} .

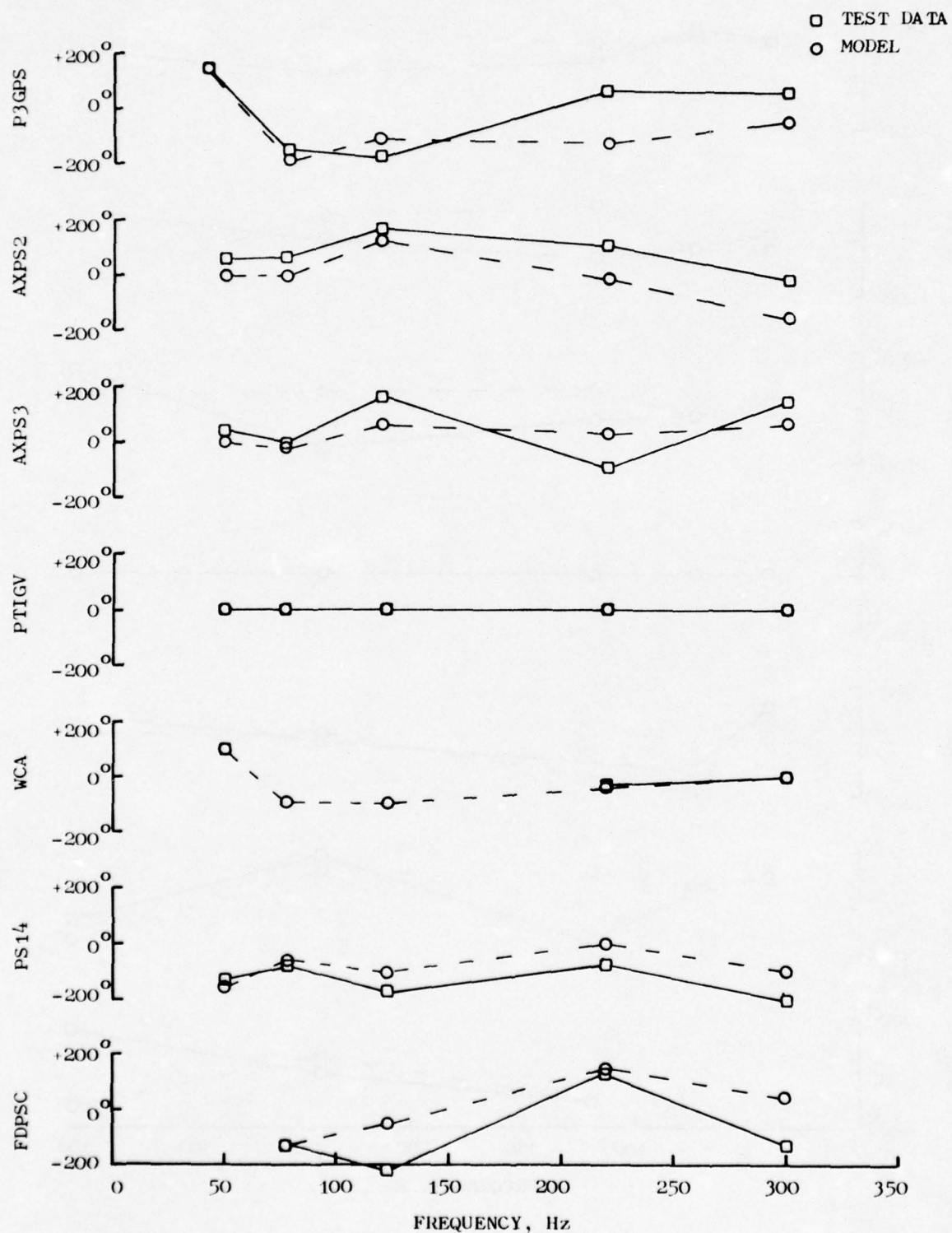


Figure 22. Phase Angle Comparison of Model and Test Results, 100% N/\sqrt{S} .

5.2.1.1 Simulation of Rdg. 71, 100% $N/\sqrt{\theta}$, 42 Hz

Figure 23 illustrates the comparison between the model results and the test data for 100% corrected speed and a Planar Pressure Pulse Generator frequency of 42 Hz. The model simulates the amplitude and phase of all variables throughout the system. The model static pressure forward of the P³G (P3GPS) shows a higher amplitude than test results. This variation is attributed to the forward boundary condition (P_T and T_T held constant) as previously discussed (See Section 4.4.3), but is not considered to have significant impact on the overall accuracy of the simulation. Both the model and the test data PS14 parameter exhibit second harmonic content although the test data exhibits it to a lesser extent. It should be noted that the model is being slowly throttled and that the amplitude of the PS14 and FDPSC are both being attenuated by the change in the operating point boundary condition. Since it was not always possible to precisely reproduce the test mean operating point, some deviation can be anticipated as a result of this operating point dissimilarity. The model "approximate" airflow matches the test data "approximate" airflow.

5.2.1.2 Simulation of Rdg. 82, 80% $N/\sqrt{\theta}$, 42 Hz

Figure 24 illustrates the 80% corrected speed, 42 Hz validation case. Results are similar to the 100% speed, 42 Hz case with the exception of the presence of a strong second harmonic contribution to both the model and test "approximate" corrected airflow and pressure waveforms downstream of the fan. The amplitudes of all model parameters show agreement with the test data. The amplitude and phase of the model second harmonic contribution is not in phase with the test values, but the shape of these waveforms are not entirely stationary. A model simulation of longer duration would probably produce better agreement between waveforms.

5.2.1.3 Simulation of Rdg. 69, 100% $N/\sqrt{\theta}$, 80 Hz

Figure 25 shows the validation curves for this case. The standing wave amplitudes and phase are illustrated by the static pressures in the duct between the P³G and the fan (AXPS2 and AXPS3). The AXPS2 measurement appears to be near a node in the pressure wave since the amplitudes are small and the waveform is erratic. AXPS3 is a pressure measurement approximately 15 inches downstream of AXPS2 and shows large pressure oscillations of uniform amplitude which are indicative of being closer to an antinode. The model results replicate the phase and amplitude of these waveforms. The test data "approximate" corrected airflow was not available for this reading. There is only a slight deviation between model and test amplitudes of the downstream pressures while the phase relationships remain well correlated.

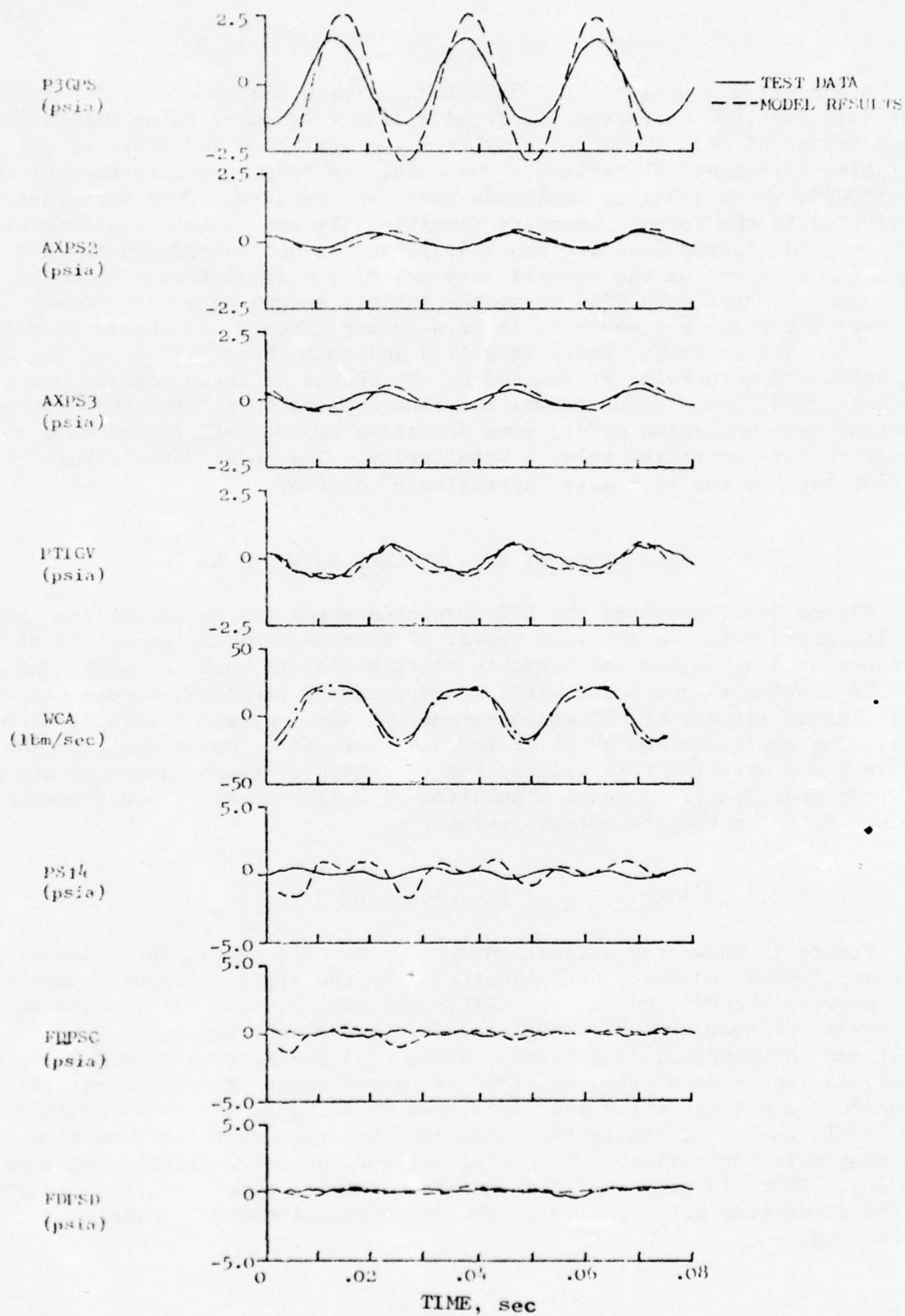


Figure 23. Simulation of Rdg. 71, 100% $N/\sqrt{\theta}$, 42 Hz.

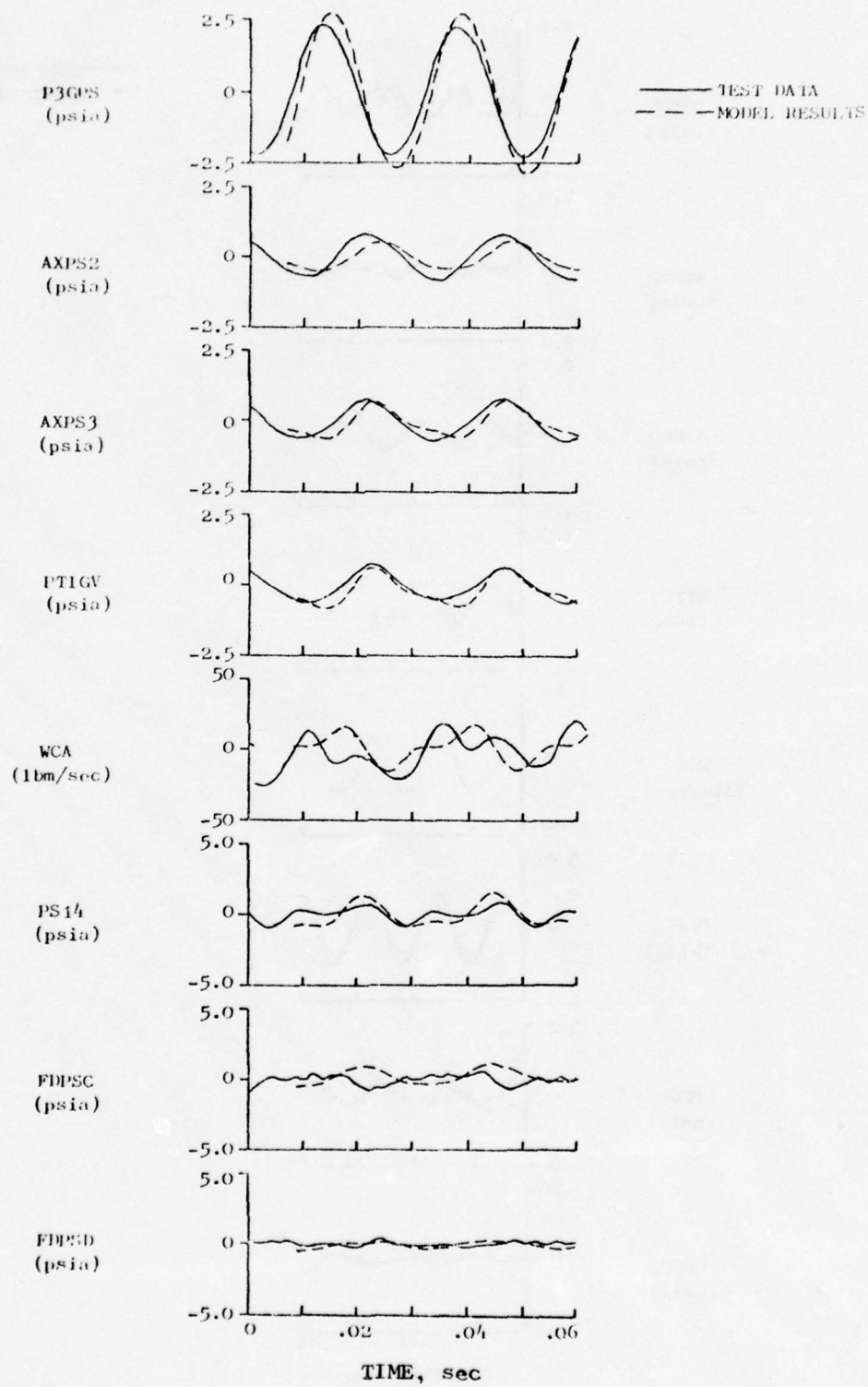


Figure 24. Simulation of Rdg. 82, 80% $N/\sqrt{\theta}$, 42 Hz.

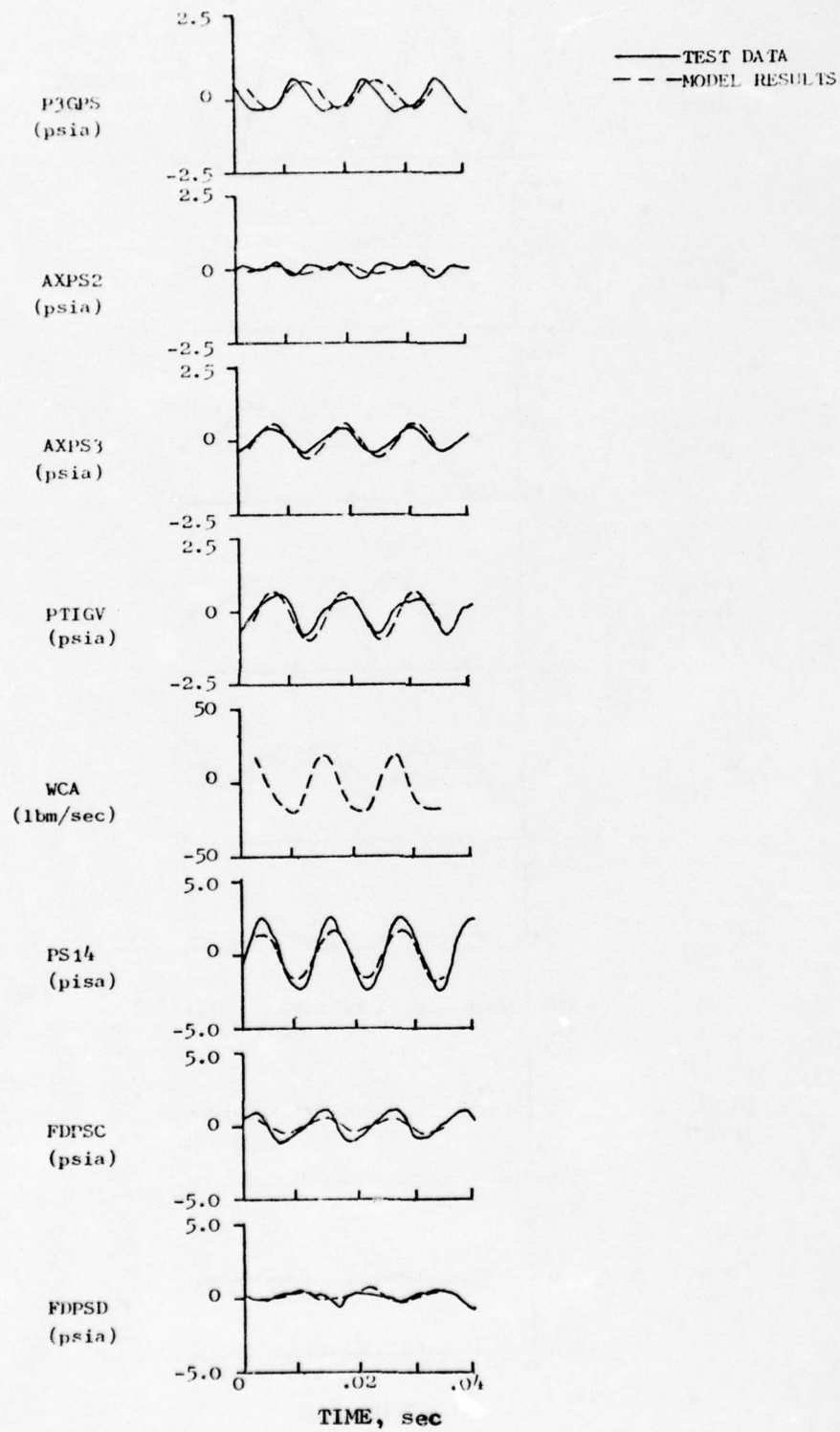


Figure 25. Simulation of Rdg. 69, 100% $N/\sqrt{\theta}$, 80 Hz.

5.2.1.4 Simulation of Rdg. 77, 80% $N/\sqrt{\theta}$, 75 Hz

Figure 26 illustrates the test and model results for this case. The duplication of phase and amplitude of pressures throughout the simulation is shown to be excellent. The model corrected airflow phase and magnitude is shown to deviate somewhat from the test data. No apparent explanation exists for this departure, but the experimental nature of the airflow measurement device must be considered when assessing the quality of this test-data measurement.

5.2.1.5 Simulation of Rdg. 64, 100% $N/\sqrt{\theta}$, 118 Hz

Figure 27 represents the simulation of this case. The 118 Hz frequency test data contained large harmonic components that distort the fundamental waveform. The model does not simulate these higher frequency components. Model and test amplitudes compare reasonably well over the entire system, but phase shifts are apparent throughout. As frequencies increase and wavelengths decrease, the positions of the instrumentation relative to each other (model versus test) and to the boundary conditions become important to the precision of the phase comparisons, especially when dealing with standing wave components.

This case also provides the base point for two other simulations. Model operation at two different pressure fluctuation amplitudes was carried out for the purposes of establishing distortion sensitivities as a function of amplitude. The results of the sensitivity variation with amplitude will be discussed later.

5.2.1.6 Simulation of Rdg. 61, 80% $N/\sqrt{\theta}$, 118 Hz

Figure 28 illustrates the model versus test comparisons for this reading. The comments addressed to the previous 118 Hz point can also be similarly applied to the 80% corrected speed case. However, the contribution of the second harmonic to the overall test waveform is somewhat less than in the previous case and the phase relationships are improved. An exception to the overall agreement is the P3GPS model results with its larger amplitude and little evidence of higher harmonic frequencies as compared to the test data. Other variables (AXPS2 and PTIGV) show similar effects, but with a reduced harmonic amplitude.

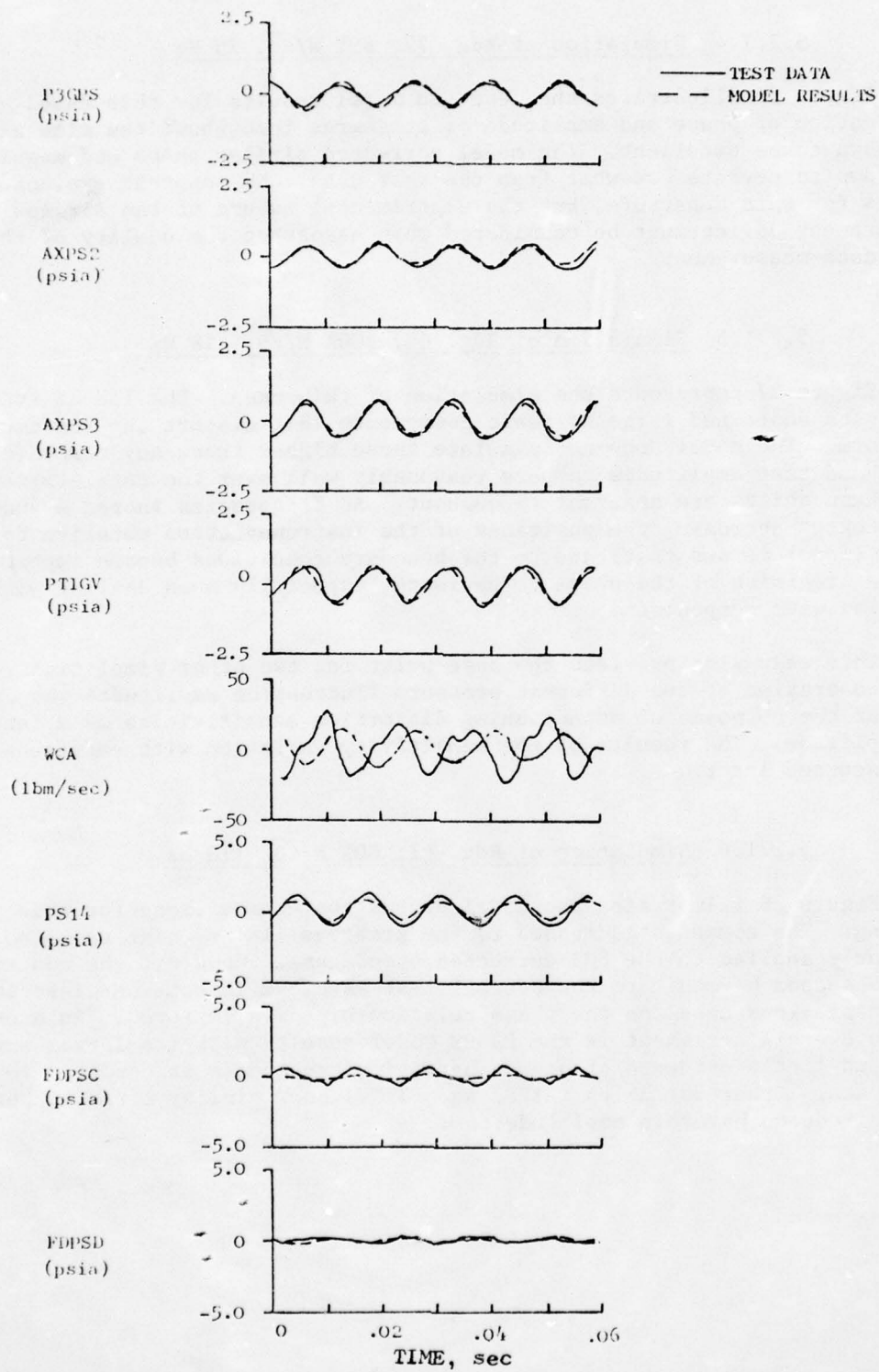


Figure 26. Simulation of Rdg. 77, 80% $N/\sqrt{\theta}$, 75 Hz.

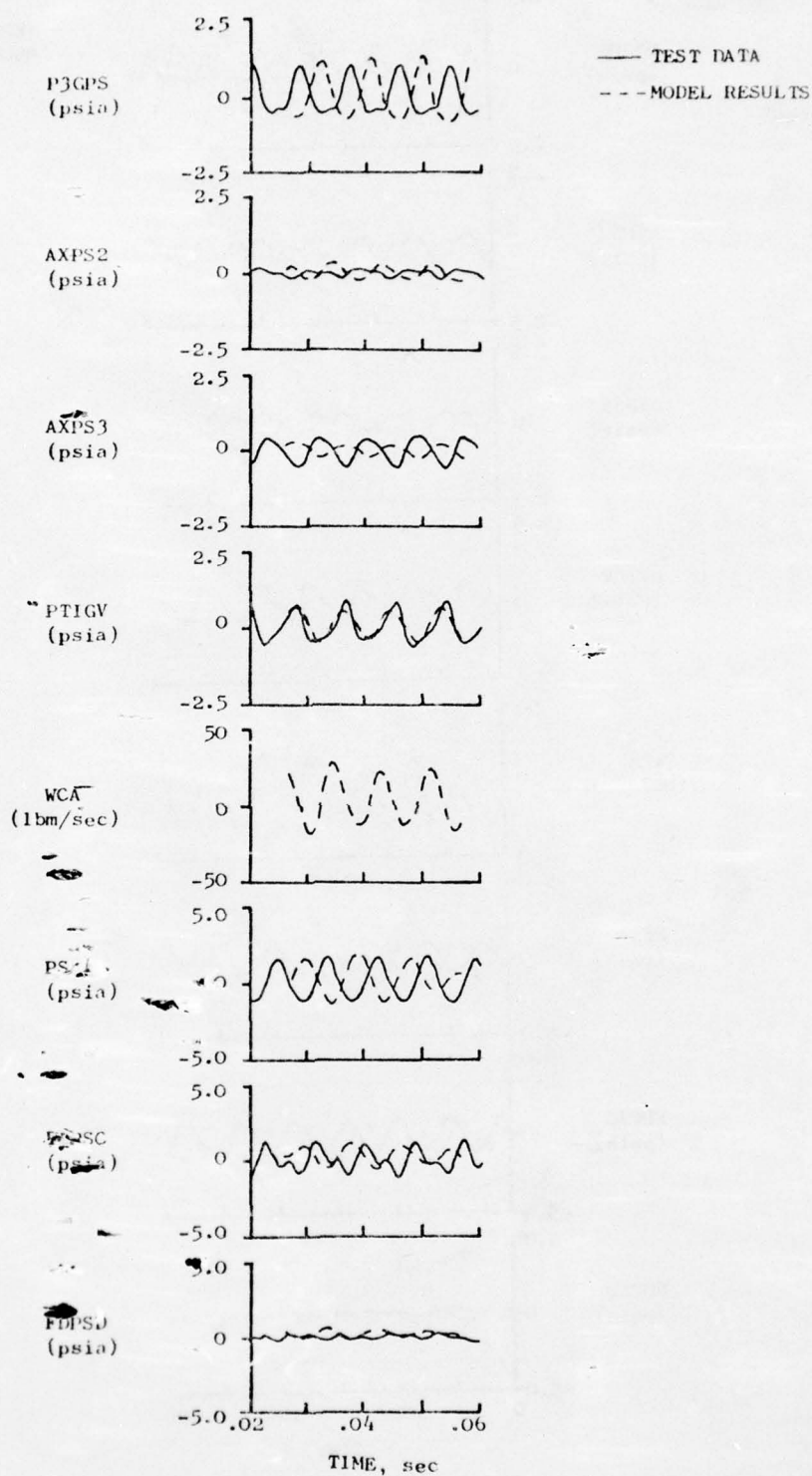


Figure 27. Simulation of Rdg. 64, 100% $N/\sqrt{\theta}$, 118 Hz.

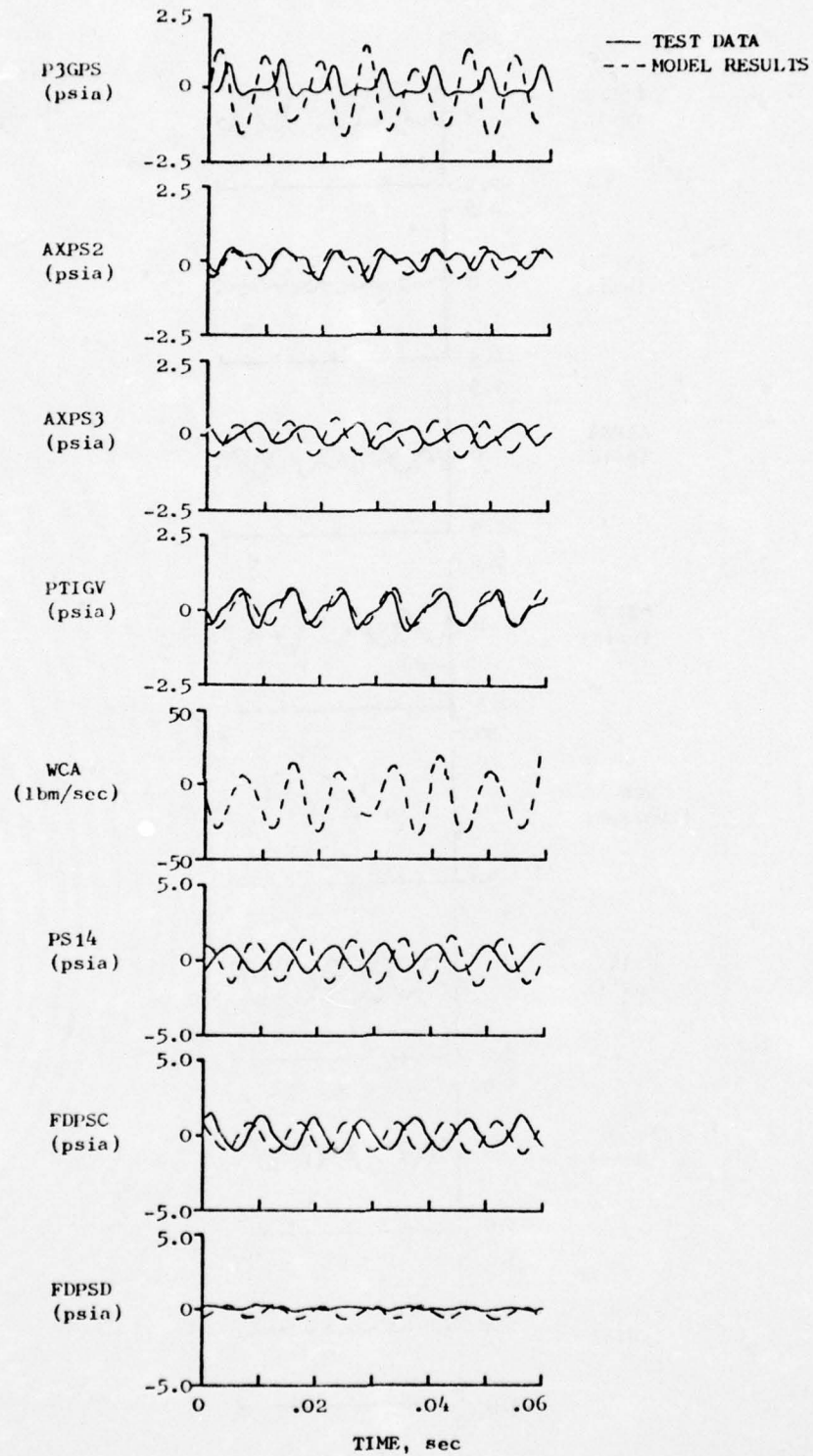


Figure 28. Simulation of Rdg. 61, $80\% N/\sqrt{\theta}$, 118 Hz.

5.2.1.7 Simulation of Rdg. 41, 100% $N/\sqrt{\theta}$, 220 Hz and Rdg. 57, 80% $N/\sqrt{\theta}$, 240 Hz

Simulations of Rdgs. 41 and 57 are shown in Figures 29 and 30, respectively. The model results show responses similar to the test data responses for both cases at these frequencies. The fundamental wave shapes and amplitudes are preserved, but the harmonics of the test data are not seen in the model results. Phase relationships are not maintained as well as with the lower frequency cases.

The amplitude and phase of the predicted airflow for the Rdg. 41 case are in agreement with the amplitude and phase of the measured airflow, despite the non-uniformity of the measured airflow waveform. Phase agreement is to be expected, since the measurement planes for both the model and the test data airflows are coincident.

The Rdg. 57, model total-pressure amplitude at the IGV station does not match the measured PTIGV value because it was necessary to hold the model amplitude at a lower value to insure stable model operation at this condition. This apparent sensitivity of the model is attributed to the extremely large variation in "approximate" corrected airflow at the fan inlet (WCA amplitude $\approx 30\%$). Measured airflows were not available at this condition for comparison.

5.2.1.8 Simulation of Rdg. 43, 100% $N/\sqrt{\theta}$, 350 Hz and Rdg. 53, 80% $N/\sqrt{\theta}$, 350 Hz

Simulations of Rdgs. 43 and 53 are shown in Figures 31 and 32, respectively. The most significant feature of these comparisons is the apparent attenuation of model static pressures as the distance from the Planar Pressure Pulse Generator increases. At this frequency for both the 100% and 80% conducted speeds, the model P3GPS parameter shows an attenuation of pulse amplitude relative to test data, while at lower frequencies the model P3GPS parameter had tended to exhibit amplitudes greater than these of the test data. Attenuation of the amplitudes is thought to be a function of the model transmission characteristics at this fundamental frequency, in the same manner as the higher harmonics of the lower frequencies appeared to be attenuated.

5.2.2 Sample Plotted Results

The overall analysis of each model case was facilitated by the use of machine plots of pertinent aerodynamic variables displayed as a function of time. A set of these plots are shown in Figures 33 through 39 for the Rdg. 82, 100% corrected speed, 42 Hz case simulation.

Figure 33 shows the variation of physical airflow entering each rotor as a function of time. The phase differences in flow are suggestive of stage mismatch in flow handling. Figure 34 illustrates the variation of

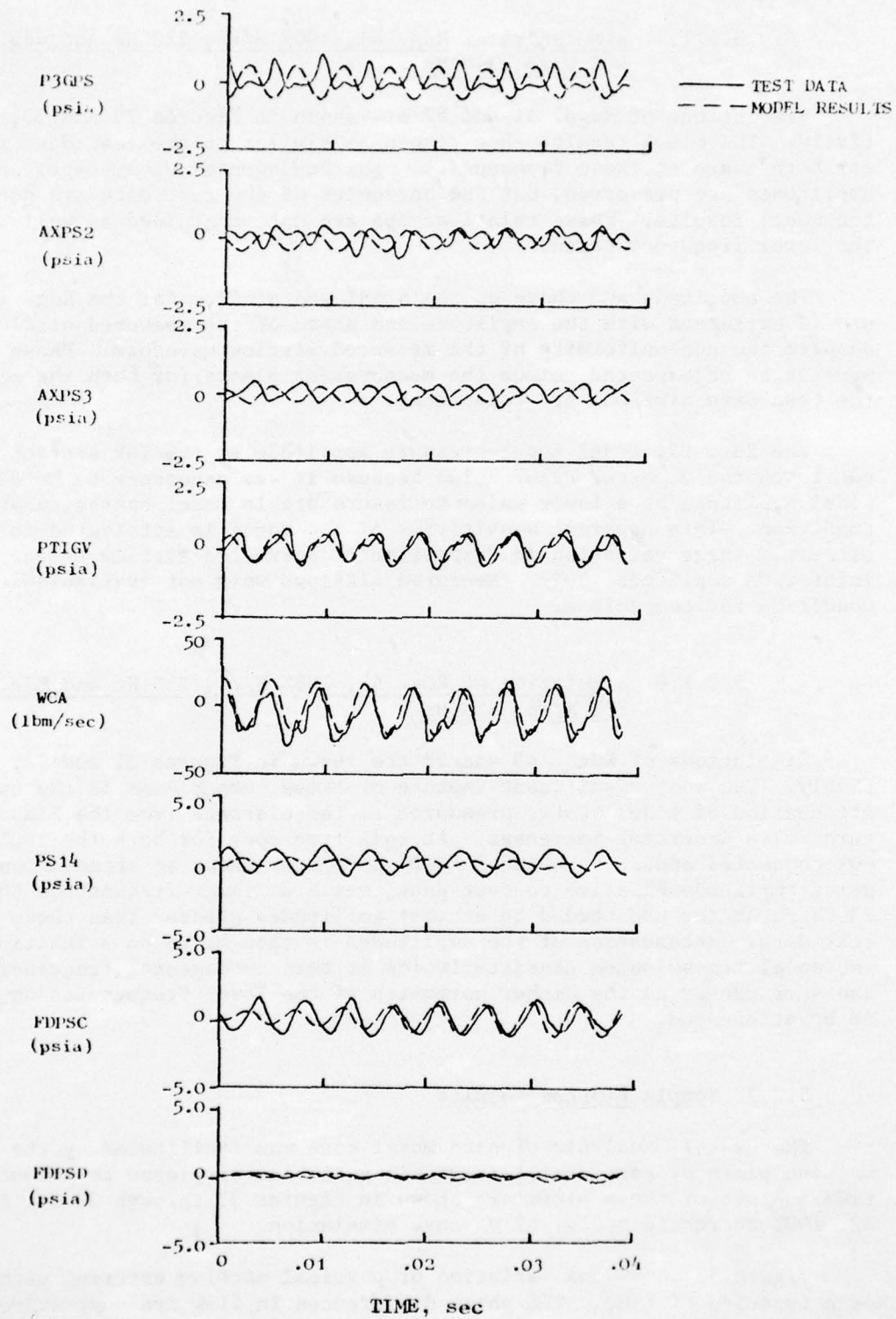


Figure 29. Simulation of Rdg. 41, 100% $N/\sqrt{\theta}$, 220 Hz.

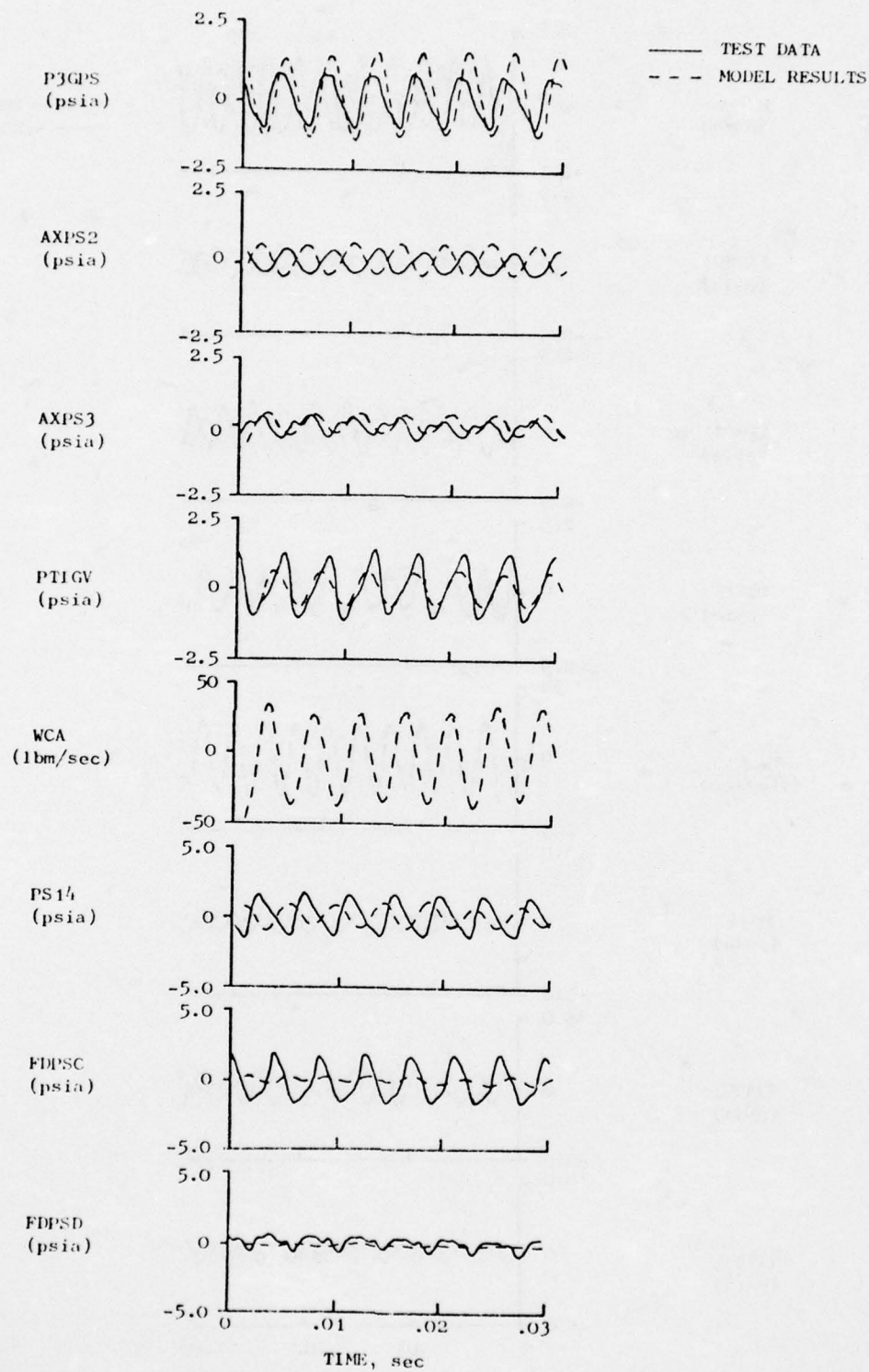


Figure 30. Simulation of Rdg. 57, $80\% N/\sqrt{\theta}$, 240 Hz.

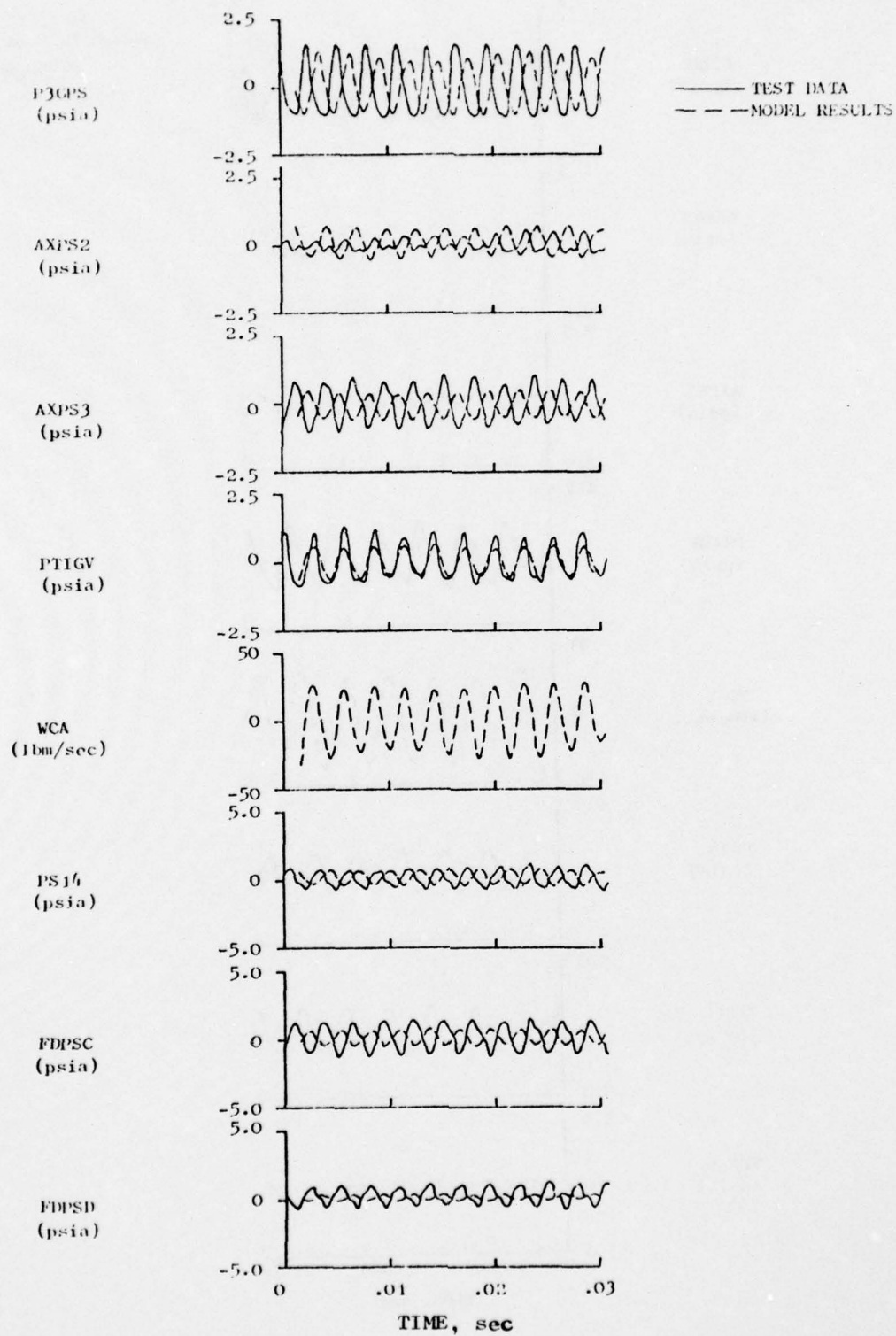


Figure 31. Simulation of Rdg. 43, 100% $N/\sqrt{\theta}$, 350 Hz.

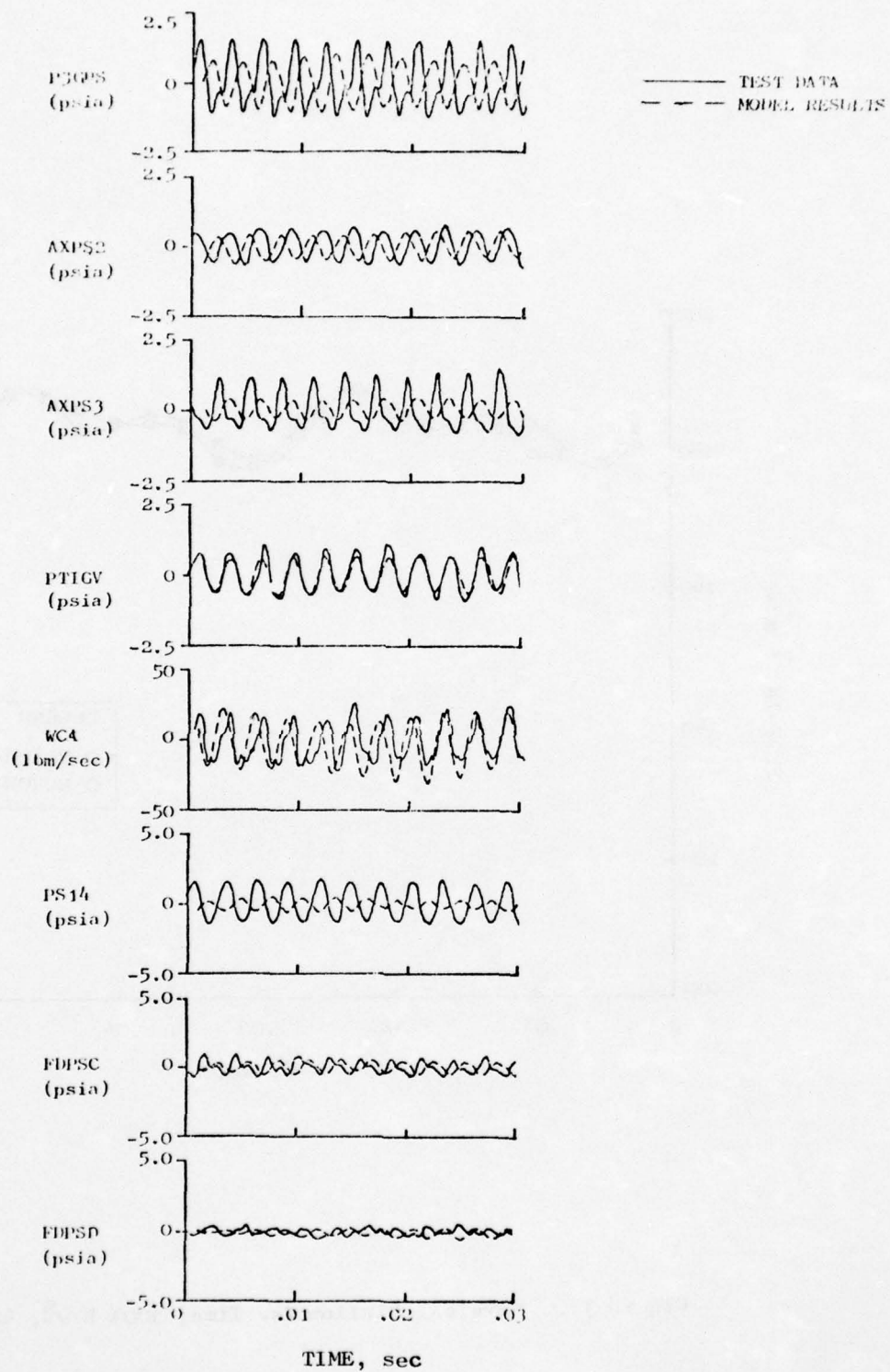


Figure 32. Simulation of Rdg. 53, 80% $N/\sqrt{\theta}$, 350 Hz.

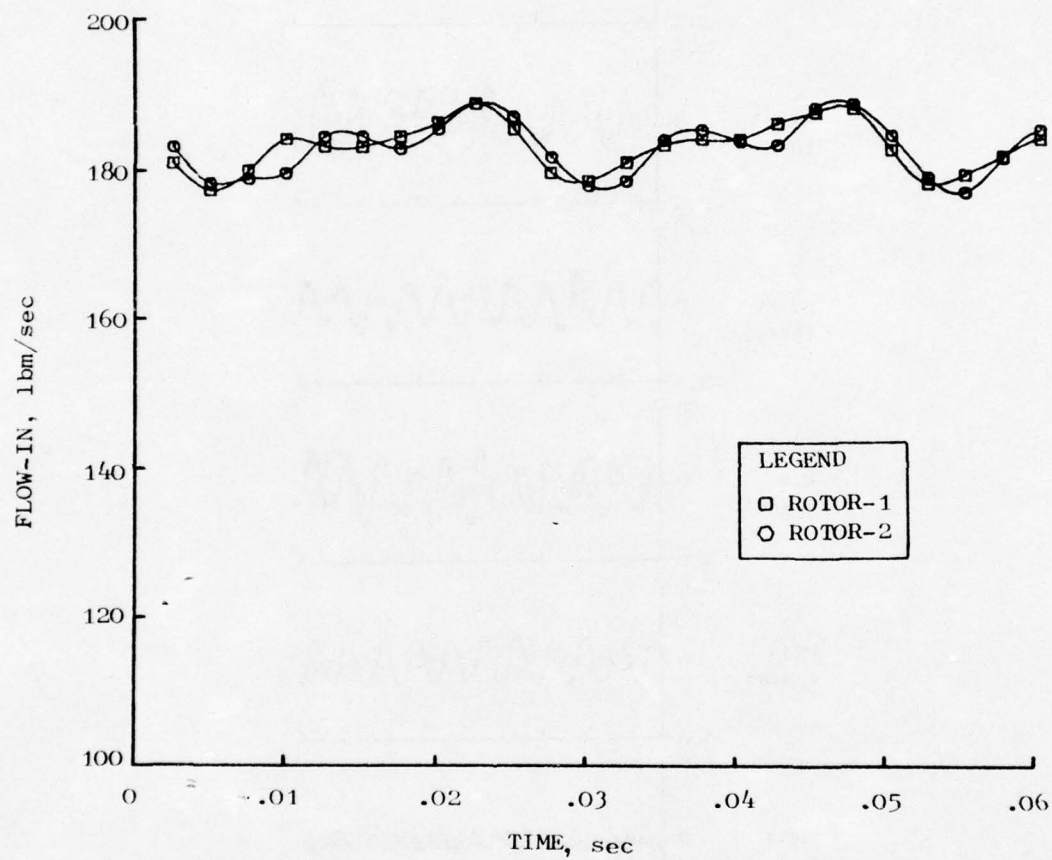


Figure 33. Physical Airflow Vs. Time, 100% $N/\sqrt{\theta}$, 42 Hz.

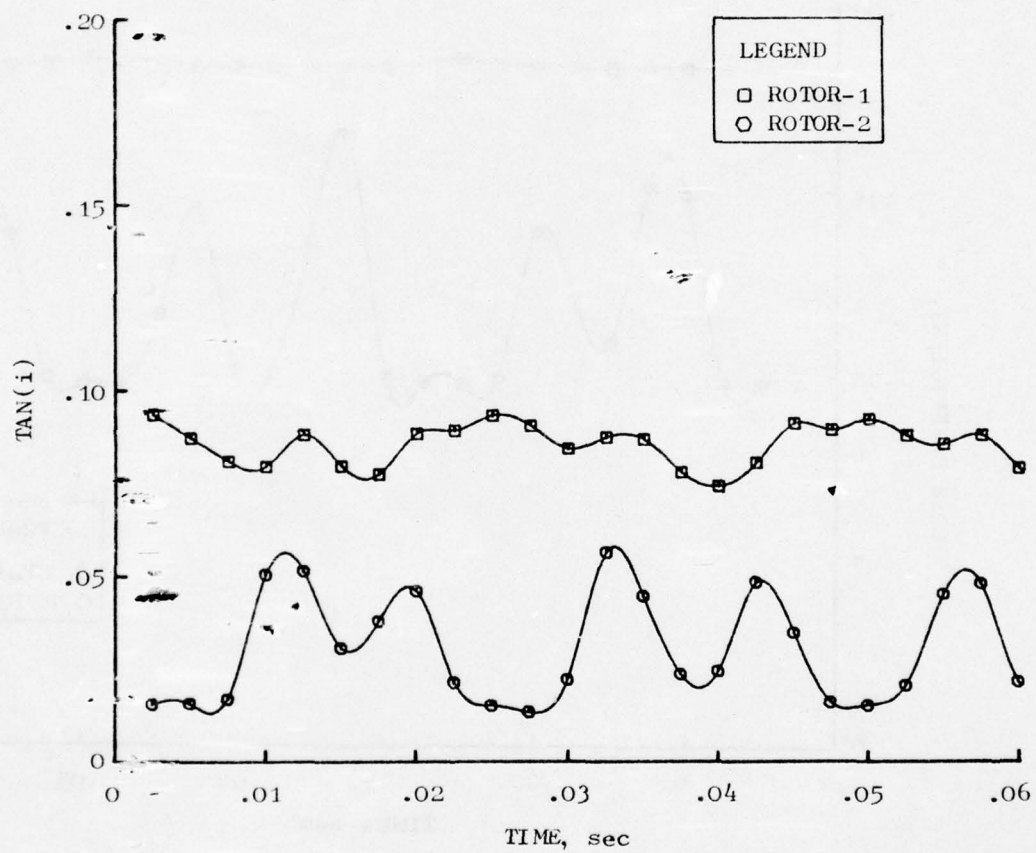


Figure 34. Tangent of Incidence Angle Vs. Time, 100% $N/\sqrt{\theta}$, 42 Hz.

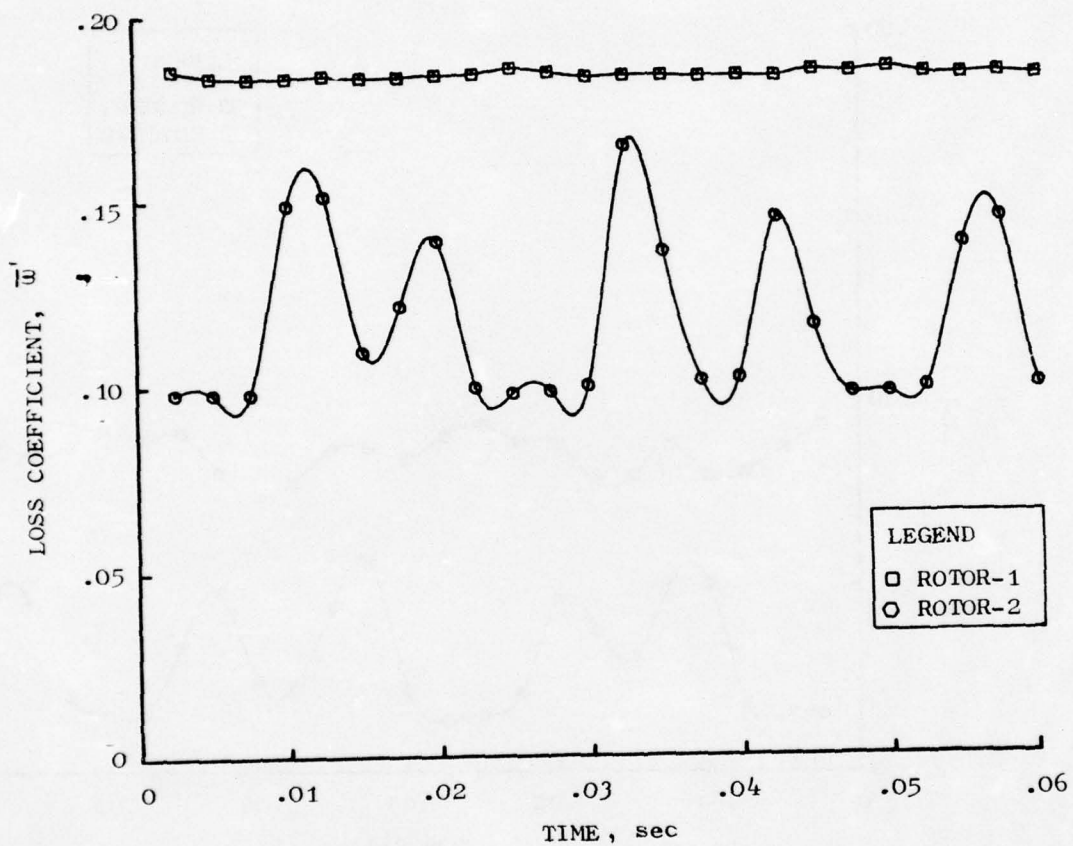


Figure 35. Loss Coefficient Vs. Time, 100% $N/\sqrt{\theta}$, 42 Hz.

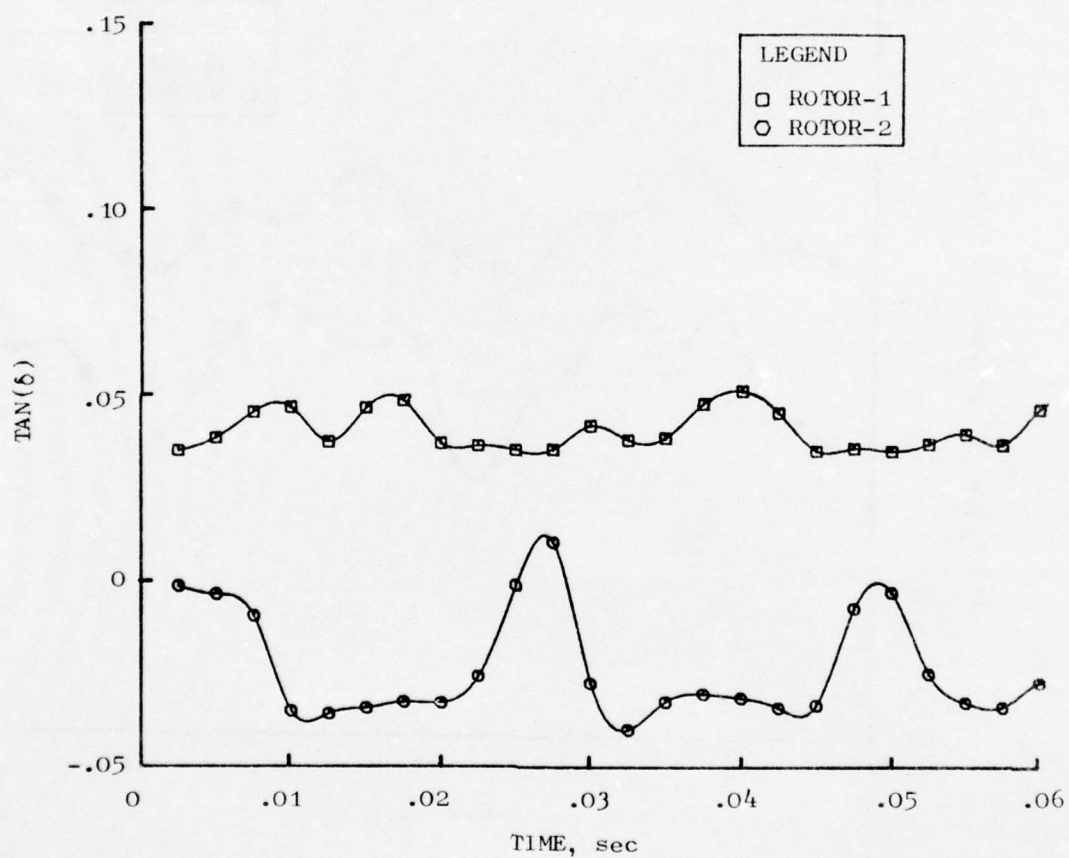


Figure 36. Tangent of Deviation Angle Vs. Time, 100% $N/\sqrt{\theta}$, 42 Hz.

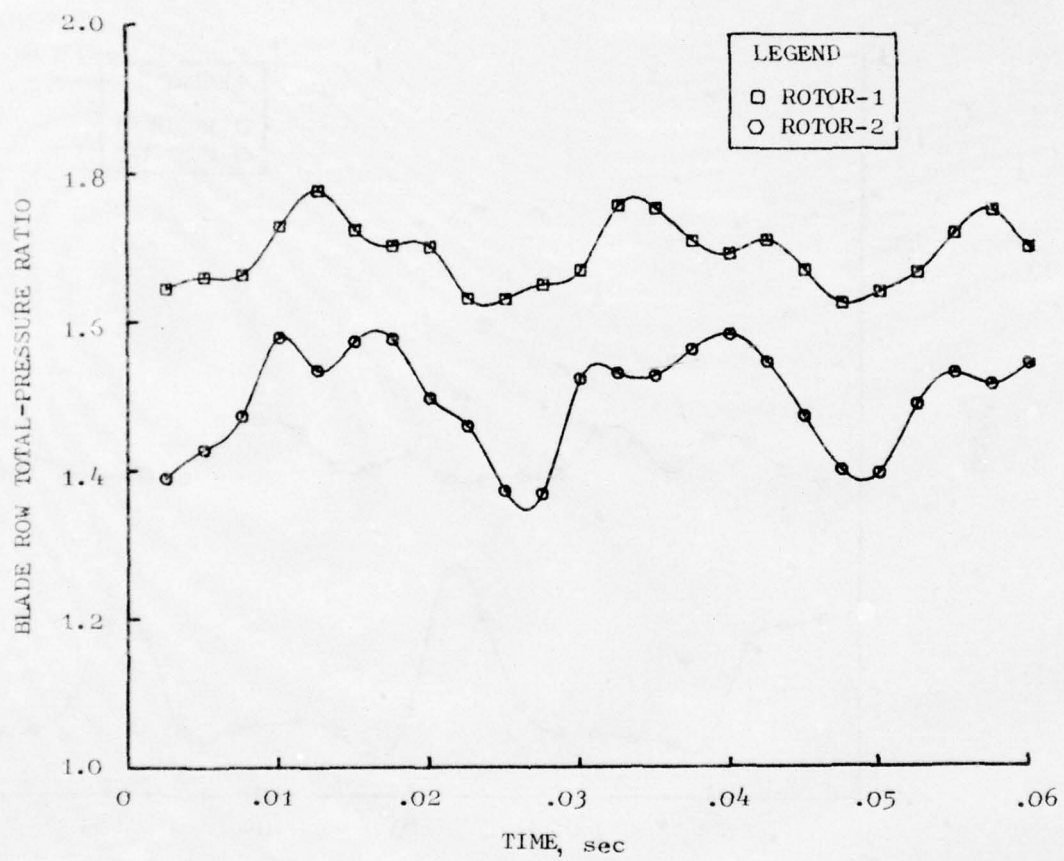


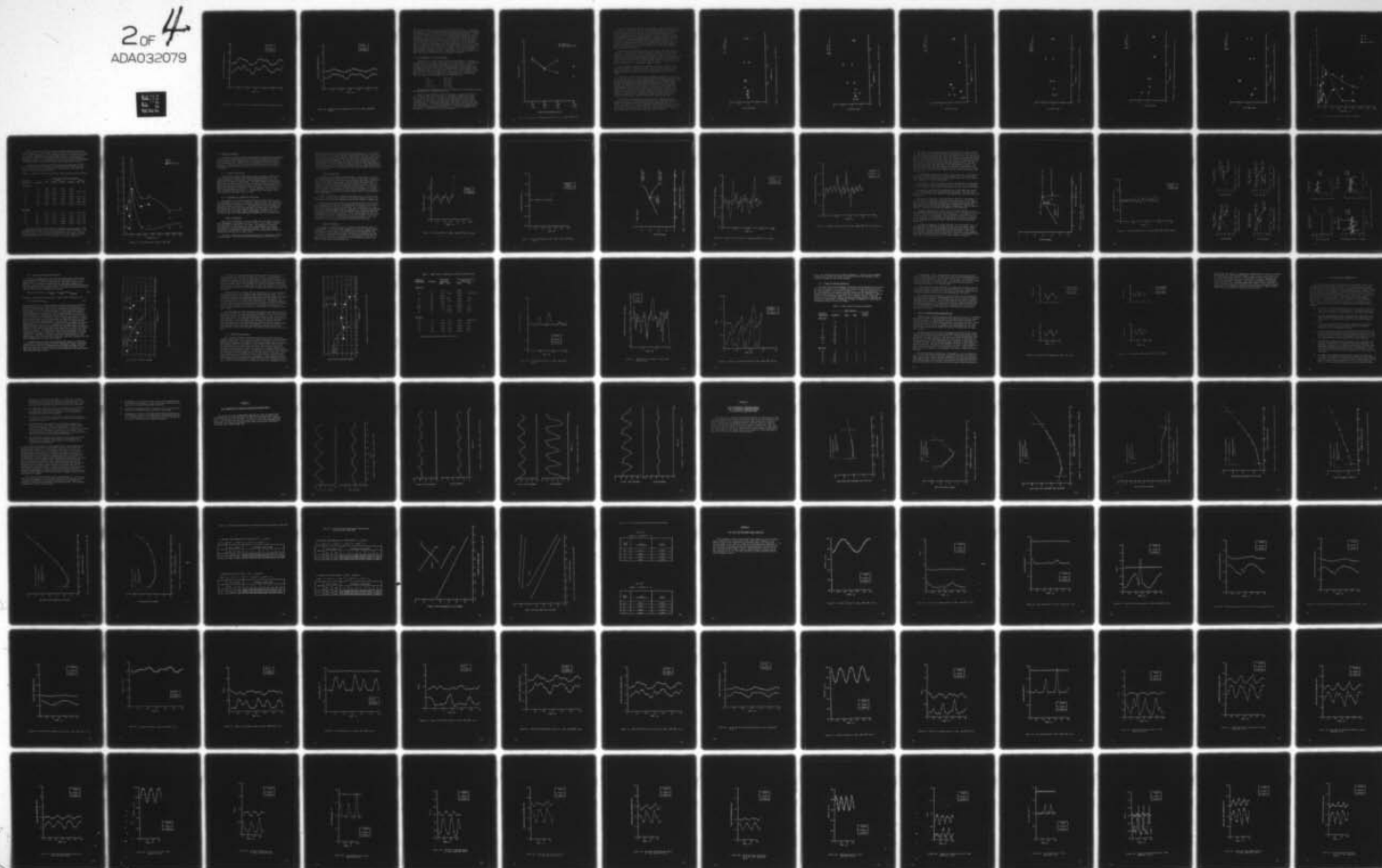
Figure 37. Blade Row Total-Pressure Ratio Vs. Time, 100% $N/\sqrt{\theta}$, 42 Hz.

AD-A032 079

GENERAL ELECTRIC CO CINCINNATI OHIO AIRCRAFT ENGINE GROUP F/G 1/3
DYNAMIC DIGITAL BLADE ROW COMPRESSION COMPONENT STABILITY MODEL--ETC(U)
AUG 76 G G REYNOLDS, W G STEENKEN F33615-75-C-2029
R76AEG299 AFAPL-TR-76-76 NL

UNCLASSIFIED

2 of 4
ADA032079



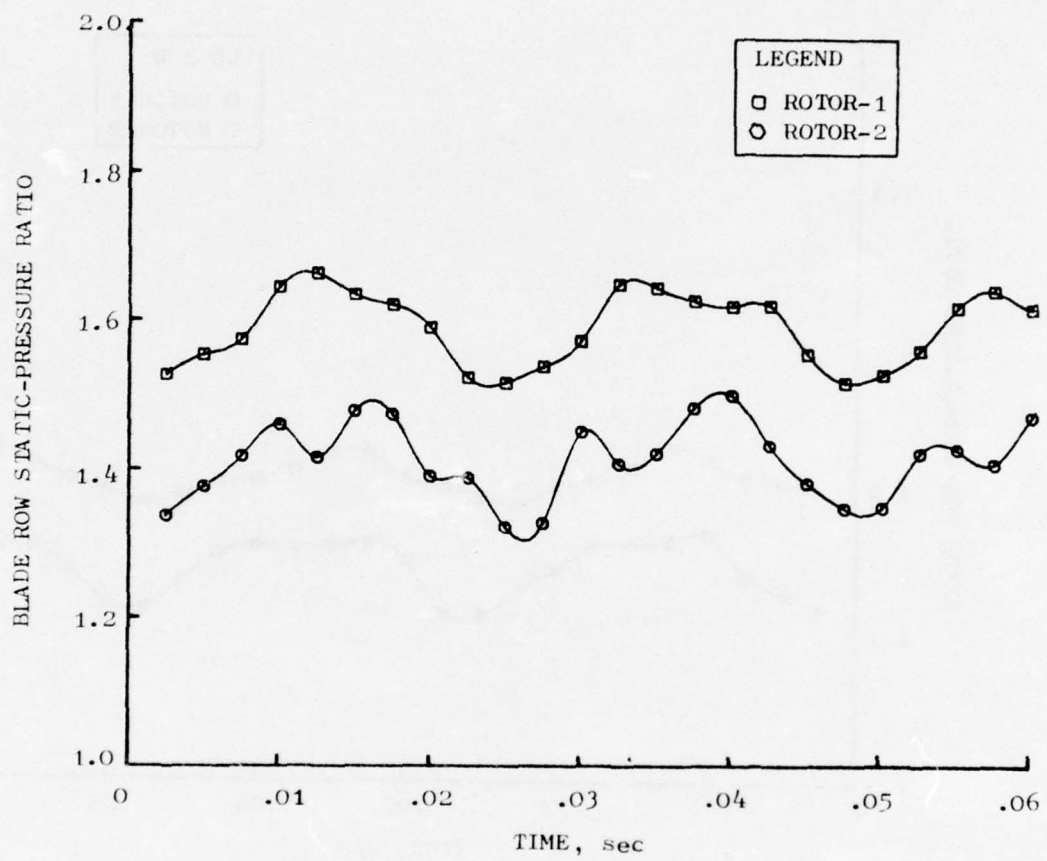


Figure 38. Blade Row Static-Pressure Ratio Vs. Time, 100% $N/\sqrt{\theta}$, 42 Hz.

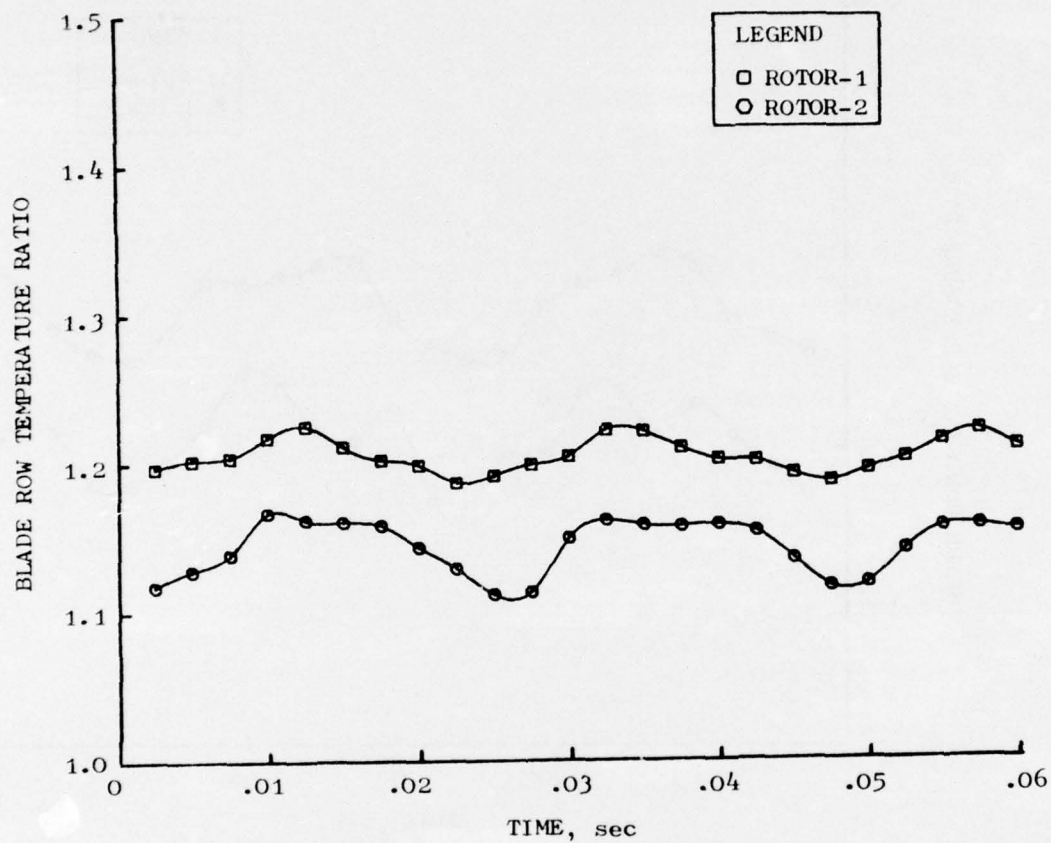


Figure 39. Blade Row Total-Temperature Ratio Vs. Time, 100% $N/\sqrt{\theta}$, 42 Hz.

the incidence angle as a function time for both rotor inlets. As indicated in Section 4.4.2, the incidence angle is functionally related to the relative total-pressure loss coefficient and the deviation angle parameters. Figures 35 and 36 respectively, illustrate the nonlinearities introduced by these parameters. Specifically, the rotor 1 incidence angle (Figure 34) is experiencing low level oscillations which occur on the flat part of the loss coefficient-incidence angle curve and thus, give rise to very low levels of loss coefficient oscillations. On the other hand, the rotor 2 incidence angle is going through a significant range which happens to fall on a rising portion of the loss coefficient-incidence angle curve and thus introduces large variations in loss coefficient. Figures 37, 38, and 39 illustrate the time-dependent variation in rotor total-pressure ratio, static-pressure ratio, and total-temperature ratio, respectively. The sets of plots for all model simulation baseline points are presented in Appendix C.

5.3 FAN PLANAR WAVE DISTORTION TRANSFER

The detailed fan model results permit the investigation of unsteady total-pressure wave propagation through the fan test vehicle. The amplitude transmission ratio parameter established for analyzing these results is defined as the nondimensional total-pressure variation $((\max-\min)/\text{avg})$ at the downstream station divided by the nondimensional total pressure variation $((\max-\min)/\text{avg})$ at the upstream station. The stations chosen for this analysis were: The IGV entrance, rotor 1 entrance, rotor 2 entrance and plane 14. The fan sections which were analyzed and the associated amplitude transmission-ratio designations are tabulated below.

IGV	-	P_{TR1}/P_{TIGV}
Stage 1	-	P_{TR2}/P_{TR1}
Stage 2	-	P_{T14}/P_{TR2}
Overall Fan	-	P_{T14}/P_{TIGV}

The amplitude transmission ratios for baseline and near instability points were determined for each model test case.

Figure 40 illustrates the computed amplitude transmission characteristics for the 100% corrected speed, 42 Hz frequency simulations of Rdg. 71. As shown, the stage 2 characteristic shows a marked decrease when throttling from the baseline points towards instability and is the major contributor to the attenuation exhibited by the overall transfer characteristic P_{T14}/P_{TIGV} . The detailed amplitude transmission characteristics for each model test case are given in Appendix D. Plots such as these graphically provide information on which parts of a compression component are amplifying or attenuating unsteady disturbances.

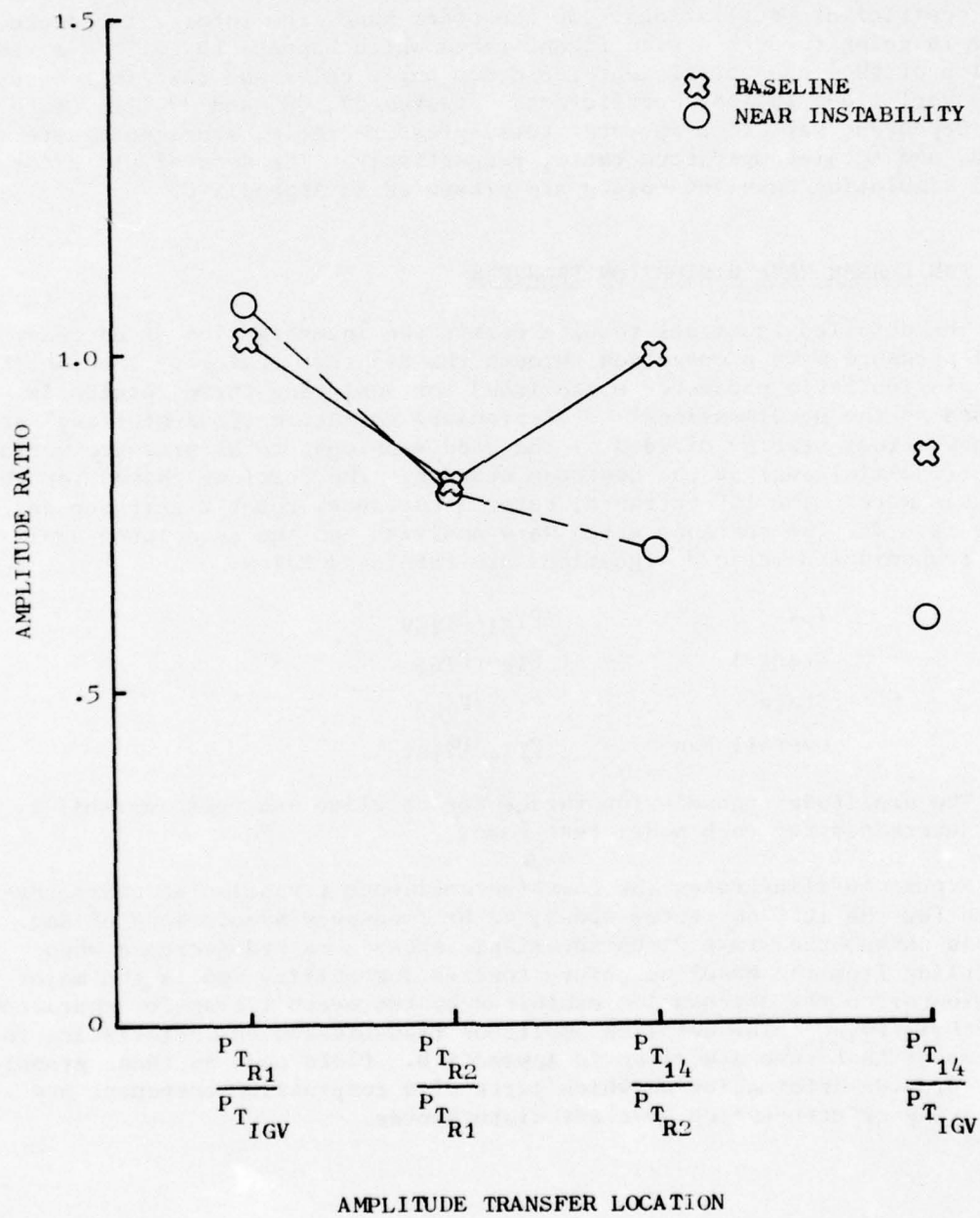


Figure 40. Amplitude Transmission Characteristics, 100% $N/\sqrt{\theta}$, 42 Hz.

Figures 41 through 43 illustrate the internal transfer characteristics as a function of frequency for 100% corrected speed operation for the IGV, stage 1, and stage 2, respectively. Values of amplitude ratio greater than one occur across the IGV. The existence of this amplification is not readily understood; however, other model and test data for other compression components tend to support this result. Stage 1 (Figure 42) is shown to generally attenuate the unsteady waves at frequencies below 100 Hz and at 350 Hz. The 118 Hz and 220 Hz points indicate that amplification of entering flow disturbances would occur in this frequency range. The stage 2 amplitude ratio (Figure 43) varies significantly across the frequency range. Transmission ratios are 1.0 or less in all cases with the 25 Hz case falling as low as 0.18.

The 80% corrected speed IGV, stage 1, and stage 2 amplitude ratios as a function of frequency are shown in Figures 44 through 46. The IGV amplitude ratio is again equal to 1.0 or greater in most cases with the near instability data showing an increase in transfer in every case relative to the baseline point. Stage 1 attenuation increases with increasing frequency and the near surge data demonstrates somewhat lower transfer coefficients than the operating line data. The stage 2 transfer shows that attenuation exists across this stage for all frequencies except at 118 Hz.

Near instability conditions as compared to baseline conditions, are not widely different operational points. The 80% corrected speed transfer results are the more definitive set since these points were generally throttled further in terms of flow from the baseline point to near instability.

The overall planar wave distortion transmission properties of the fan are defined by the ratio of the nondimensionalized amplitude $[(\max - \min) / \text{avg}]$ of the exiting (plane 14) total-pressure wave to the nondimensionalized amplitude of the entering (IGV plane) total-pressure wave. Fan-planar-wave transfer was determined from test data for both the hub- and tip flow of the fan. The hub transfer was based on data taken at radial immersions corresponding to 10% and 30% of the flow area and the tip transfer was based on data taken at radial immersions of 70% and 90% of the flow area. The test data indicated a significant change in transfer properties with respect to radial location and since the model calculations are based on pitch line characteristics, comparison of model and test results must include both hub and tip transfer coefficients from the test data.

The transfer characteristics as a function of frequency for 100% corrected speed are illustrated in Figure 47. The general behavior of the model results matches the test data and falls between the hub and tip results as might be anticipated. The model results indicate large variations in transfer properties at low frequencies. The transfer coefficients at 25 Hz and 60 Hz are very small but at 42 Hz an increased transfer of approximately 300% above both the 25 Hz and 60 Hz cases is noted.

○ BASELINE
◇ NEAR INSTABILITY

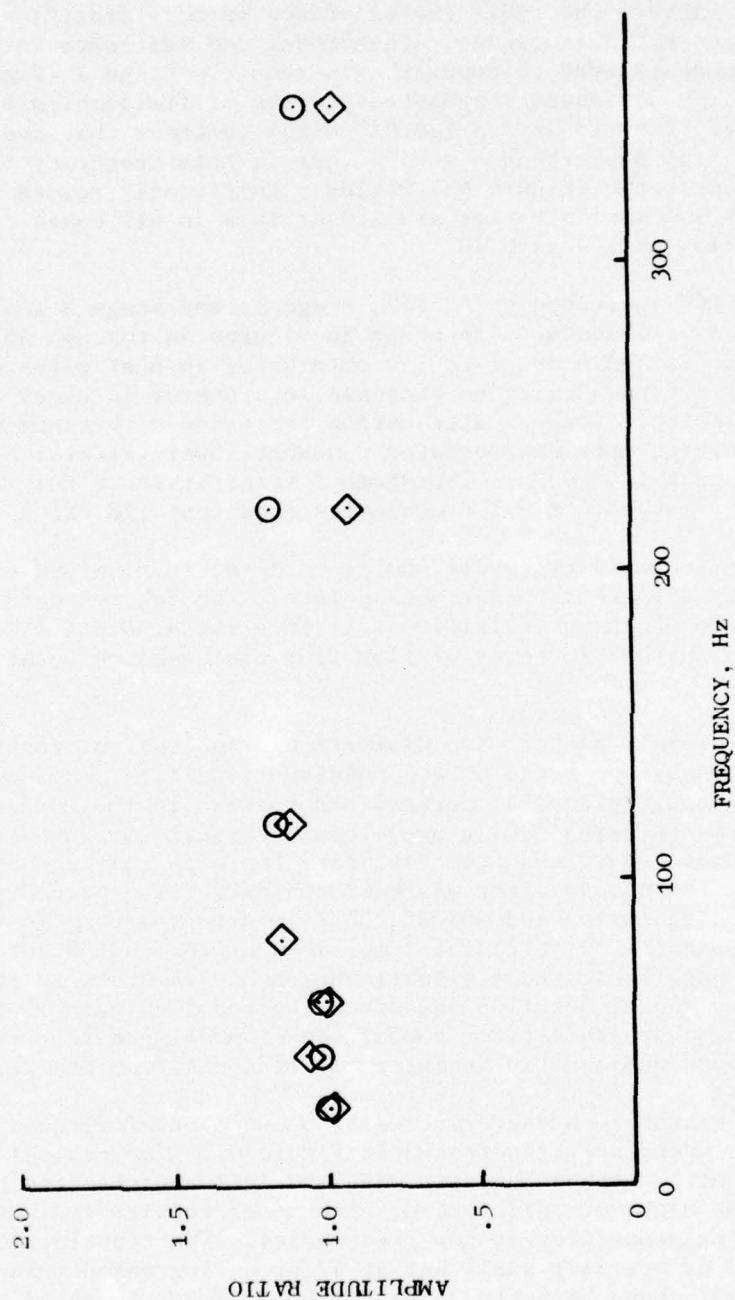


Figure 41. Amplitude Transmission Characteristics, 100% $N/\sqrt{\theta}$, IGV.

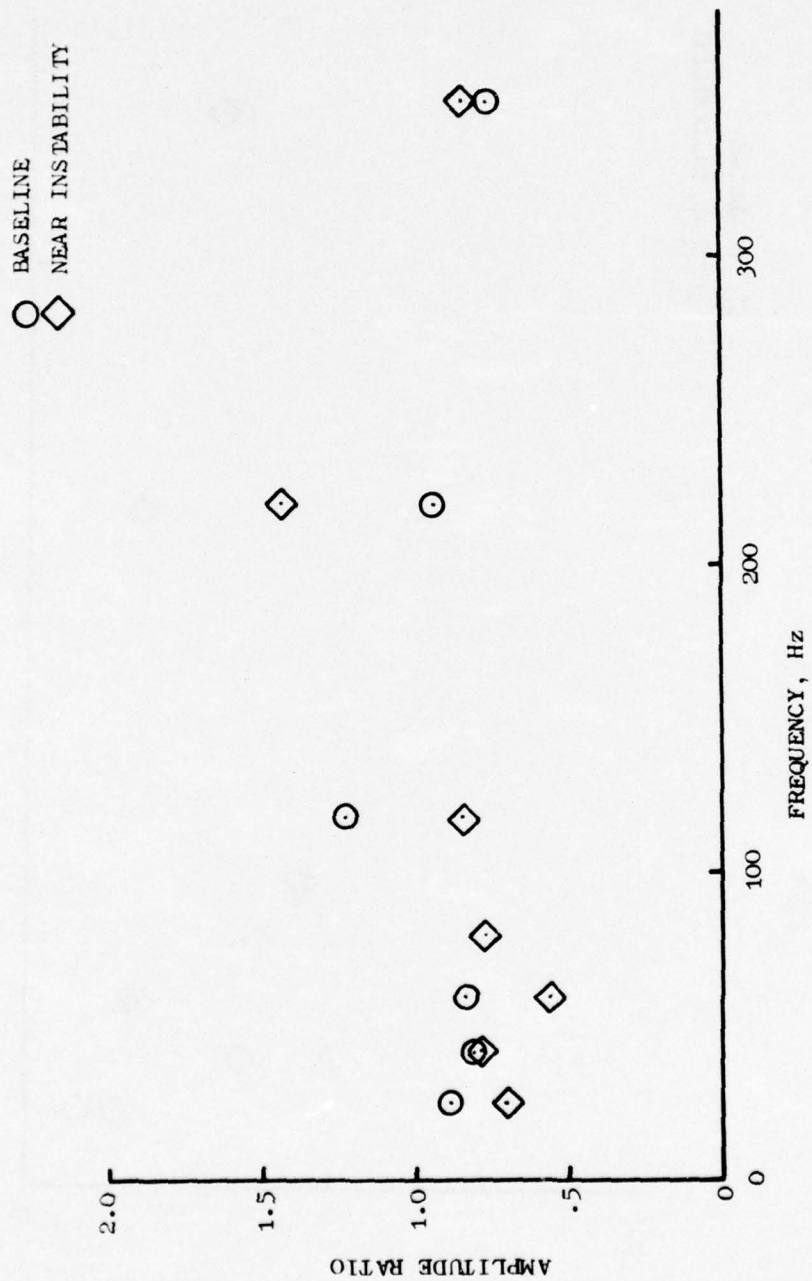


Figure 42. Amplitude Transmission Characteristics, 100% $N/\sqrt{\theta}$, Stage 1.

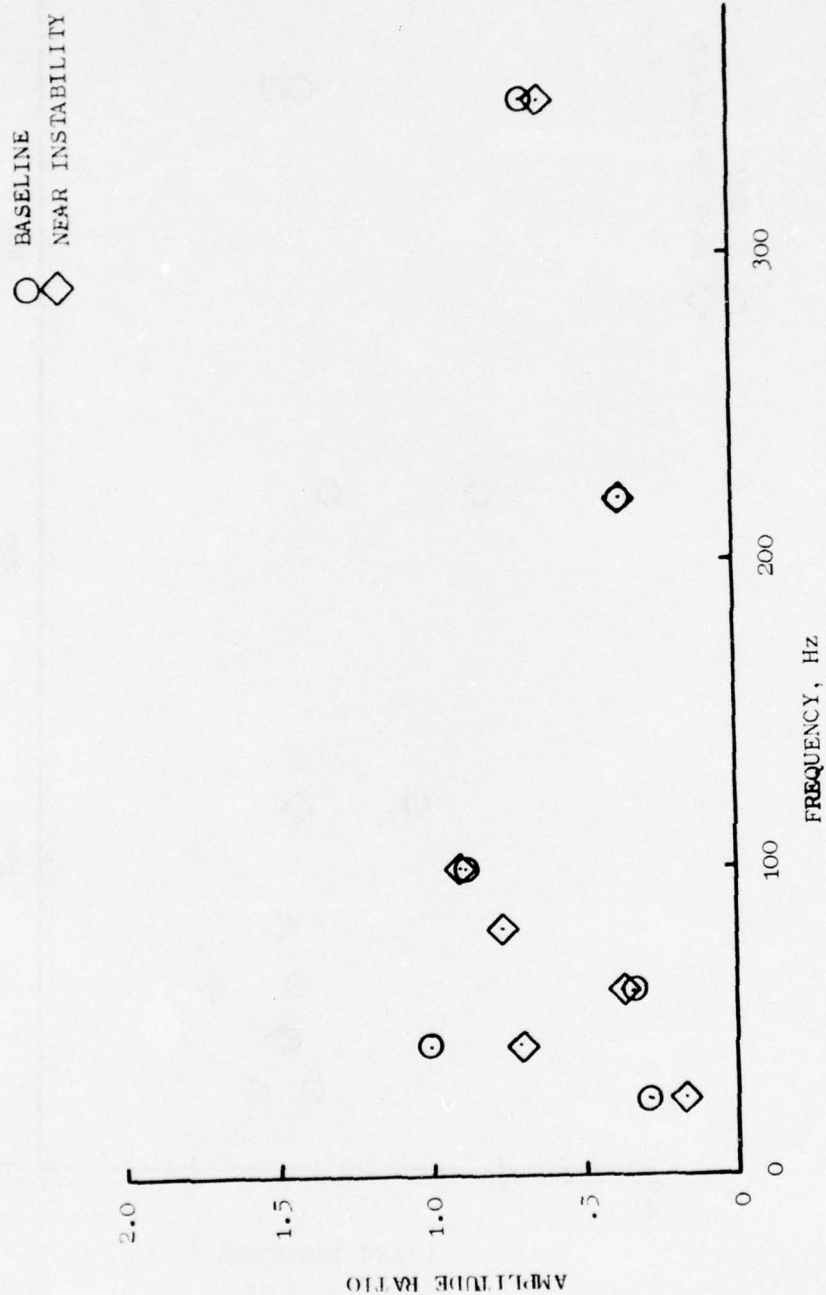


Figure 43. Amplitude Transmission Characteristics, 100% $N/\sqrt{\theta}$, Stage 2.

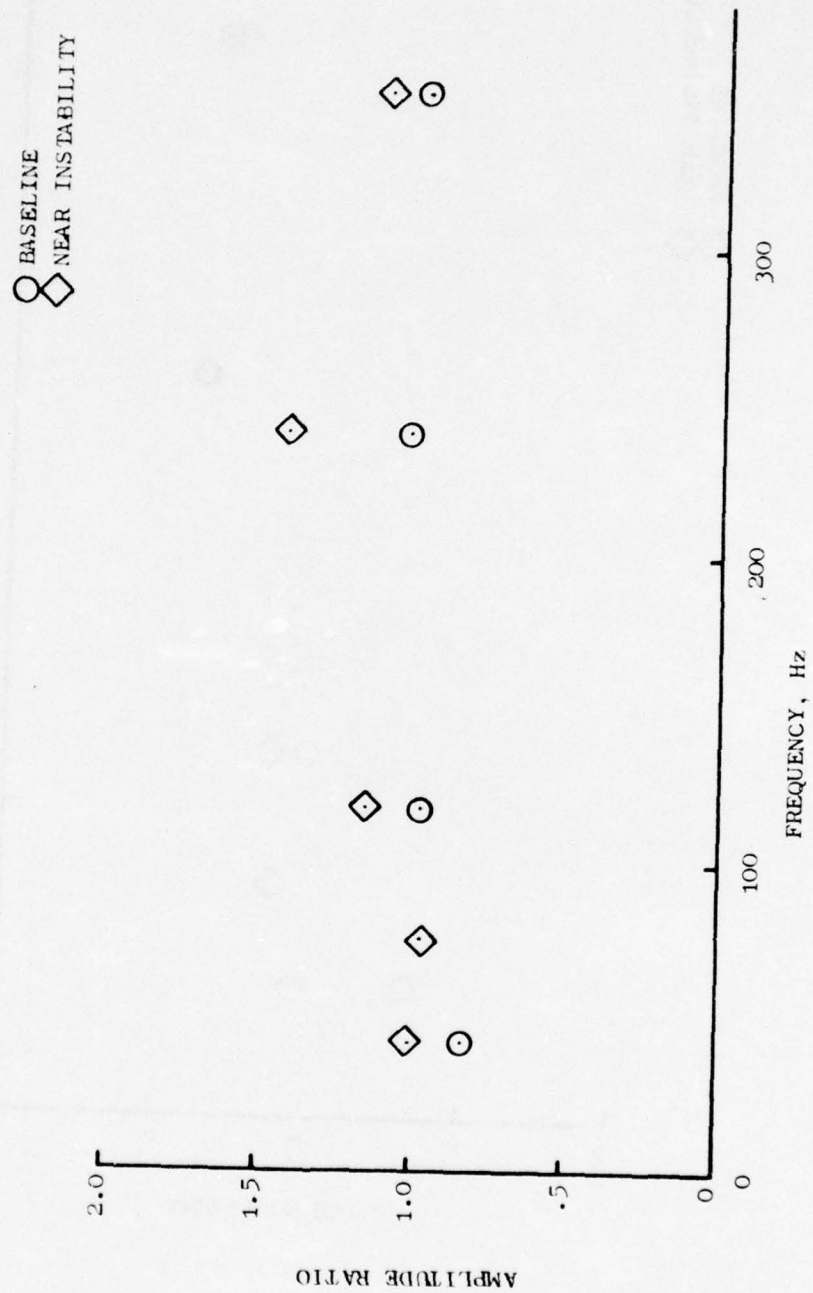


Figure 44. Amplitude Transmission Characteristics, 80% $N/\sqrt{\theta}$, IGv.

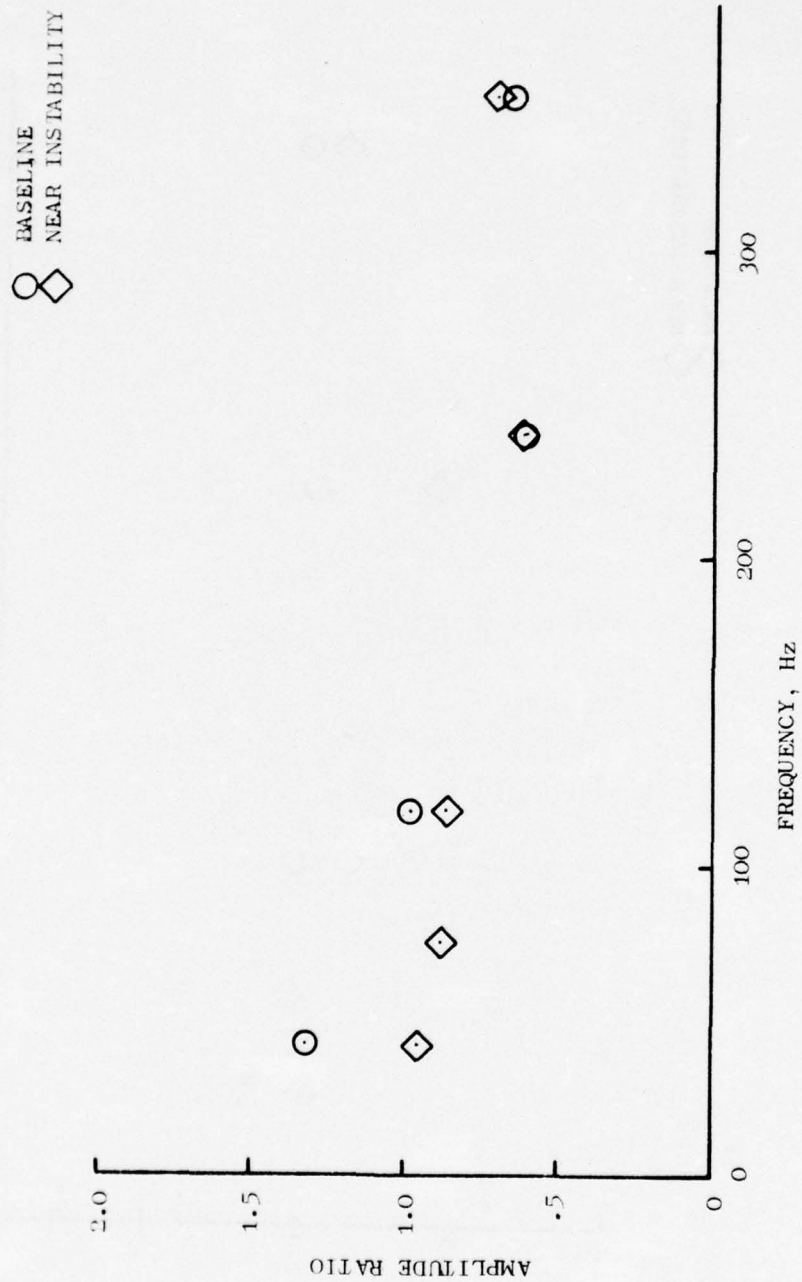


Figure 45. Amplitude Transmission Characteristics, $80\% N/\sqrt{\theta}$, Stage 1.

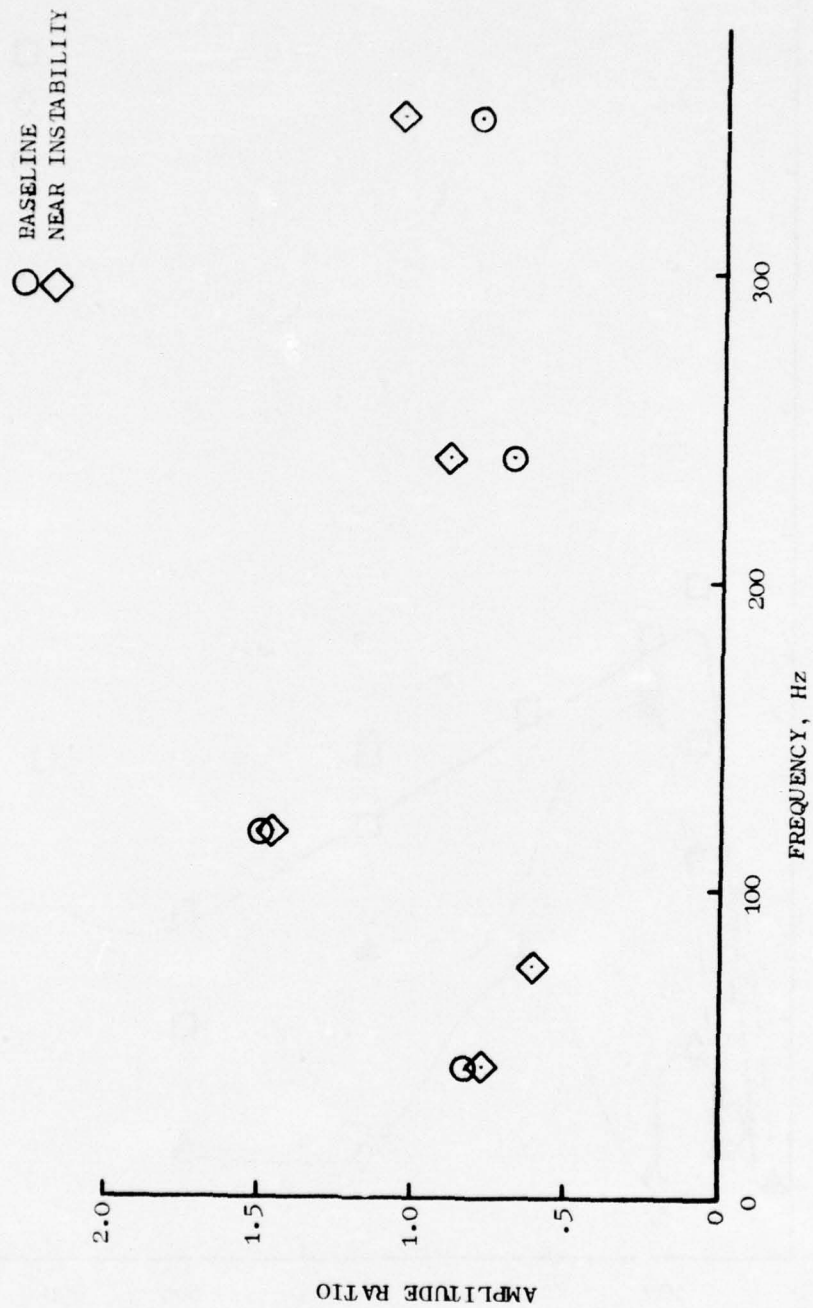


Figure 46. Amplitude Transmission Characteristics, 80% $N/\sqrt{\theta}$, Stage 2.

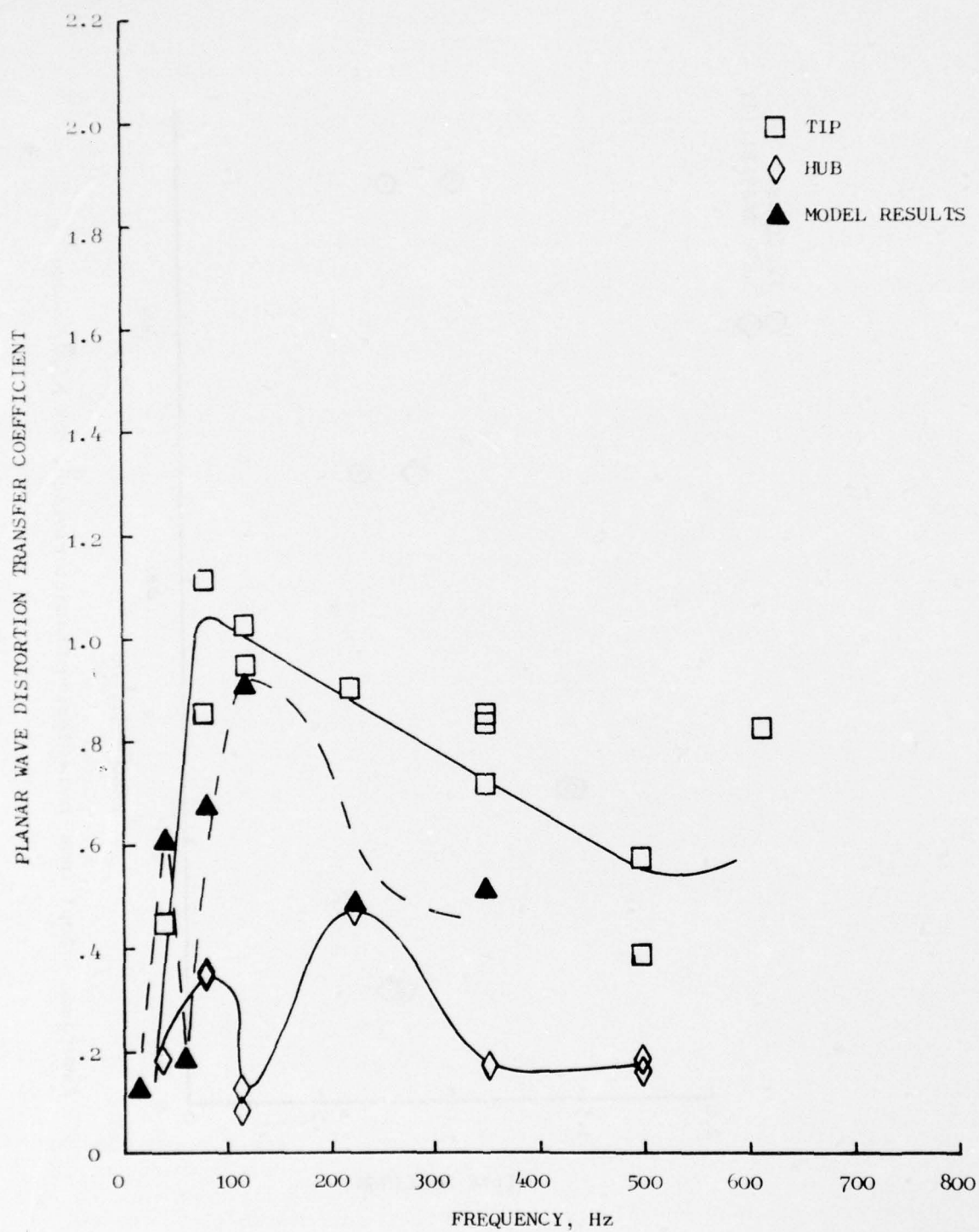


Figure 47. Fan Planar Wave Transfer, 100% N/\sqrt{B} .

Figure 48 illustrates the 80% corrected speed overall transfer coefficient comparisons. The transfer "spike" at 118 Hz shown by the test data is the predominate feature of the characteristic and is reproduced accurately by the model. Although these results suggest that the fan may act as an amplifier at 118 Hz, this interpretation of the results would probably be misleading. Rather, it is suspected that the results arise from the presence of standing waves in the ducting upstream and/or downstream of the fan.

The planar wave distortion transfer results are summarized in Table 6. It is noticed that the model overall transfer values lie between the hub and tip test values for all cases but one. These results were expected since the model is a pitch line model.

Table 6. Summary of Model and Test Planar Wave Distortion Transfer Results.

Simulated Reading No.	Frequency	Planar Wave Distortion Transfer					
		Model				Test	
		IGV	Stage 1	Stage 2	Overall	Hub	Tip
<u>100% Speed</u>							
-	25	1.000	0.702	0.177	0.125	-	-
71	42	1.074	0.792	0.706	0.601	0.19	0.45
-	60	1.006	0.560	0.379	0.180	-	-
69	80	1.148	0.767	0.766	0.676	0.36	1.12
64	118	1.119	0.842	0.907	0.907	0.13	1.03
41	220	0.923	1.433	0.373	0.494	0.18	0.91
43	350	0.970	0.838	0.622	0.505	0.17	0.72
<u>80% Speed</u>							
82	42	1.002	0.954	0.772	0.739	0.22	0.80
77	75	0.967	0.890	0.610	0.520	0.15	0.92
61	118	1.148	0.765	1.453	1.280	1.21	2.14
57	240	1.423	0.619	0.888	0.783	0.47	1.02
66	350	1.102	0.712	1.048	0.823	0.17	1.08

The fact, that the model predicts the abnormally large transfer at 80% corrected speed, 118 Hz and that the model results follow the trends of the test data with the model values falling between hub and tip test results, is clear evidence of the validity and capability of this model to properly handle the interaction of planar waves with a compression component.

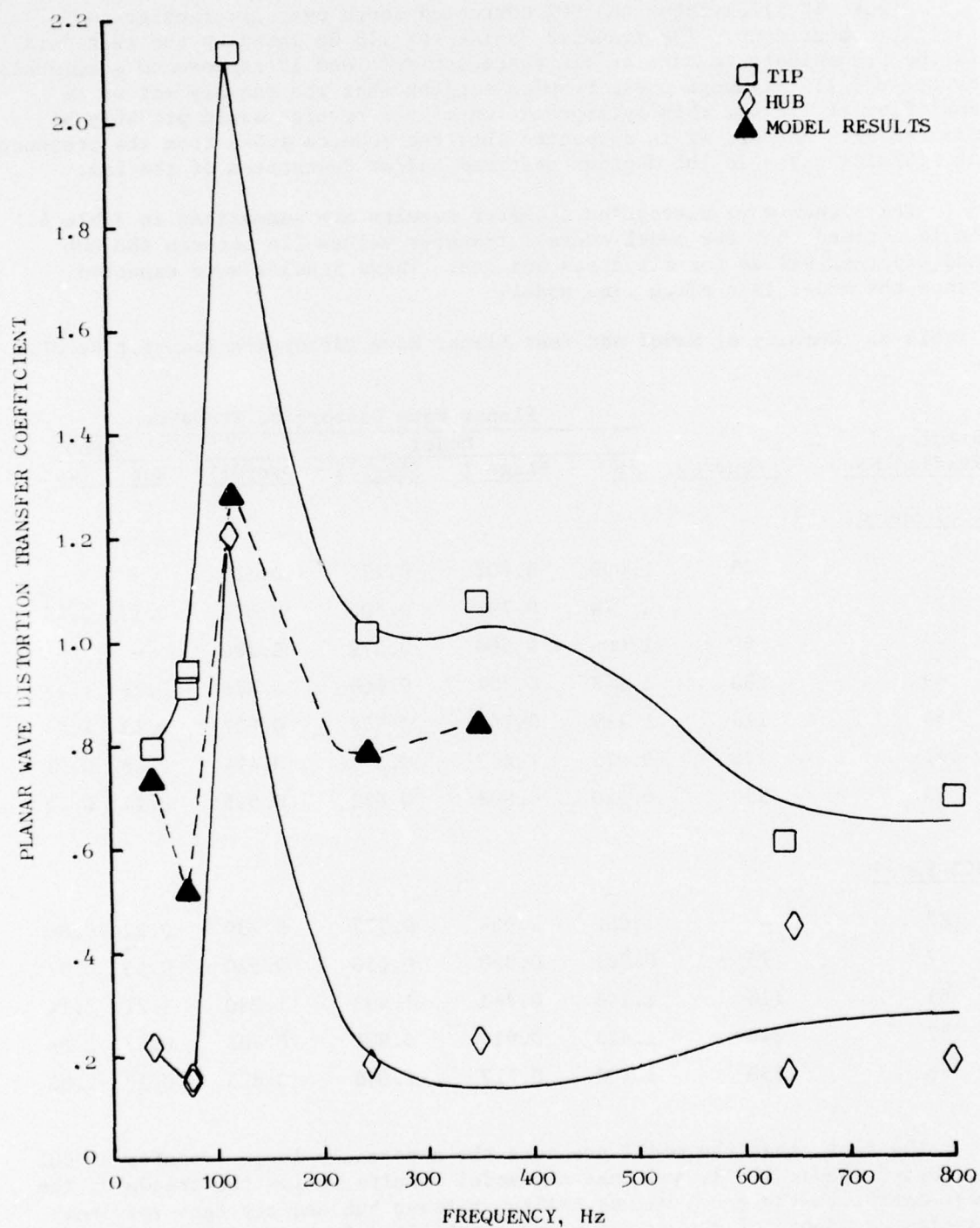


Figure 48. Fan Planar Wave Transfer, $80\% N/\sqrt{\theta}$.

5.4 INSTABILITY ANALYSIS

The results obtained by throttling the model to instability are presented in this section. Depending upon corrected speed and planar wave frequency, it has been possible to characterize four distinctly different types of model instability which appear to have counterparts during actual vehicle operation. These types of instability, planar wave distortion sensitivity, and stage initiating instability results are presented in the following paragraphs.

5.4.1 General Observations

The similarity between model behavior when aerodynamic instabilities occur and actual fan surge is the most significant observation of the entire instability point analysis. Model response parallels the trends defined by test data in several areas. The "hard" surges associated with high speed fan operation and the "softer" surges seen during medium and low speed operation are reproduced by instabilities which develop within the model. Non-stationary events which may be analogous to rotating stalls are observed in the model calculations. Finally, migration of the fan model mean operating point, especially near instability at low speeds, shows close qualitative agreement with test data.

5.4.2 Discussion of Instability Point Data

The analysis of the model instability point is based upon the parameters discussed in Section 4.6 Instability Identification. The instability encountered when throttling the clean-inlet model was discussed under Clean Inlet Flow results in Section 5.1. The blade-row flow ratio technique for determining the stage initiating instability and the point of instability was illustrated for the 80% and 100% speed corrected-speed lines. This instability has been termed a Type 1 Instability. Analysis and illustration of each of the remaining types of instability are presented below.

Type 2 Instability

This type of instability occurred at 100% corrected speed for planar wave frequencies in the range of 42 Hz to 220 Hz. All of these instabilities developed very abruptly in the model. The migration of the mean operating point on the steady-state fan map was nominally well behaved until the point of model instability was reached. Model computational instability occurred within a few time steps after aerodynamic instability occurred for the majority of these cases.

The Type 2 Instability is illustrated by the 80 Hz simulation at 100% corrected speed. The stage initiating instability was derived from the

W_2/W_1 relationship and was substantiated by the response of the "unsteady" blade force. Figure 49 and Figure 50 illustrate the behavior of W_2/W_1 and the blade force as a function of time, respectively. The flow ratios across both rotors are periodically higher than the values at steady-state surge without producing instability. The periodicity of the imposed unsteady fluctuations permits these high flow ratios to exist without surge until a large deviation occurs in rotor 2 as seen in Figure 49. The unsteady blade force term (Figure 50) shows similar behavior in rotor 2 where an apparently instantaneous breakdown is observed as a sharp rise and marks rotor 2 as the initiating stage.

Type 3 Instability

This type of instability occurred at 80% corrected speed for planar wave frequencies in the range of 42 Hz to 240 Hz. This class of instability differs considerably from the 100% corrected speed instability characteristics in the same frequency range. None of these cases experienced a numerical instability that would cause the solution to abort. Large fluctuations occur in the internal aerodynamics of the fan, but the mean performance is well behaved until the fan is throttled higher on its speed line. The point of instability for this class of instability is defined by the last position of the mean operating conditions prior to initiation of erratic mean behavior.

A Type 3 Instability is illustrated by Figure 51 for the 240 Hz, 80% speed case. The operating condition at the abrupt change in slope of the speed line is defined as the instability point for the Type 3 Instability.

The initiating stage for this type of instability may be best defined by the amplification function. This parameter is defined as the ratio of the time derivative of the volume averaged flow in a given rotor to the ratio of the time derivative of flow in the exit volume where the throttling process is controlled ($AMPF = DW(x)_{\text{rotor}}/DW(x)_{\text{exit}}$). Figure 52 represents the behavior of this function for the period of time associated with the development of the Type 3 Instability. It is clearly shown that the rotor 2 amplification function exhibits large excursions relative to the rotor 1 amplification function. On the basis of these observations, rotor 2 is determined to be the stage initiating instability for this case.

Type 4 Instability

This type of instability occurs at 350 Hz at both 80% and 100% corrected speeds. The point of model instability for both of these cases was determined to be very close to the steady-state clean-inlet-surge line. The behavior of these points was such that a clear determination of the initiation of surge could not be made. Occasional disturbances which may be physically analogous to rotating stalls were observed in the data as shown in Figure 53 which represents the near instability portion of the 100% corrected speed, 350 Hz simulation.

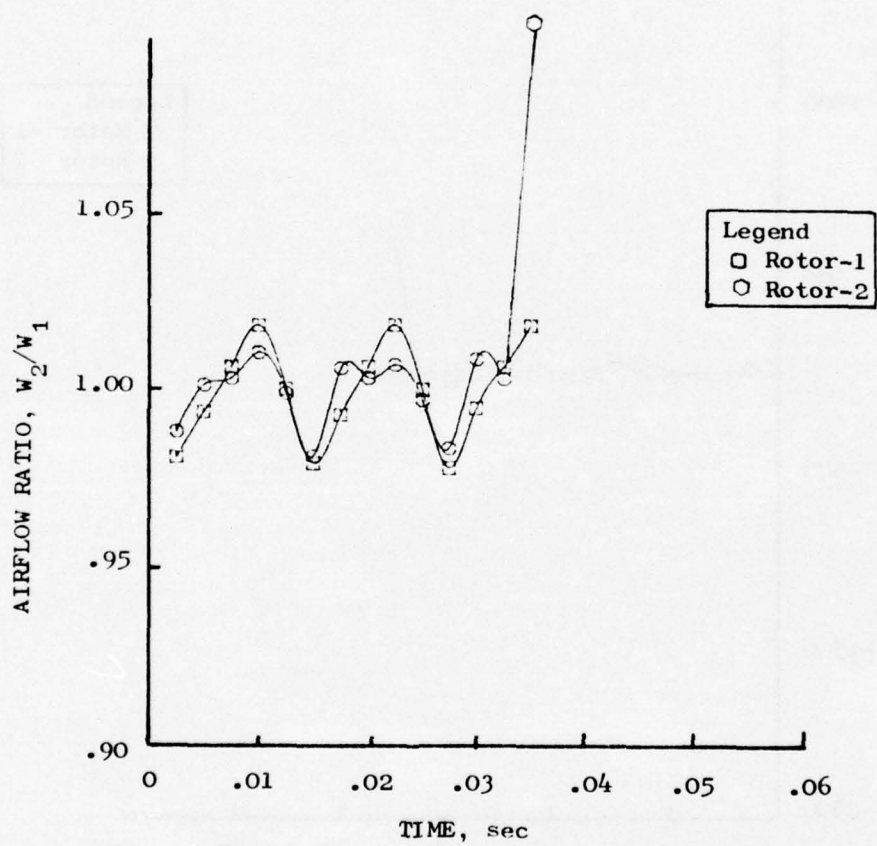


Figure 49. Airflow Ratio Vs. Time, 100% $N/\sqrt{\theta}$, 80 Hz, Surge.

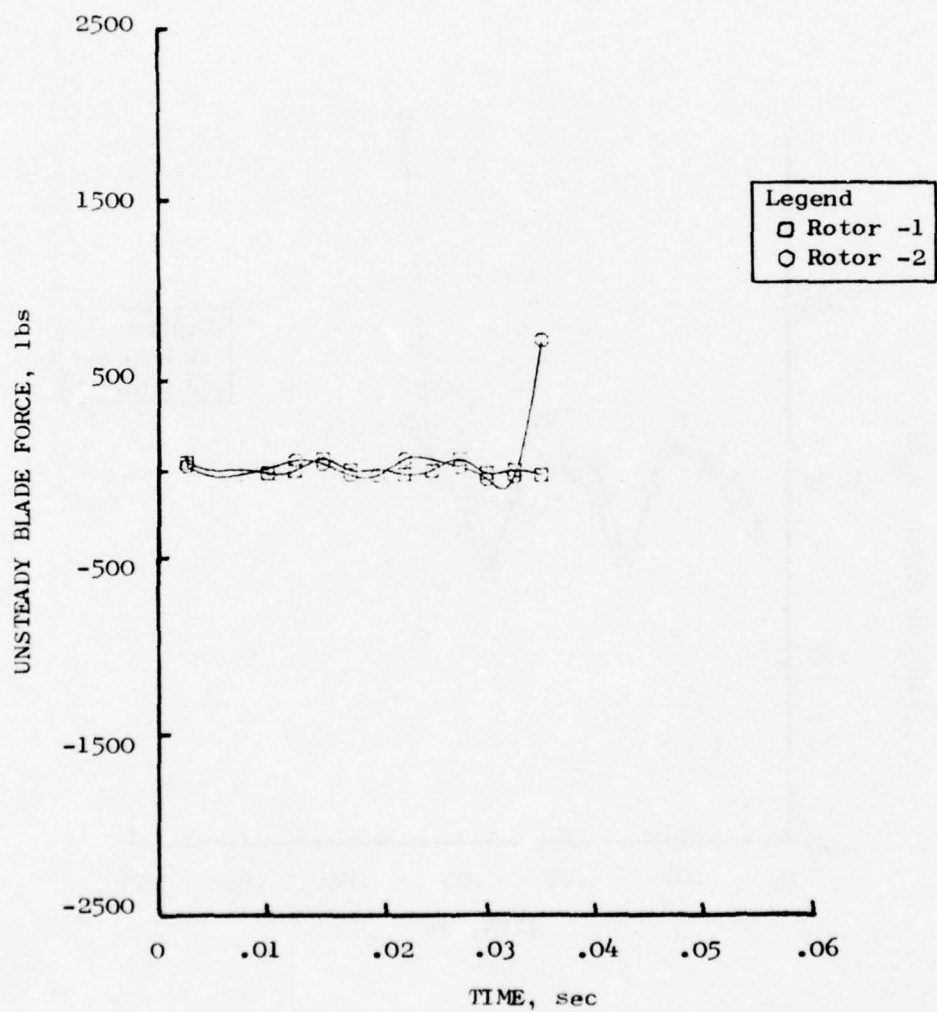


Figure 50. Unsteady Blade Force Vs. Time, 100% $N/\sqrt{\theta}$, 80 Hz, Surge.

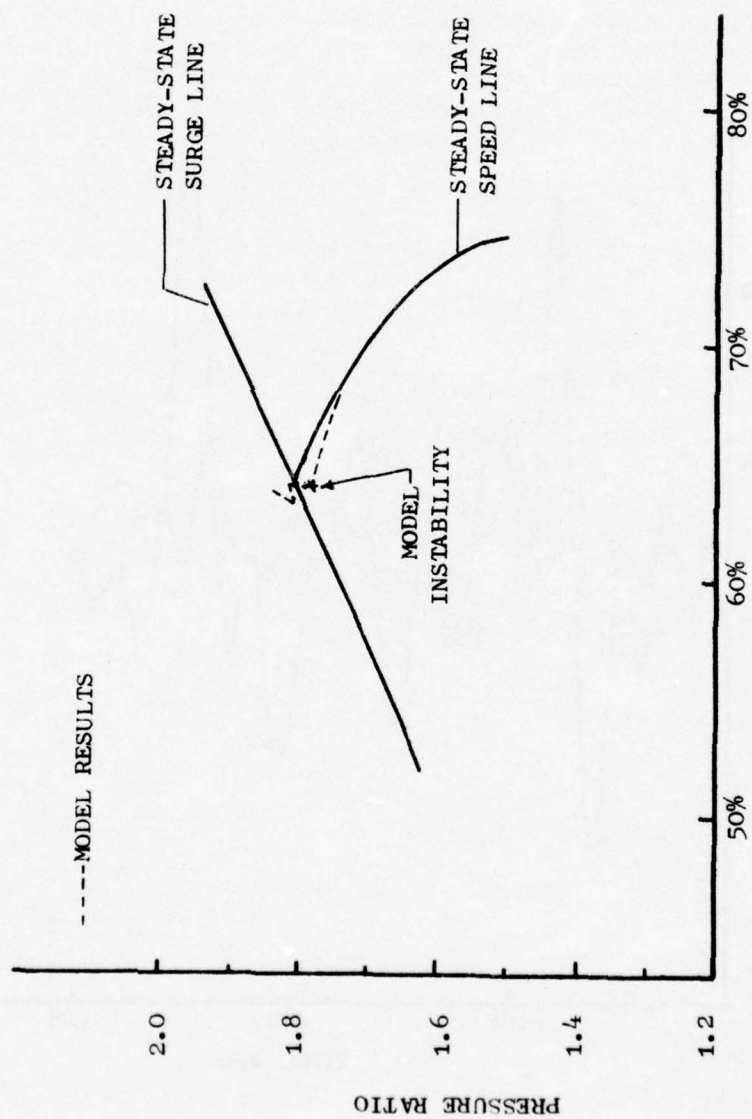


Figure 51. Path of Model Mean Operating Point, 80% $N/\sqrt{\theta}$, 240 Hz, Surge.

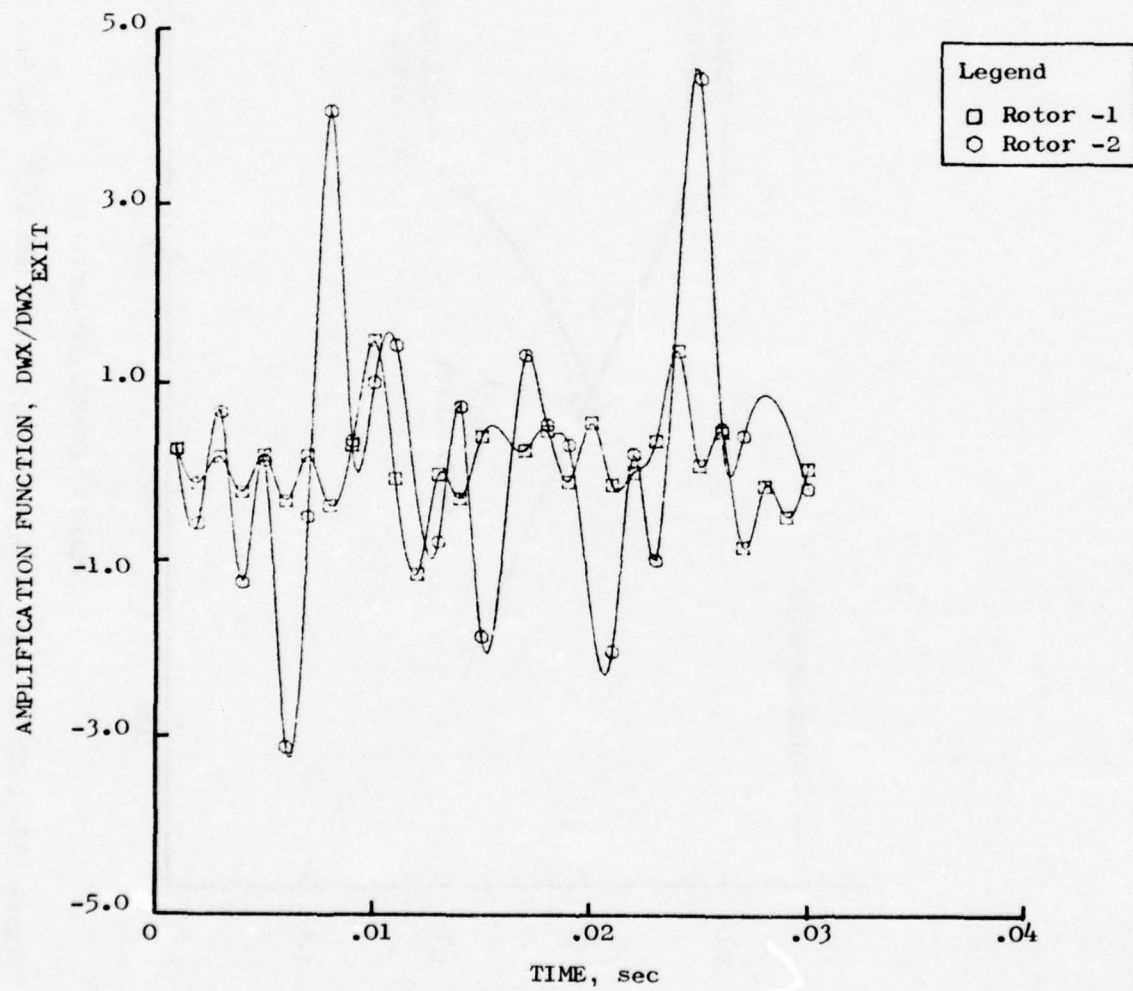


Figure 52. Amplification Function Vs. Time, $80\% N/\sqrt{\theta}$, 240 Hz, Surge.

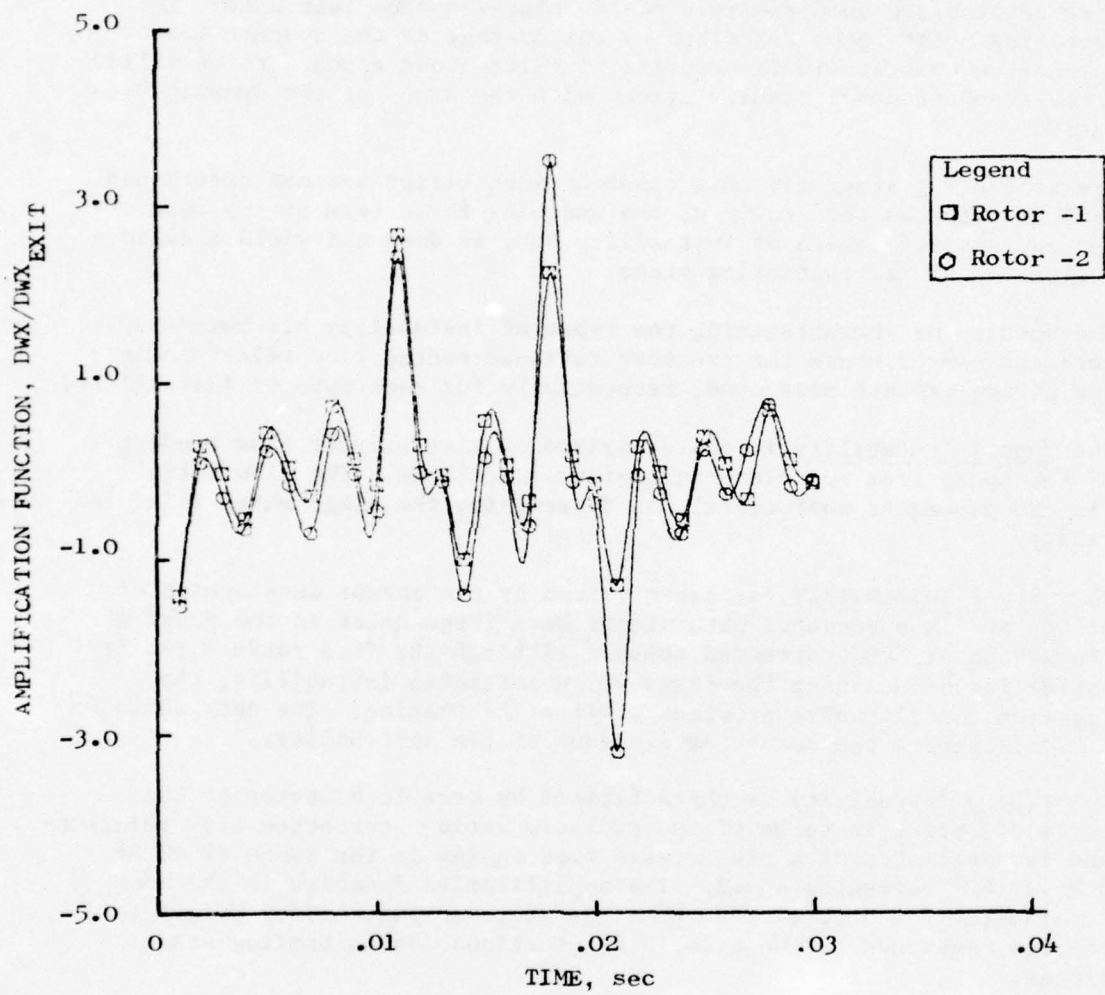


Figure 53. Amplification Function Vs. Time, 100% $N/\sqrt{\theta}$, 350 Hz. Stationary.

The path of the mean operating point for this case is shown in Figure 54. The speed line described by the mean operating point "rolls-over" and moves down the positive slope portion of the characteristic for some distance prior to model-calculation abort. The point chosen to represent instability was the zero slope position. This choice is consistent with the interpretation of steady-flow fan stability, speed line slope, and with previous test data analyses. Figure 54 also shows the path described by the fan mean operating point based upon analysis of the high-response test data. The mean operating point rotor described by the average of the dynamic test data may not be quantitatively accurate, but its trend appears to be valid. Hence, the trend of model results agrees with the trend of the dynamic-data calculation.

The initiating stage for this class of instability was not determined. Figure 55 illustrates the growth of the unsteady force term as the mean point moves into the region of instability but, it does not yield a definitive evaluation of the initiating stage.

The results of characterizing the types of instability are summarized in Figures 56 and 57 where the pressure ratio-corrected flow relationships and flow parameters are presented, respectively for each type of instability.

The Type 1 Instability is characterized by a relatively slow bending over of the speed line for clean-inlet-flow conditions. The flow ratio W_2/W_1 is the parameter most useful for determining the stage which initiates instability.

The Type 2 Instability is characterized by the abrupt development of instability and is associated with planar wave frequencies in the range of 42 Hz to 220 Hz at 100% corrected speed. Although the flow ratio W_2/W_1 is very useful for determining the stage which initiates instability, the amplification function also provides similar information. The data shown on Figure 57 illustrate the abrupt development of the instability.

The Type 3 Instability is characterized by erratic behavior of the mean operating point in terms of the pressure ratio - corrected flow relationship and is associated with planar wave frequencies in the range of 42 Hz to 240 Hz at 80% corrected speed. The amplification function is the most useful parameter for determining the stage where an instability originates by the large magnitude of the erratic fluctuations the initiating stage experiences.

The Type 4 Instability is characterized by the rapid bending over of the speed line at 350 Hz for both 80% and 100% corrected speeds. None of the parameters that were being examined during the course of this study were useful in determining the stage where an instability of this type was initiated. However, behavior was noted in the amplification parameter which might be associated with rotating stall, that is, anti-phasing between stages was noted during the first few cycles as shown on Figure 57.

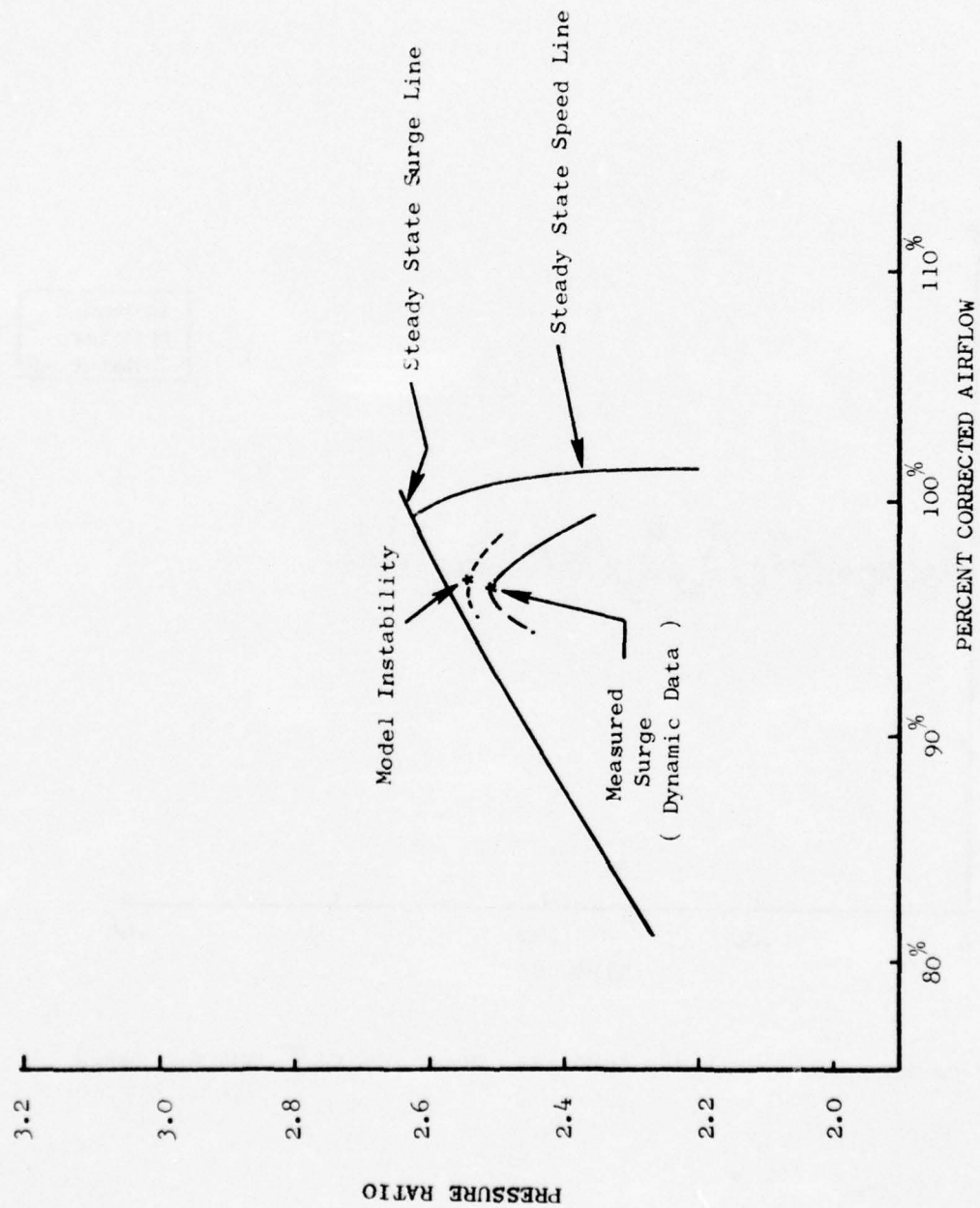


Figure 54. Comparison of Model Vs. Test, Mean Operating Point Path, $100\% N/\sqrt{\theta}$, 350 Hz.

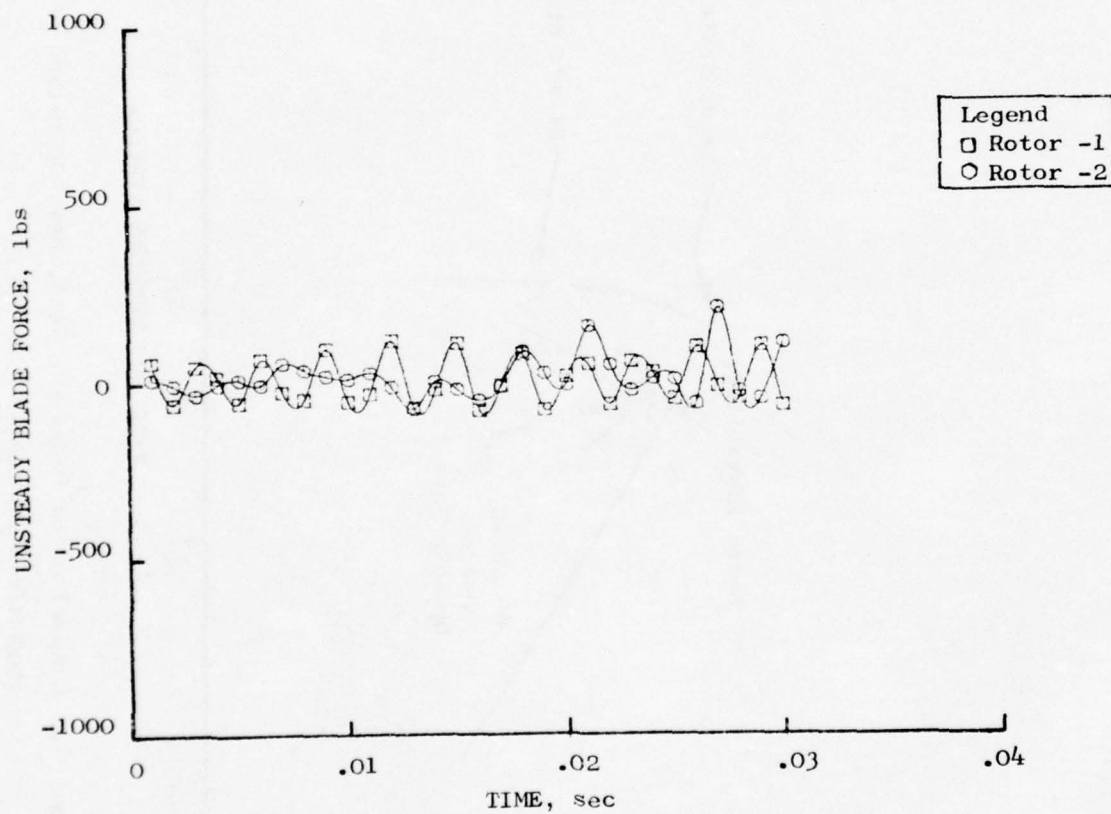


Figure 55. Unsteady Blade Force Vs. Time, $80\% N/\sqrt{\theta}$, 350 Hz, Surge.

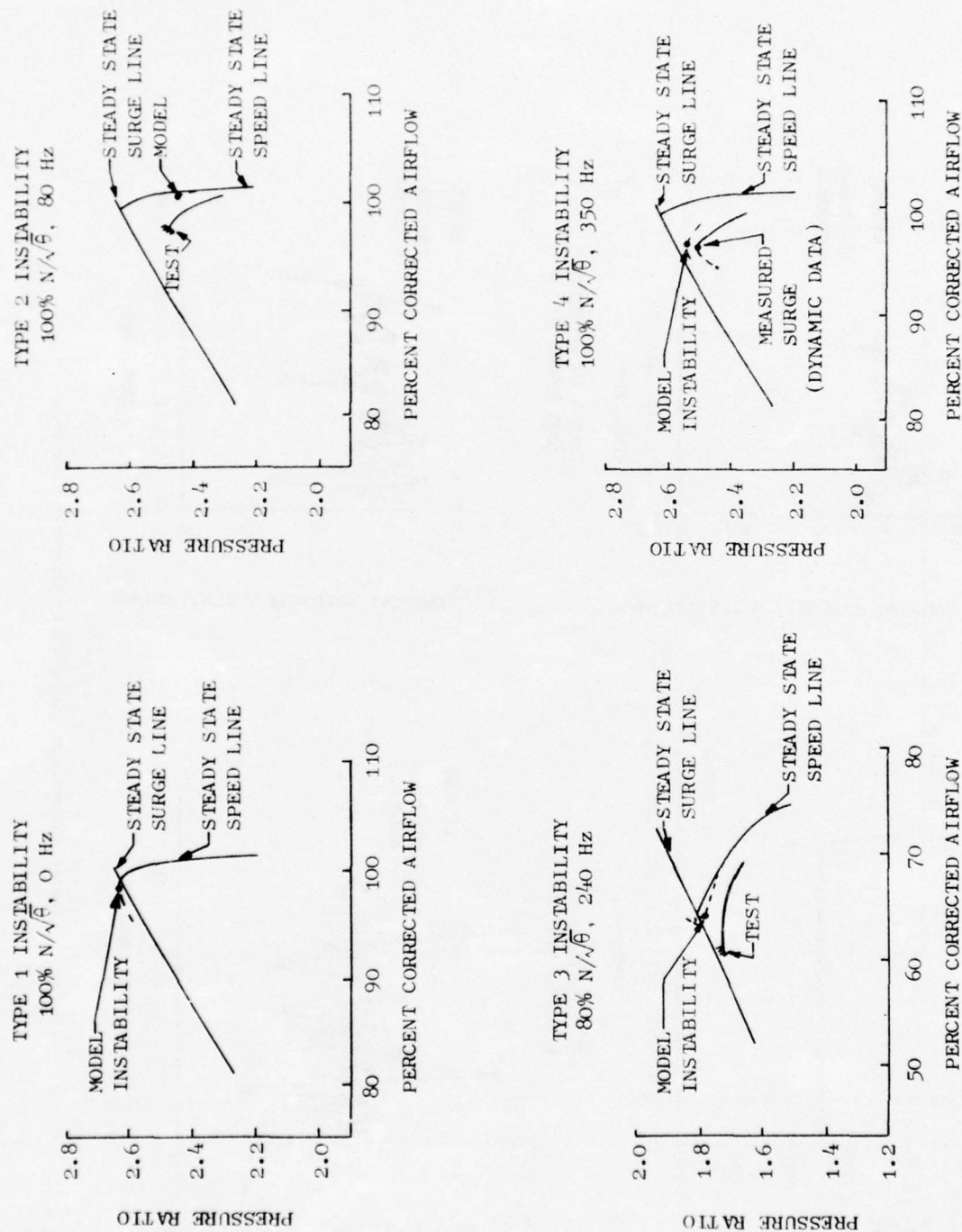


Figure 56. Fan Map Representation of Model Instability Characteristics.

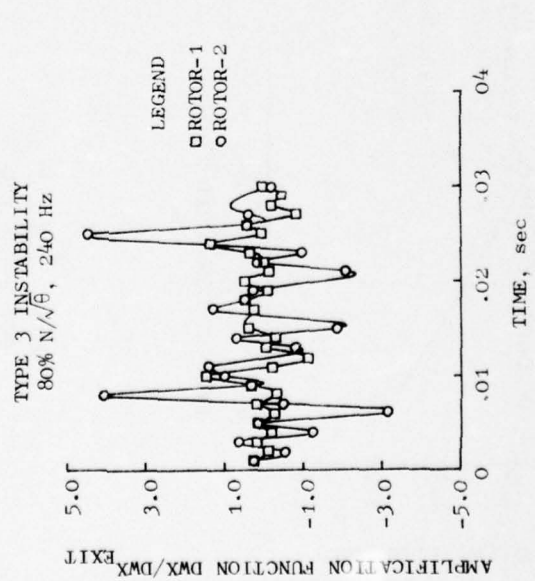
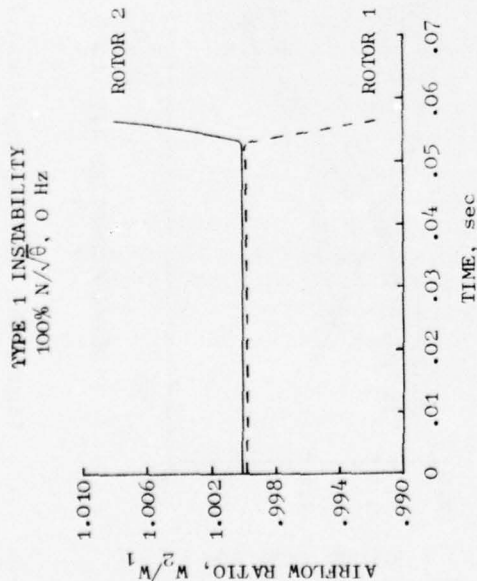
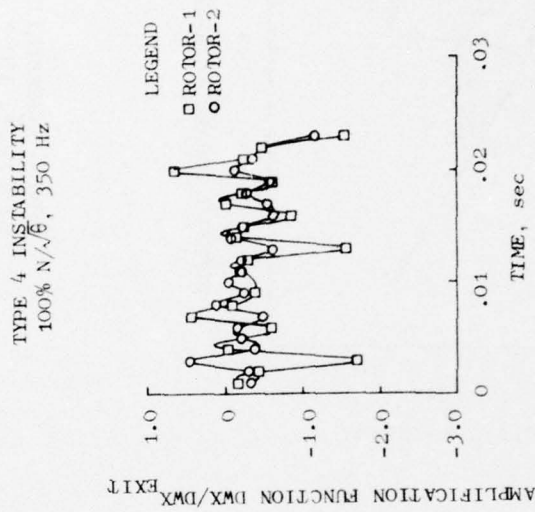
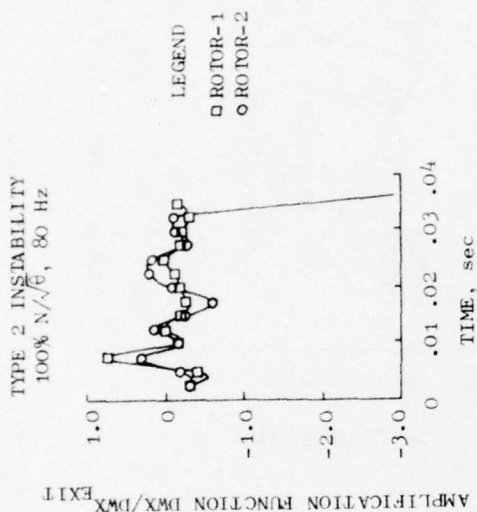


Figure 57. Model Interstage Instability Characteristics.

5.4.3 Surge Pressure Ratio Sensitivity

The loss in surge pressure ratio per unit amplitude of inflow planar wave distortion is defined as surge pressure ratio sensitivity. Loss in surge pressure ratio (ΔPRS) is defined as the incremental change in the pressure ratio at surge as measured from the clean-inlet surge line at constant corrected airflow to the surge line with distorted inflow divided by the clean-inlet-surge-line pressure ratio. The planar wave distortion amplitude is defined by the following relationship:

$$\text{Distortion Amplitude} = [P_{T_{IGV_{MAX}}}(t) - P_{T_{IGV_{MIN}}}(t)] / (2P_{T_{IGV_{AVERAGE}}}) \quad (56)$$

Therefore, the distortion sensitivity to planar waves is defined to be

$$DS = \Delta PRS / [\Delta P_T / (2\bar{P}_T)_{IGV}] \quad (57)$$

The definition of loss of surge pressure ratio with planar wave distortion requires additional constraints in order to specify the surge pressure ratio with inflow planar waves since the instantaneous fan operating point is not fixed. The loss in surge pressure ratio was determined using the mean operating point of the fan just prior to instability as determined from steady-state instrumentation. The analogous procedure in the model is to time average the instantaneous pressure ratio and flow values for each cycle. As the model is throttled, a locus of the average values is scribed on the steady-state fan map and represents the model version of the progression of the fan mean operating point. The mean point at instability was selected based upon the instability analyses that were conducted according to the discussion of Section 5.4.2. Comparison of the model 100% corrected-speed planar-wave distortion sensitivities with the test results is shown in Figure 58. The trend of model calculated sensitivity is shown to be similar to the test results. Two additional model points are shown for which test data does not exist (25 Hz and 60 Hz). These cases were added to the simulation matrix in order to develop the sensitivity characteristic at lower frequencies. The shape of the model sensitivity characteristic in this region suggests that this function is more non-linear with frequency than had been concluded from the earlier test results.

A consideration not previously discussed with respect to sensitivity is the effect of deterioration on the test sensitivity results. The potential variation in the 42 Hz sensitivity is also shown on Figure 58 if the post-test surge line is used instead of the pre-test surge line. Since this surge came near the end of the test, the inclusion of the deterioration effect should be more correct.

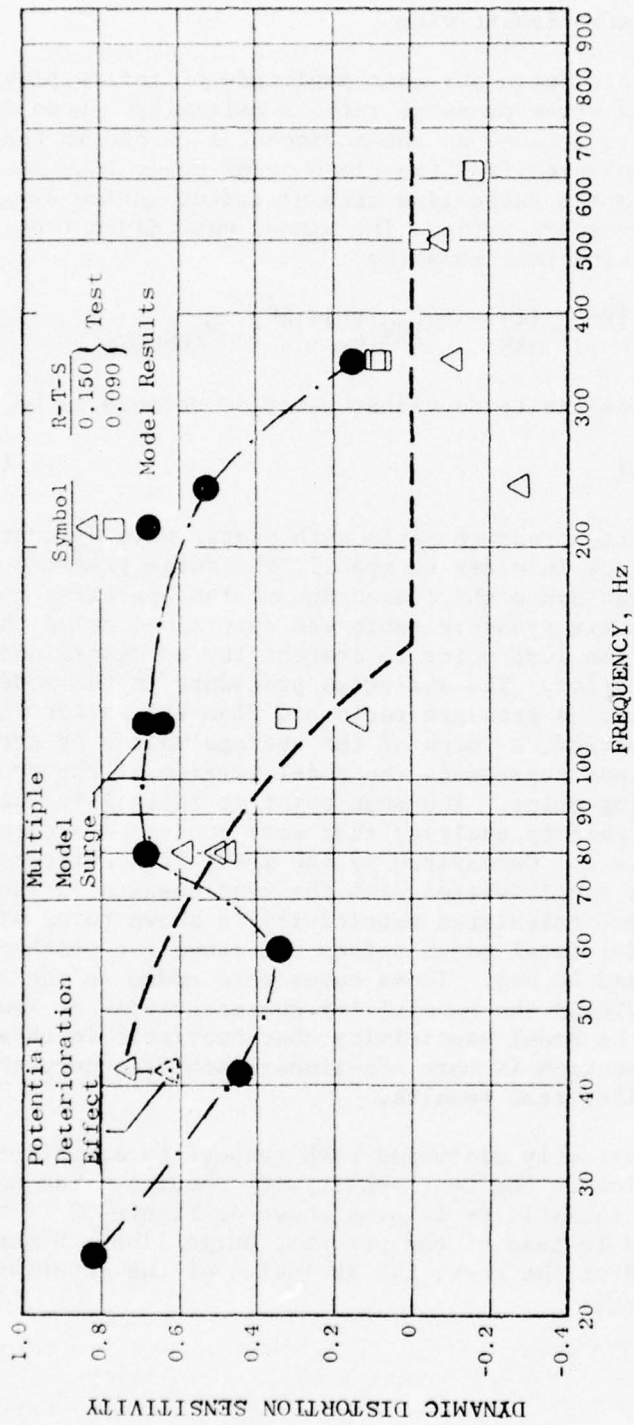


Figure 58. Planar Wave Distortion Sensitivity, 100% $N/\sqrt{\theta}$.

The effect of varying amplitude on dynamic distortion sensitivity at a given frequency is shown also in Figure 58 at 118 Hz. Total-pressure amplitudes of 8.20, 9.66, and 11.40 percent were evaluated for point of instability and dynamic distortion sensitivity. Sensitivities of 0.634, 0.673, and 0.640, respectively, were computed for these total-pressure amplitudes. When normal data scatter and the effect of the small magnitude of the surge pressure ratio loss in the computation are taken into account, the variability of test data sensitivity does not have a strong relationship with planar wave amplitude.

The overall levels of model and test sensitivity are in good agreement with the exception of the frequency range between 100 and 300 Hz. It is possible that part of the variation seen in this frequency range is due to the differences between the extrapolated model-blade-row characteristics in the post-surge region and the actual fan characteristics. In addition, the unsteady flow effects on blade characteristics become increasingly important in this region and the model analyses have not taken this factor into account. The decrease in measured sensitivity with increasing frequency until the effect of the unsteady flow on stability is negligible is reproduced by the model results.

The 80% speed planar wave distortion sensitivity model and test results are shown in Figure 59. Model sensitivities simulate test results across the frequency range with the possible exception of the 42 Hz case. As with the 100% speed, 42 Hz case, the deterioration effect may be taken into account as shown in Figure 59. The 80% model sensitivity characteristic shape has not been explored at other additional low frequencies as was done for 100% corrected speed, but it is assumed that its behavior would be similar to the 100% corrected speed sensitivity characteristic at frequencies below 42 Hz. The amplitudes used to determine the planar wave sensitivities and the sensitivities are tabulated in Table 7 for both the model results and the test data.

5.4.4 Sample Plotted Results

The instability analyses were based largely upon a selected group of parameters which exhibited a strong functional relationship to the breakdown of stable fan operation. These parameters were the unsteady blade force, the amplification function, the tangent of the incidence angle, and the flow ratio. The unsteady blade force behavior is shown in Figure 60 for 118 Hz, 100% corrected speed as the model enters the region of aerodynamic instability. The unsteady force term is a function of the blade row volume dynamics and is sensitive to destabilizing forces. An example of the behavior of the amplification function is shown in Figure 61 for the 100% speed, 118 Hz case. Figure 62 illustrates the instantaneous behavior of the tangent of the incidence angle at the entrance to each rotor. Observation of this parameter relative to the location of the steady-state surge incidence angle gave some insight into the blade row characteristic fluctuations relative to steady-state operation. Each of these parameters are shown for each surge in Appendix E as an

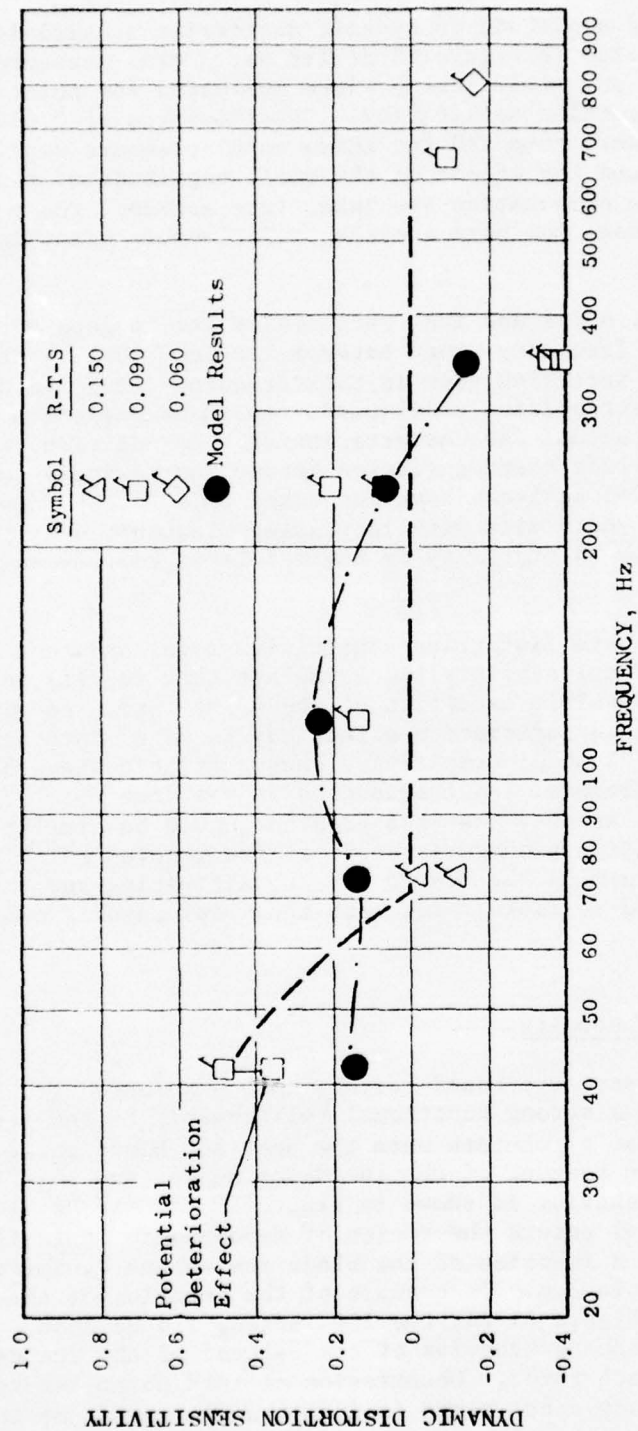


Figure 59. Planar Wave Distortion Sensitivity, 80% $N/\sqrt{\theta}$.

Table 7. Model and Test Planar Wave Distortion Sensitivities.

<u>Simulated Reading No.</u>	<u>Frequency</u>	<u>Planar Wave Amplitude</u>		<u>Planar Wave Distortion Sensitivity</u>	
		<u>Model</u>	<u>Test</u>	<u>Model</u>	<u>Test</u>
<u>100% $N/\sqrt{\theta}$</u>					
-	25	7.20	-	0.803	-
71	42	7.40	6.88	0.432	0.74/0.651*
-	60	11.82	-	0.333	-
69	80	10.80	10.67	0.682	0.59
64	118	8.20	8.79	0.634	0.14
64	118	9.66	-	0.673	-
65/66	118	11.40	15.39	0.640	0.39
41	220	7.07	6.06	0.555	-0.28
43	350	8.70	10.48	0.162	-0.11
<u>80% $N/\sqrt{\theta}$</u>					
82	42	6.70	5.84	0.164	0.480/0.362*
77	75	6.05	7.09	0.152	-0.02
61	118	5.99	5.11	0.230	0.14
57	240	6.36	9.66	0.044	0.07
53	350	6.05	6.41	-0.139	-0.35

*Potential deterioration taken into account.

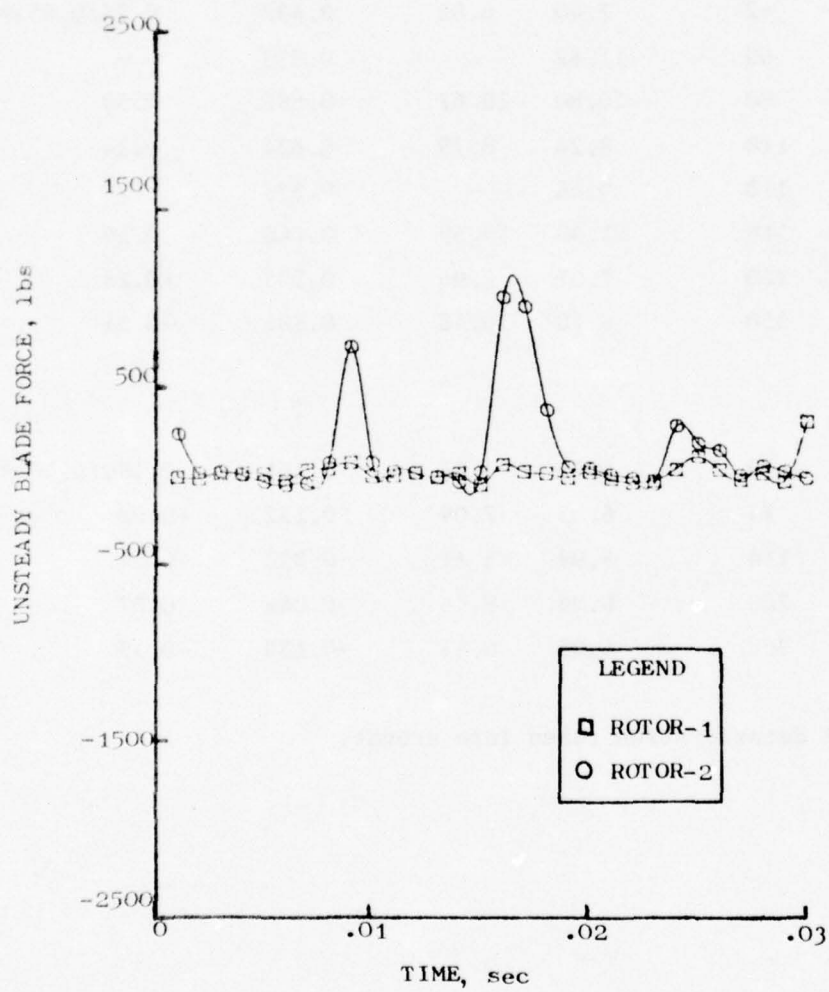


Figure 60. Unsteady Blade Force Vs. Time, 100% $N/\sqrt{\theta}$, 118 Hz.

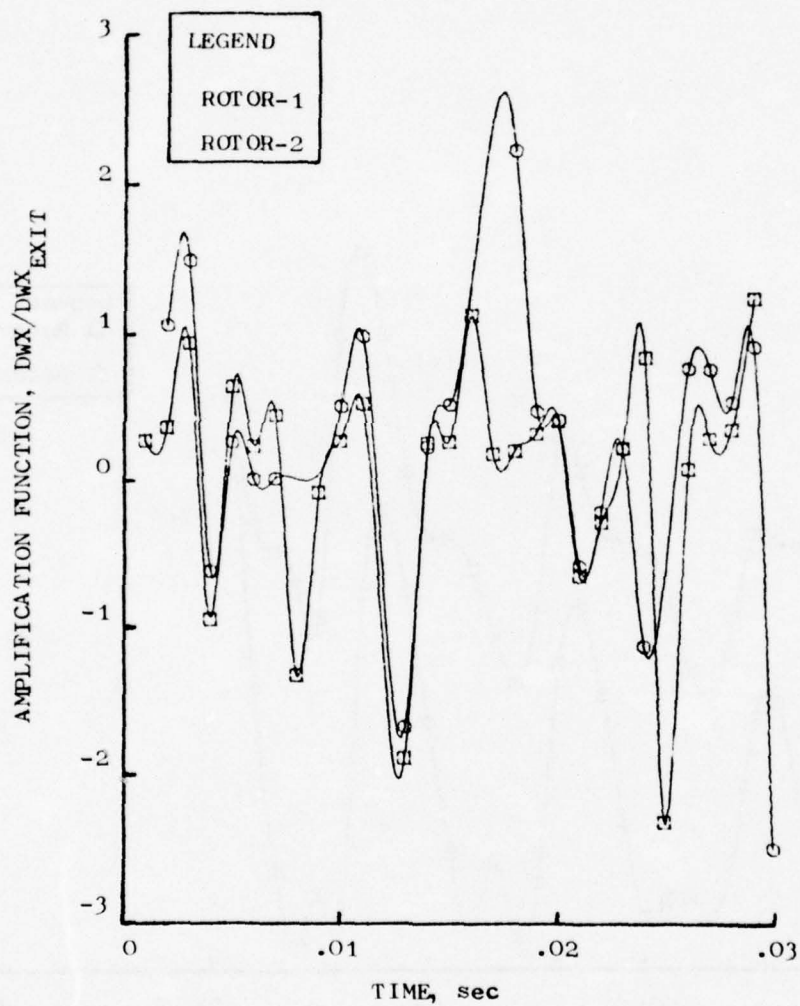


Figure 61. Amplification Function Vs. Time, 100% $N/\sqrt{\theta}$, 118 Hz.

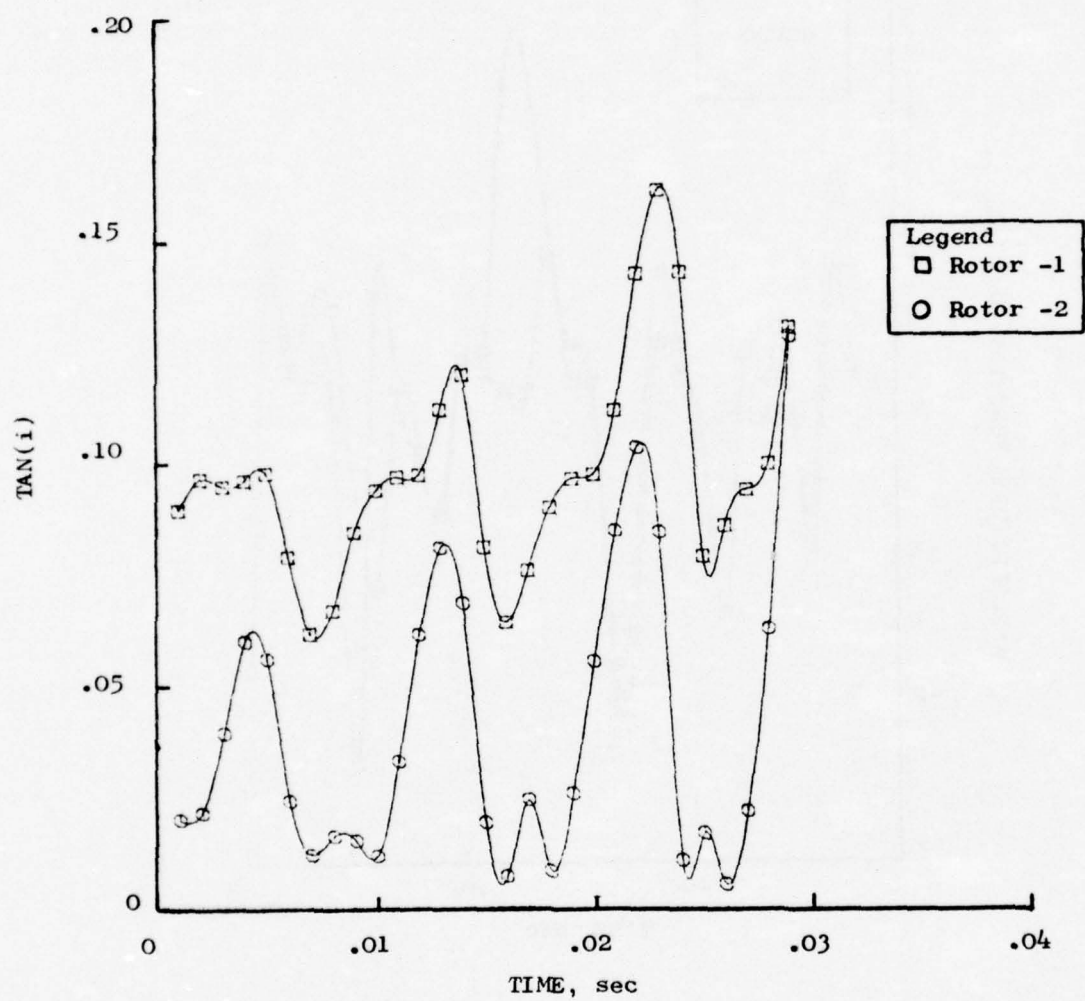


Figure 62. Tangent of Incidence Angle Vs. Time, 100% $N/\sqrt{\theta}$, 118 Hz.

aid to the interpretation of the model instability. The flow ratio parameter (W_2/W_1) was not always available in plotted form, but was available in the computer listings for use in the analyses.

5.4.5 Stage Initiating Instability

The stage initiating aerodynamic instability was determined by the criteria set forth in Section 5.4.2 on instability identification and with the aid of the plotted parameters described in Section 5.4.4. Based upon analysis of each of these parameters, the stage initiating instability was determined where positive identification could be made and the results are presented in Table 8. Behavior of the individual stages fall into a general pattern. Stage two activity level was usually high in comparison to stage one and as the fan was throttled to instability, the behavior of stage two appeared to contribute to increasing levels of activity in stage 1.

Table 8. Model Stage Initiating Instability.

	Model Results			
<u>Simulated Reading No.</u>	<u>Frequency</u>	<u>W₂/W₁</u>	<u>AMPF</u>	<u>Unsteady Force</u>
<u>100% N/√θ</u>				
-	25	1	?	?
71	42	1	1	?
-	60	1	?	1
69	80	2	2	2
64	118	2	2	2
64	118	2	?	?
65/66	118	2	?	2
41	220	2	2	?
43	350	?	?	?
<u>80% N/√θ</u>				
82	42	2	2	2
77	75	2	2	2
61	118	?	2	?
57	240	?	2	2
53	350	?	?	?

At 100% speed, rotor 1 operated with its mean incidence angle much nearer steady-state surge than did rotor 2 and as the fan approached instability at low frequencies, the activity level of rotor 1 was sufficient to initiate instability in the first stage. As frequency was increased, stage two activity became so pronounced that instability initiation must be attributed to behavior of the second stage.

In the case of 80% speed operation, the mean rotor incidence angle is positioned nominally the same for both rotor 1 and rotor 2 relative to the steady-state surge location. For each case that the stage initiating the instability could be identified, it was determined to be stage 2.

The stage initiating instability for the 350 Hz case at both 80% and 100% rotor speed could not be identified by any of the current instability identification techniques. These instabilities did not appear to exhibit any abrupt or discontinuous activity that could be useful in establishing the initiating stage. It is noted that the results obtained from each of the three parameters given in Table 8 are consistent with each other and tend to justify the technique employed for identifying the stage where instability initiated.

5.5 EFFECT OF UNSTEADY BLADE CHARACTERISTICS

Analysis of the stationary waveform data shown in Section 5.2.1 revealed that above 75-80 Hz, a phase difference developed between the model results and the test data. It appeared that the PS14 model results led the test data and at 118 Hz the phase angle appeared to be greater than 100°. These results seemed to be the first indication that the response of the blade circulation could no longer be assumed to be instantaneous and that the finite time required for the blade circulation to readjust must be taken into account.

The method of Section 4.2.3 for including the effects of blade circulation readjustments was included in the model and new simulations corresponding to the simulations of the Section 5.2.1 100% corrected speed, 80 Hz and 118 Hz cases were conducted. The results are shown in Figures 63 and 64 for just the PTIGV and PS14 parameters. The results at 80 Hz show no significant effect of time required for blade circulation readjustment, but at 118 Hz the blade circulation readjustment introduces a lag of approximately 25 degrees. This lag is not sufficient to cause a match between the model results and test data, but the trend is correct. As was stated in Section 4.2.3, refinement of the parameter time constant coefficient C_3 is required.

Two interesting facts emerge from this analysis: 1) The introduction of the finite time required for blade circulation adjustment introduces a phase lag not only in the parameters downstream of the fan, but introduces noticeable waveform changes in both the upstream and downstream parameters. This finding supports the growing realization that unsteady flows in compression components and associated ducting form highly coupled systems and

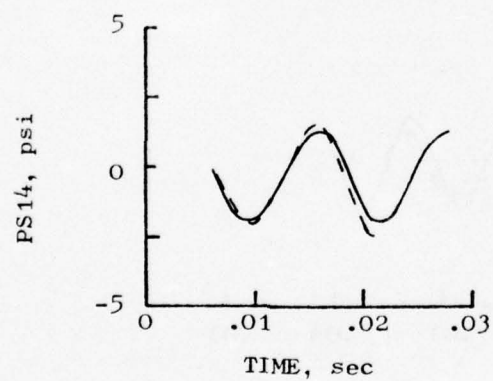
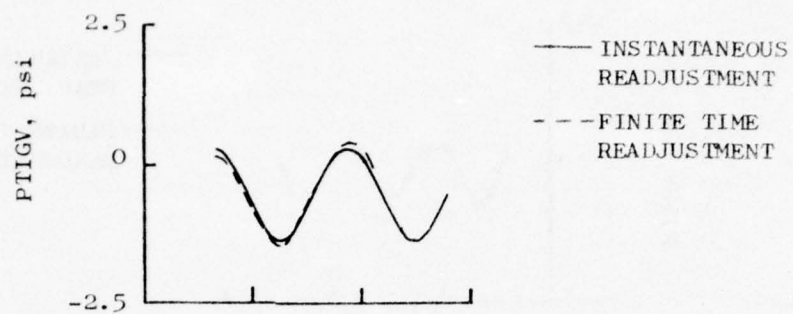


Figure 63. Circulation Readjustment, 100% $N/\sqrt{\theta}$, 80 Hz.

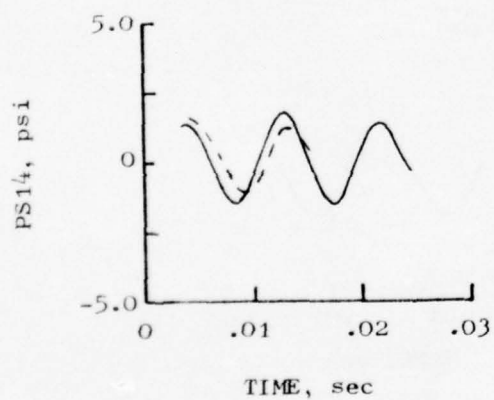
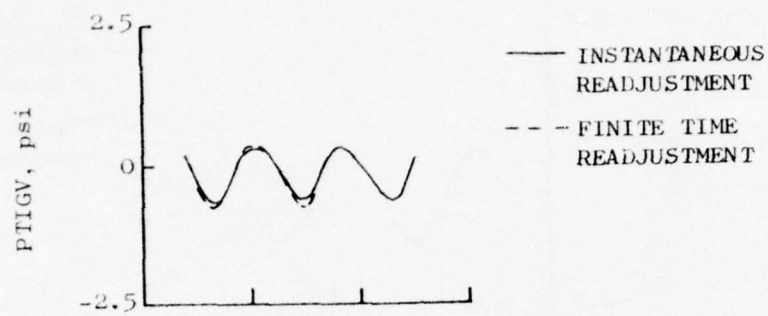


Figure 64. Circulation Readjustment, 100% $N/\sqrt{\theta}$, 118 Hz.

implies that any change to a compression component must be carefully evaluated by examining the system unsteady response rather than just an evaluation of the local-steady-flow response. 2) The largest incidence angle lag occurs in stator 2 at both 80 Hz and 118 Hz while there is almost insignificant lag in the other four blade rows. This occurs in response to the greater activity of the rotor 2 incidence angle which leads to large variations in rotor 2 deviation angle, and thereby directly affects the stator 2 response. Examination of the Appendix C plots at 80 Hz and 118 Hz at 100% corrected speed will provide graphic illustration of this effect.

6.0 CONCLUSIONS AND RECOMMENDATIONS

This program has provided the opportunity to investigate some of the capabilities of a dynamic digital model of a fan component and to compare the simulation results against test data. This verification step has been missing in most of the previously conducted dynamic modeling studies. Based upon the results of this program, it has been concluded that the Dynamic Digital Blade Row Compression Component Stability Model correctly calculated the manner in which unsteady flows interact with ducts and a fan component and is limited only by knowledge of the blade characteristics input. Further, it is concluded that this type of sophisticated one-dimensional model offers a unique method for studying compression component stability characteristics, especially where the disturbance is of a nearly planar nature. These general conclusions are supported by the following specific findings.

- The clean-inlet-flow fan map was accurately reproduced at 80% and 100% corrected speeds. The prediction of aerodynamic instability initiation occurred at the experimentally determined surge points.
- Accurate simulations in terms of waveform shape, amplitude, and phase angle were obtained with unsteady inflow conditions at both 80% and 100% corrected speeds over the 42 Hz to 80 Hz frequency range.
- At frequencies greater than 80 Hz, the simulations give proper amplitude trends, but do not properly reproduce the harmonic frequencies of the fundamental waveform.
- As anticipated, the values of the predicted planar-wave distortion-transfer pitch-line coefficients fall between the hub and tip test values at both 80% and 100% corrected speeds over the 42 Hz to 350 Hz frequency range. Further, the anomolous "amplification" at 80% corrected speed with 118 Hz planar wave inflow is predicted.
- The amplitude transmission characteristics results show that even though a fan component will attenuate planar wave amplitudes, the individual stages or the IGV blade row can amplify the planar wave disturbance depending on corrected speed and planar wave frequency. Amplification within an IGV blade row is not understood, but has been noted in the IGV blade row for simulations of other compression components.
- The planar wave distortion sensitivities obtained by throttling the model to instability reproduced the experimental data relatively accurately over the 42 Hz to 350 Hz frequency range at 80% corrected speed. At 100% corrected speed the sensitivities are predicted only for low frequencies and only the trend is predicted at high

frequencies. This lack of agreement is attributed to an input data deficiency, that is, the relative total-pressure loss coefficients and deviation angles in the post steady-state surge region are based upon extrapolations which are not directly verifiable.

- The planar wave distortion sensitivity determination is sensitive to compression component deterioration and thus indicates that the clean-inlet-flow surge line should be carefully monitored throughout any stability test program.
- Accounting for the finite time needed for the blade circulations to readjust led to better agreement in the phase of flow parameters downstream of the fan.
- It was found that the stability of the tangential blade force component due to the storage of angular momentum within a blade row is very sensitive to the fan aerodynamics. The fact that under some conditions this force exhibits high frequency oscillations as the region of experimental instability is approached, may be an indication that this force may be relatable to the aeromechanical behavior exhibited by blade and vane strain gages.
- The aerodynamic instabilities encountered during model throttling simulations occurred where test surges were encountered and exhibited characteristics which replicated the behavior of the actual physical instability.

As a point of discussion, it was observed that as model instabilities develop, it was often difficult to determine precisely which stage was initiating the instability. At the heart of this matter is an age old question, "Which comes, first, the chicken or the egg?" In the context of the initiating stage discussions, the question was whether the lightly loaded downstream stage (mean point operating well away from steady-state incidence angle at surge) which was experiencing large oscillations, was the initiator, or was the highly loaded upstream stage (mean point operating close to steady-state incidence angle at surge) which was experiencing small oscillations the initiator. The coupling between stages is quite obvious and in this study it was assumed that the downstream stage was the initiator since its dynamics seems to cause the upstream, more heavily loaded stage to enter and remain in the post steady-state surge line region for a significant amount of time. Clearly, more study and analysis of instability development are needed if the fan and compressor designers are to know, without ambiguity, which stage requires refinements when stability improvements are needed.

As a result of the simulations and the ensuing analysis, it has become clear that the capabilities of the model could be further improved and that a deeper understanding of the physical processes which take place in a compression component during unsteady flow could be gained. The following recommendations address these problems.

- Refinements to the blade-row time-constant coefficient/solidity relationship are required if a more exact match between the phase angle of test and model parameters is desired.
- A method for extrapolating the steady-state blade characteristics beyond the experimental surge point must be developed.
- Examination of the effects of free-volume lengths and blade-row-volume lengths needs to be accomplished for frequencies above 80 Hz to determine which is the controlling factor for ensuring that the harmonic frequencies are properly reproduced.

APPENDIX A

DATA ENHANCEMENT OF CORRECTED AIRFLOW AND PRESSURE RATIO

The results of the data enhancement analyses are given in Figures 65-67 for frequencies of 42, 80, and 350 Hz at 100% corrected speed and in Figure 68 for 75 Hz at 80% corrected speed. It should be noted that data enhancement results are presented only for those points where the airflow measurement was determined to be properly operating and for those points which correspond to cases that were simulated (Rdg. No).

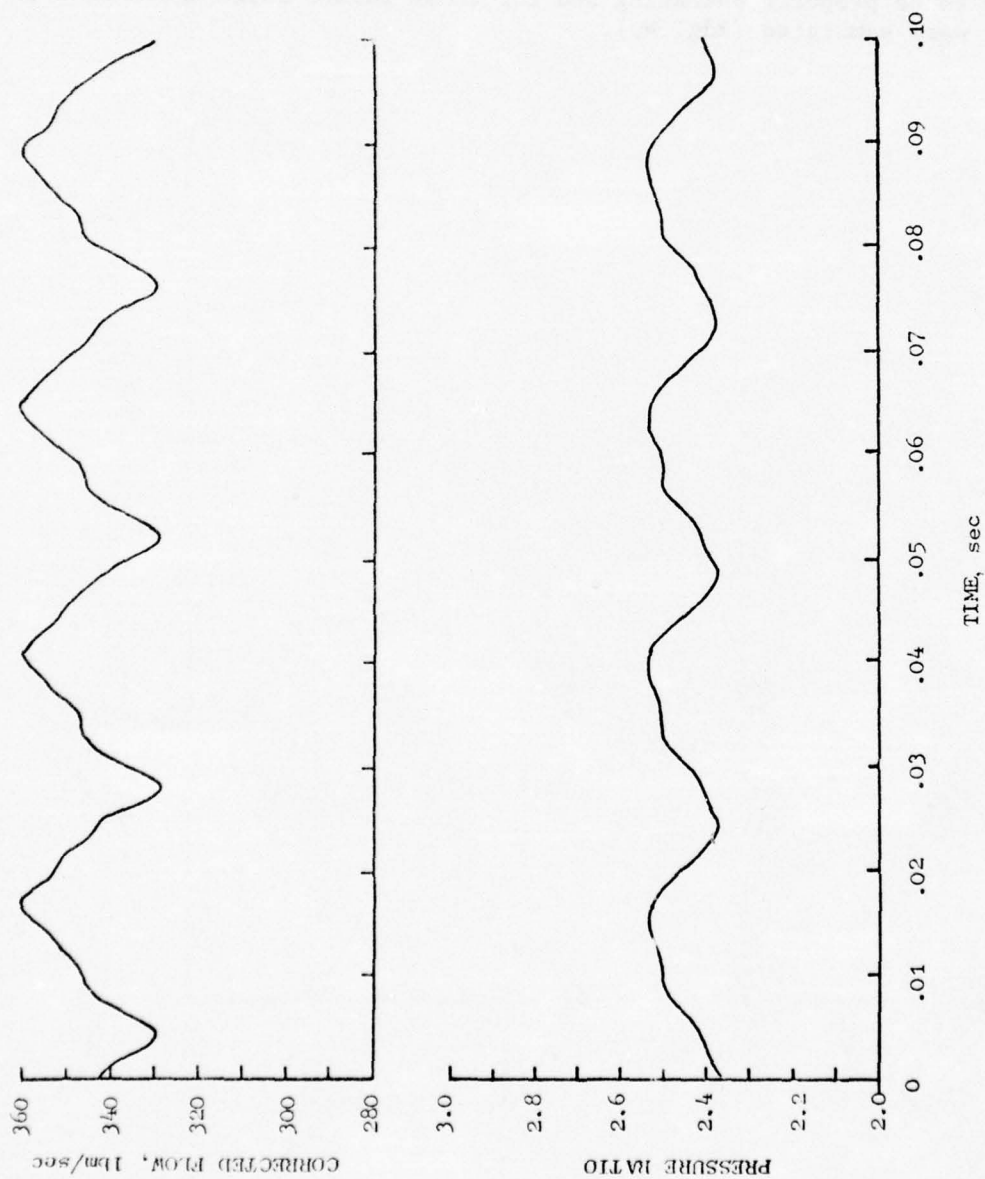


Figure 65. Enhancement of Rdg. 71 Data, 100% N/\sqrt{B} , 42 Hz.

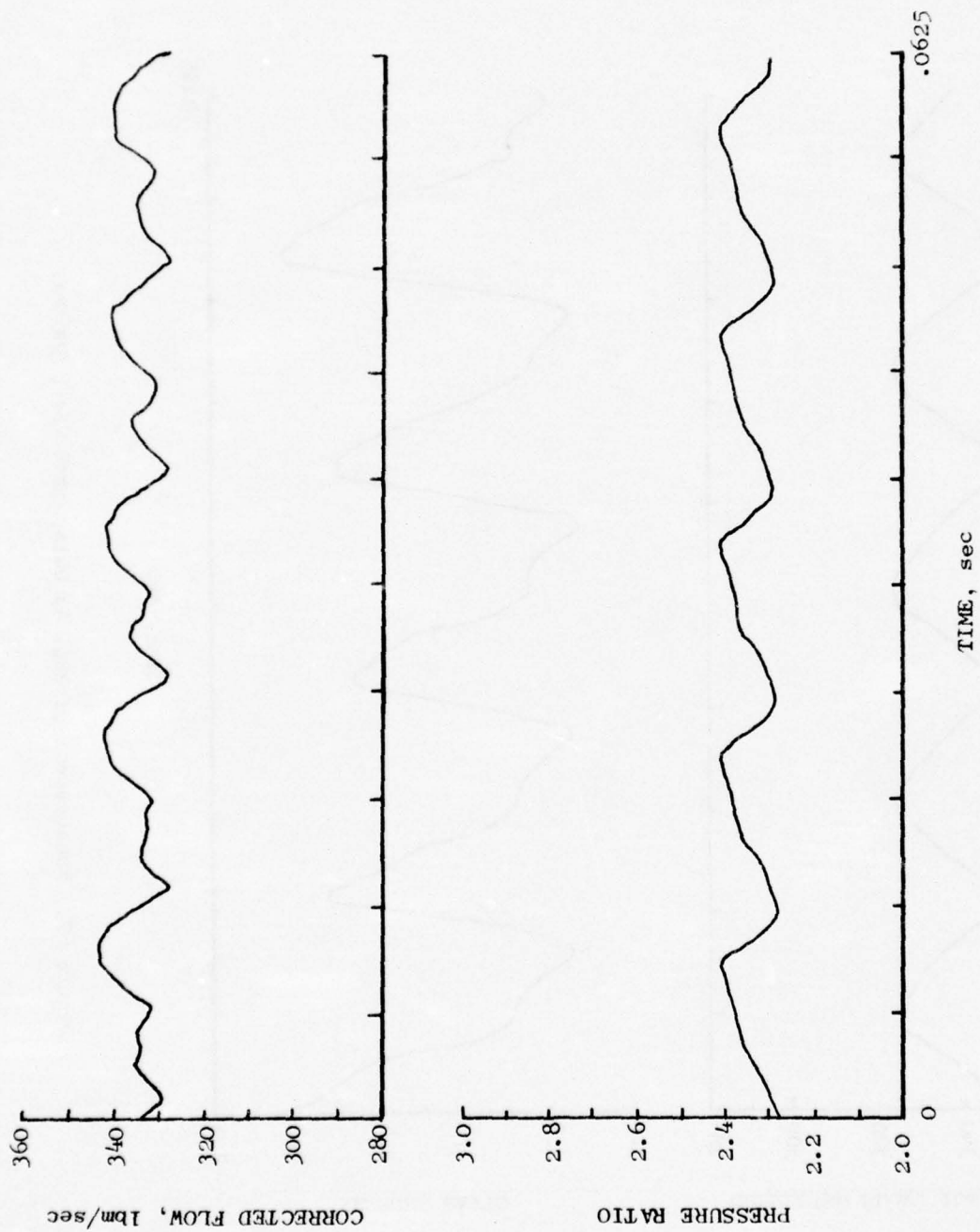


Figure 66. Enhancement of Rdg. 69 Data, 100% N/\sqrt{g} , 80 Hz.

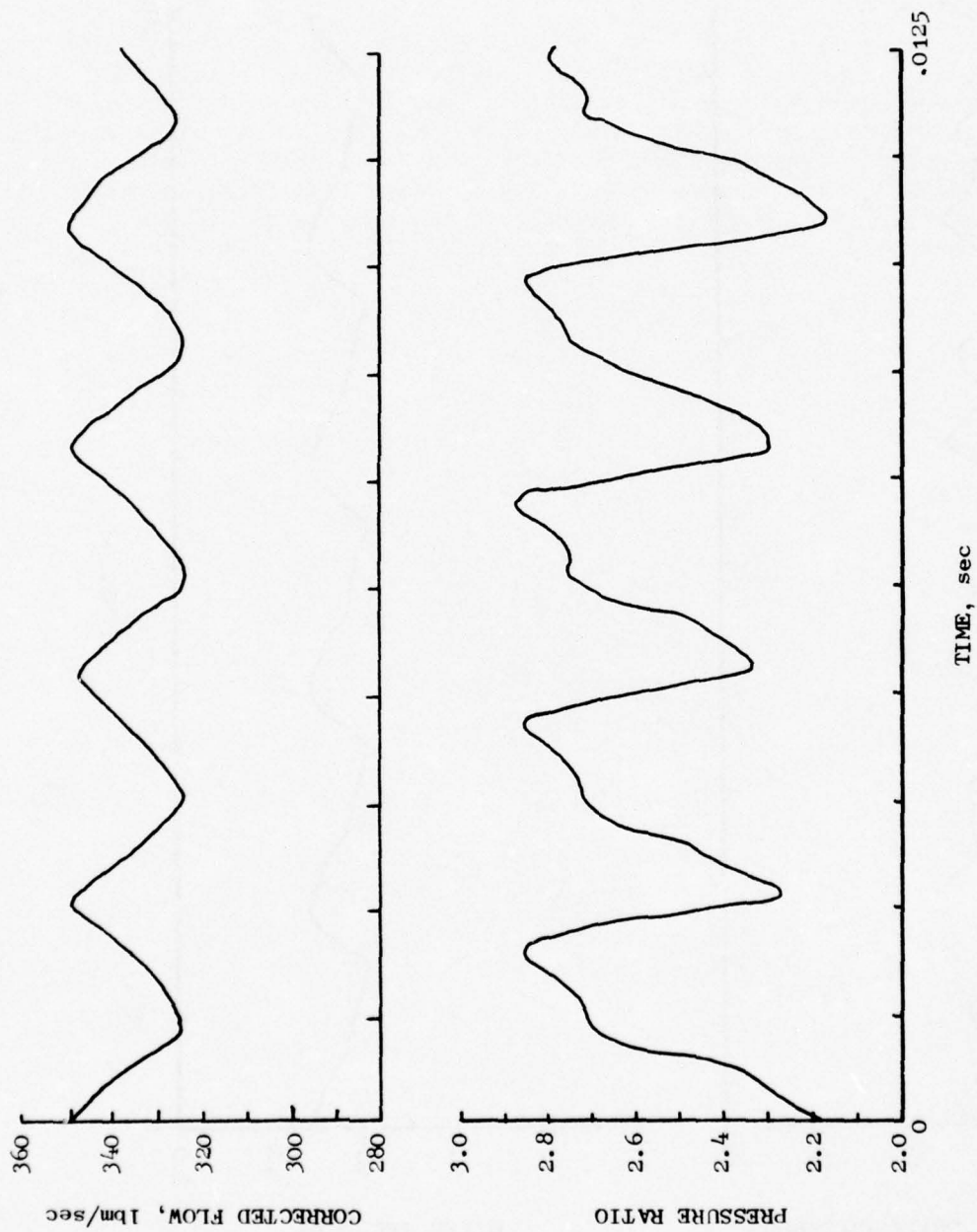


Figure 67. Enhancement of Rdg. 43 Data, 100% $N/\sqrt{\delta}$, 350 Hz.

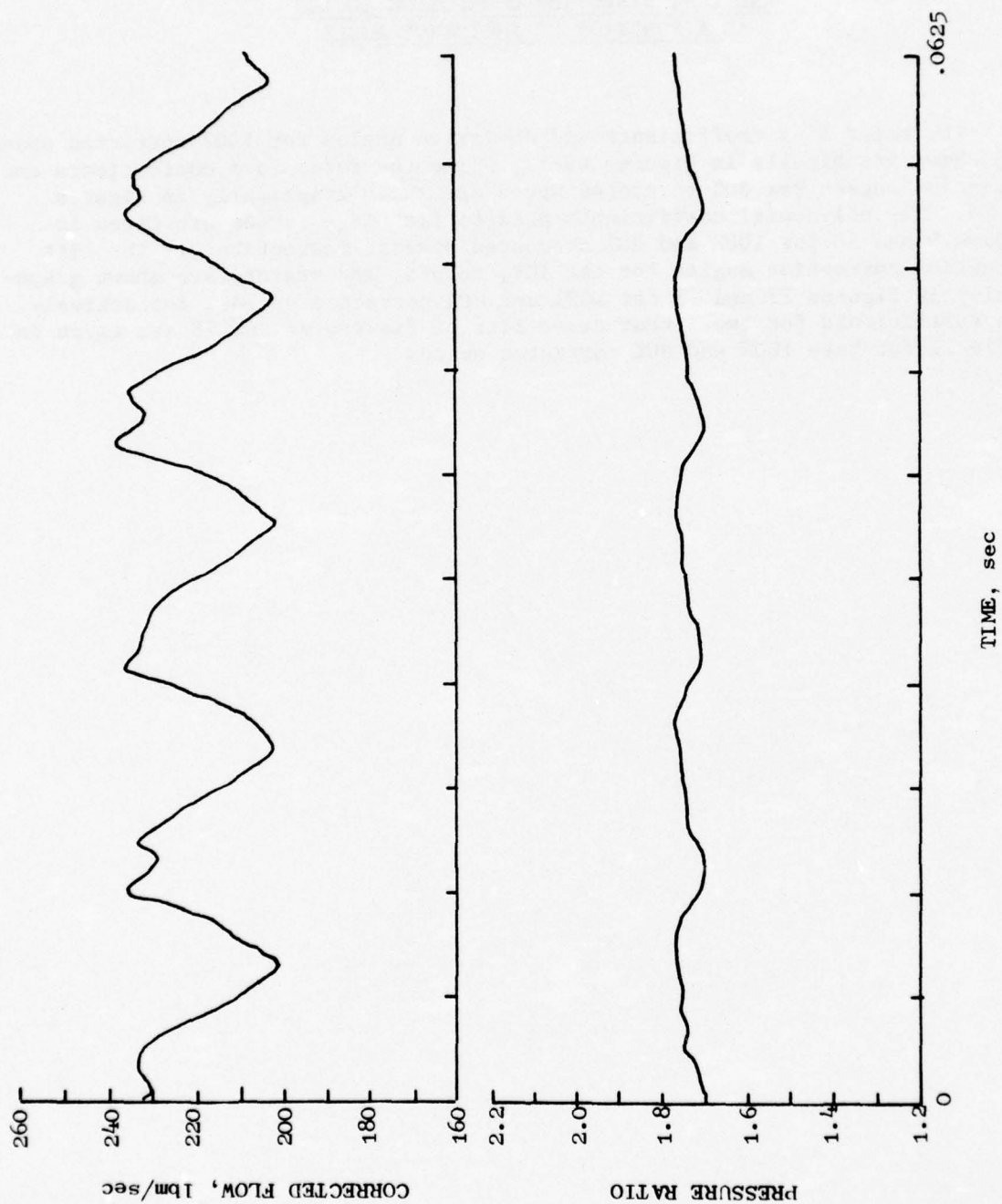


Figure 68. Enhancement of Rdg. 77 Data, 80% $N/\sqrt{\delta}$, 75 Hz.

APPENDIX B

LOSS COEFFICIENTS, DEVIATION ANGLES, AND LIFT DIRECTION CORRECTION ANGLES AS A FUNCTION OF INCIDENCE ANGLE

The rotor loss coefficients and deviation angles for 100% corrected speed are shown graphically in Figures 69-72, while the rotor loss coefficients and deviation angles for 80% corrected speed are shown graphically in Figures 73-76. The polynomial coefficients used to fit these curves are given in Tables 9 and 10 for 100% and 80% corrected speeds, respectively. The lift direction correction angles for the IGV, rotors, and stators are shown graphically in Figures 77 and 78 for 100% and 80% corrected speeds, respectively. The coefficients for the linear curve fits of Figures 77 and 78 are given in Table 11 for both 100% and 80% corrected speeds.

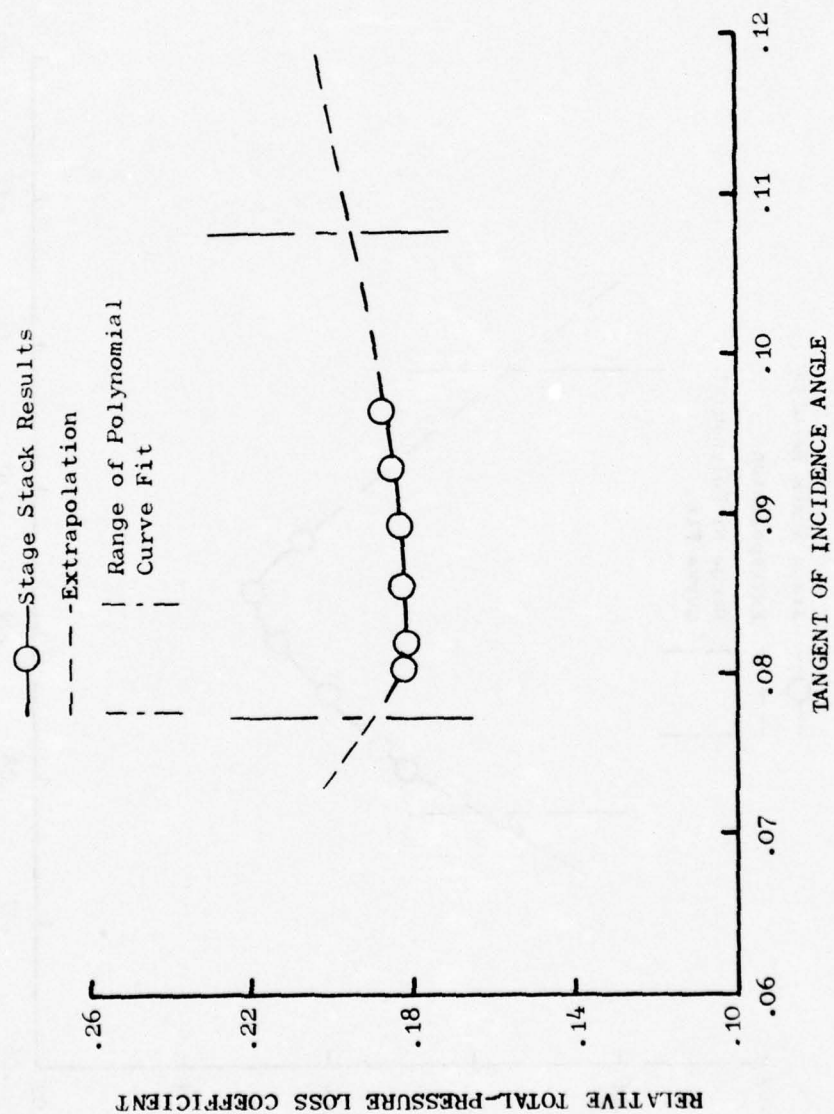


Figure 69. Two-Stage Fan Rotor 1 Total-Pressure Loss Coefficients, 100% $N/\sqrt{\theta}$.

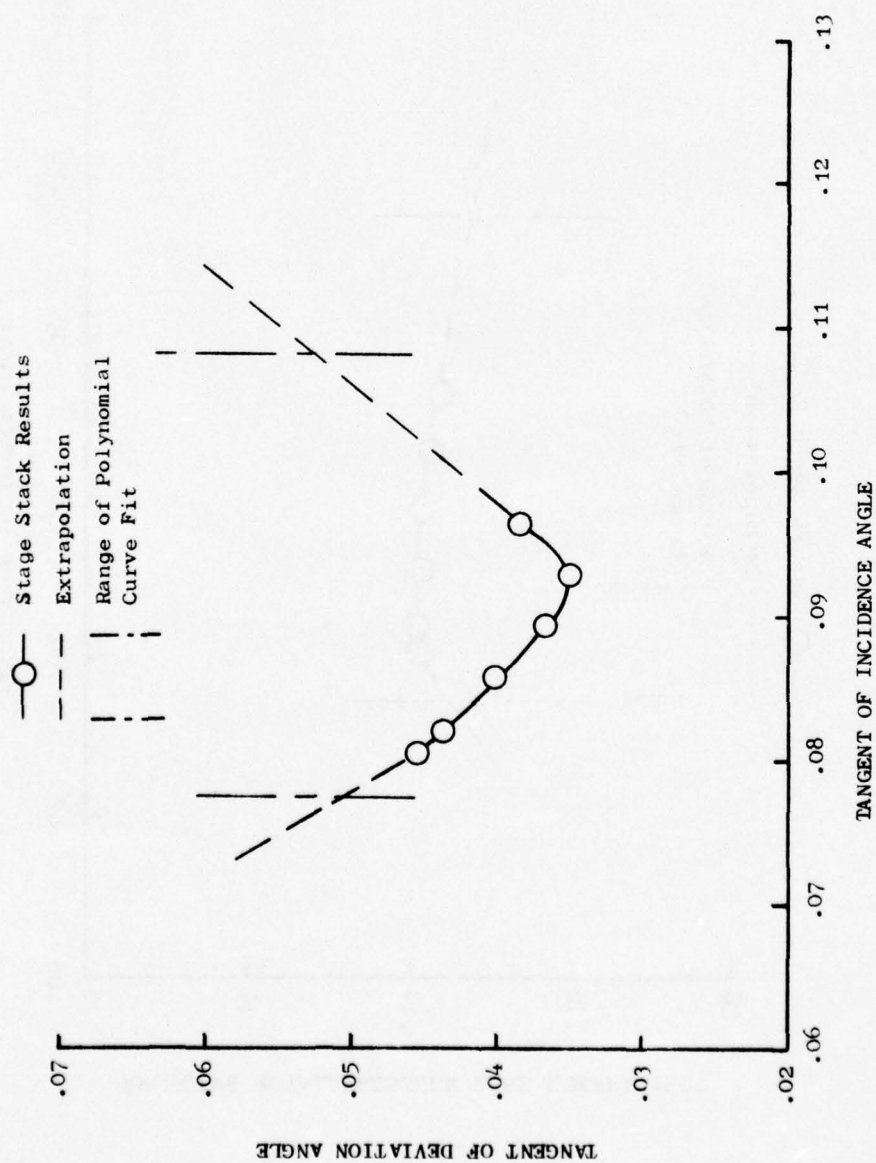


Figure 70. Two-Stage Fan Rotor 1 Deviation Angles, 100% N/\sqrt{G} .

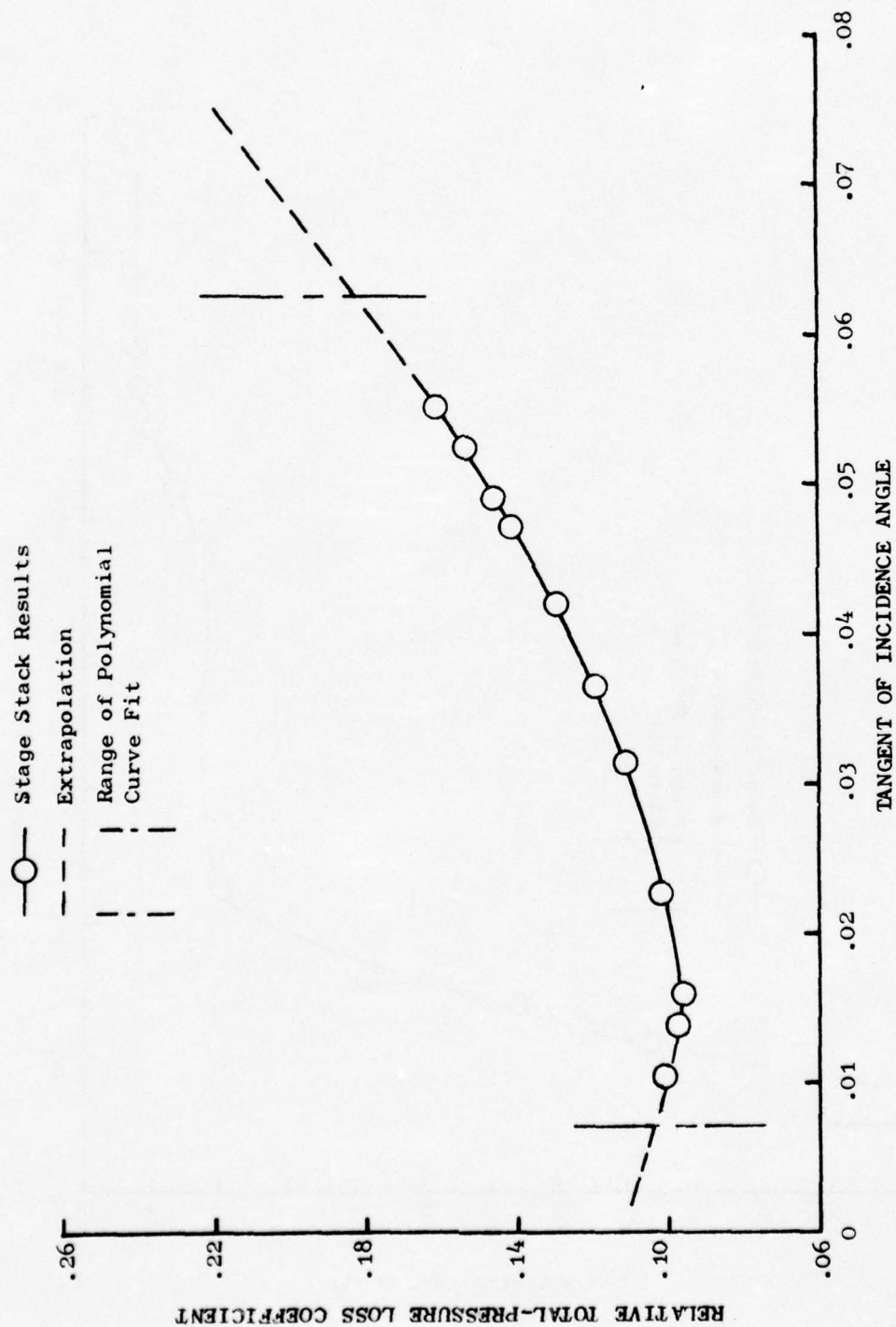


Figure 71. Two-Stage Fan Rotor 2 Total-Pressure Loss Coefficients, 100% $N/\sqrt{\theta}$.

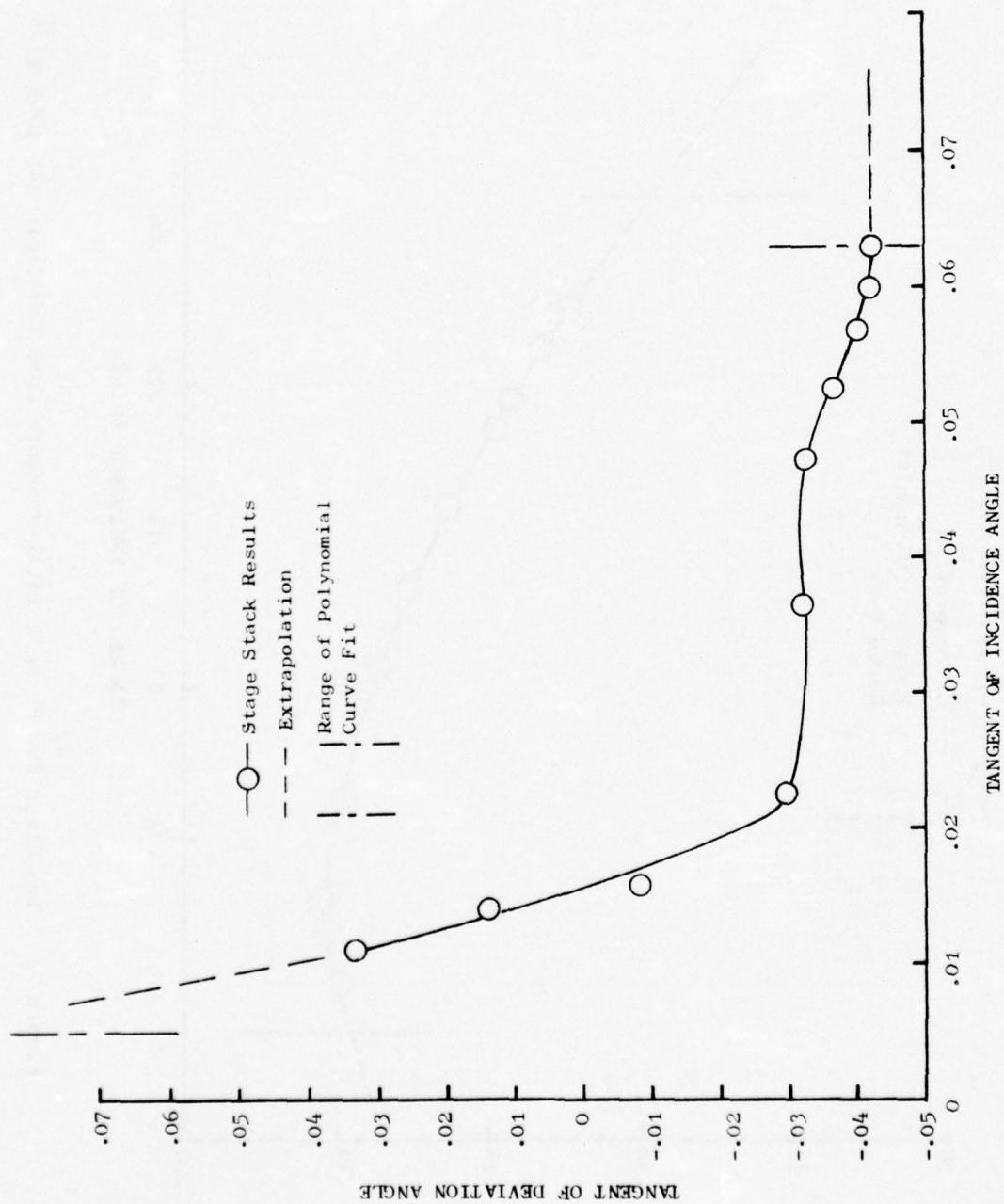


Figure 72. Two-Stage Fan Rotor 2 Deviation Angles, 100% $N/\sqrt{6}$.

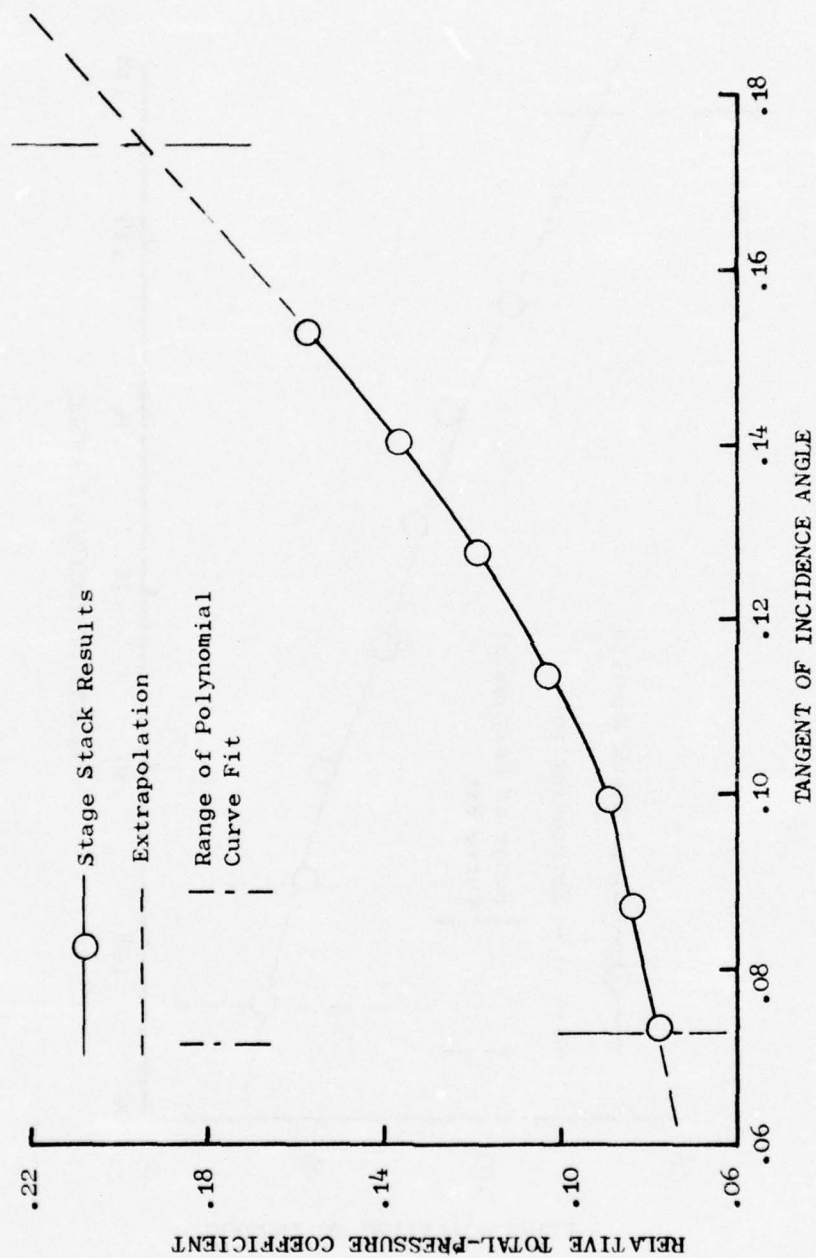


Figure 73. Two-Stage Fan Rotor 1 Total-Pressure Loss Coefficients, $80\% N/\sqrt{g}$.

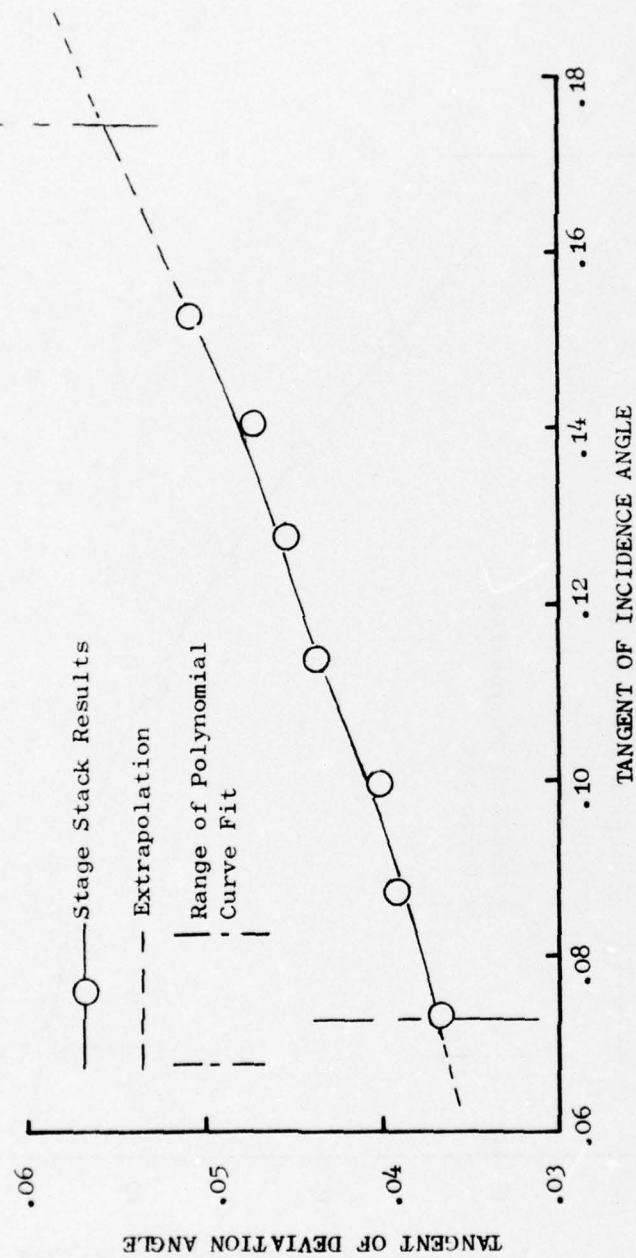


Figure 74. Two-Stage Fan Rotor 1 Deviation Angles, 80% $N/\sqrt{\theta}$.

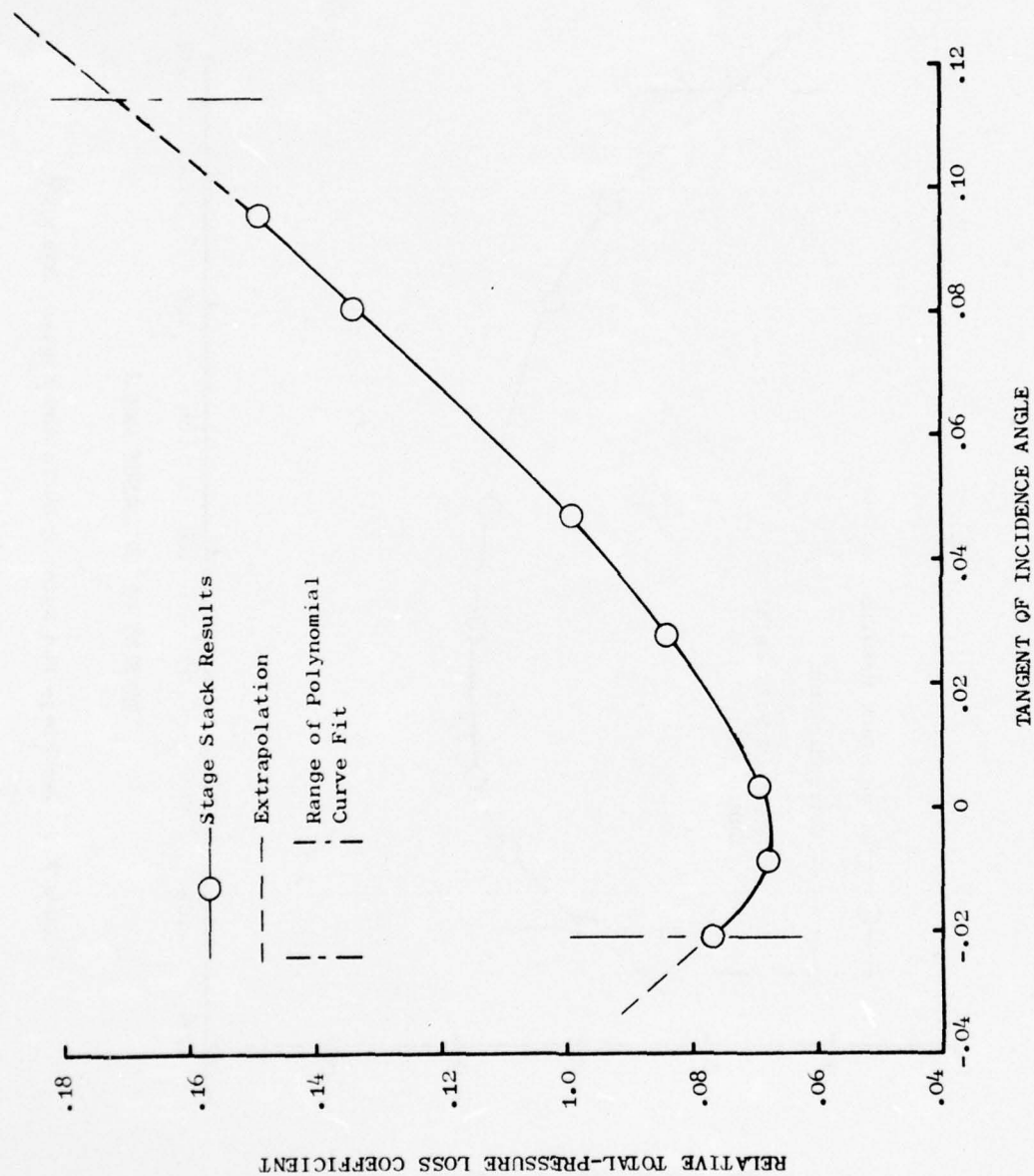


Figure 75. Two-Stage Fan Rotor 2 Total-Pressure Loss Coefficients, 80% $N/\sqrt{6}$.

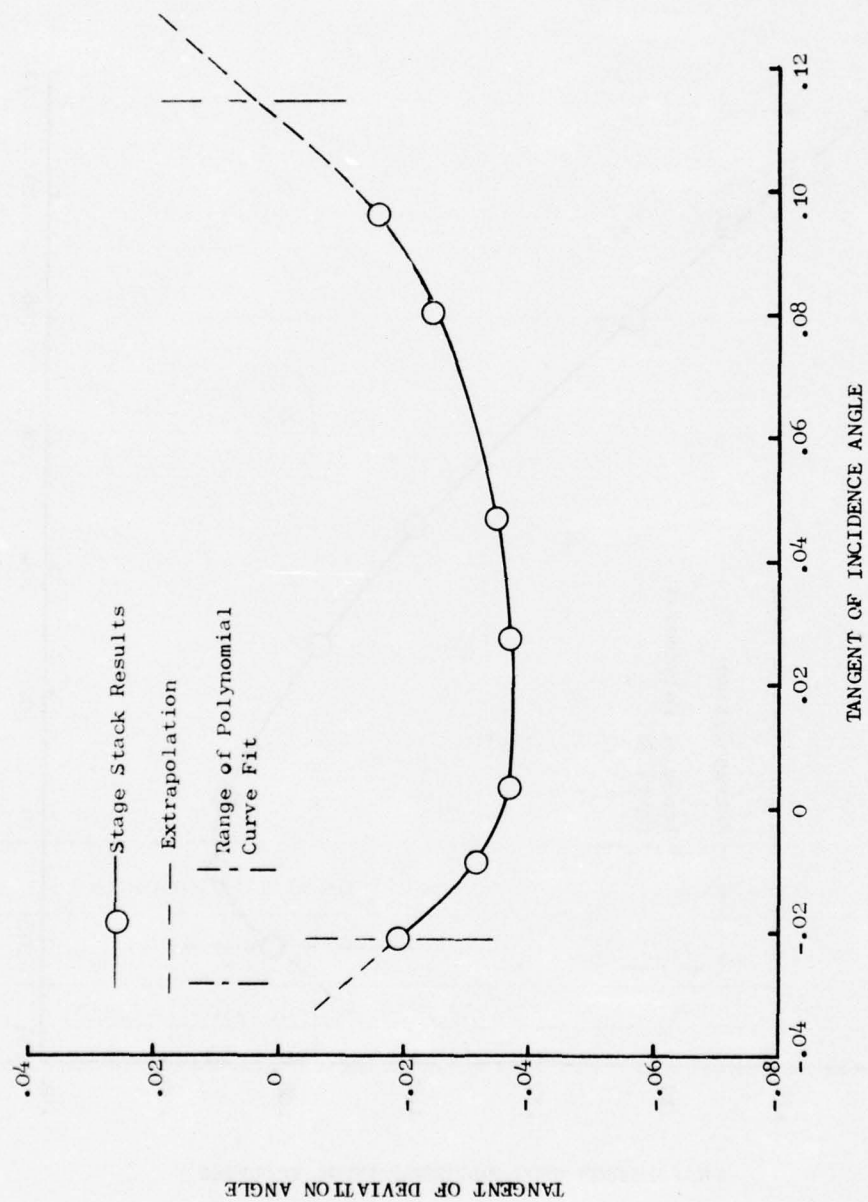


Figure 76. Two-Stage Fan Rotor 2 Deviation Angles, 80% $N/\sqrt{\beta}$.

Table 9. Polynomial Representation of Two-Stage Fan Characteristics, 100% $N/\sqrt{\theta}$.

A) RELATIVE TOTAL-PRESSURE LOSS COEFFICIENT, $\bar{w} = P_N(\text{TAN}(i))$

$$\bar{w} = C_1 \text{TAN}(i)^4 + C_2 \text{TAN}(i)^3 + C_3 \text{TAN}(i)^2 + C_4 \text{TAN}(i) + C_5$$

ROTOR	TAN(i) DOMAIN		POLYNOMIAL COEFFICIENTS				
	MAX	MIN	C_1	C_2	C_3	C_4	C_5
1	.108	.0775	-20924.87	7550.7963	-999.939	57.8357	-1.0535
2	.10	.0825	-336721.8	127168.94	-17844.64	1103.111	-25.3164

B) TANGENT OF DEVIATION ANGLE, $\text{TAN}(\delta) = P_N(\text{TAN}(i))$

$$\text{TAN}(\delta) = D_1 \text{TAN}(i)^4 + D_2 \text{TAN}(i)^3 + D_3 \text{TAN}(i)^2 + D_4 \text{TAN}(i) + D_5$$

ROTOR	TAN(i) DOMAIN		POLYNOMIAL COEFFICIENTS				
	MAX	MIN	D_1	D_2	D_3	D_4	D_5
1	.07	.005	4608.7463	-1085.795	110.9104	-2.8132	.1184
2	.0625	.00725	78204.009	-14049.63	903.2485	-24.7233	.2109

Table 10. Polynomial Representation of Two-Stage Fan Characteristics, 80% $N/\sqrt{\theta}$.

A) RELATIVE TOTAL-PRESSURE LOSS COEFFICIENT, $\bar{w} = P_N(\text{TAN}(i))$

$$\bar{w} = C_1 \text{TAN}(i)^4 + C_2 \text{TAN}(i)^3 + C_3 \text{TAN}(i)^2 + C_4 \text{TAN}(i) + C_5$$

ROTOR	TAN(i) DOMAIN		POLYNOMIAL COEFFICIENTS				
	MAX	MIN	C_1	C_2	C_3	C_4	C_5
1	.174	.073	-401.9521	185.92190	-21.34740	1.01032	.05717
2	.115	-.021	692.14865	-190.8235	19.66726	.10287	.06824

B) TANGENT OF DEVIATION ANGLE, $\text{TAN}(\delta) = P_N(\text{TAN}(i))$

$$\text{TAN}(\delta) = D_1 \text{TAN}(i)^4 + D_2 \text{TAN}(i)^3 + D_3 \text{TAN}(i)^2 + D_4 \text{TAN}(i) + D_5$$

ROTOR	TAN(i) DOMAIN		POLYNOMIAL COEFFICIENTS				
	MAX	MIN	D_1	D_2	D_3	D_4	D_5
1	.174	.073	-91.63008	50.90462	-9.66728	.92079	.00375
2	.115	-.021	907.22825	-182.3455	15.06719	-.36957	-.03553

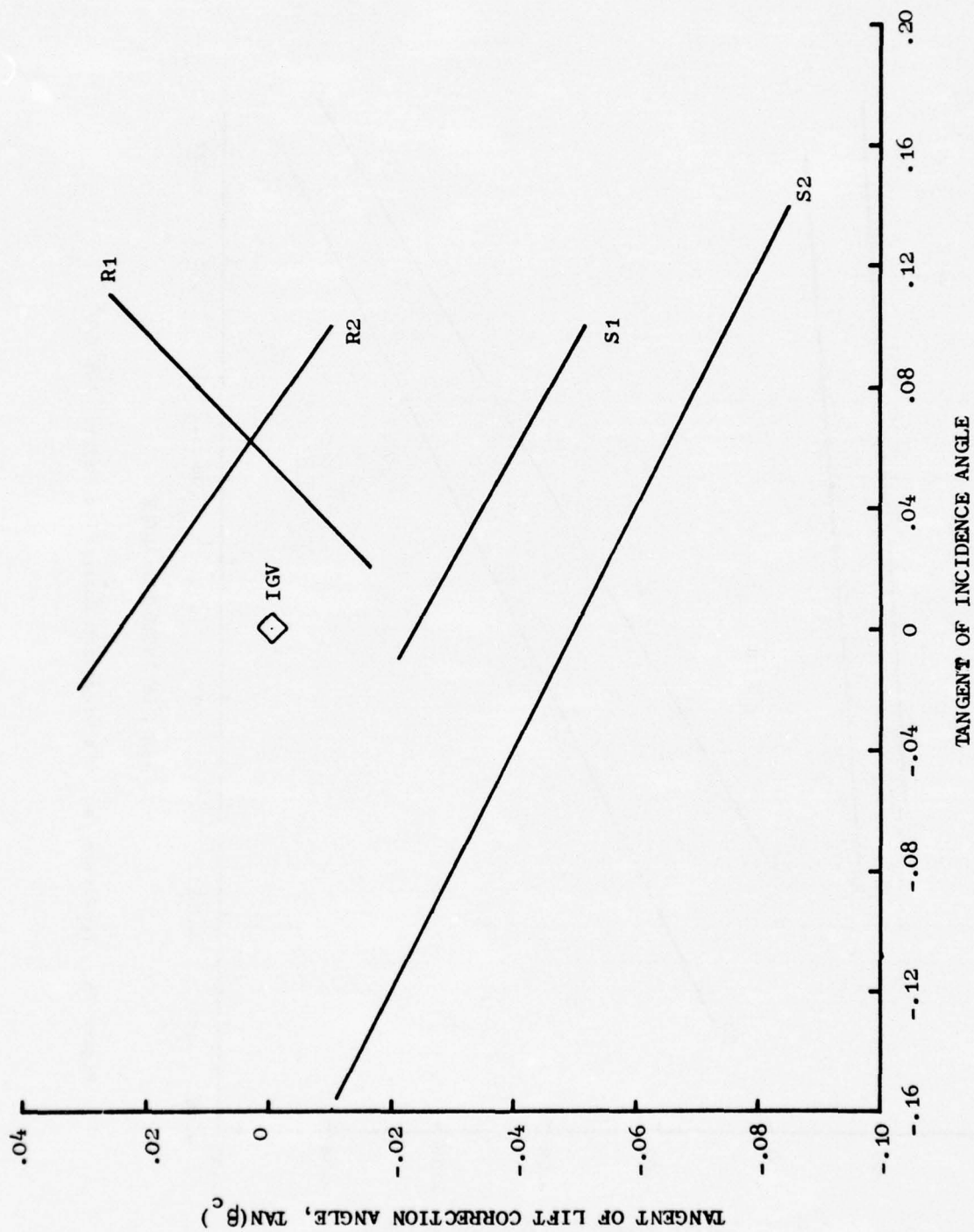


Figure 77. Two-Stage Fan Lift Direction Correction Angles, 100% $N/\sqrt{\theta}$.

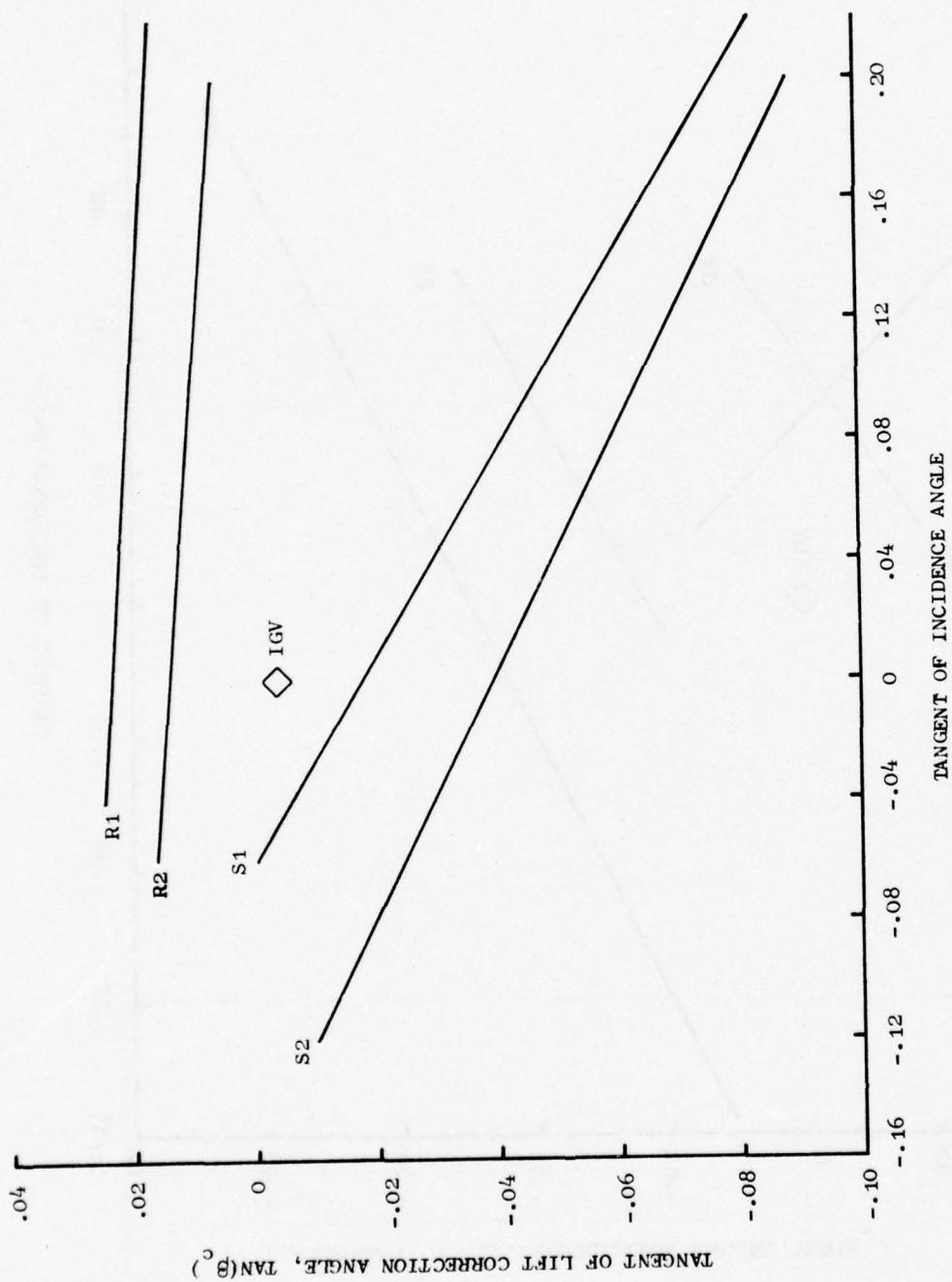


Figure 78. Two-Stage Fan Lift Direction Correction Angles, 80% N/β .

Table 11. Lift Direction Correction Angle Coefficients.

$$100\% N/\sqrt{\theta}$$

$$\text{TAN}(\beta_c) = (M)(\text{TAN}(i)) + B$$

BLADE ROW	B (Y-INTERCEPT)	M (SLOPE)
R1	-.02550	.47000
S1	-.02400	-.27800
R2	.02350	-.37300
S2	-.03900	-.35080

$$80\% N/\sqrt{\theta}$$

$$\text{TAN}(\beta_c) = (M)(\text{TAN}(i)) + B$$

BLADE ROW	B (Y-INTERCEPT)	M (SLOPE)
R1	.02311	-.03043
S1	-.01802	-.29283
R2	.01362	-.03913
S2	-.03971	-.24588

APPENDIX C

PLOT DATA FROM STATIONARY MODEL OPERATION

This appendix contains rotor entrance flow, tangent of rotor incidence angle, rotor relative total-pressure loss coefficient, tangent or rotor deviation angle, rotor blade-row total-pressure ratio, rotor blade row static-pressure ratio, and rotor blade-row total-temperature waveforms for the case where the simulation had established stationary operation prior to the initiation of throttling to surge. The waveforms for 25, 42, 60, 80, 118, 220, and 350 Hz at 100% corrected speed are given in Figures 79-127. The waveforms for 42, 75, 118, 240, and 350 Hz at 80% corrected speed are given in Figures 128-162.

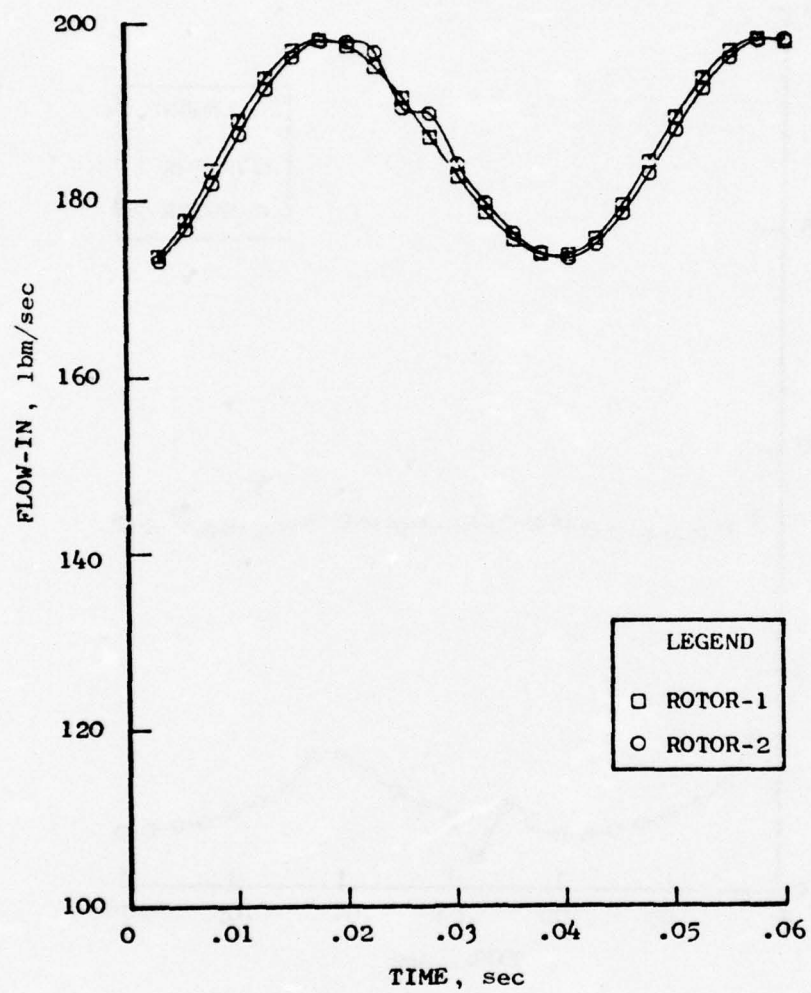


Figure 79. Physical Airflow Vs. Time, 100% $N/\sqrt{\theta}$, 25 Hz.

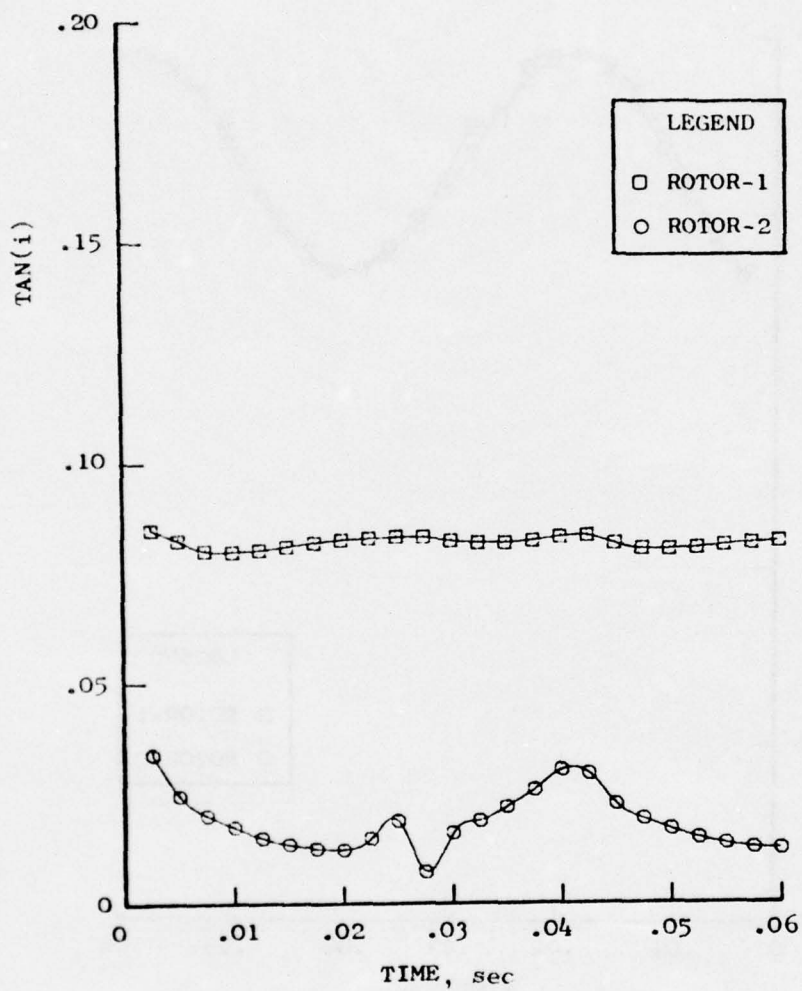


Figure 80. Tangent of Incidence Angle Vs. Time, 100% $N/\sqrt{\theta}$, 25 Hz.

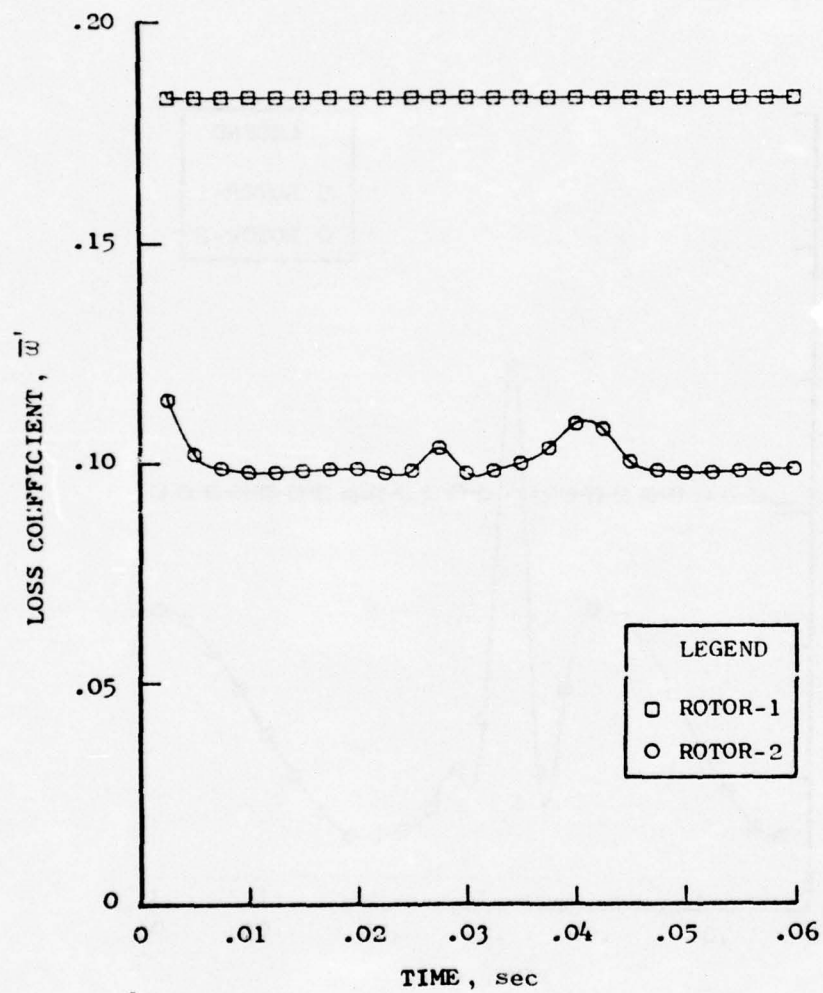


Figure 81. Loss Coefficient Vs. Time, 100% $N/\sqrt{\theta}$, 25 Hz.

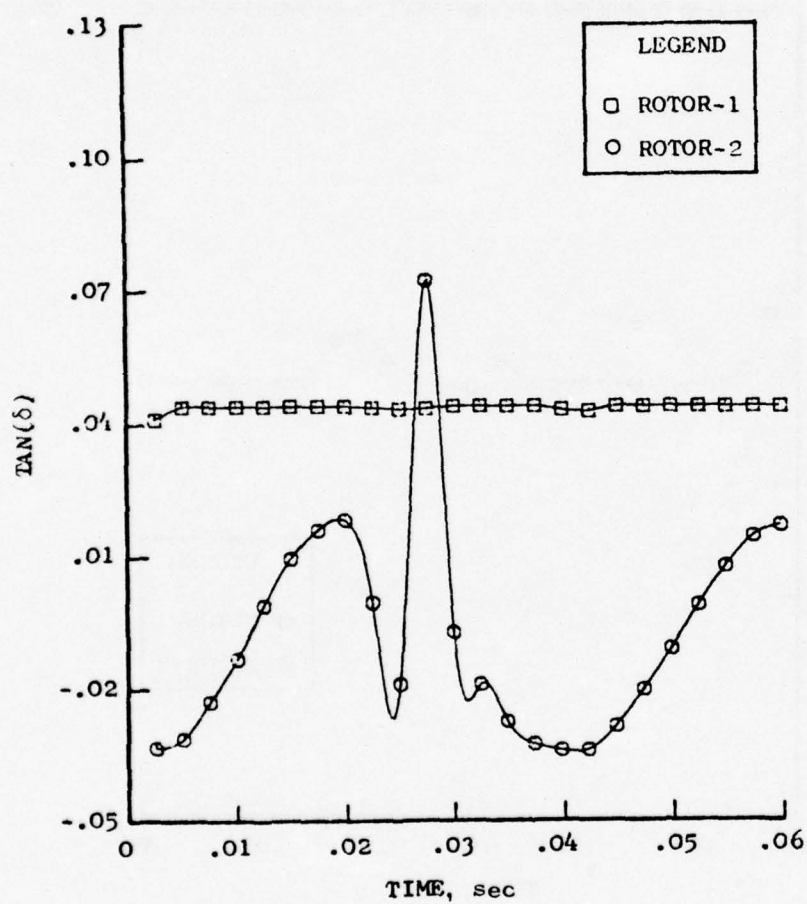


Figure 82. Tangent of Deviation Angle Vs. Time, 100% $N/\sqrt{\theta}$, 25 Hz.

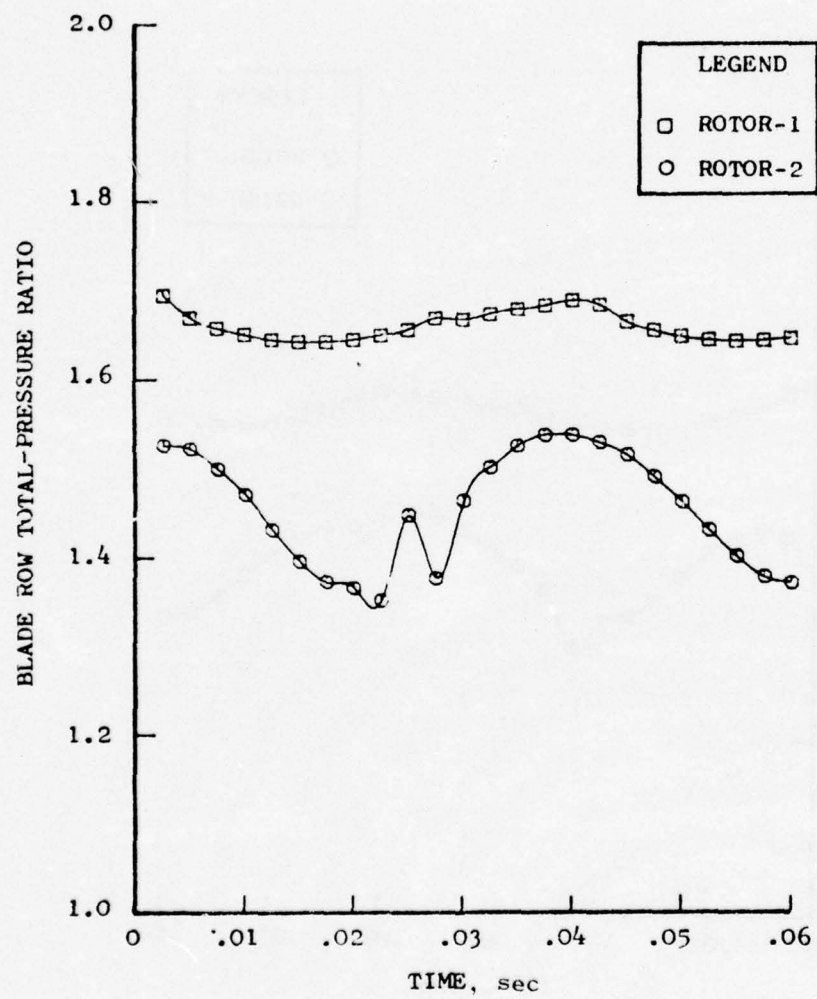


Figure 83. Blade Row Total-Pressure Ratio Vs. Time, 100% $N/\sqrt{\theta}$, 25 Hz.

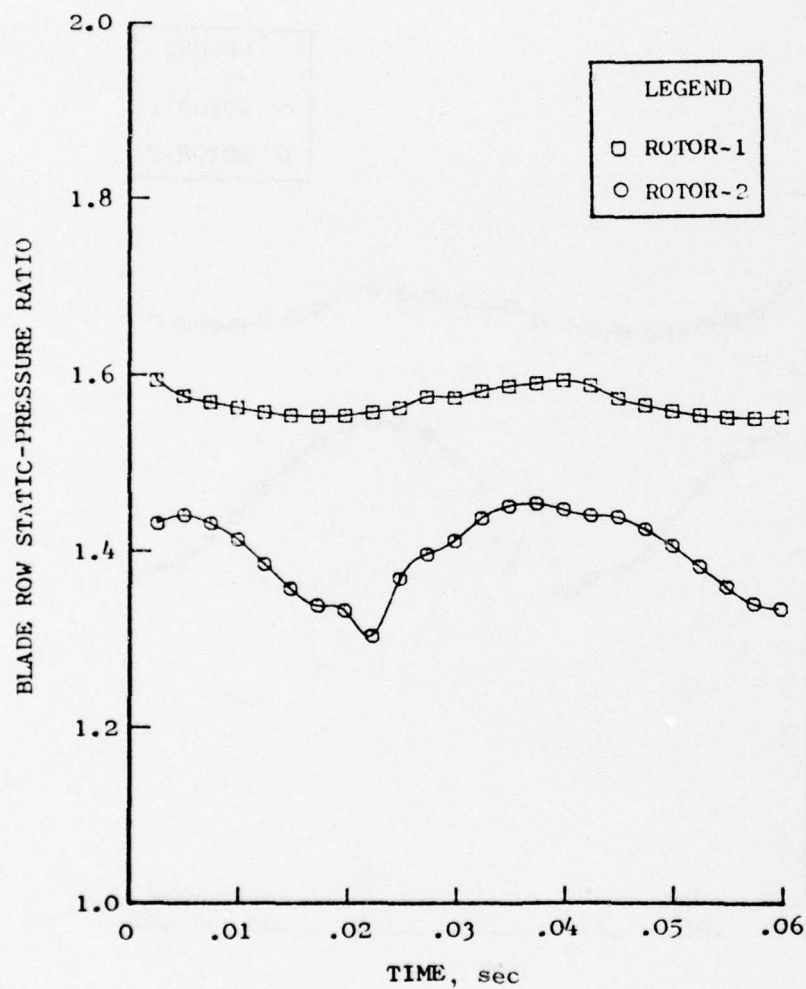


Figure 84. Blade Row Static-Pressure Ratio Vs. Time, 100% $N/\sqrt{\theta}$, 25 Hz.

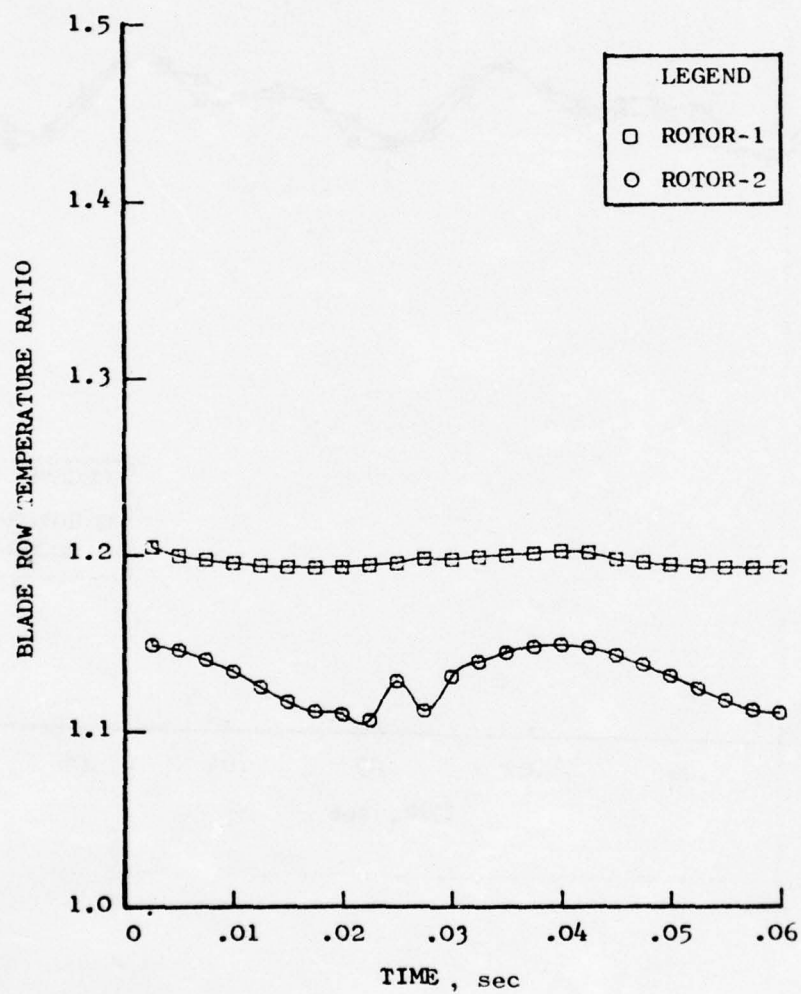


Figure 85. Blade Row Total-Temperature Ratio Vs. Time, 100% $N/\sqrt{\theta}$, 25 Hz.

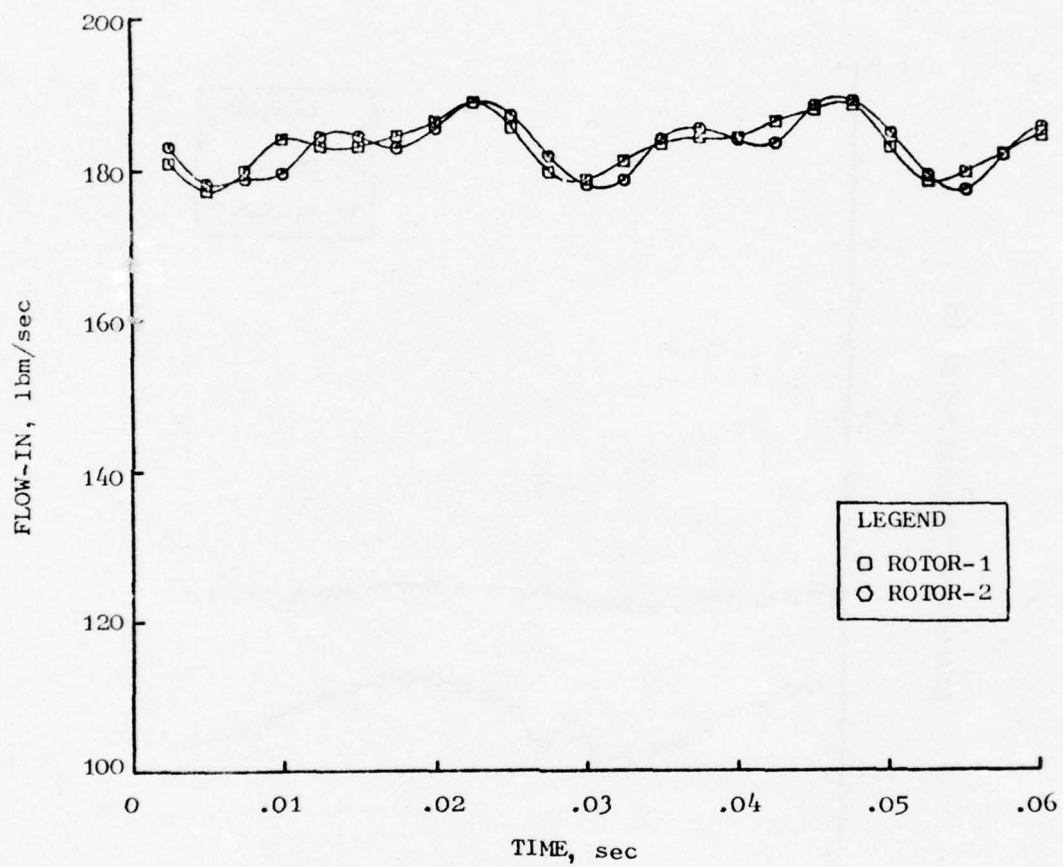


Figure 86. Physical Airflow Vs. Time, 100% $N/\sqrt{\theta}$, 42 Hz.

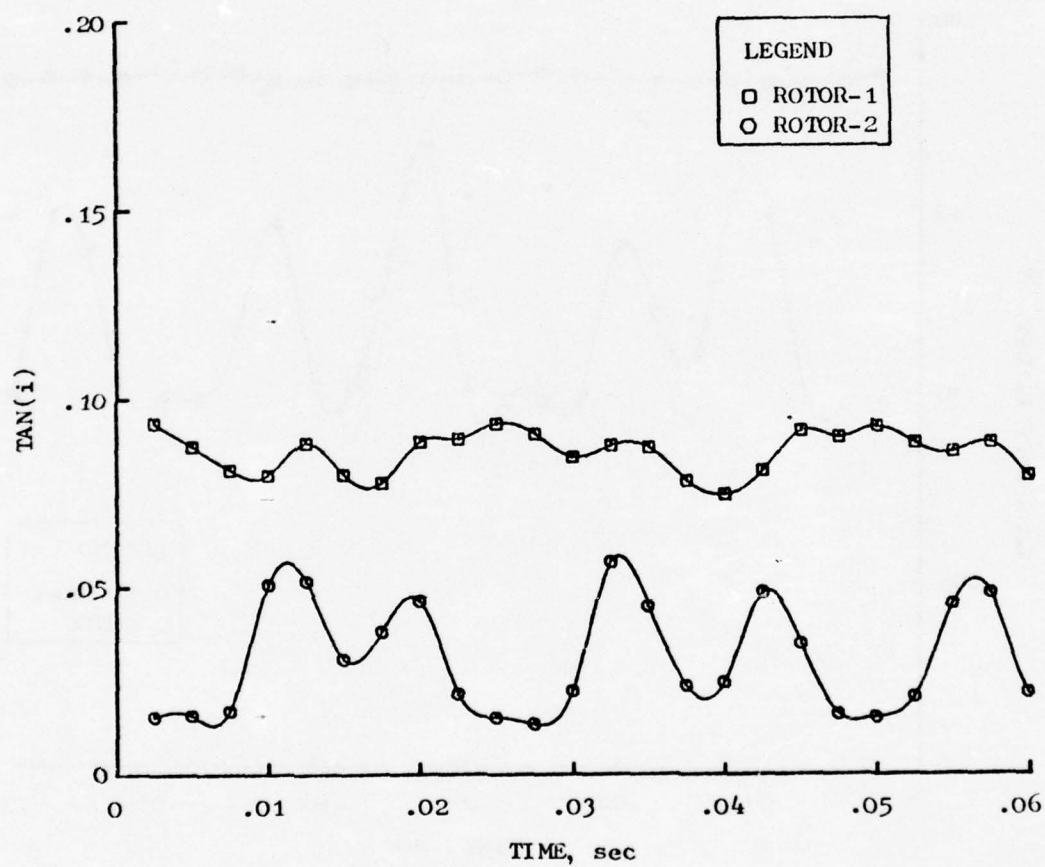


Figure 87. Tangent of Incidence Angle Vs. Time, 100% $N/\sqrt{\theta}$, 42 Hz.

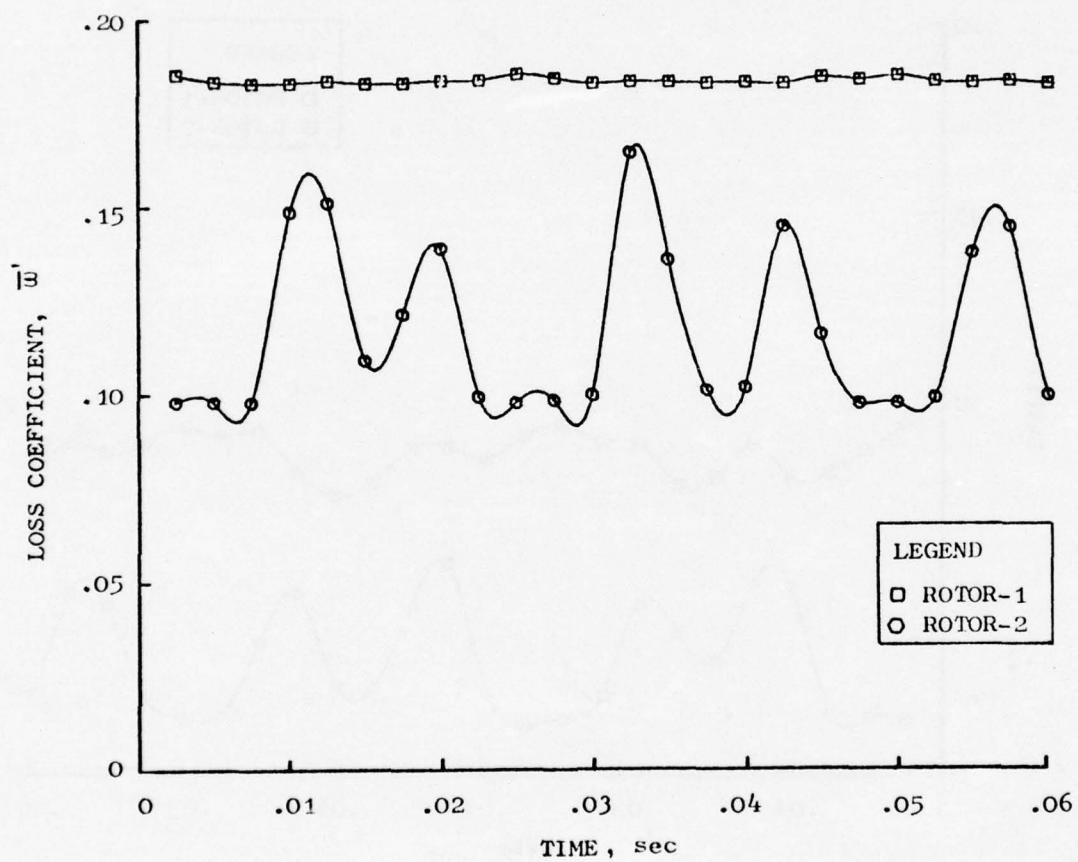


Figure 88. Loss Coefficient Vs. Time, 100% $N/\sqrt{\theta}$, 42 Hz.

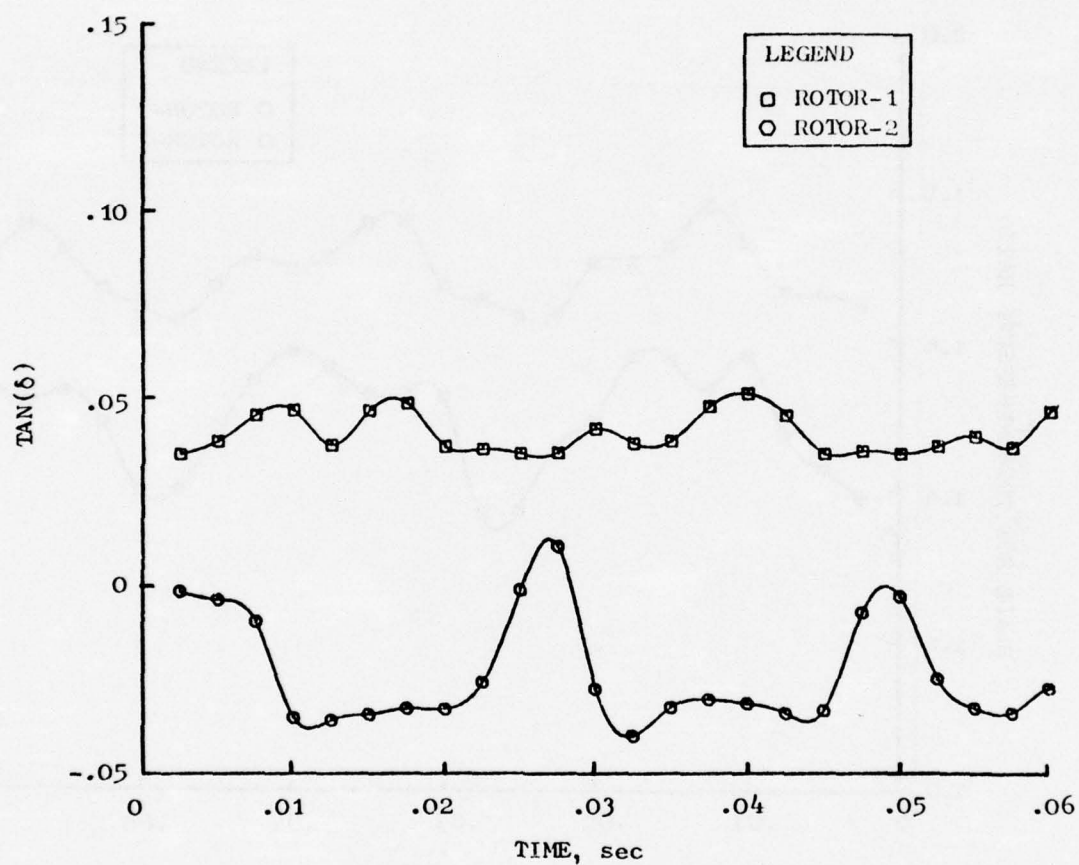


Figure 89. Tangent of Deviation Angle Vs. Time, 100% $N/\sqrt{\theta}$, 42 Hz.

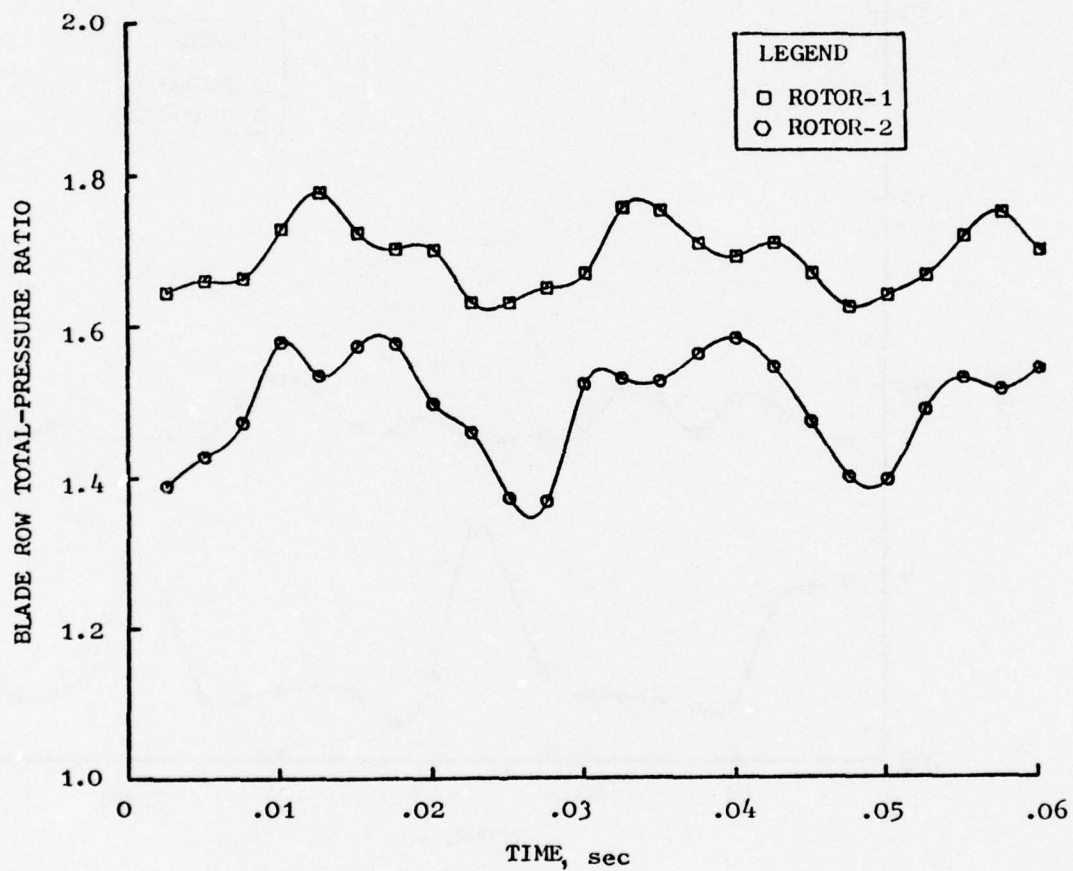


Figure 90. Blade Row Total-Pressure Ratio Vs. Time, 100% $N/\sqrt{\theta}$, 42 Hz.

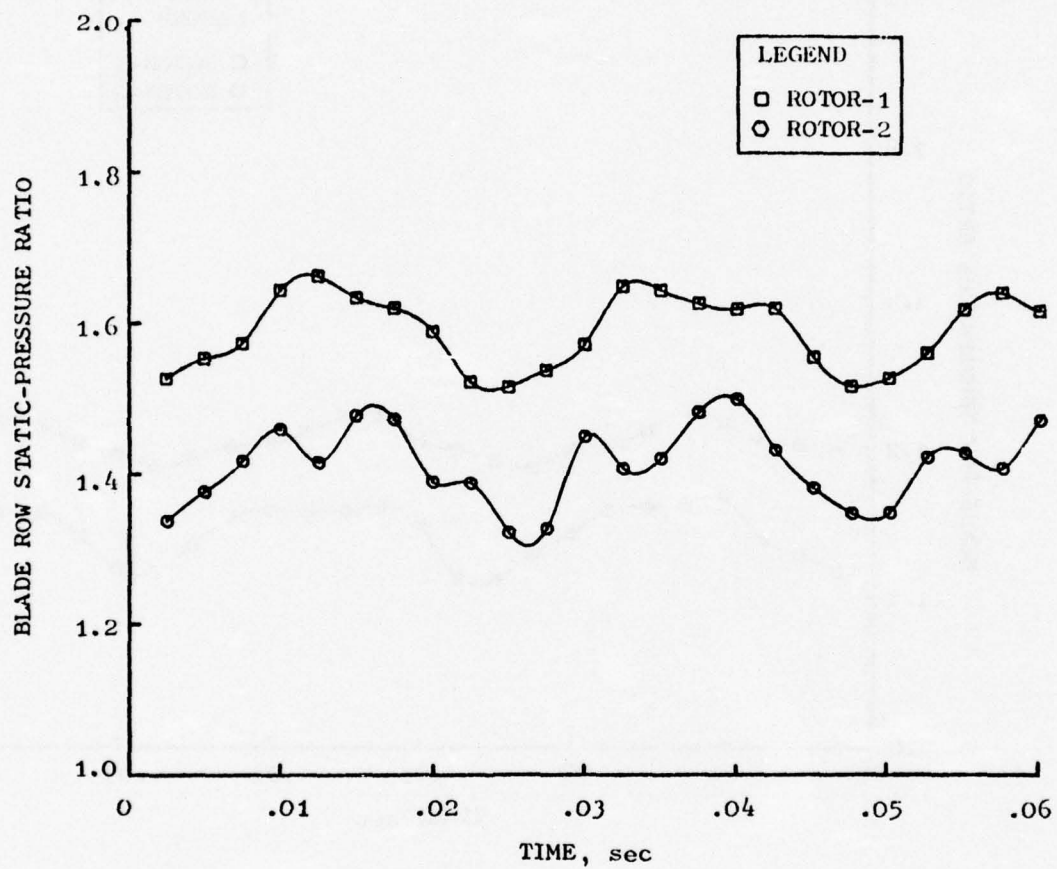


Figure 91. Blade Row Static-Pressure Ratio Vs. Time, 100% $N/\sqrt{\theta}$, 42 Hz.

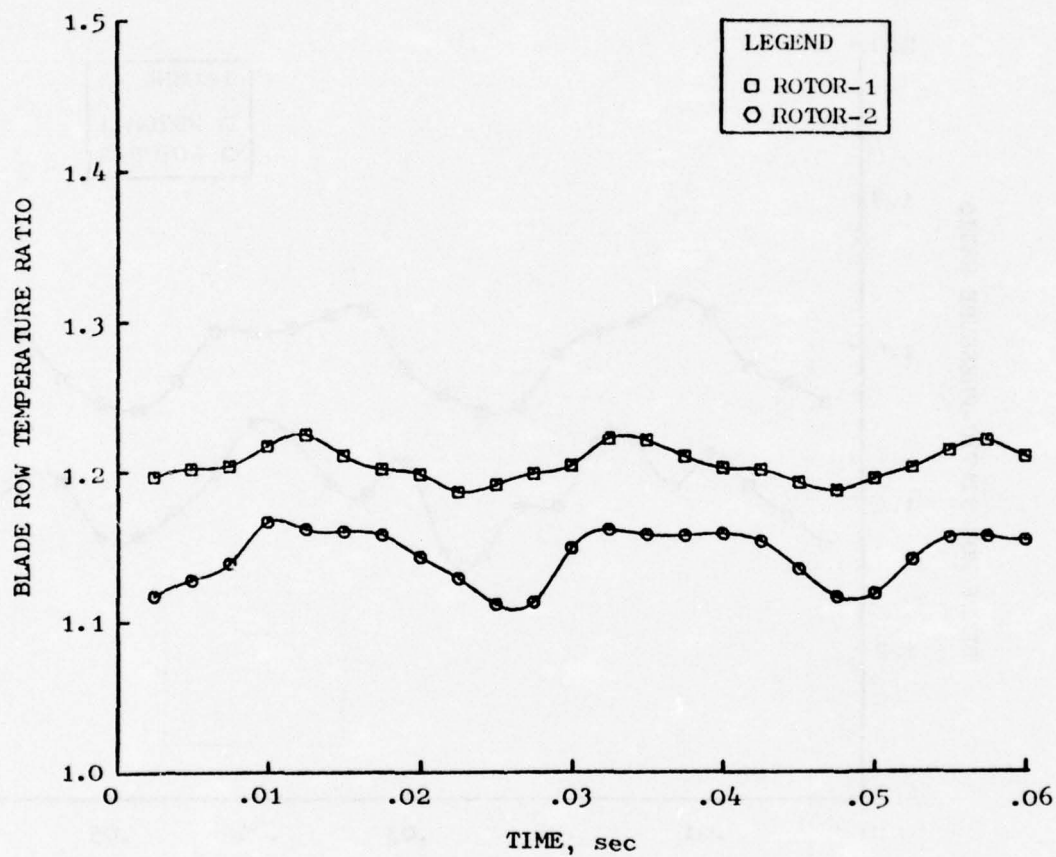


Figure 92. Blade Row Total-Temperature Ratio Vs. Time, 100% $N/\sqrt{\theta}$, 42 Hz.

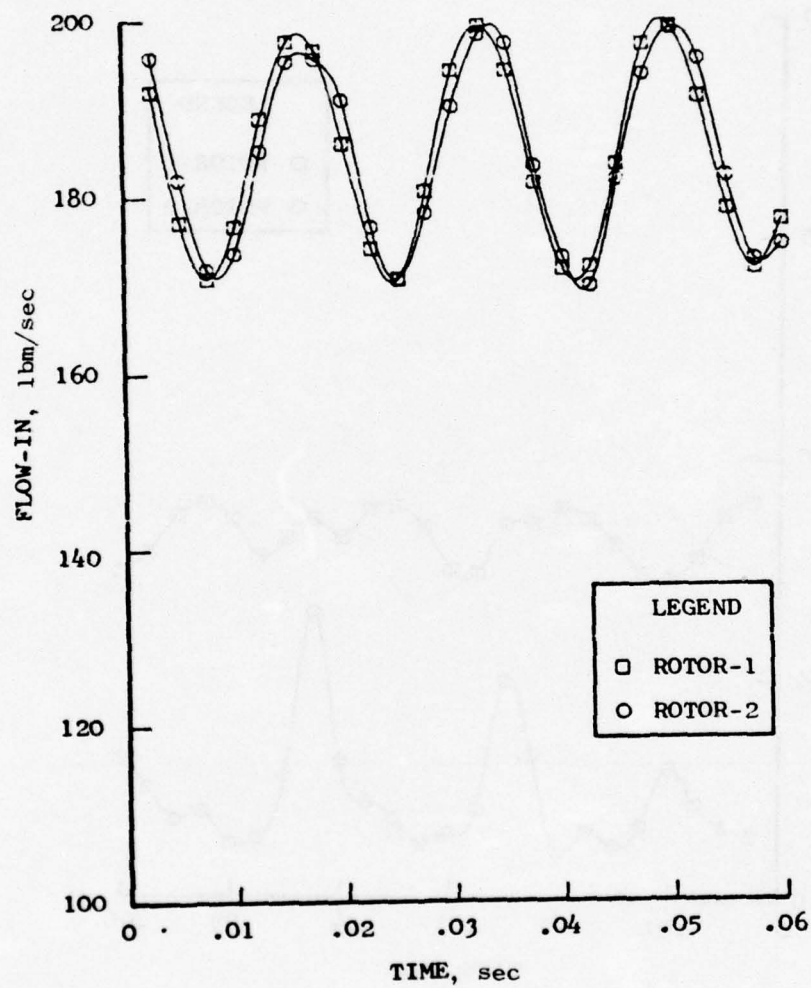


Figure 93. Physical Airflow Vs. Time, 100% $N/\sqrt{\theta}$, 60 Hz.

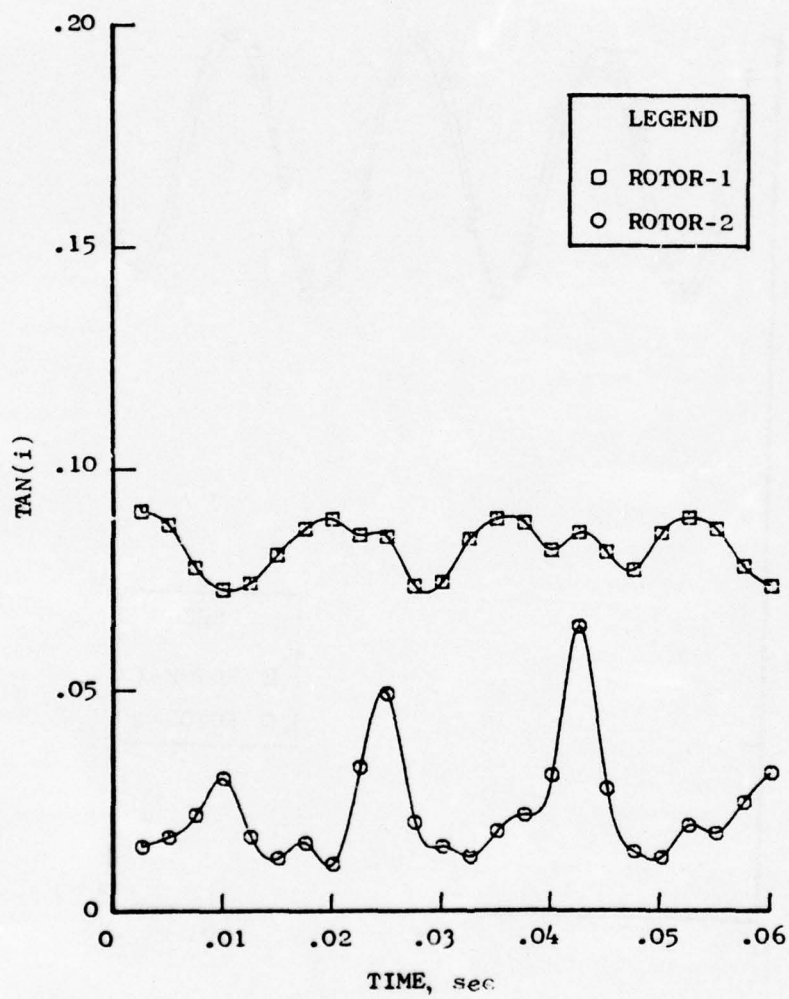


Figure 94. Tangent of Incidence Angle Vs. Time, $100 N/\sqrt{\theta}$, 60 Hz.

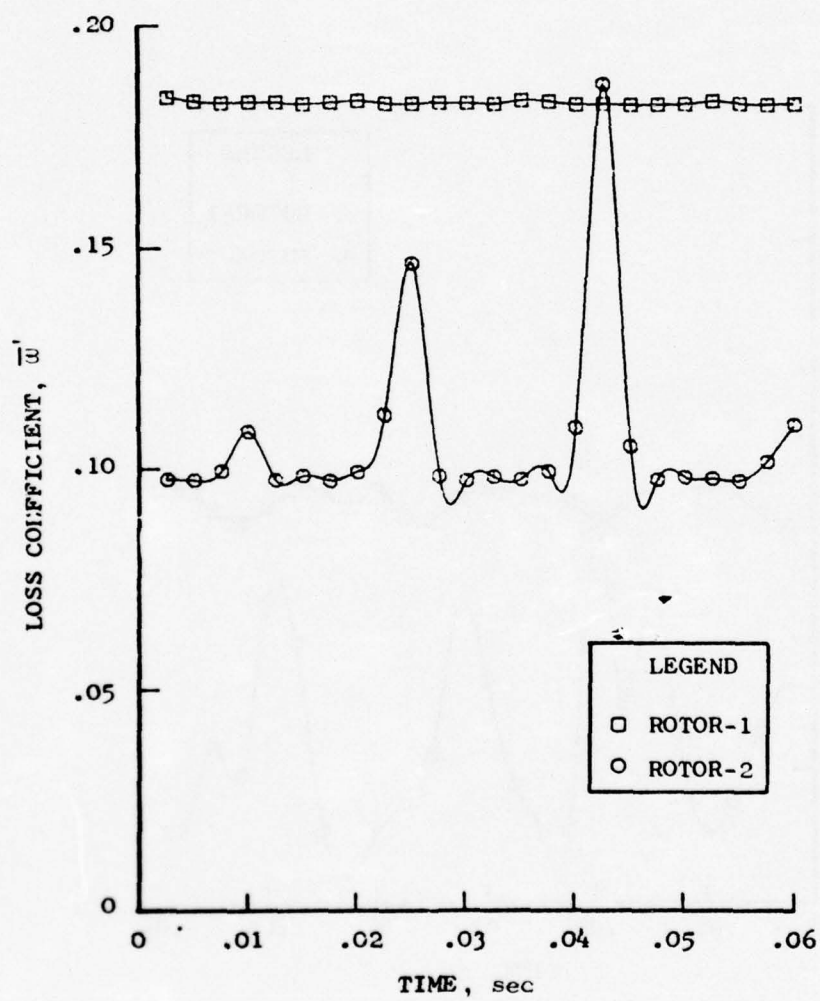


Figure 95. Loss Coefficient Vs. Time, 100% $N/\sqrt{\theta}$, 60 Hz.

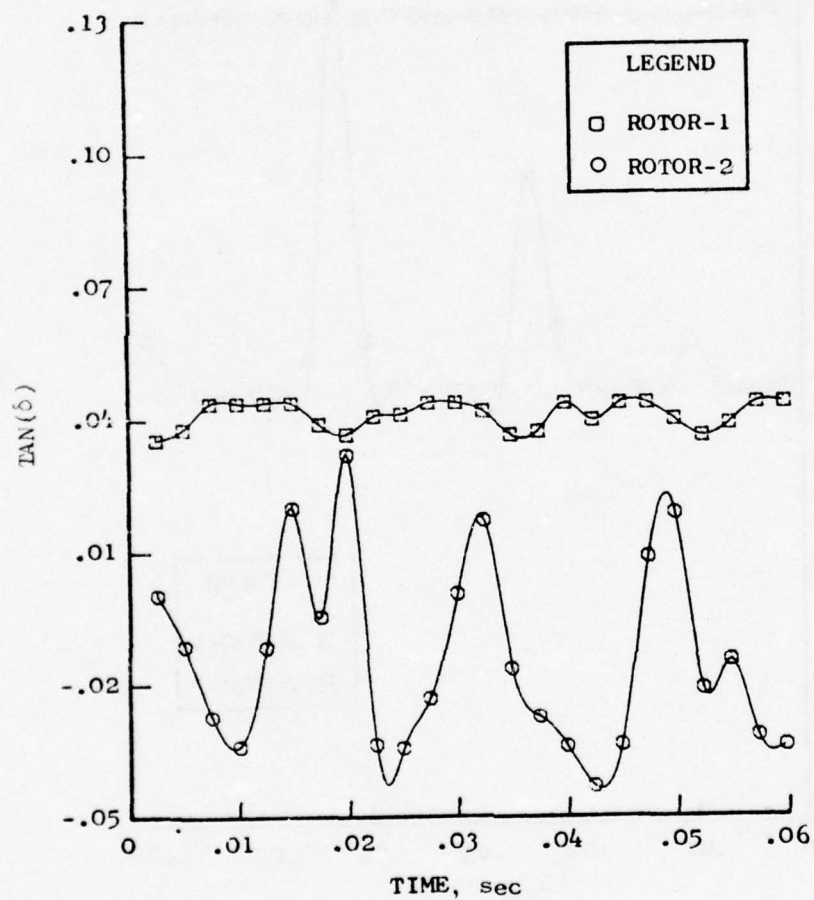


Figure 96. Tangent of Deviation Angle Vs. Time,
100% $N/\sqrt{\theta}$, 60 Hz.

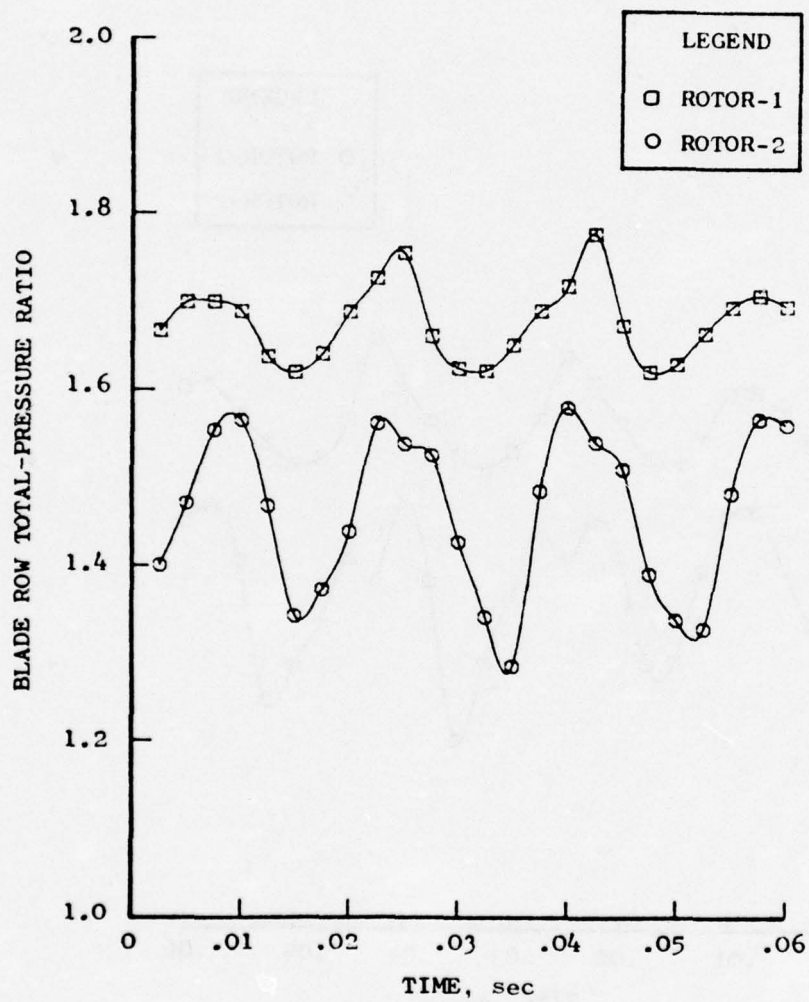


Figure 97. Blade Row Total-Pressure Ratio Vs. Time, 100% $N/\sqrt{\theta}$, 60 Hz.

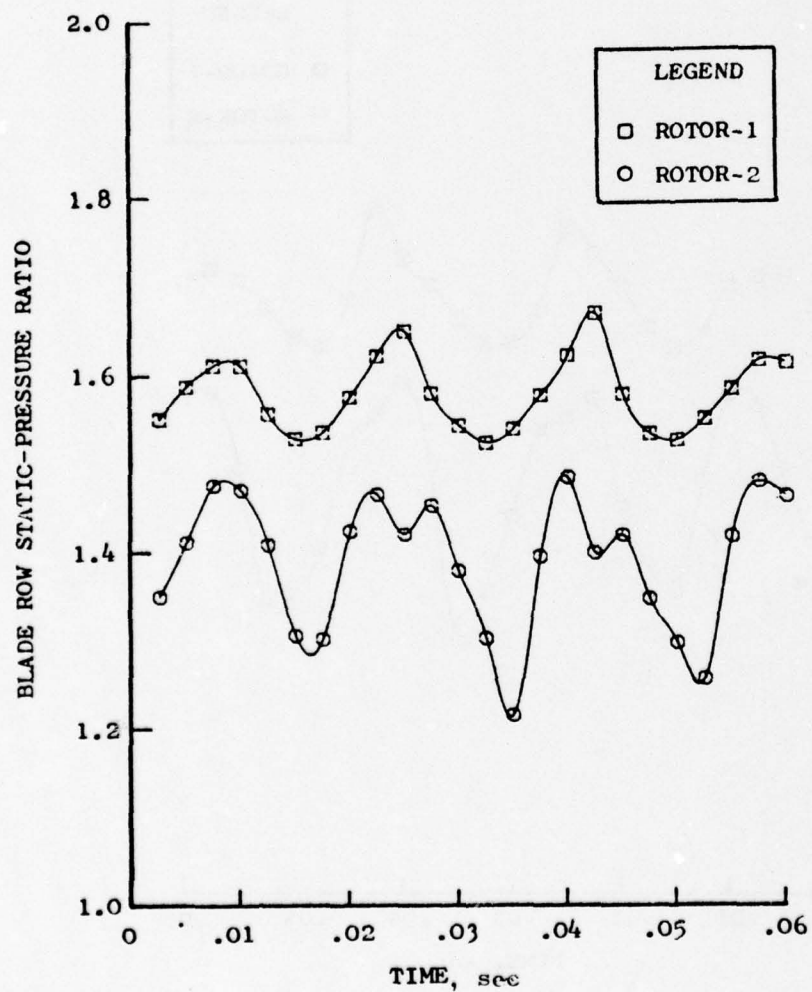


Figure 98. Blade Row Static-Pressure Ratio Vs. Time,
100% $N/\sqrt{\theta}$, 60 Hz.

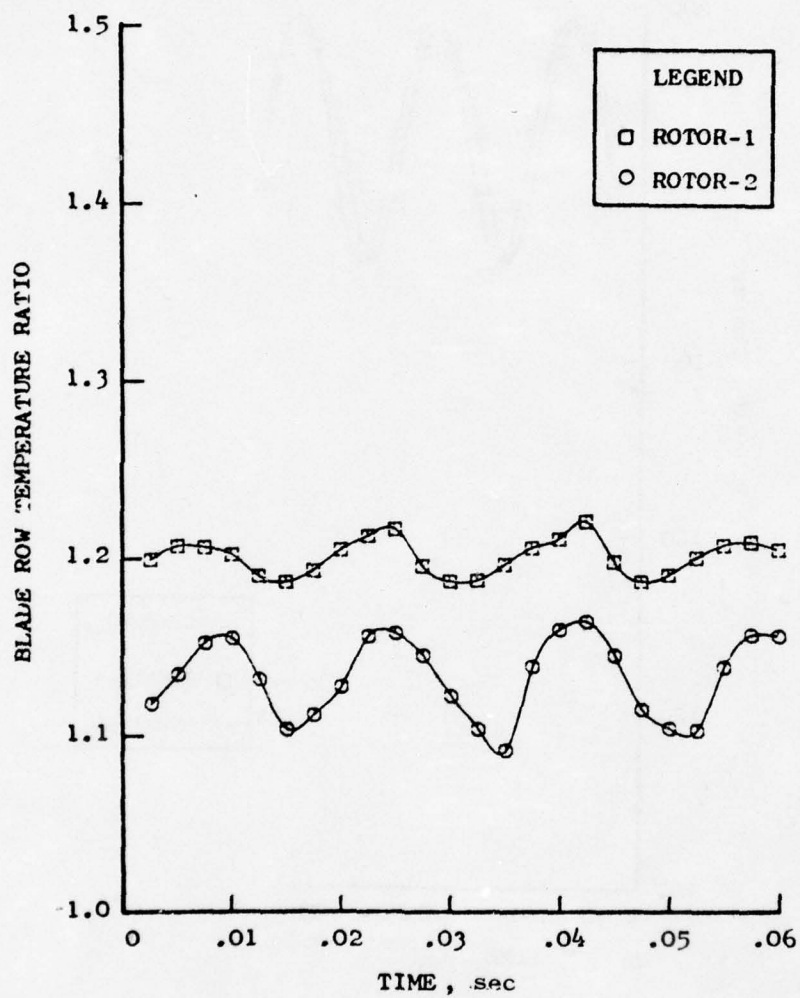


Figure 99. Blade Row Total-Temperature Ratio Vs. Time, 100% $N/\sqrt{\theta}$, 60 Hz.

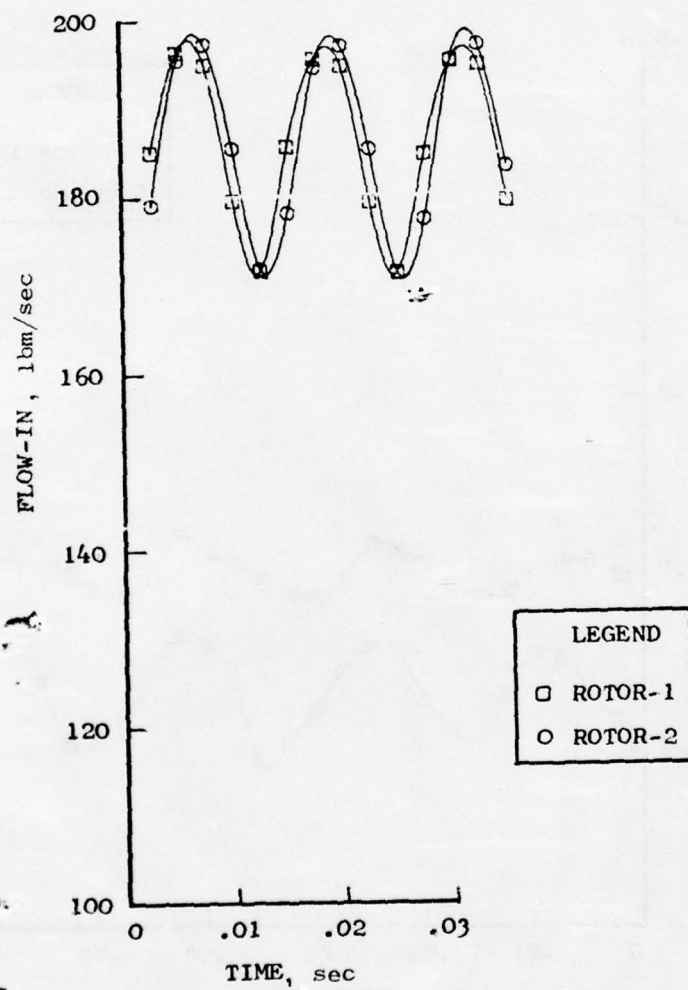


Figure 100. Physical Airflow Vs. Time,
100% $N/\sqrt{\theta}$, 80 Hz.

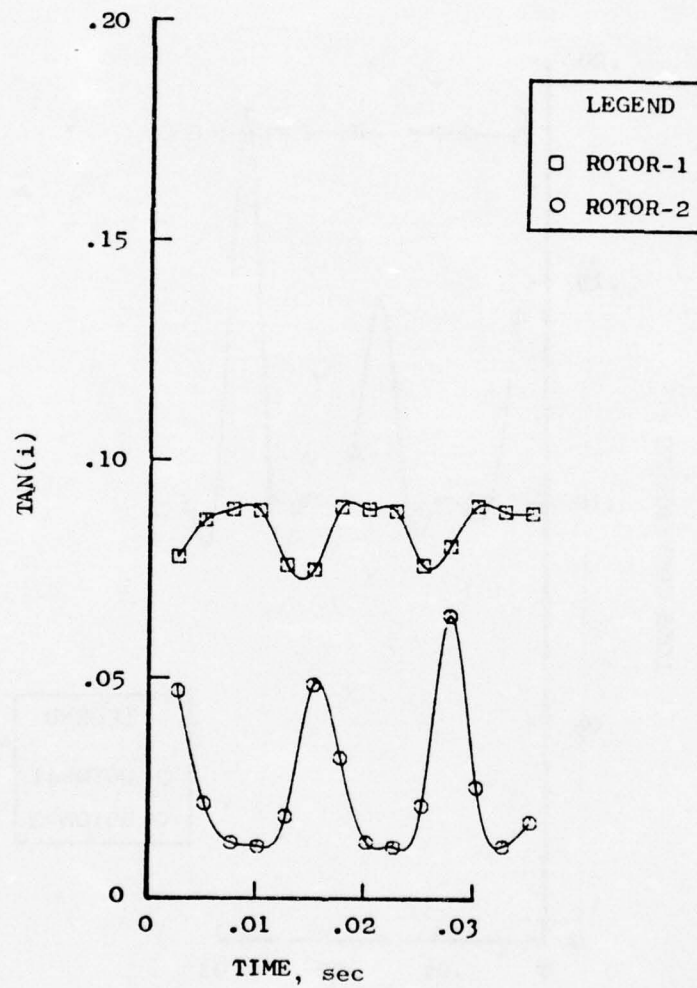


Figure 101. Tangent of Incidence Angle
Vs. Time, 100% $N/\sqrt{\theta}$, 80 Hz.

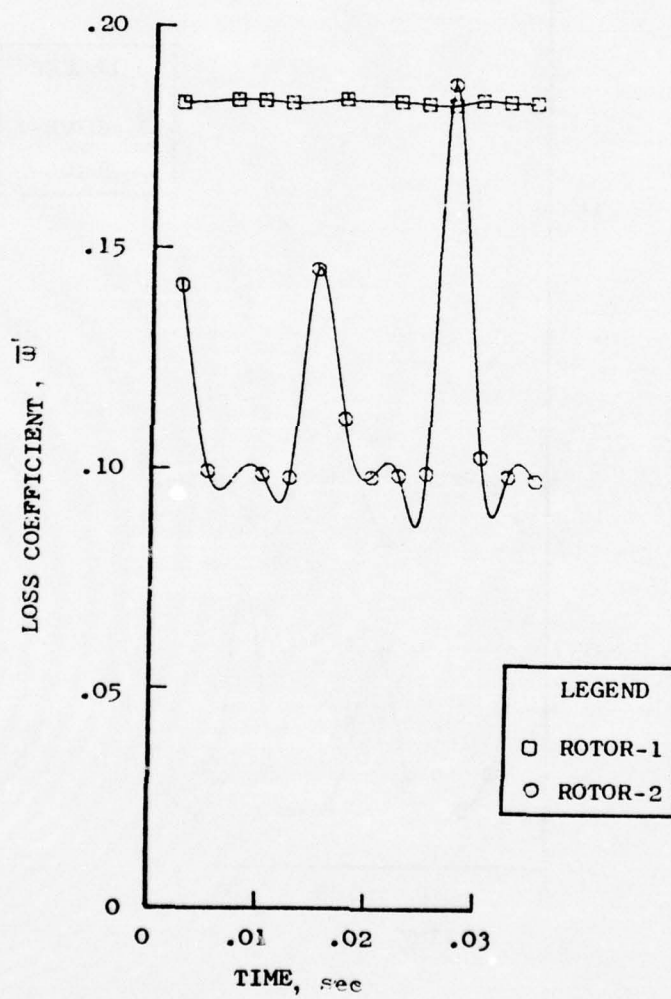


Figure 102. Loss Coefficient Vs. Time,
100% $N/\sqrt{\theta}$, 80 Hz.

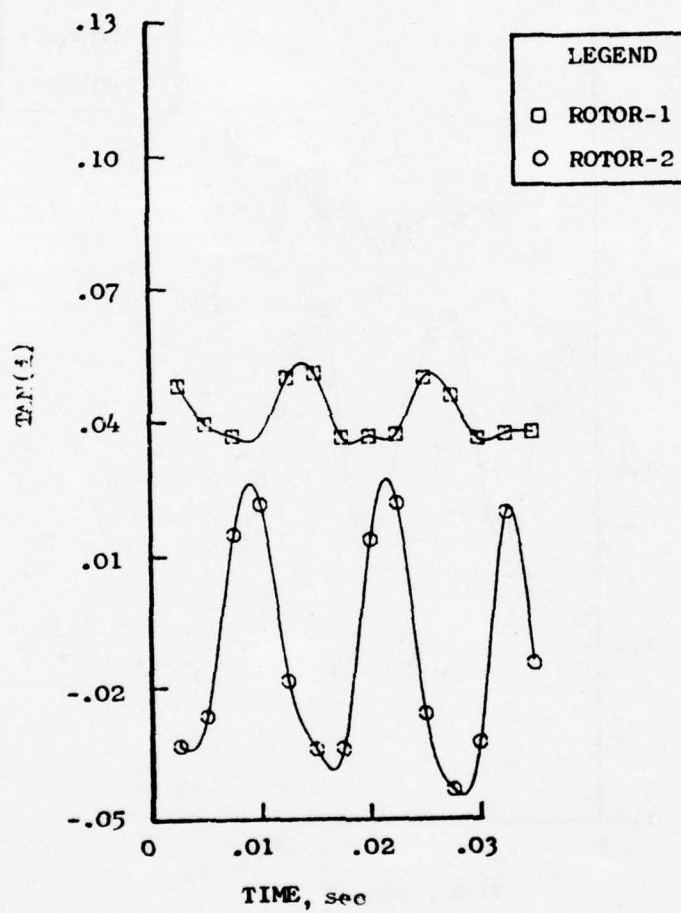


Figure 103. Tangent of Deviation Angle,
Vs. Time, 100% $N/\sqrt{\theta}$, 80 Hz.

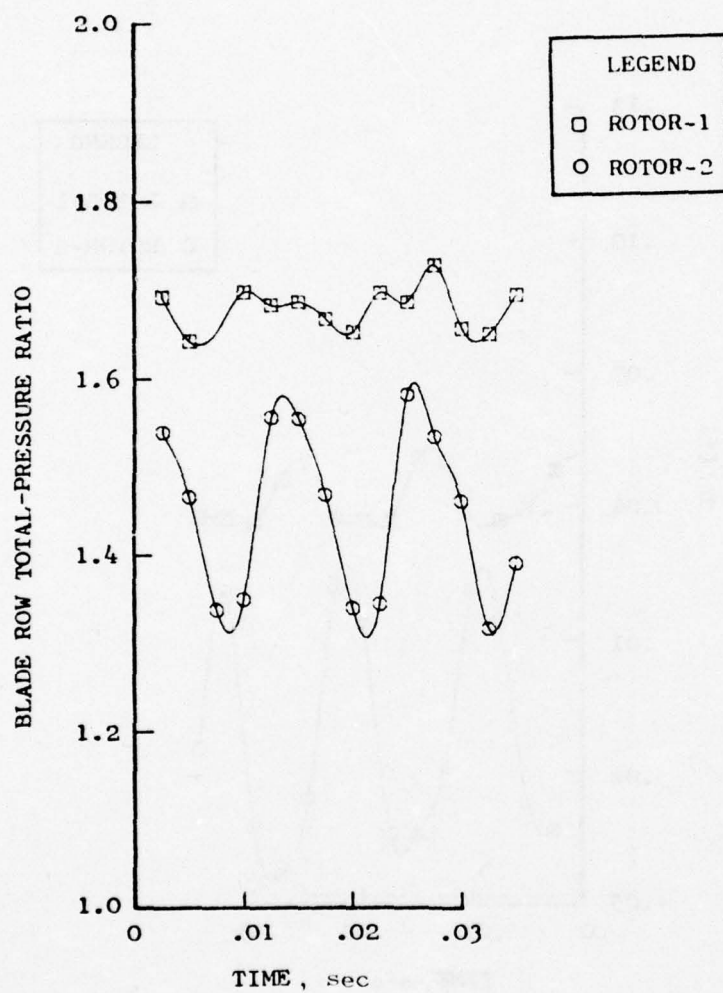


Figure 104. Blade Row Total-Pressure Ratio,
Vs. Time, 100% $N/\sqrt{\theta}$, 80 Hz.

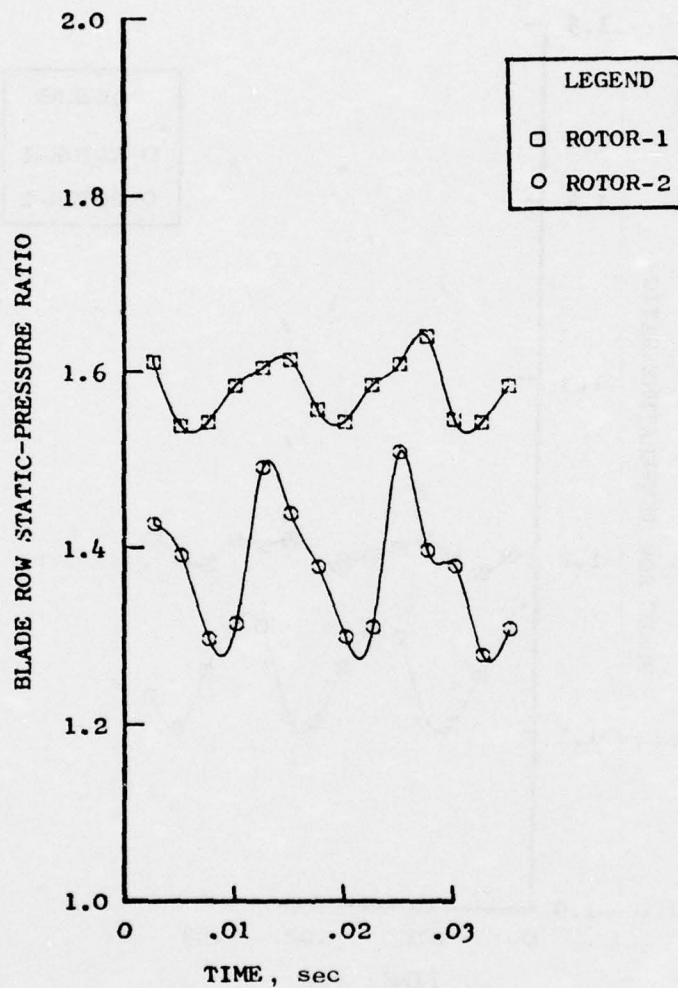


Figure 105. Blade Row Static-Pressure Ratio
Vs. Time, 100% $N/\sqrt{\theta}$, 80 Hz.

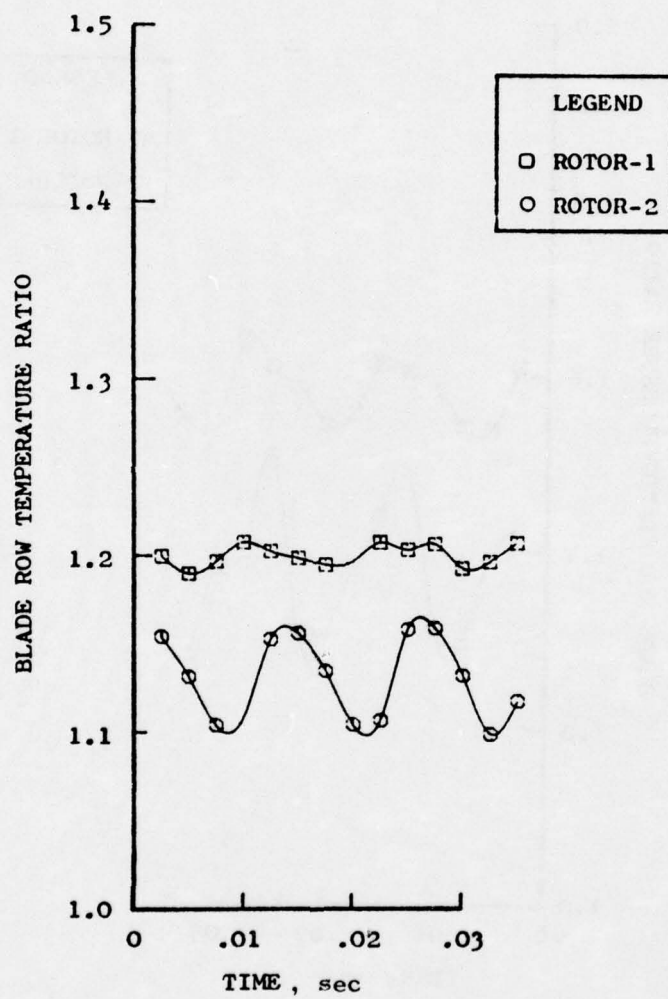


Figure 106. Blade Row Total-Temperature Ratio Vs. Time, 100% $N/\sqrt{\theta}$, 80 Hz.

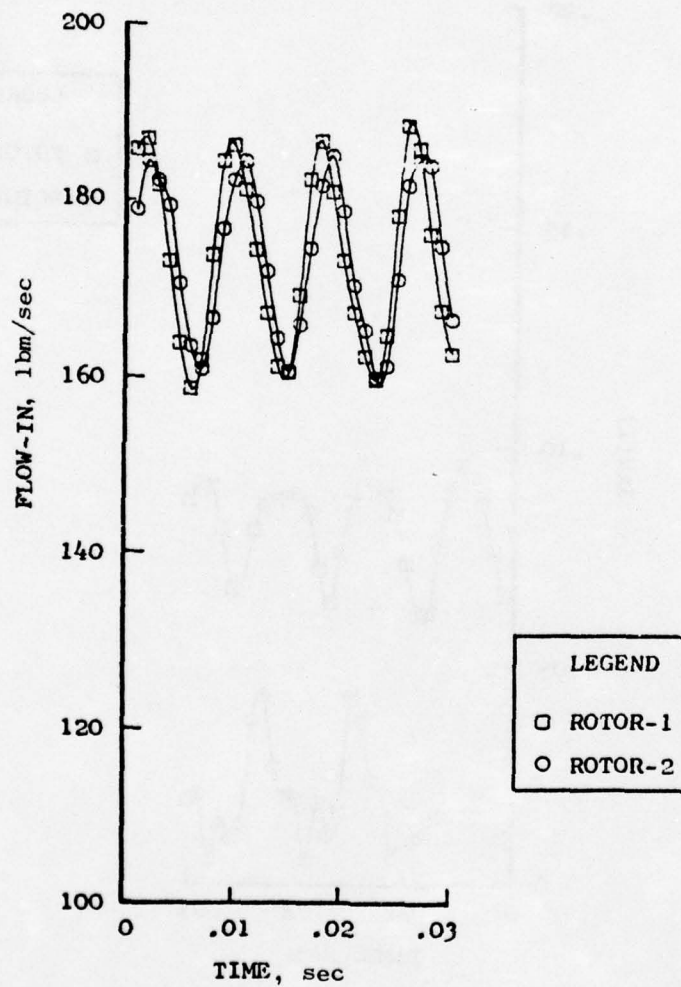


Figure 107. Physical Airflow Vs. Time,
100% $N/\sqrt{\theta}$, 118 Hz.

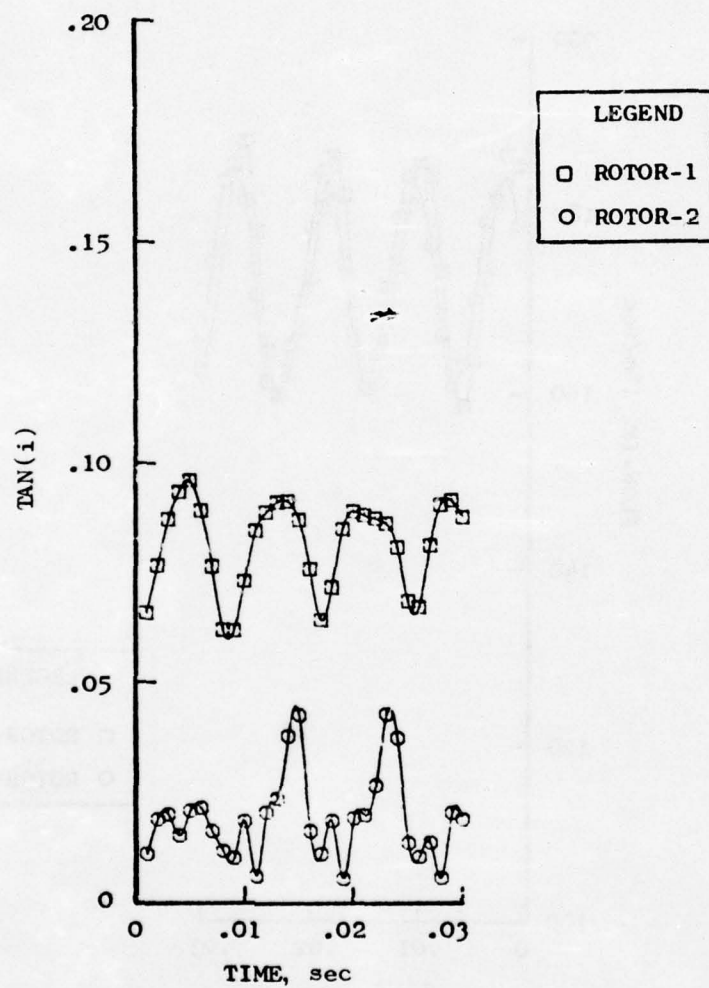


Figure 108. Tangent of Incidence Angle Vs. Time, 100% $N/\sqrt{\theta}$, 118 Hz.

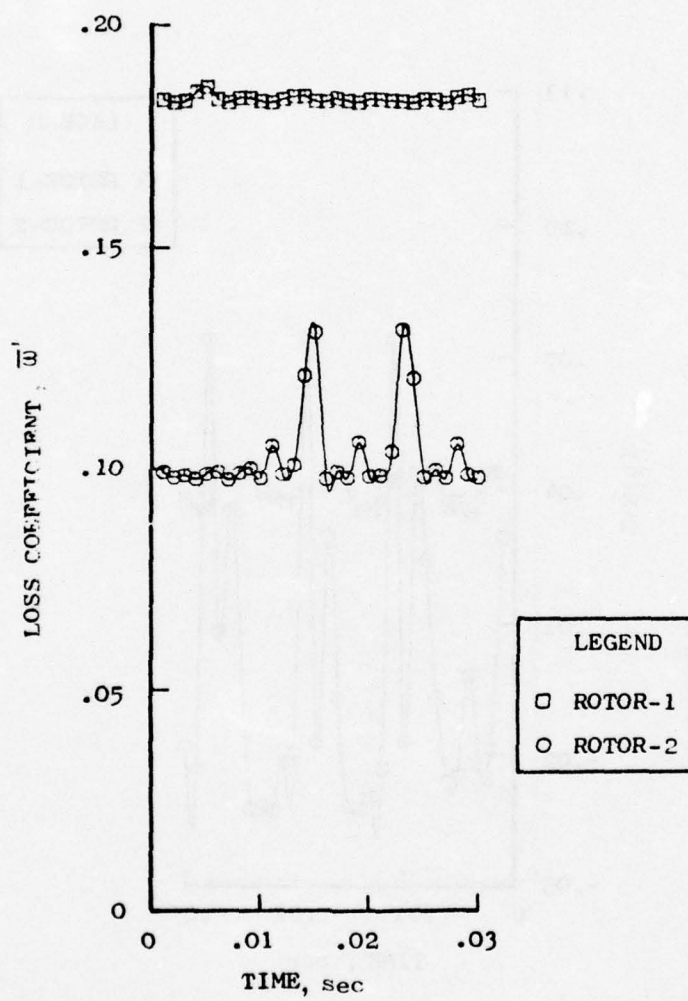


Figure 109. Loss Coefficient Vs. Time,
100% $N/\sqrt{\theta}$, 118 Hz.

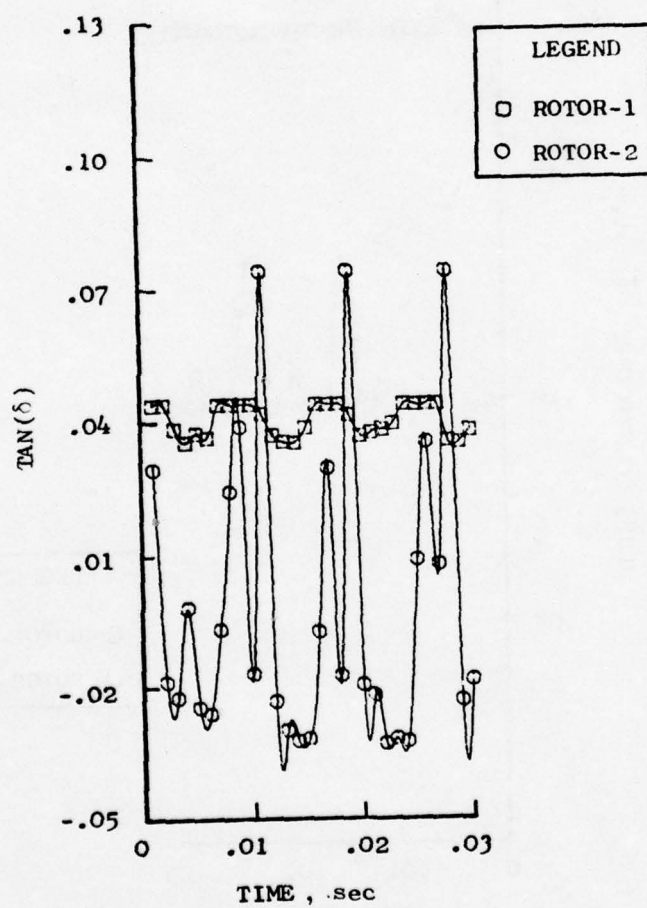


Figure 110. Tangent of Deviation Angle Vs. Time, 100% $N/\sqrt{\theta}$, 118 Hz.

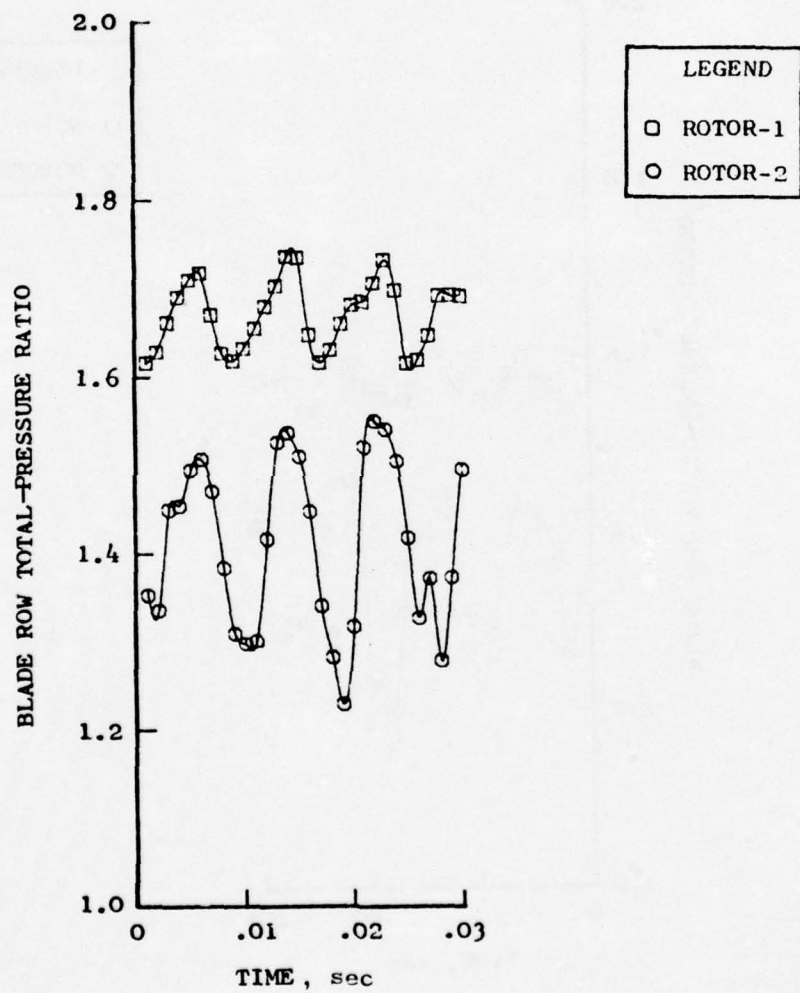


Figure 111. Blade Row Total-Pressure Ratio
Vs. Time, 100% $N/\sqrt{\theta}$, 118 Hz.

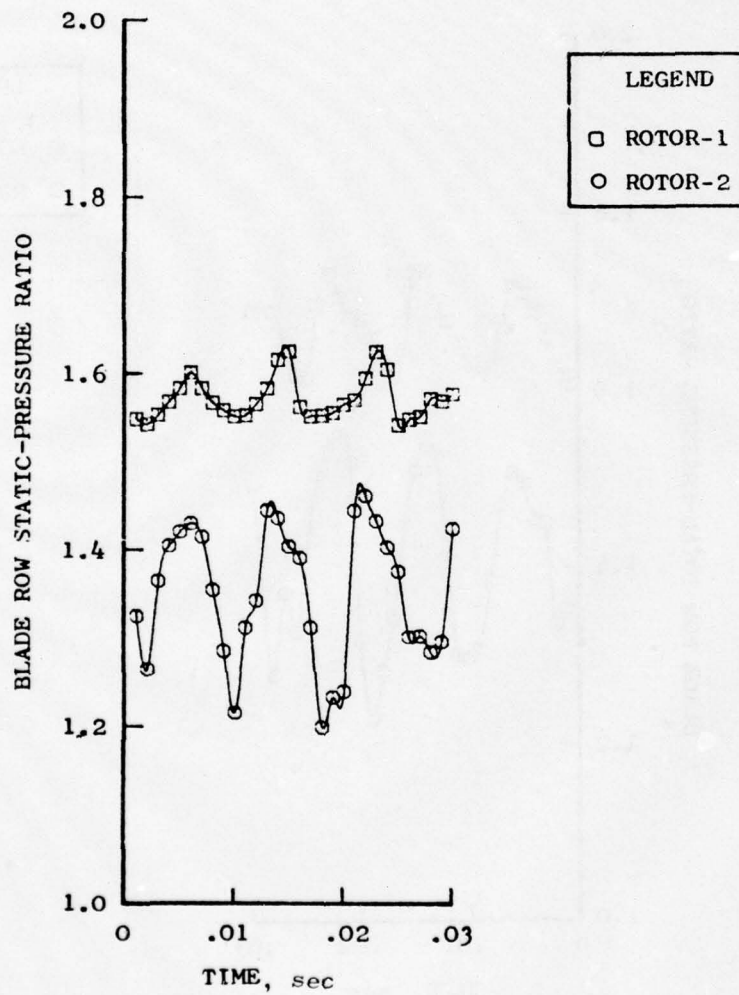


Figure 112. Blade Row Static-Pressure Ratio Vs. Time, 100% $N/\sqrt{\theta}$, 118 Hz.

AD-A032 079

GENERAL ELECTRIC CO CINCINNATI OHIO AIRCRAFT ENGINE GROUP F/G 1/3
DYNAMIC DIGITAL BLADE ROW COMPRESSION COMPONENT STABILITY MODEL--ETC(U)
AUG 76 G G REYNOLDS, W G STEENKEN F33615-75-C-2029
R76AEG299 AFAPL-TR-76-76 NL

UNCLASSIFIED

3 of 4
ADA032079



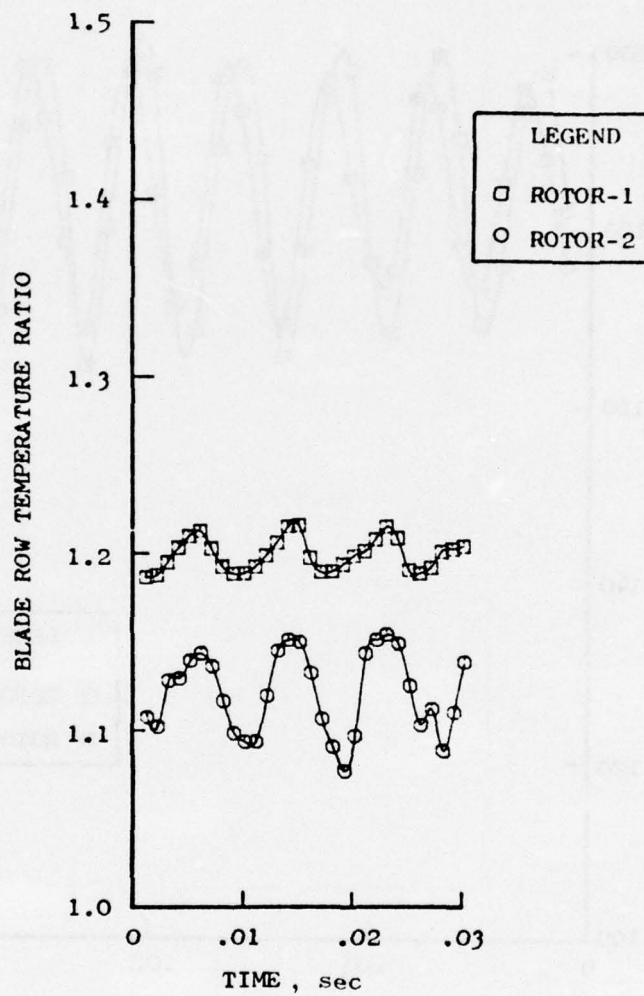


Figure 113. Blade Row Total-Temperature Ratio Vs. Time, 100% $N/\sqrt{\theta}$, 118 Hz.

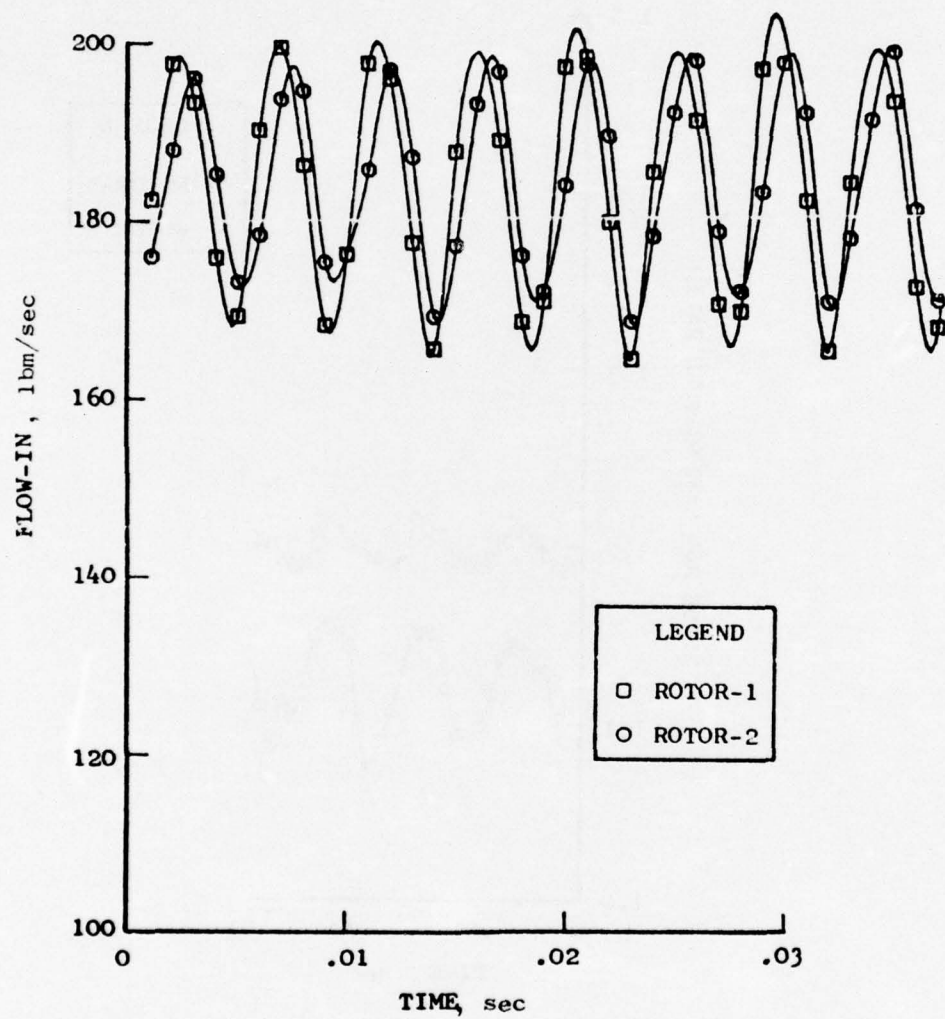


Figure 114. Physical Airflow Vs. Time, 100% $N/\sqrt{\theta}$, 220 Hz.

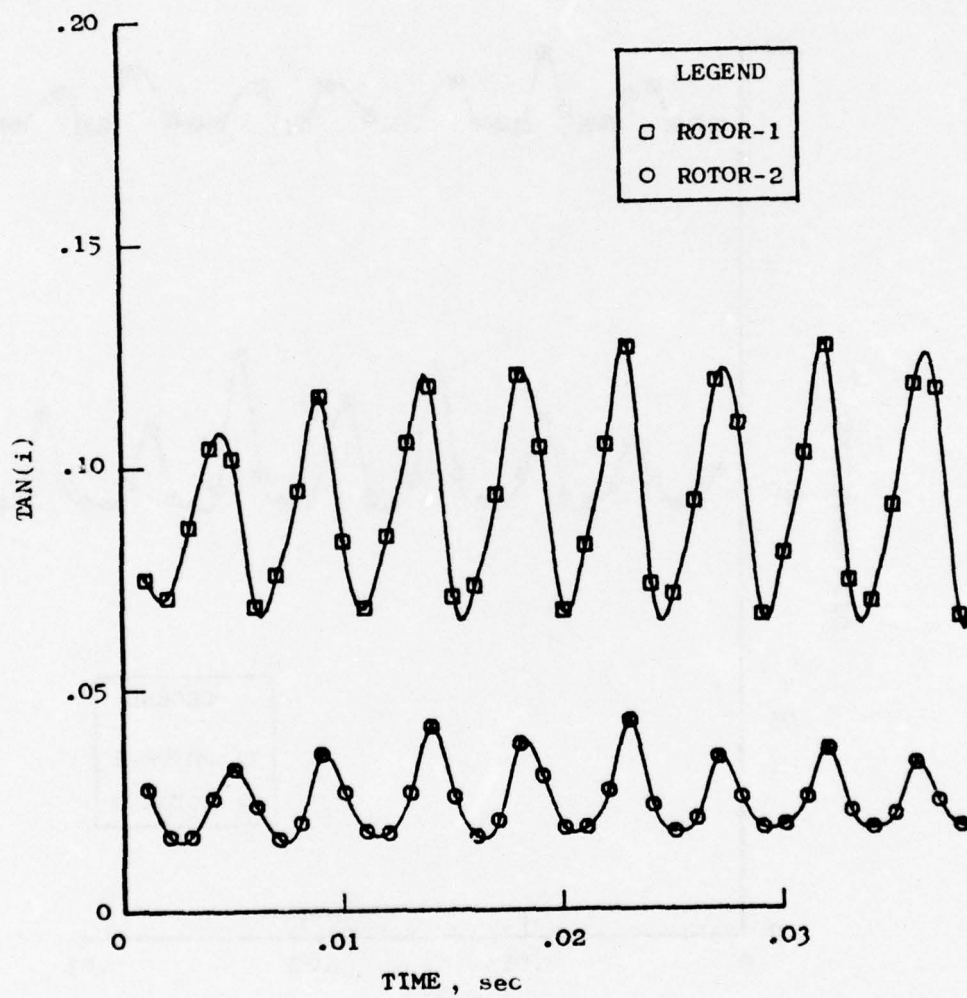


Figure 115. Tangent of Incidence Angle Vs. Time, 100% $N/\sqrt{\theta}$, 220 Hz.

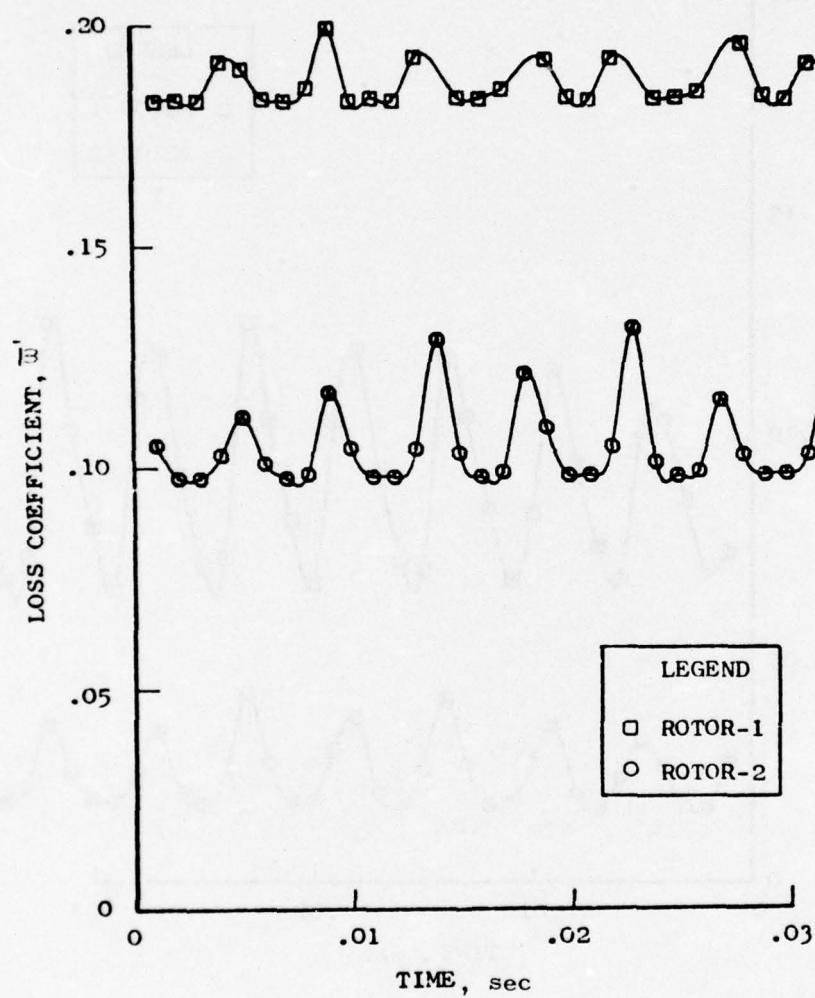


Figure 116. Loss Coefficient Vs. Time, $100\% N/\sqrt{\theta}$, 220 Hz.

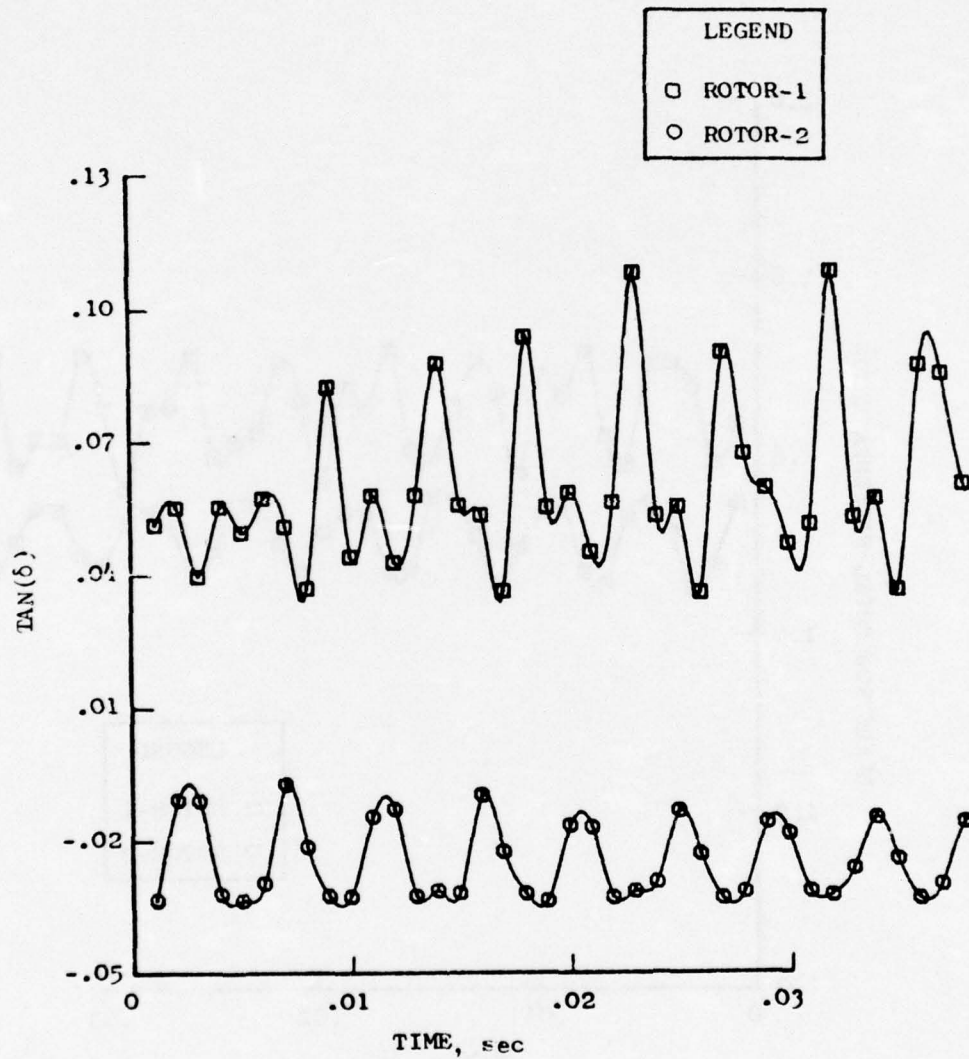


Figure 117. Tangent of Deviation Angle Vs. Time, 100% $N/\sqrt{\theta}$, 220 Hz.

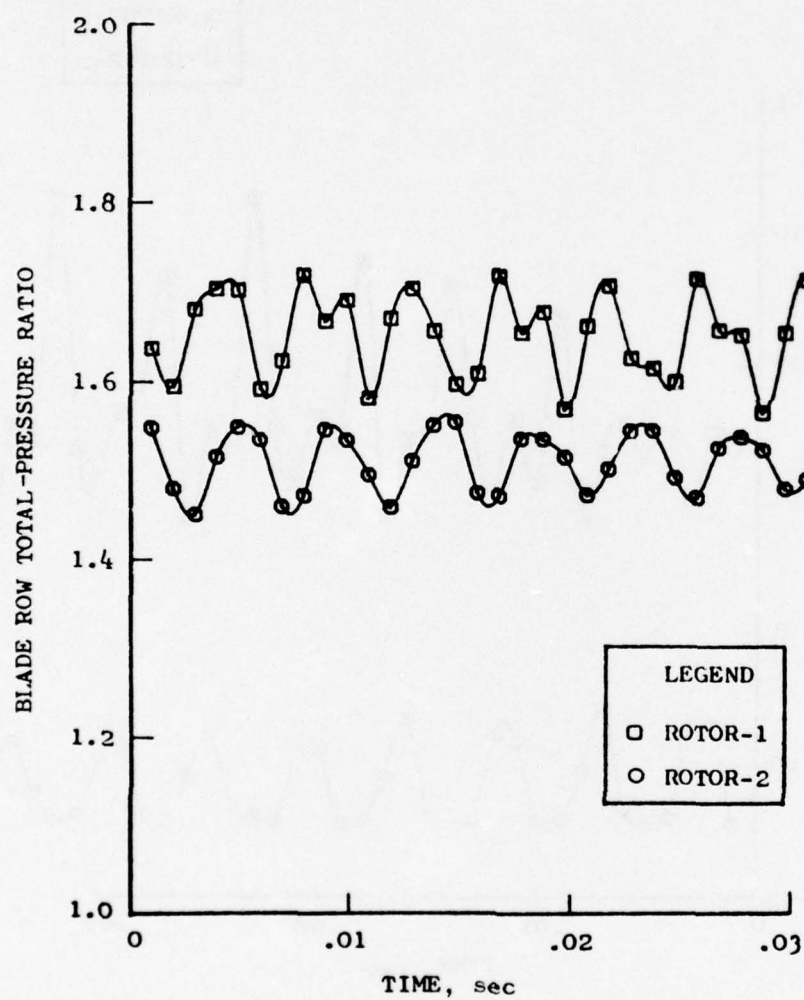


Figure 118. Blade Row Total-Pressure Ratio Vs. Time, 100% $N/\sqrt{\theta}$, 220 Hz.

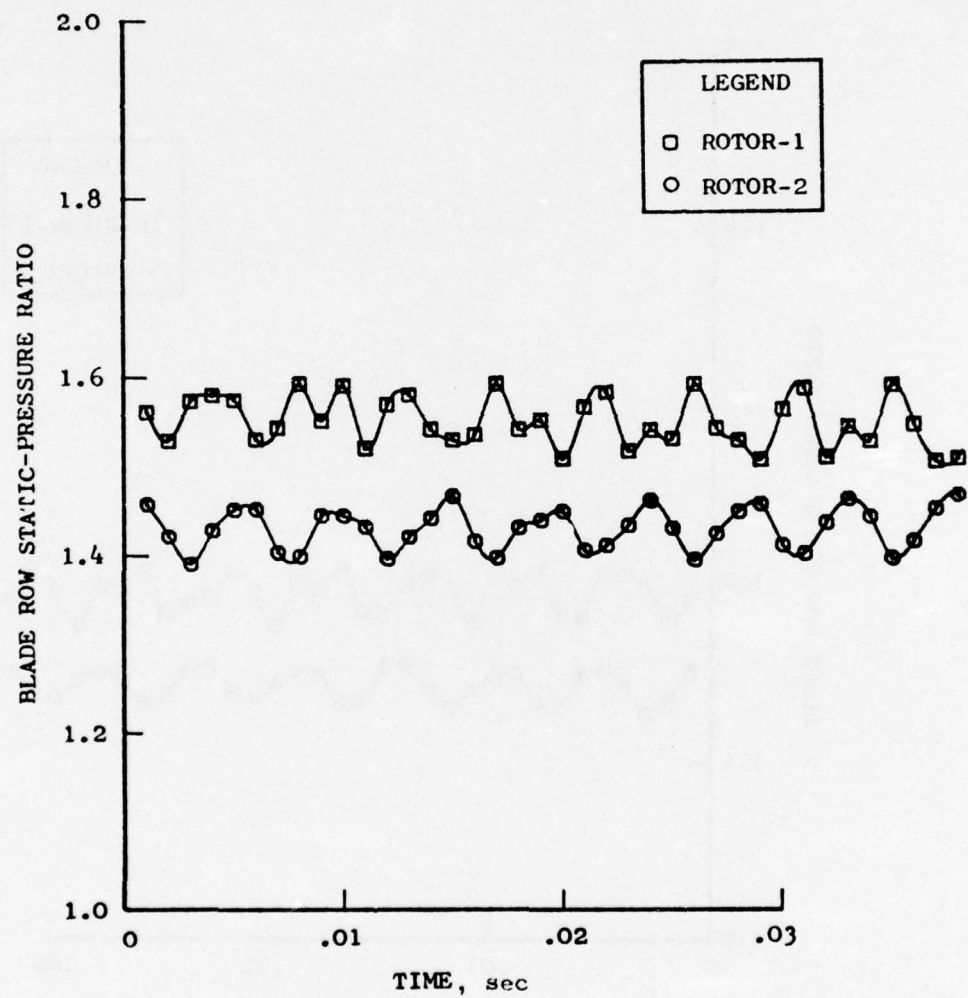


Figure 119. Blade Row Static-Pressure Ratio Vs. Time, 100% $N/\sqrt{\theta}$, 220 Hz.

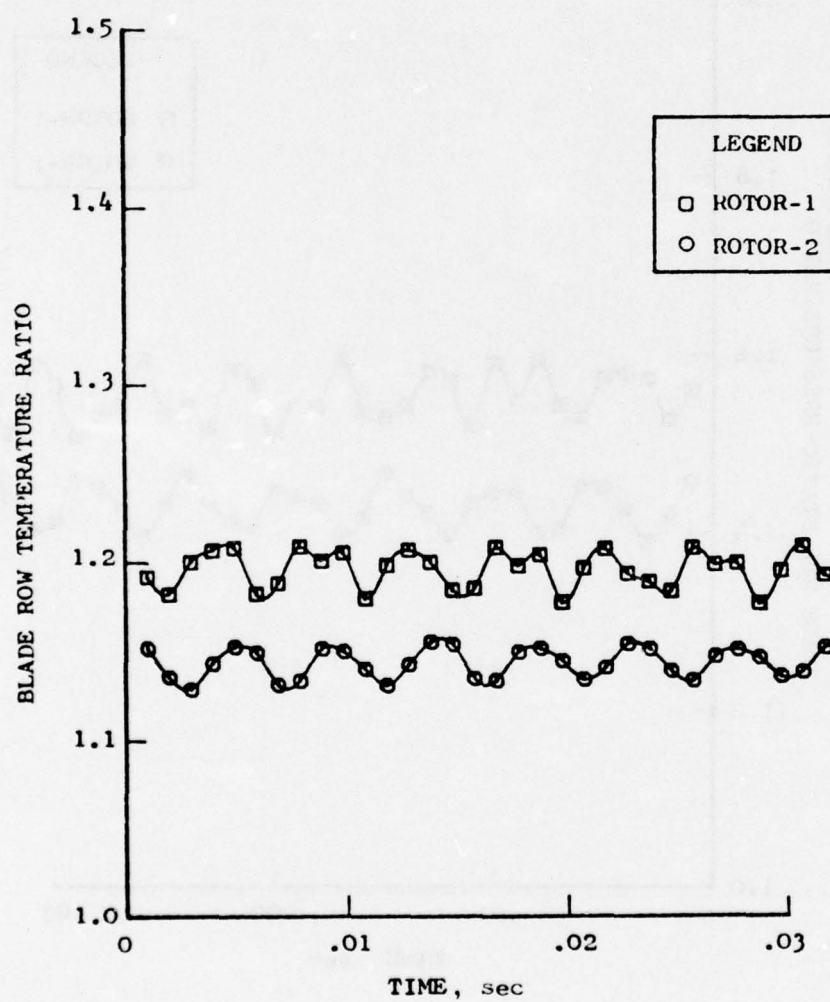


Figure 120. Blade Row Total-Temperature Ratio Vs. Time, 100% $N/\sqrt{\theta}$, 220 Hz.

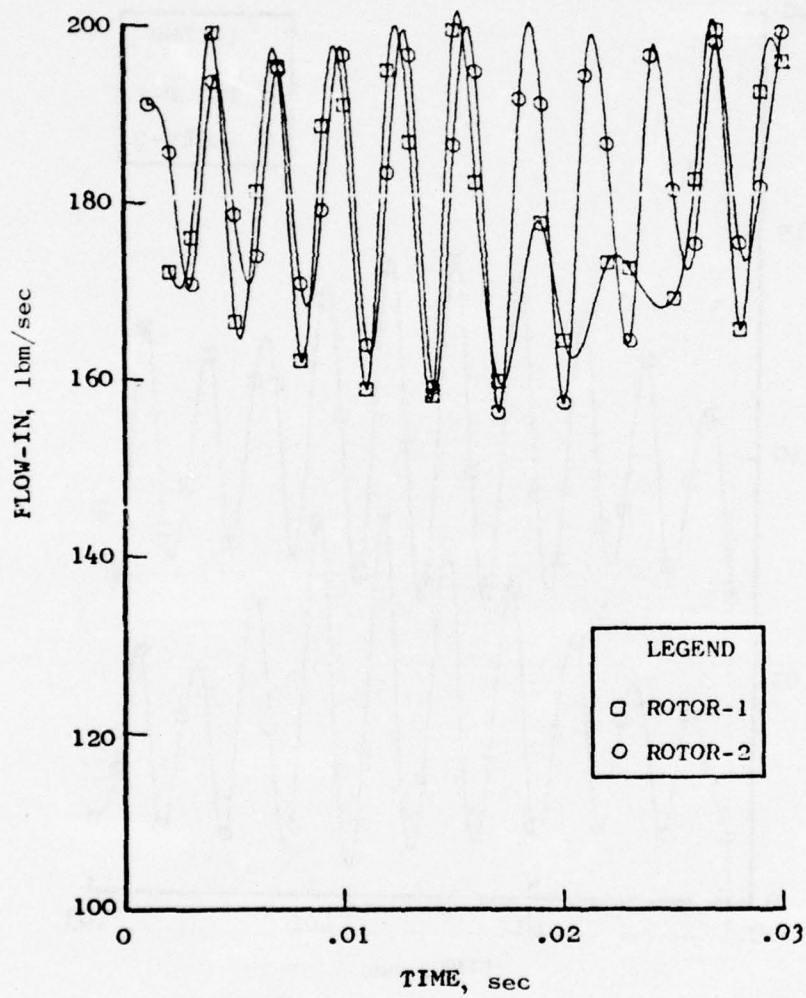


Figure 121. Physical Airflow Vs. Time, 100% $N/\sqrt{\theta}$, 350 Hz

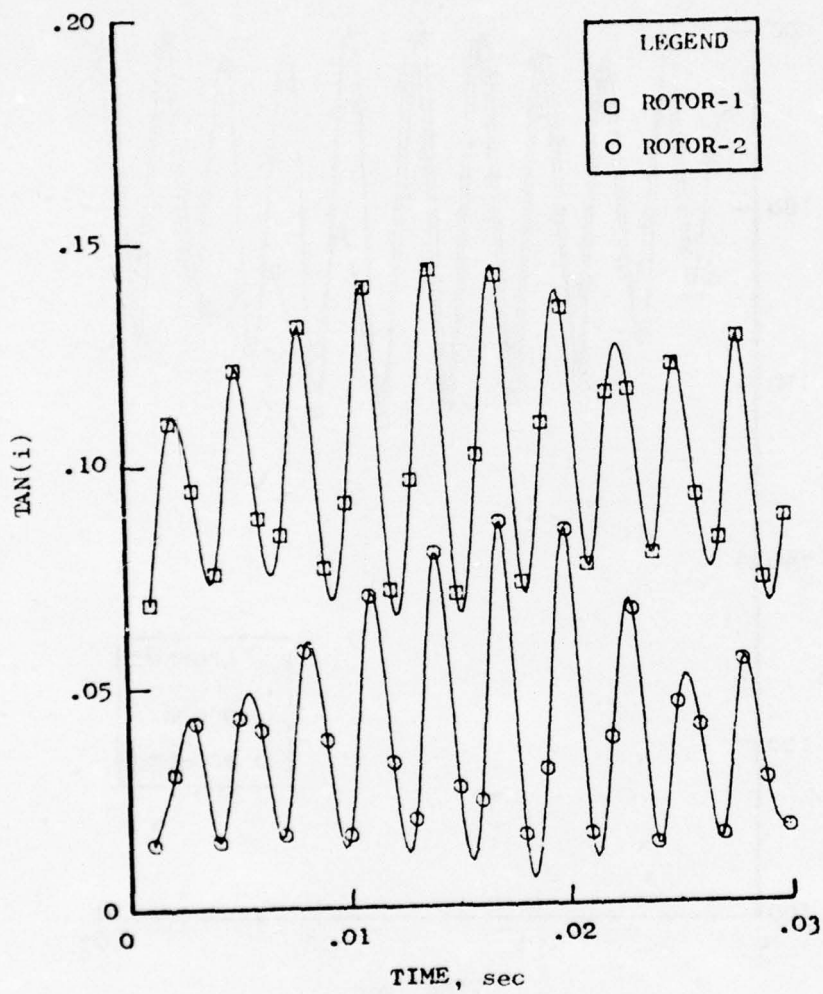


Figure 122. Tangent of Incidence Angle Vs. Time,
100% N/\sqrt{h} , 350 Hz.

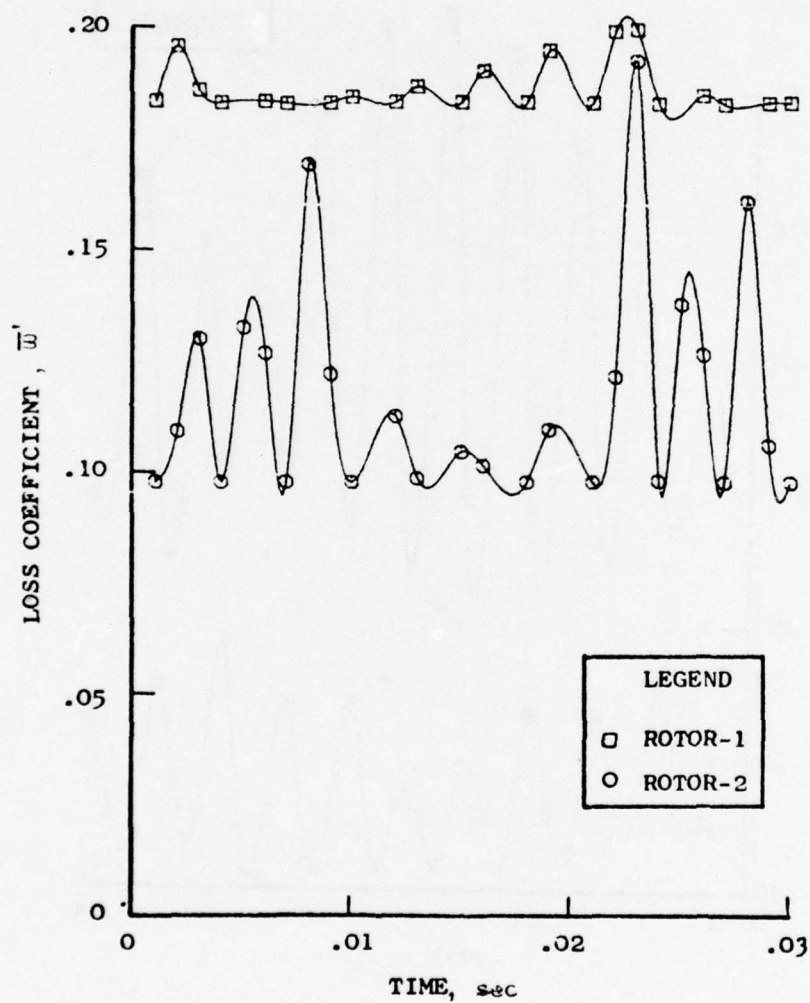


Figure 123. Loss Coefficient Vs. Time, 100% $N/\sqrt{\theta}$, 350 Hz.

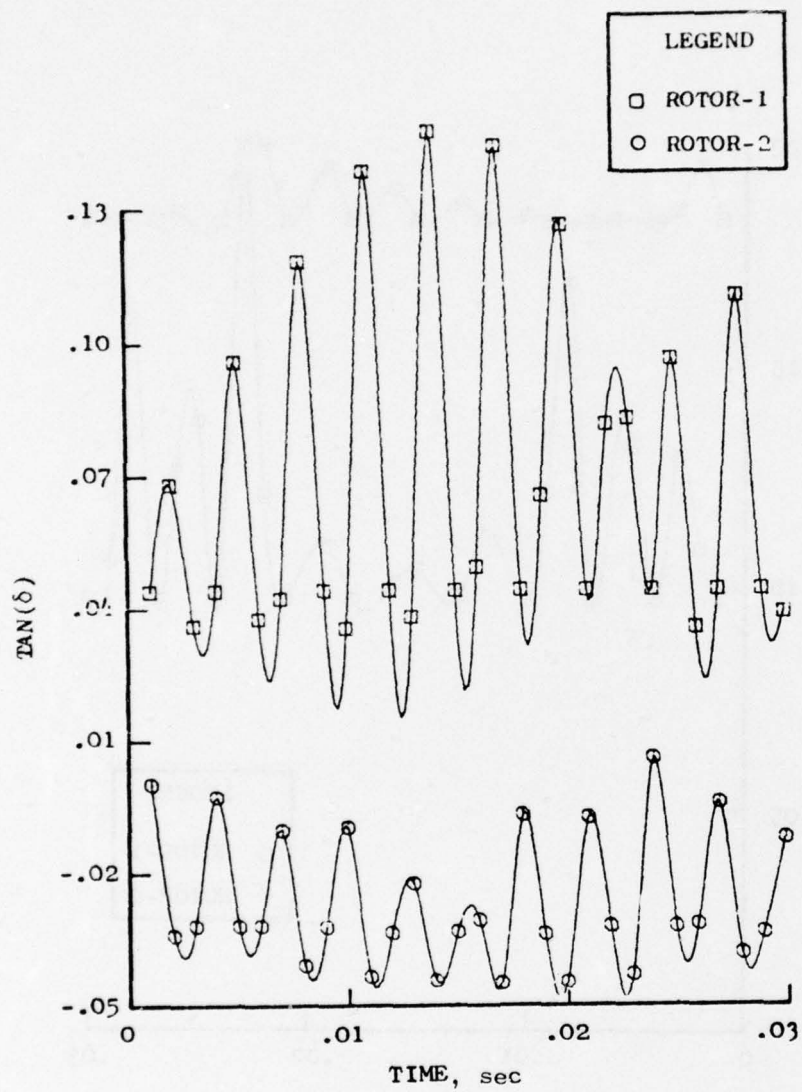


Figure 124. Tangent of Deviation Angle Vs. Time, 100% $N/\sqrt{\theta}$, 350 Hz.

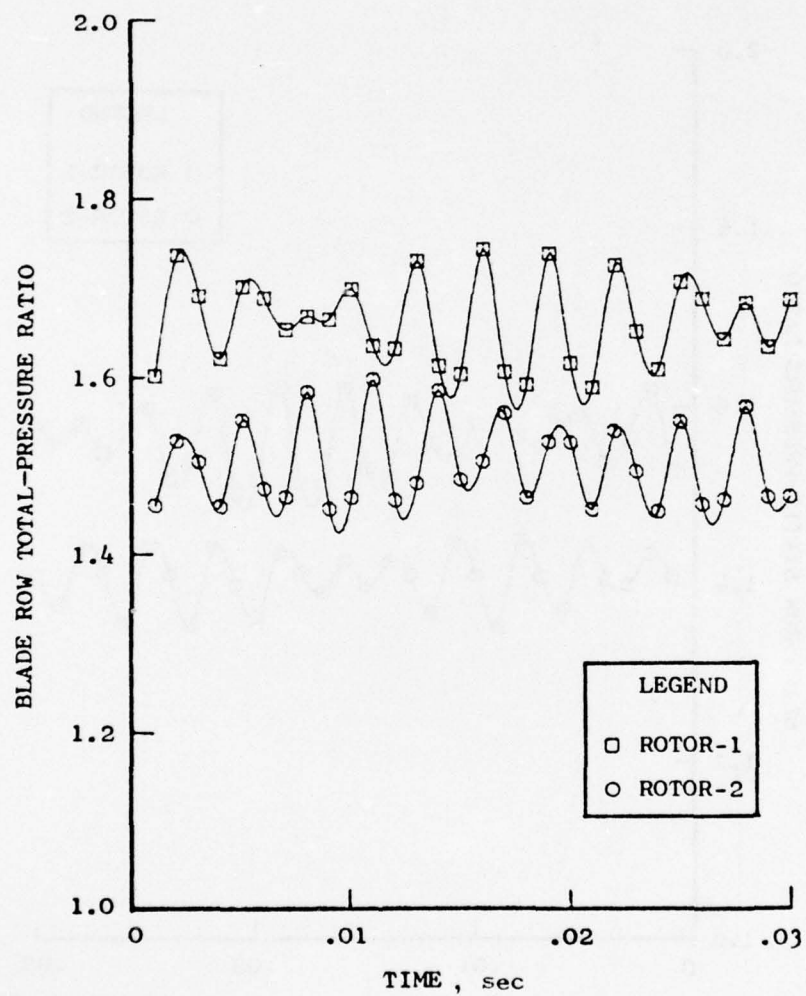


Figure 125. Blade Row Total-Pressure Ratio Vs. Time, 100% $N/\sqrt{\theta}$, 350 Hz.

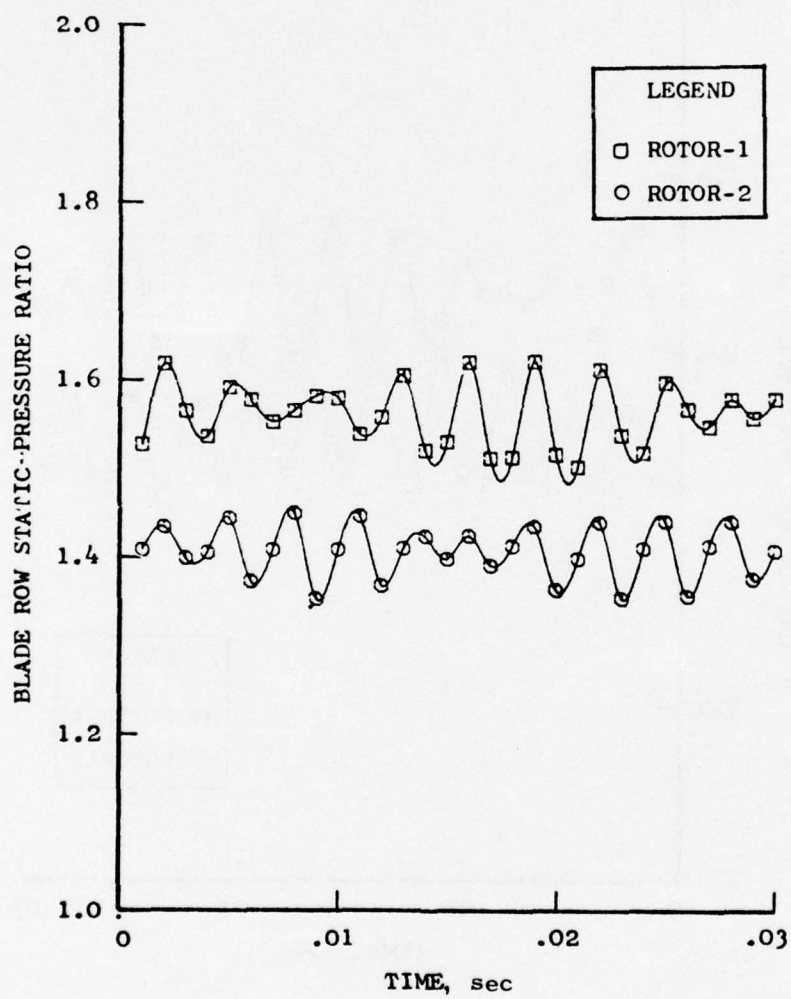


Figure 126. Blade Row Static-Pressure Ratio Vs. Time, 100% $N/\sqrt{\theta}$, 350 Hz.

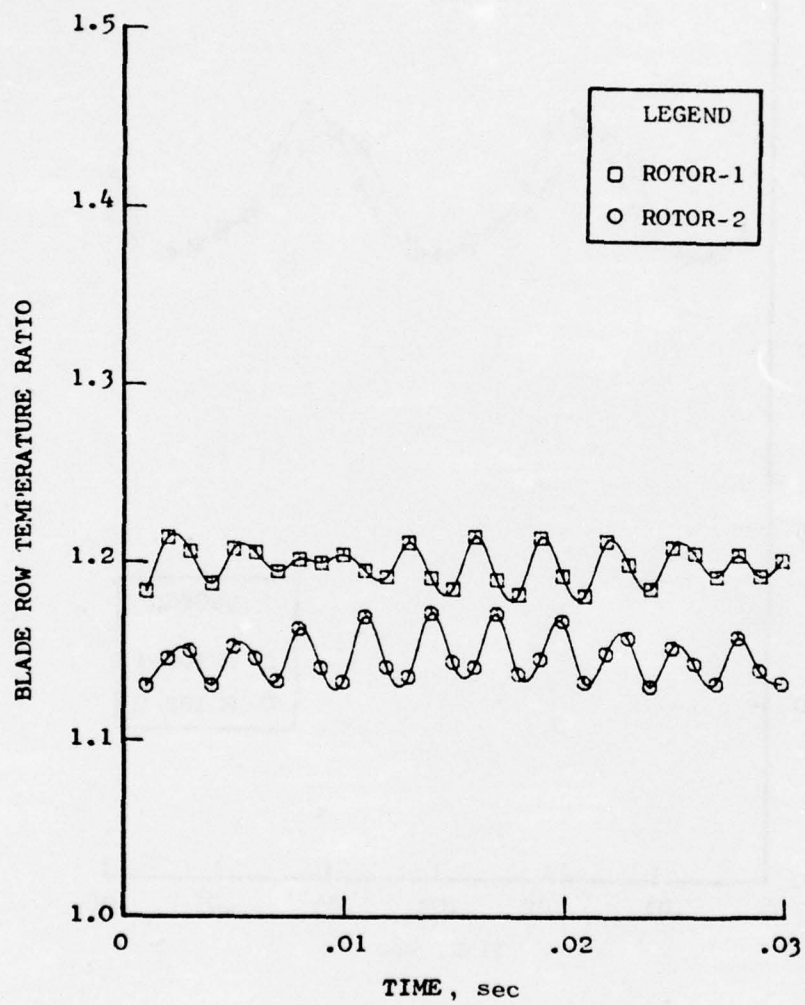


Figure 127. Blade Row Total-Temperature Ratio Vs. Time, 100% $N/\sqrt{\theta}$, 350 Hz.

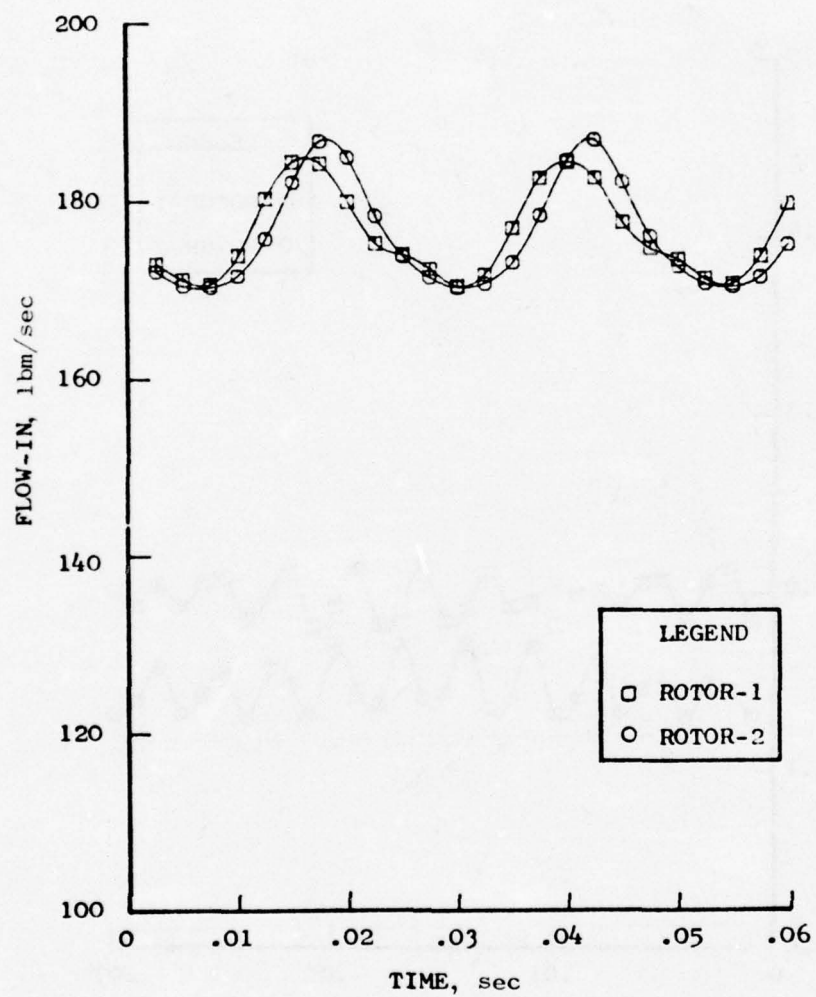


Figure 128. Physical Airflow Vs. Time, $80\% N/\sqrt{\theta}$, 42 Hz.

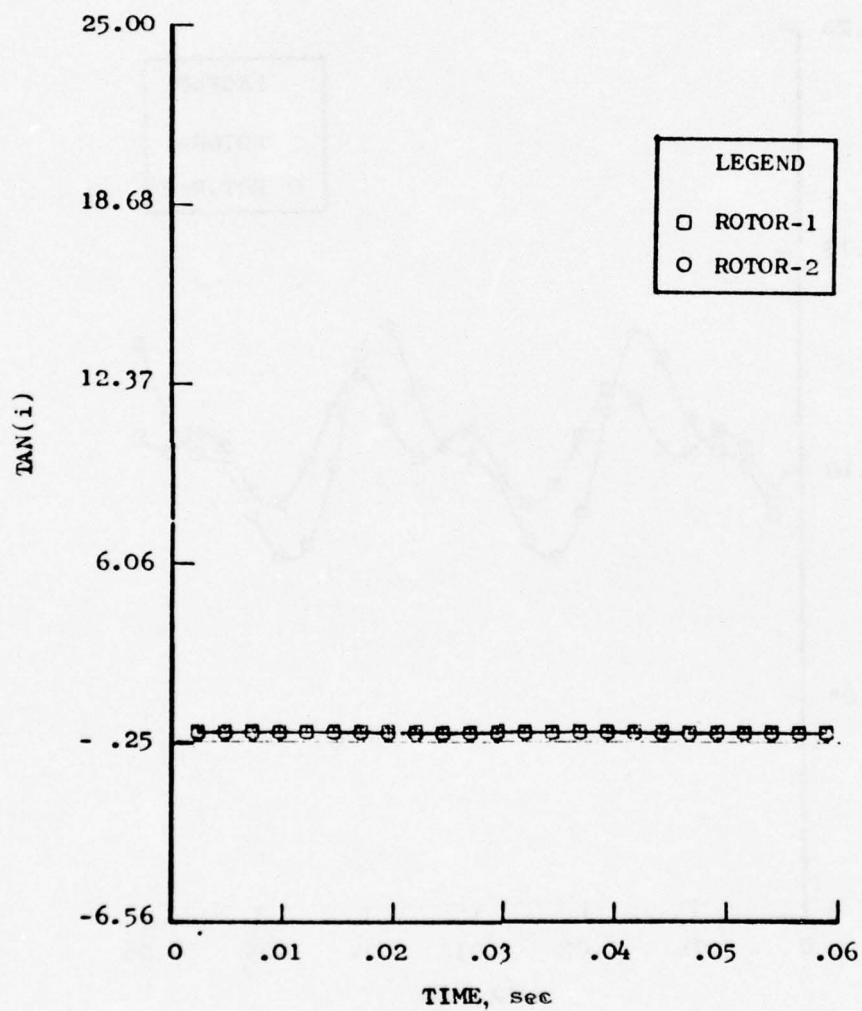


Figure 129. Tangent of Incidence Angle Vs. Time, 80% $N/\sqrt{\theta}$, 42 Hz.

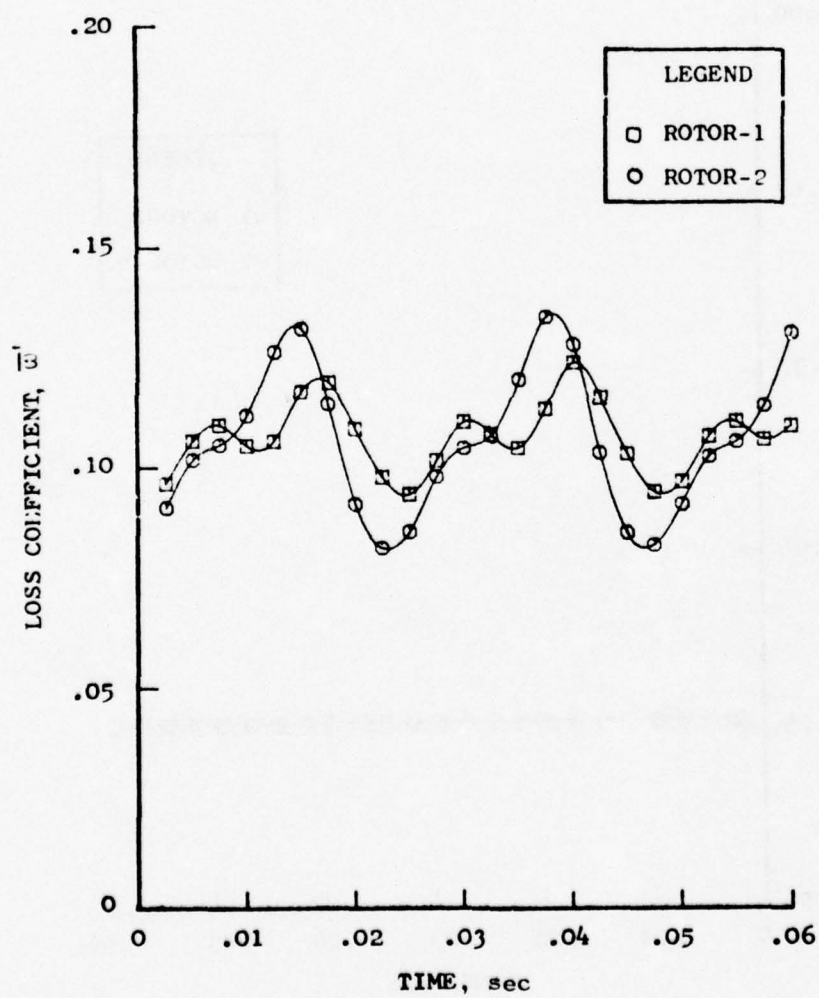


Figure 130. Loss Coefficient Vs. Time, $80\% N/\sqrt{\theta}$, 42 Hz.

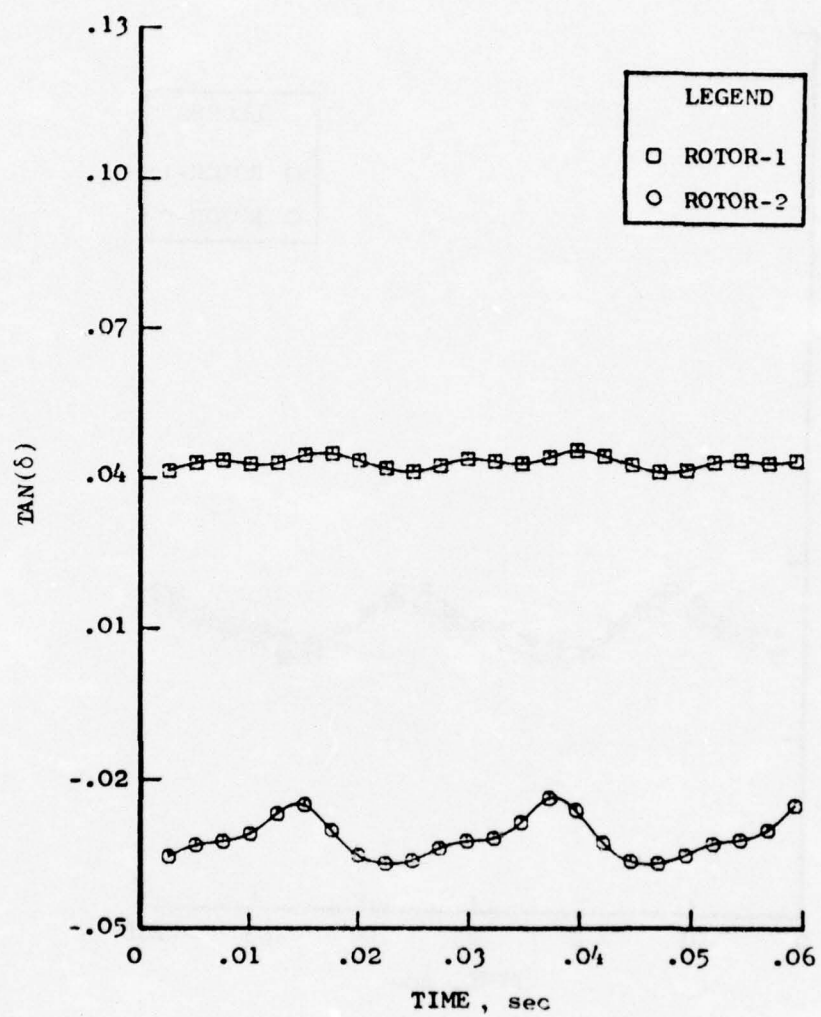


Figure 131. Tangent of Deviation Angle Vs. Time, $80\% N/\sqrt{\theta}$, 42 Hz.

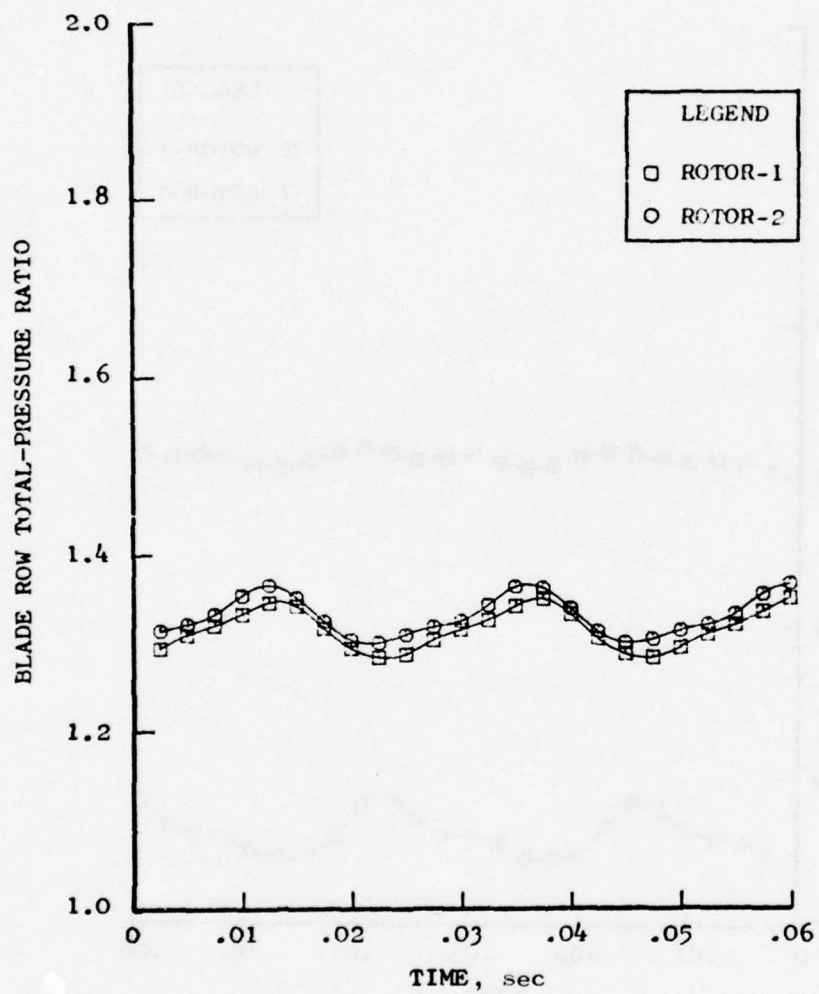


Figure 132. Blade Row Total-Pressure Ratio Vs. Time,
80% $N/\sqrt{\theta}$, 42 Hz.

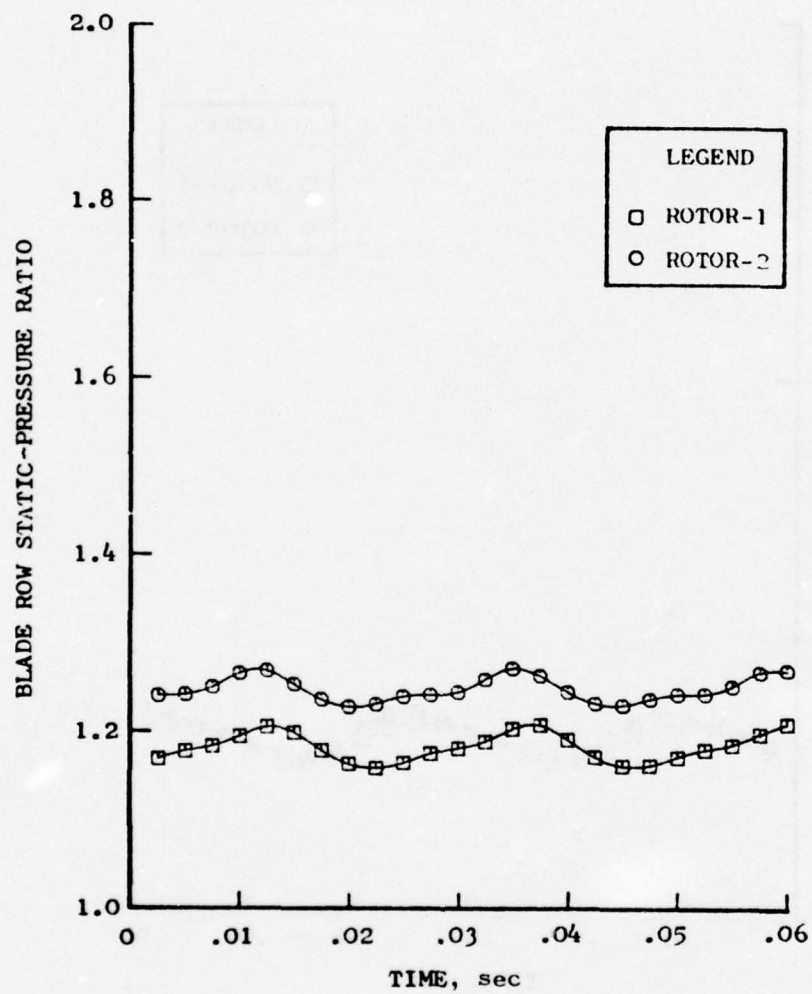


Figure 133. Blade Row Static-Pressure Ratio Vs. Time, 80% $N/\sqrt{\theta}$, 42 Hz.

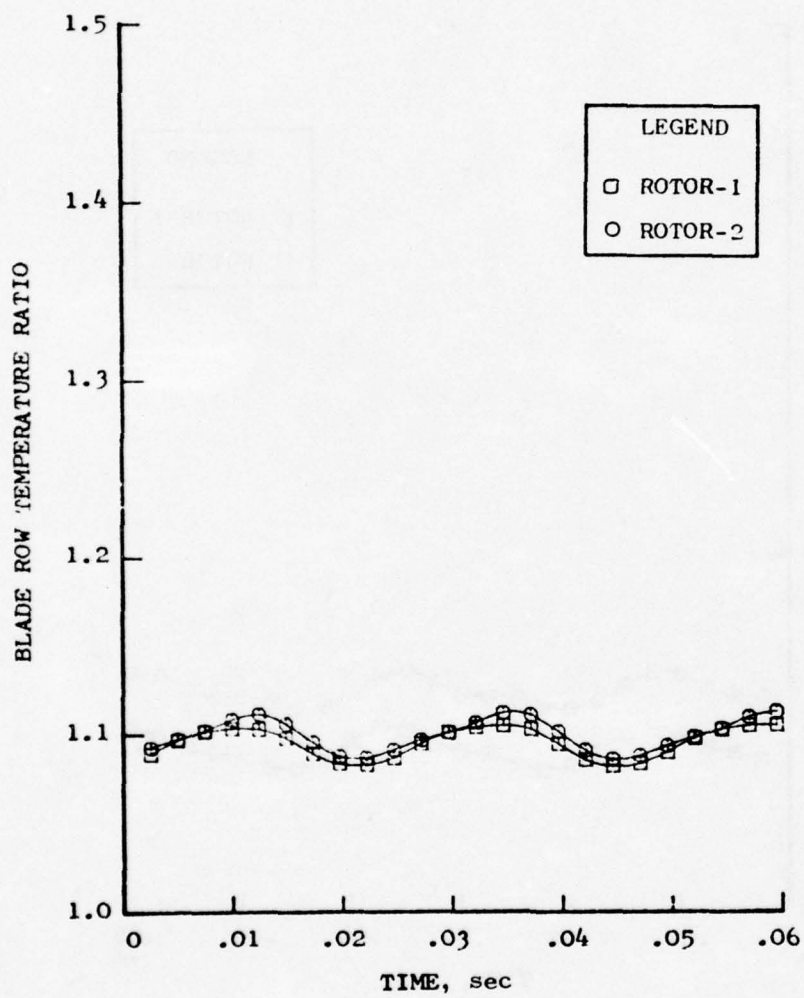


Figure 13⁴. Blade Row Total-Temperature Ratio Vs. Time, 80% $N/\sqrt{\theta}$, 42 Hz.

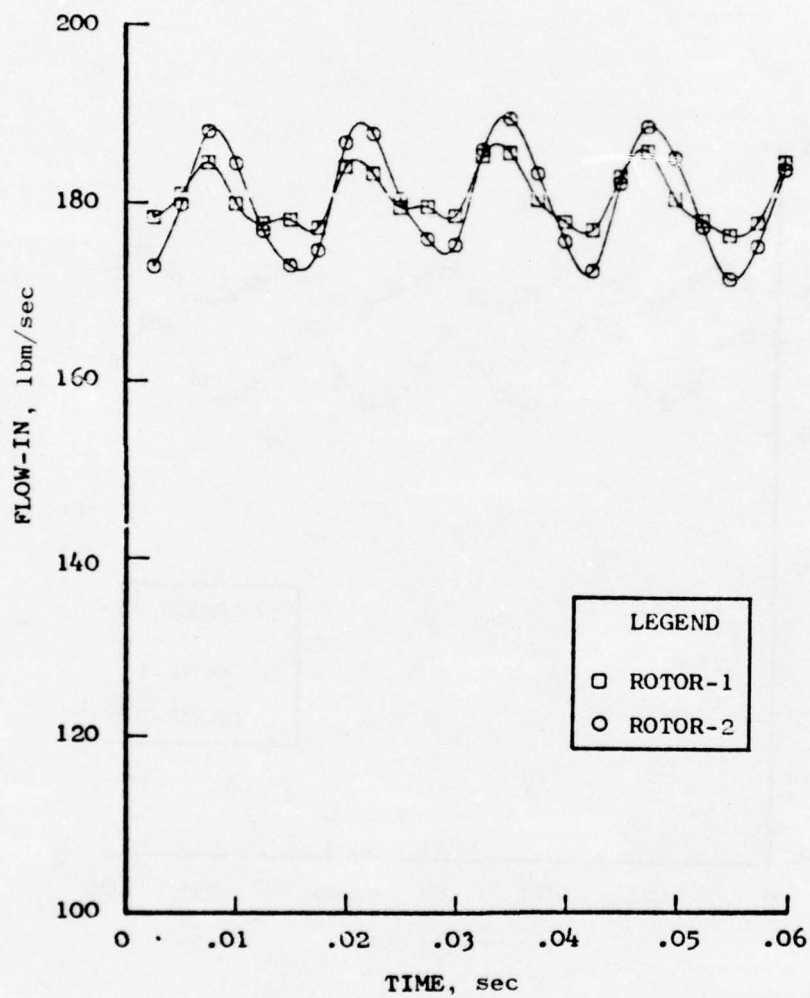


Figure 135. Physical Airflow Vs. Time, 80% $N/\sqrt{\theta}$, 75 Hz.

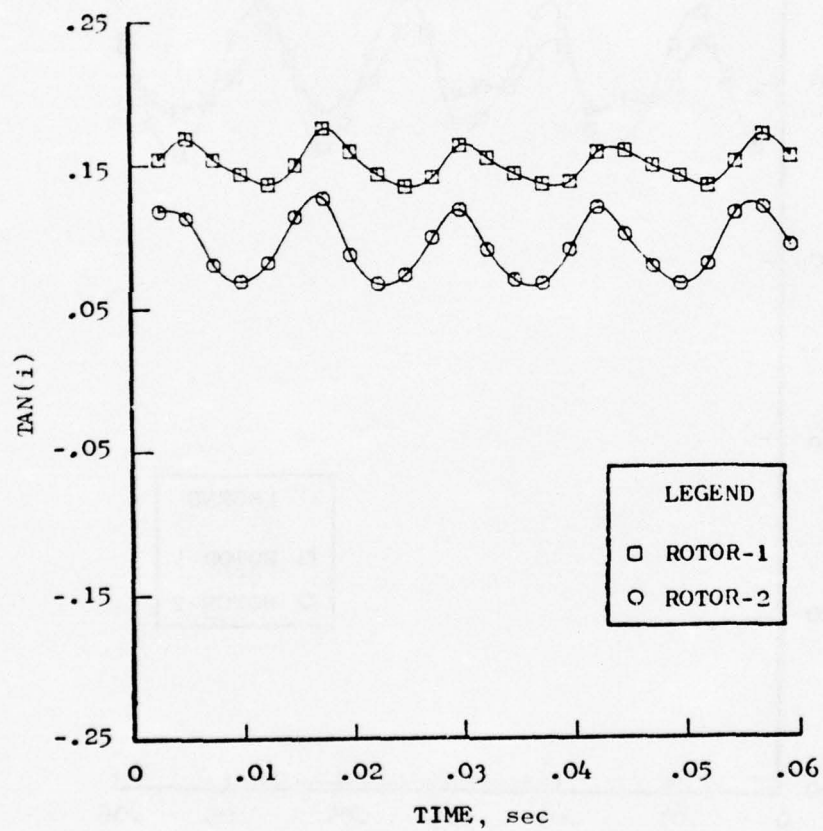


Figure 136. Tangent of Incidence Angle Vs. Time, $80\% N/\sqrt{\theta}$, 75 Hz.

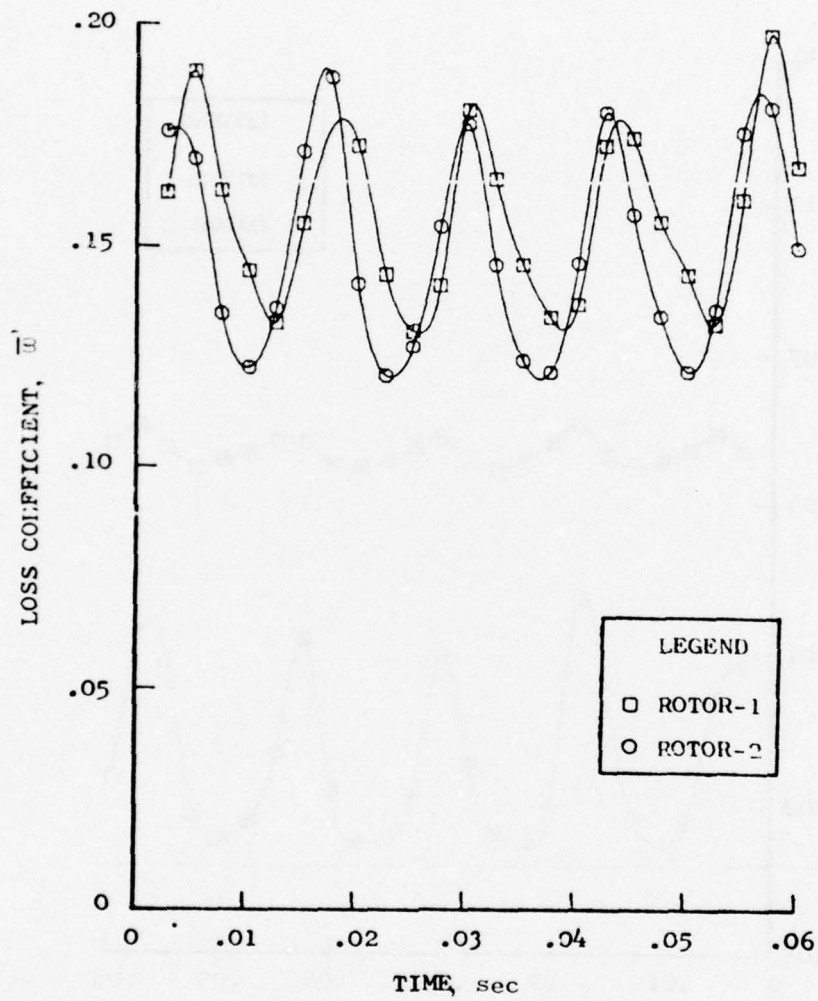


Figure 137. Loss Coefficient Vs. Time, 80% $N/\sqrt{\theta}$, 75 Hz.

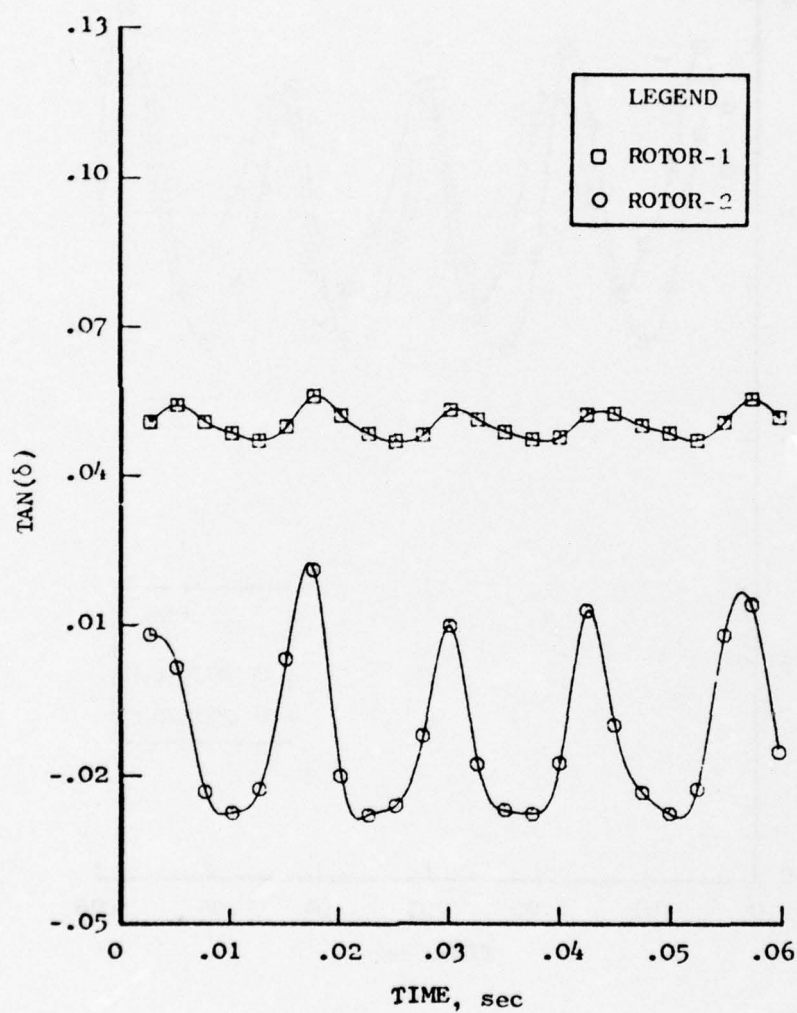


Figure 138. Tangent of Deviation Angle Vs. Time, 80%
 $N/\sqrt{\theta}$, 75 Hz.

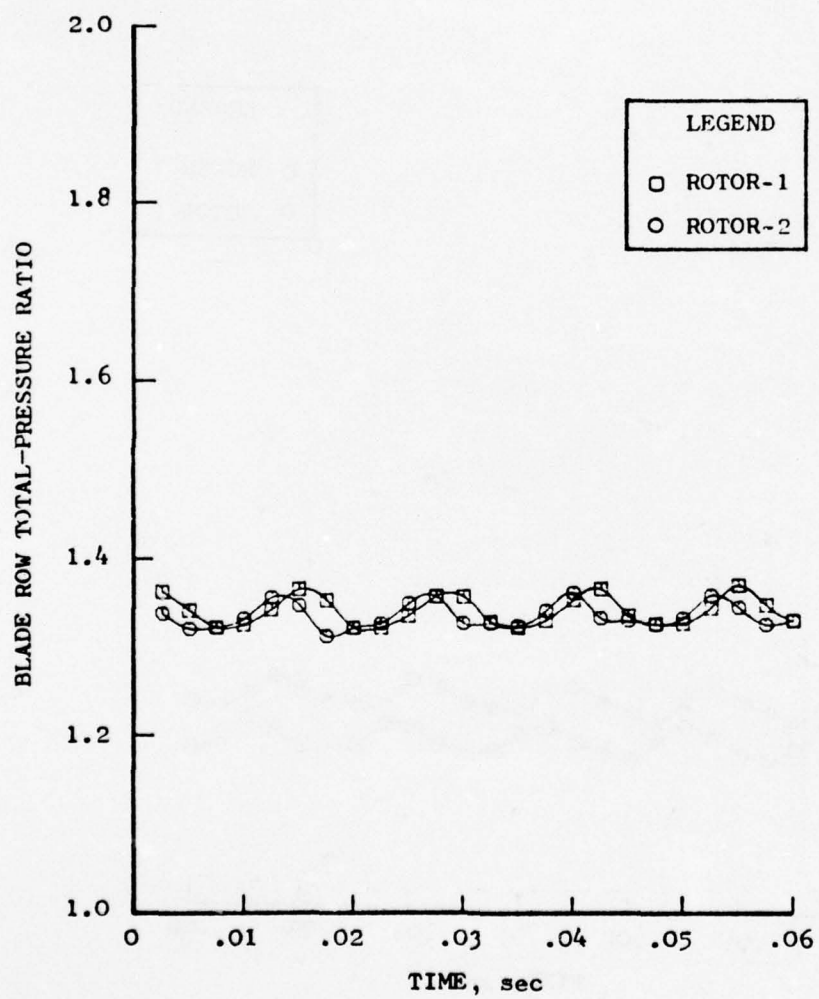


Figure 139. Blade Row Total-Pressure Ratio, 80% $N/\sqrt{\theta}$, 75 Hz.

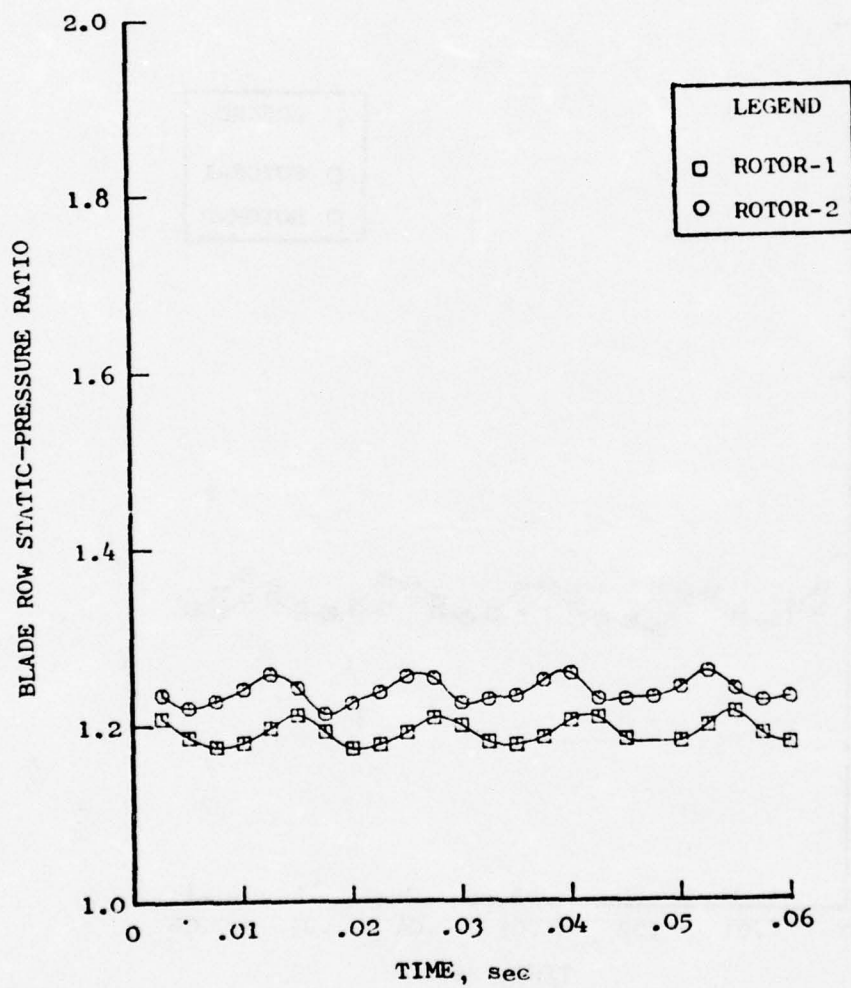


Figure 140. Blade Row Static-Pressure Ratio, 80% N/\sqrt{R} , 75 Hz.

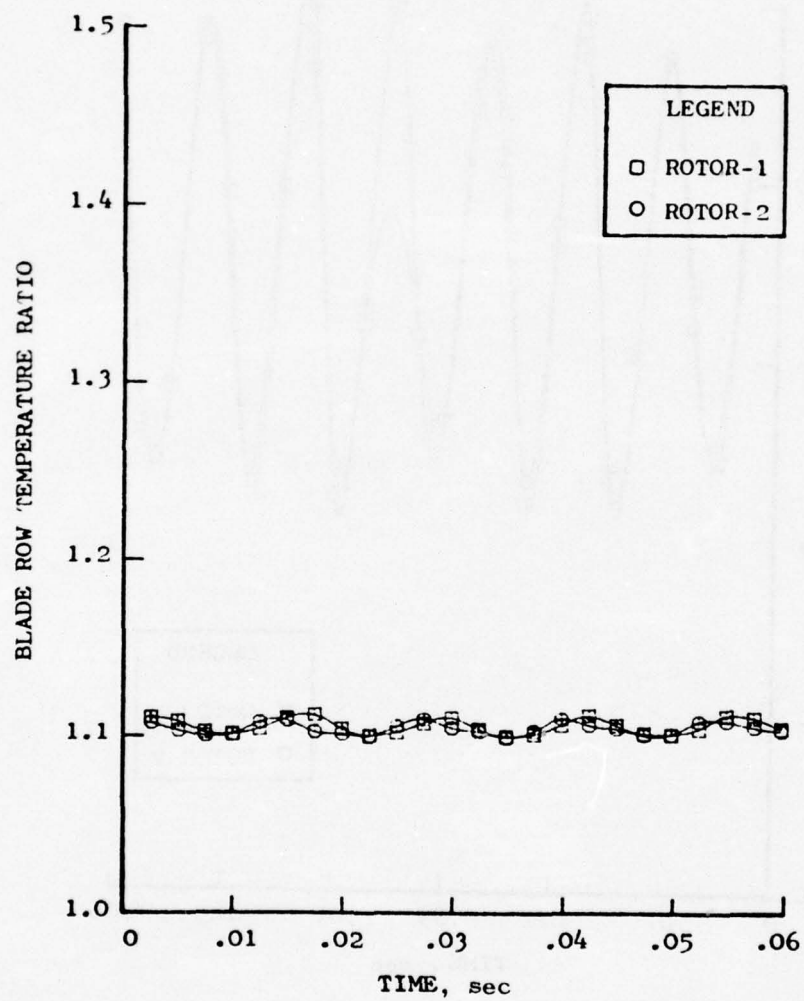


Figure 141. Blade Row Total-Temperature Ratio Vs. Time, 80% $N/\sqrt{\theta}$, 75 Hz.

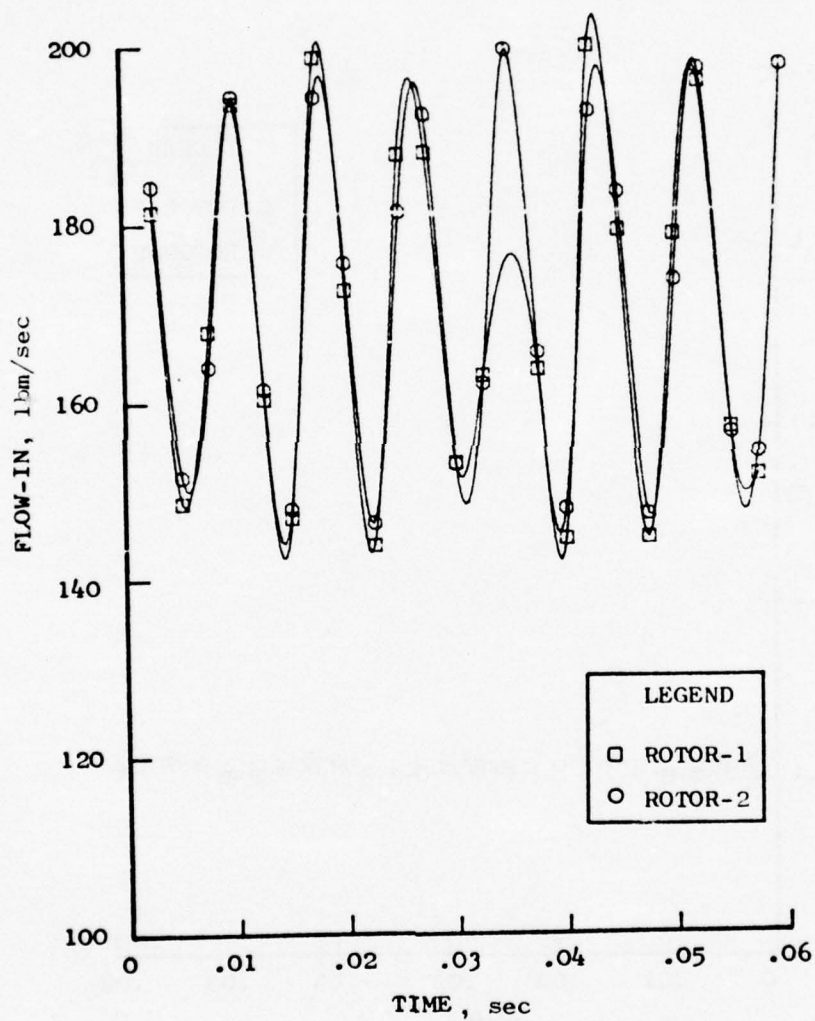


Figure 142. Physical Airflow Vs. Time, $80\% N/\sqrt{\theta}$, 118 Hz.

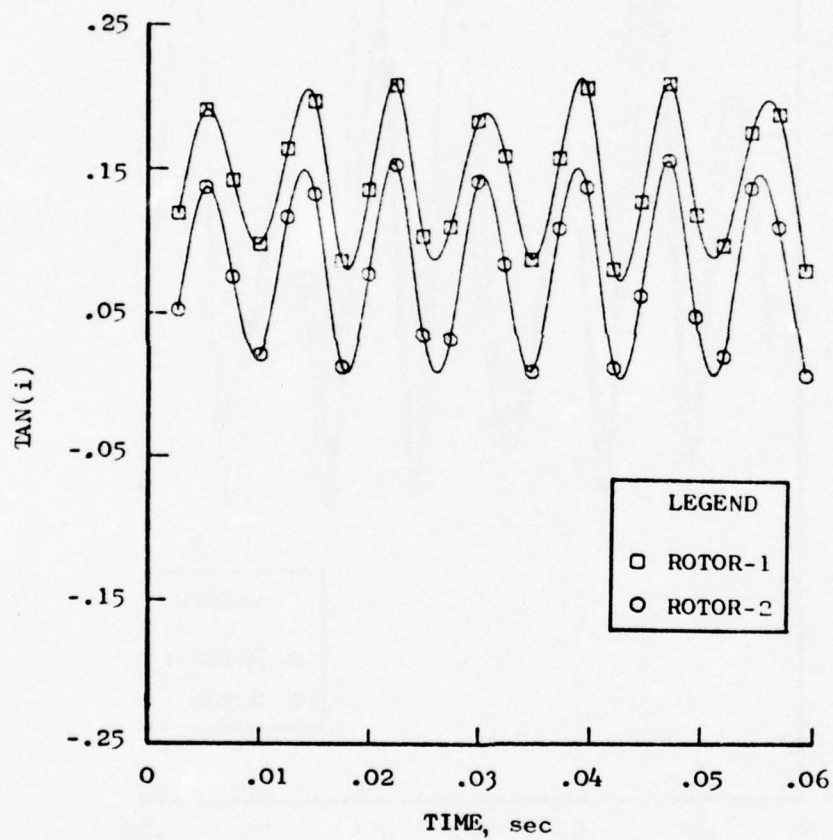


Figure 143. Tangent of Incidence Angle Vs. Time, 80% $N/\sqrt{\theta}$, 118 Hz.

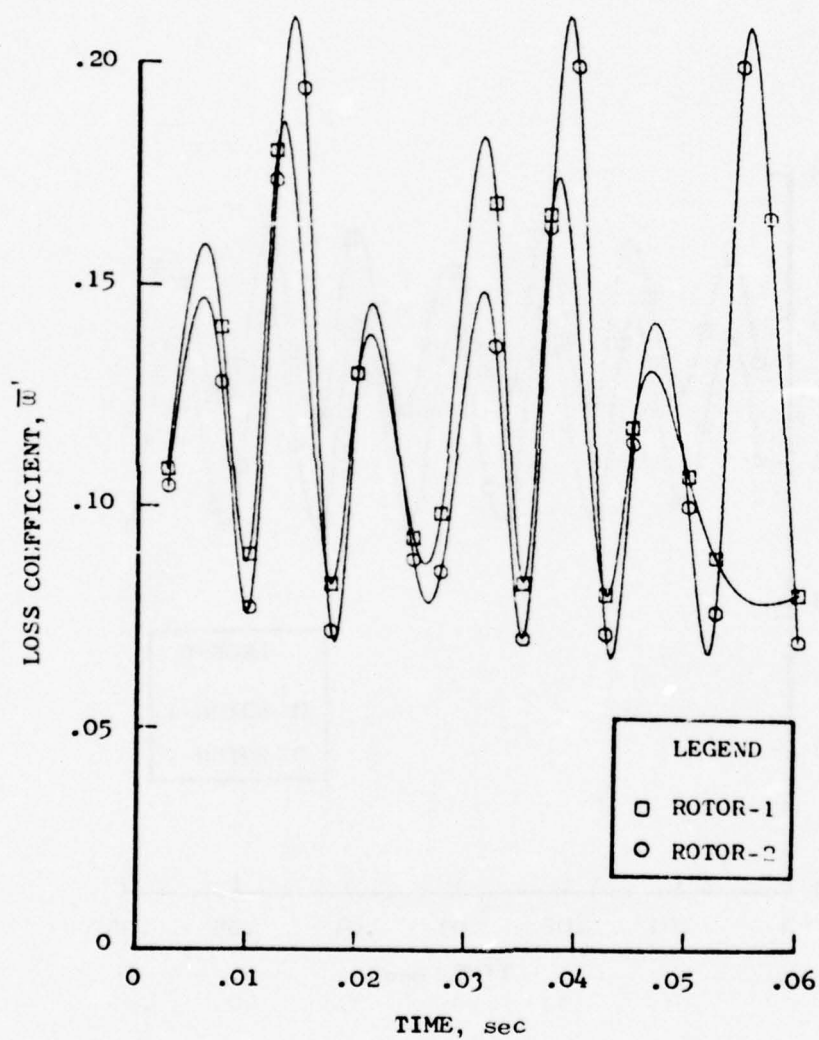


Figure 144. Loss Coefficient Vs. Time, 80% $N/\sqrt{\theta}$, 118 Hz.

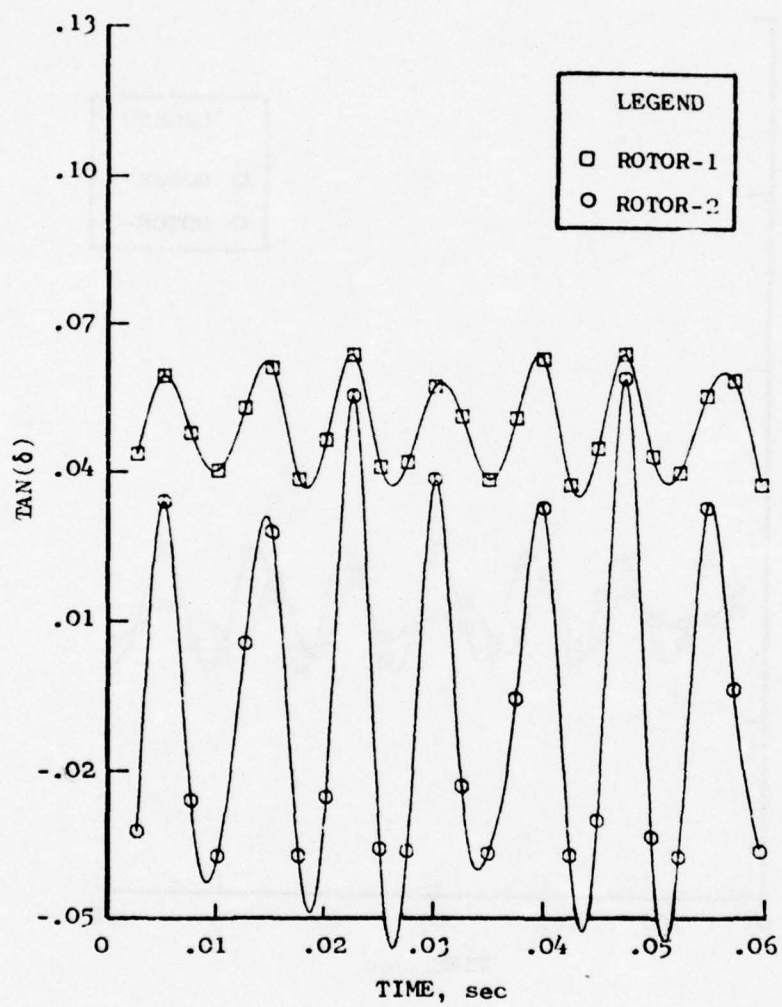


Figure 145. Tangent of Deviation Angle Vs. Time,
80% $N/\sqrt{\theta}$, 118 Hz.

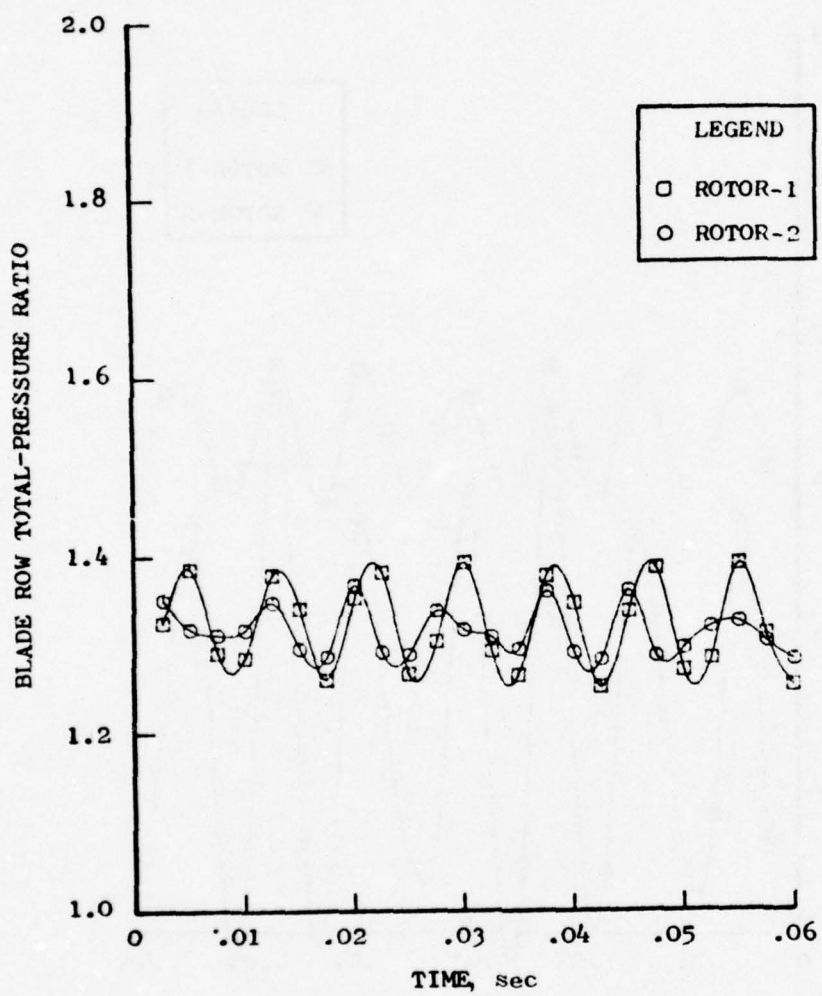


Figure 146. Blade Row Total-Pressure Ratio Vs. Time, 80% $N/\sqrt{\theta}$, 118 Hz.

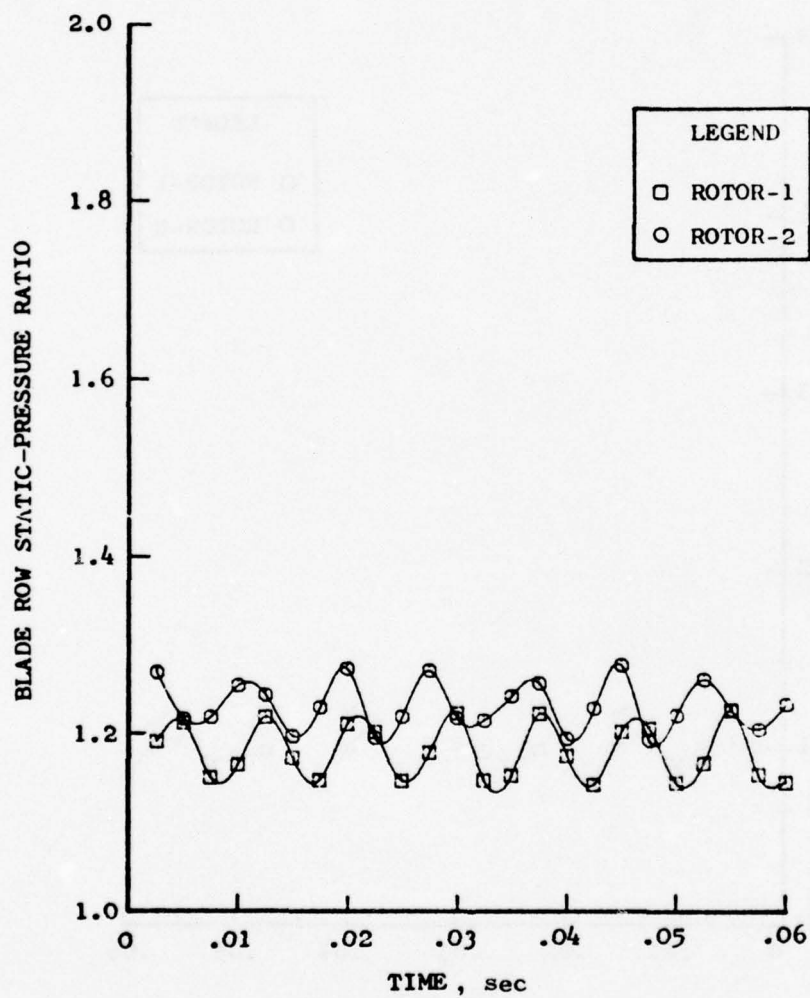


Figure 147. Blade Row Static-Pressure Ratio Vs. Time, 80% $N/\sqrt{\theta}$, 118 Hz.

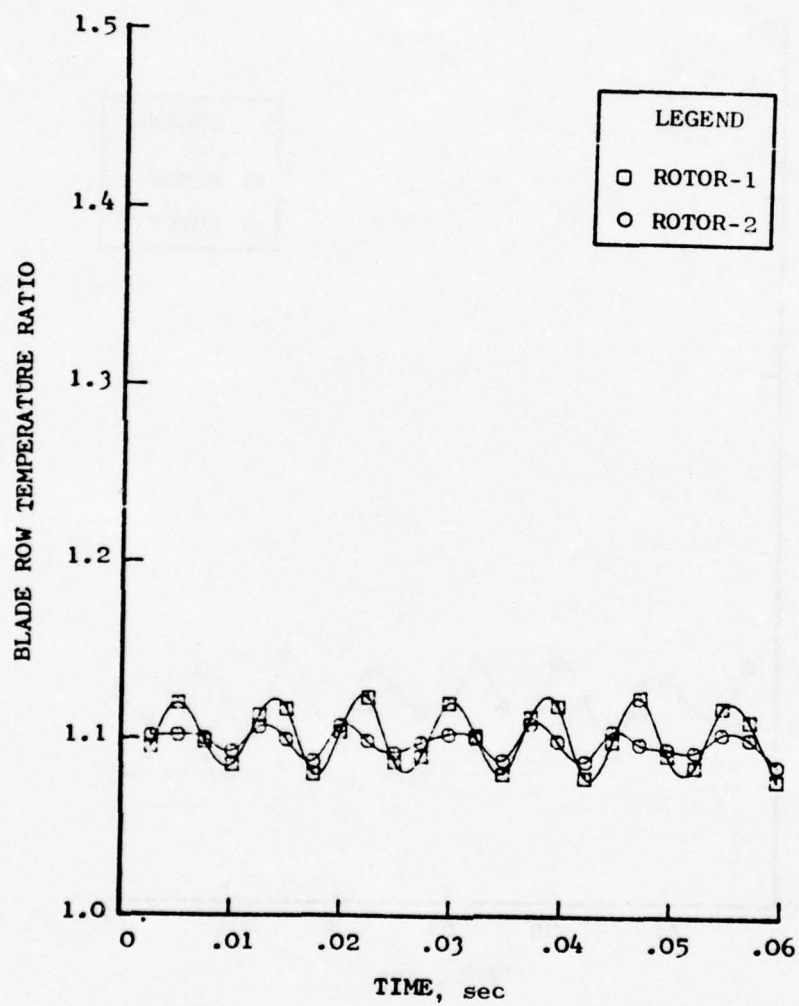


Figure 148. Blade Row Total-Temperature Ratio Vs. Time, 80% $N/\sqrt{\theta}$, 118 Hz.

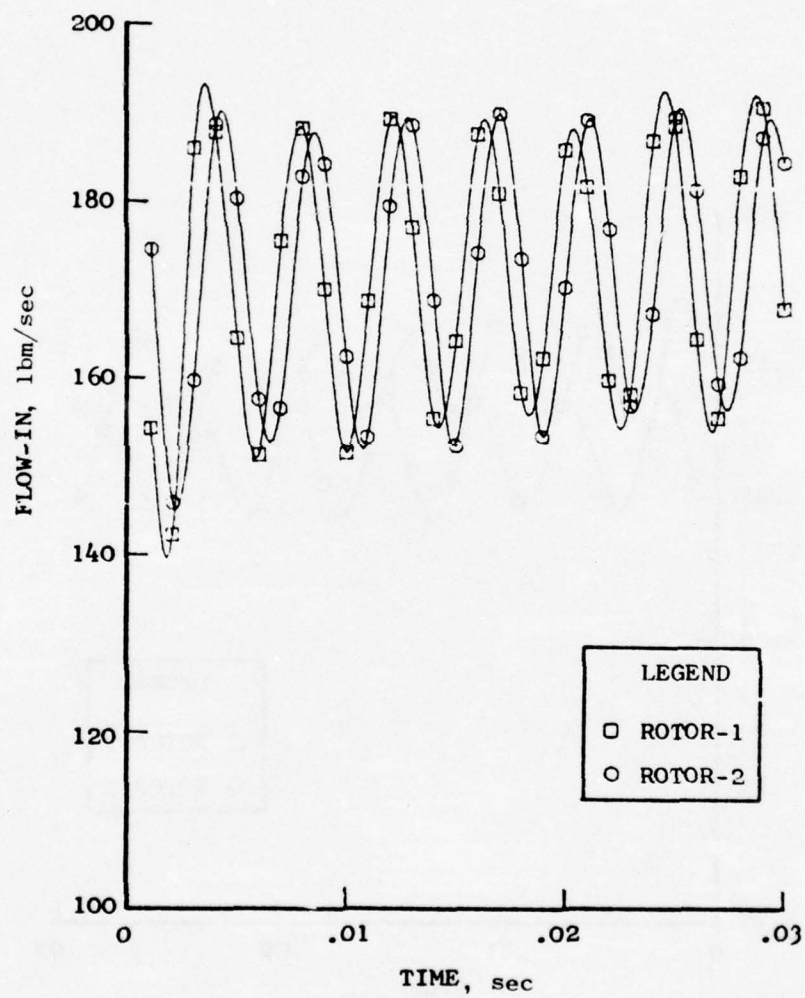


Figure 149. Physical Airflow Vs. Time, $80\% N/\sqrt{\theta}$, 240 Hz.

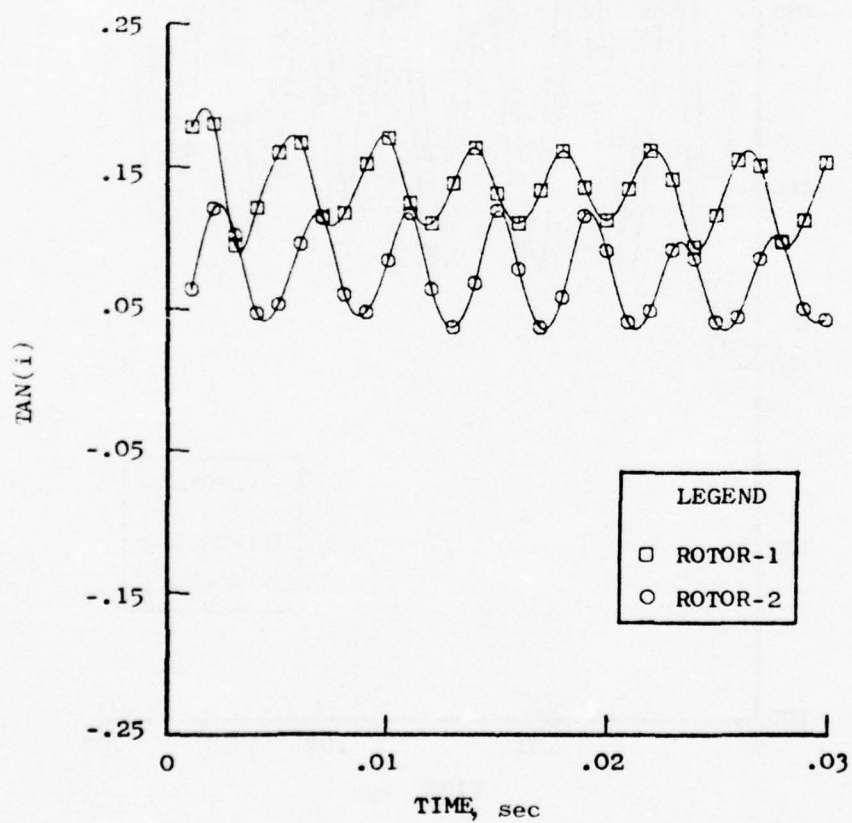


Figure 150. Tangent of Incidence Angle Vs. Time, $80\% N/\sqrt{\theta}$, 240 Hz.

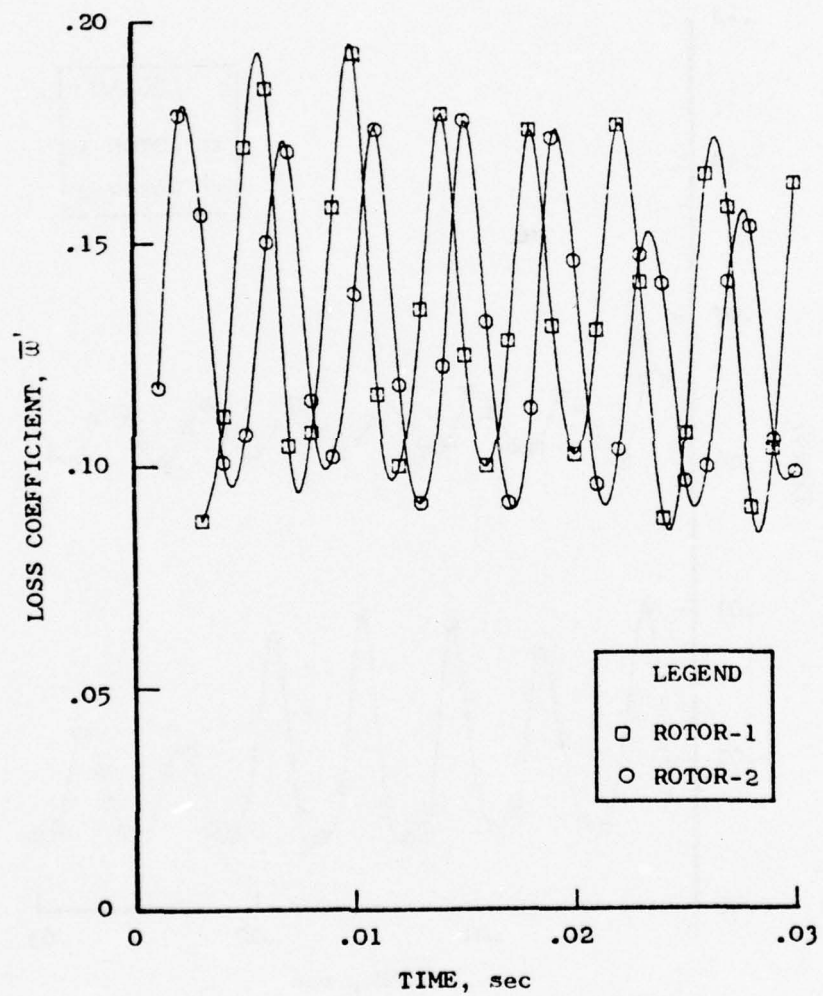


Figure 151. Loss Coefficient Vs. Time, $80\% N/\sqrt{\theta}$, 240 Hz.

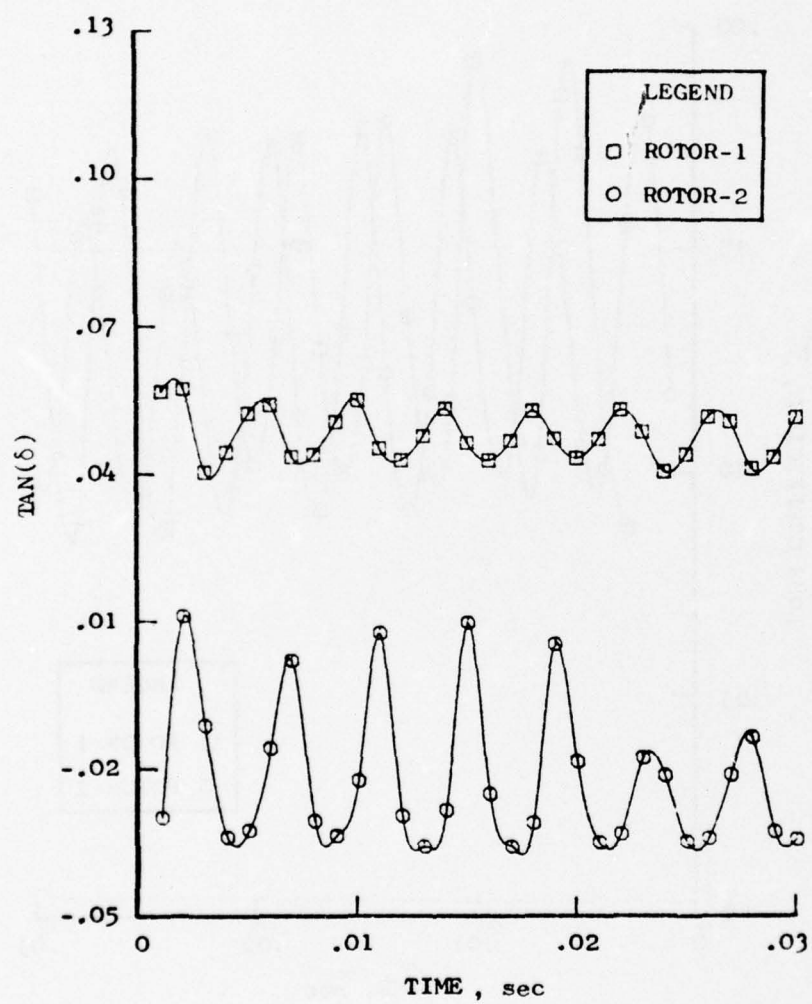


Figure 152. Tangent of Deviation Angle Vs. Time, 80% $N/\sqrt{\theta}$, 240 Hz.

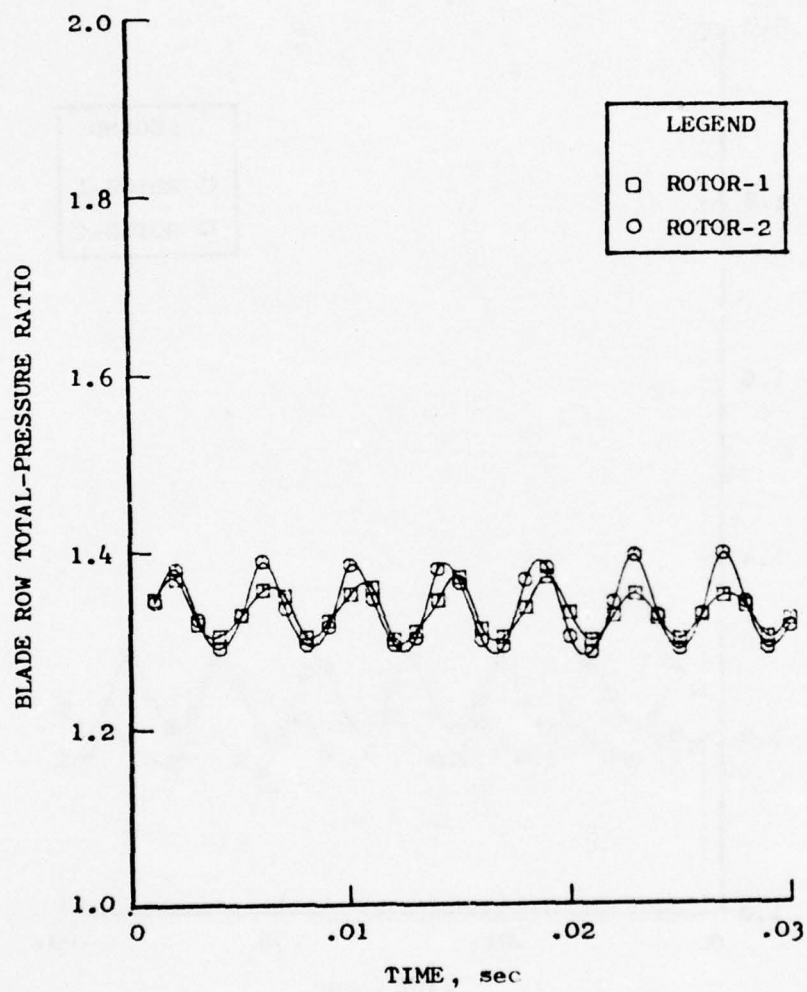


Figure 153. Blade Row Total-Pressure Ratio Vs. Time, 30% $N/\sqrt{\theta}$, 240 Hz.

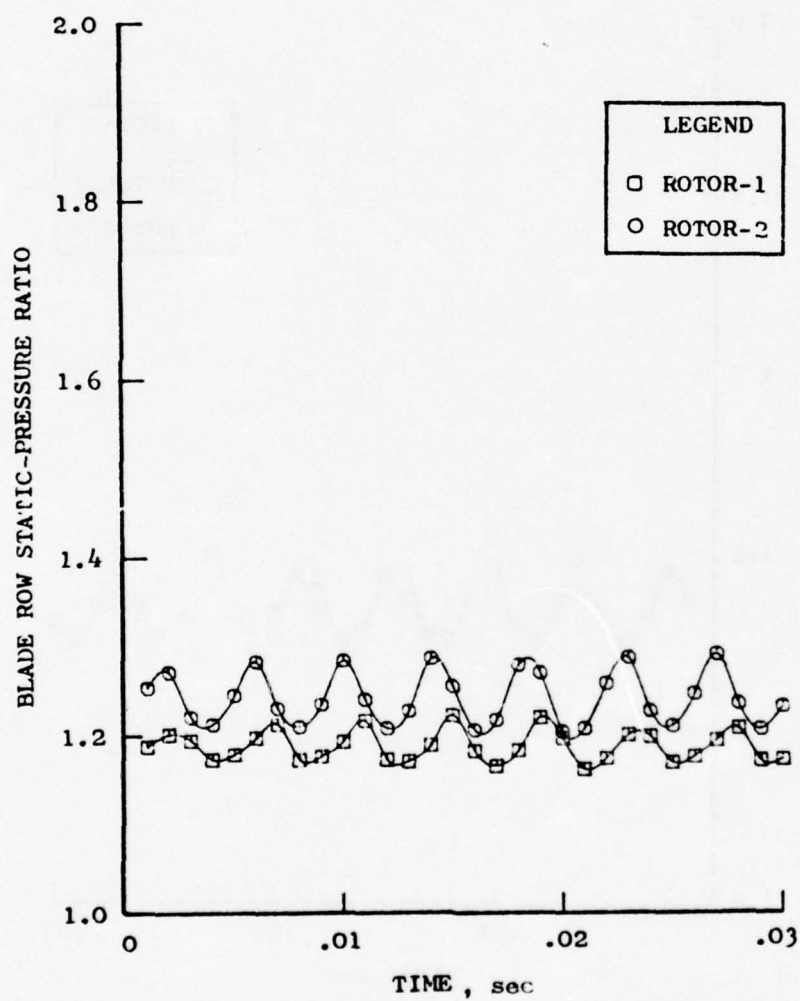


Figure 154. Blade Row Static-Pressure Ratio Vs. Time, 80% $N/\sqrt{\theta}$, 240 Hz.

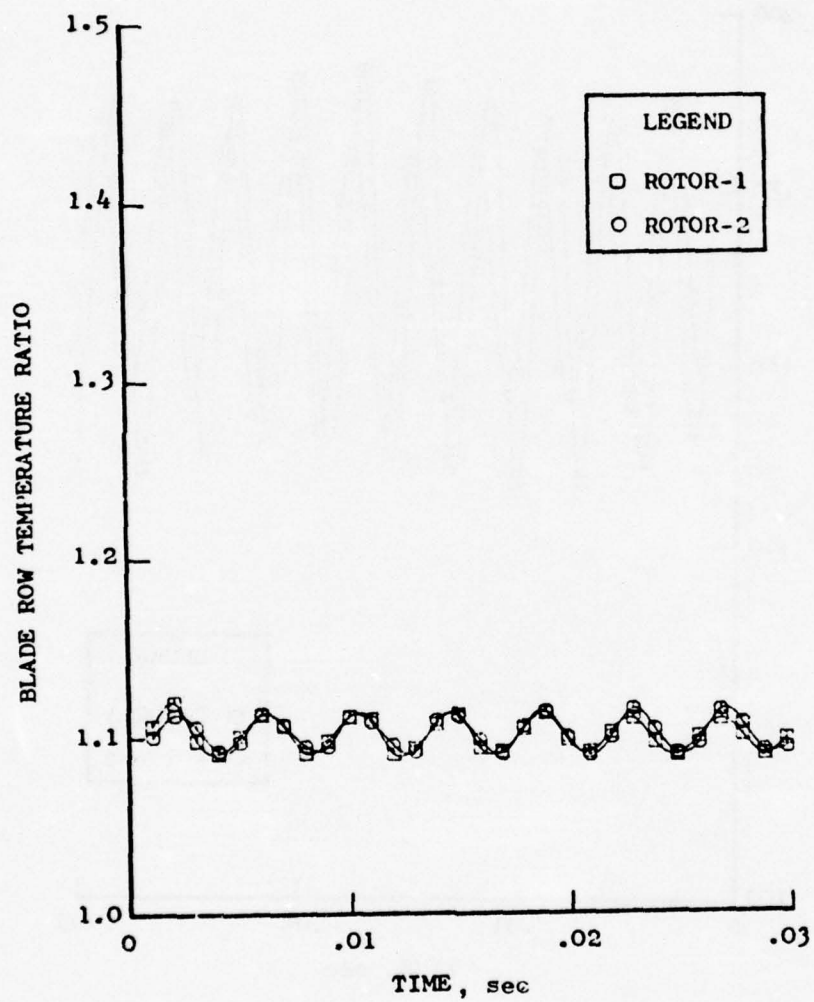


Figure 155. Blade Row Total-Temperature Vs. Time, 80% $N/\sqrt{\theta}$, 240 Hz.

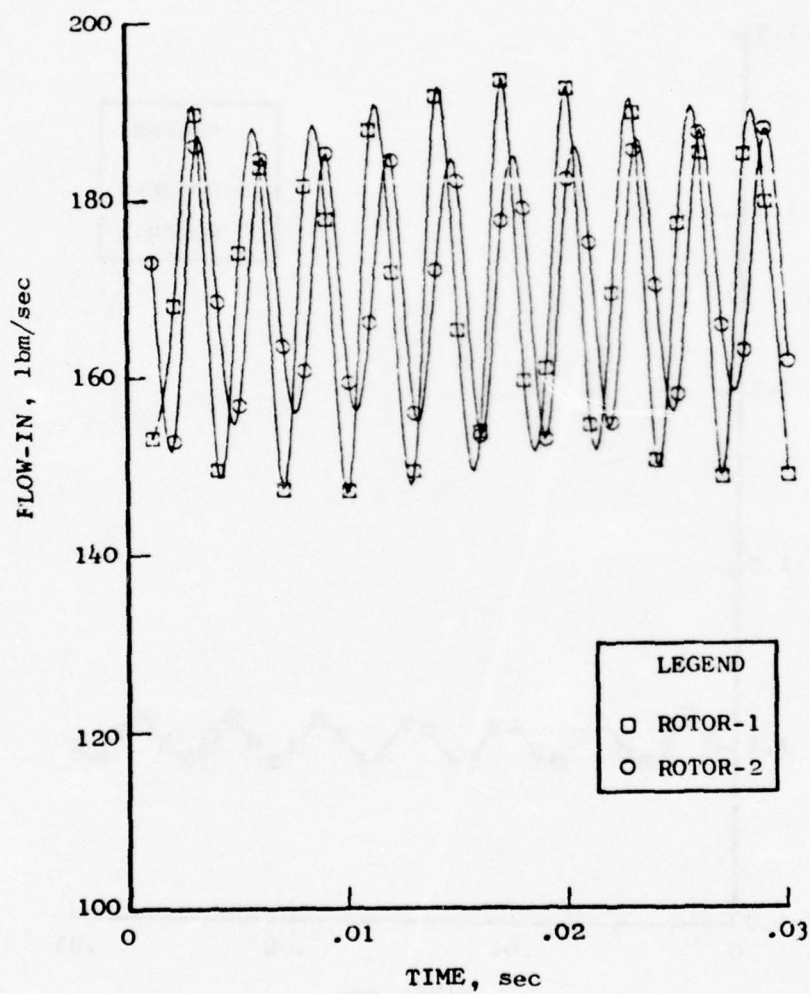


Figure 156. Physical Airflow Vs. Time, $80\% N/\sqrt{\theta}$, 350 Hz.

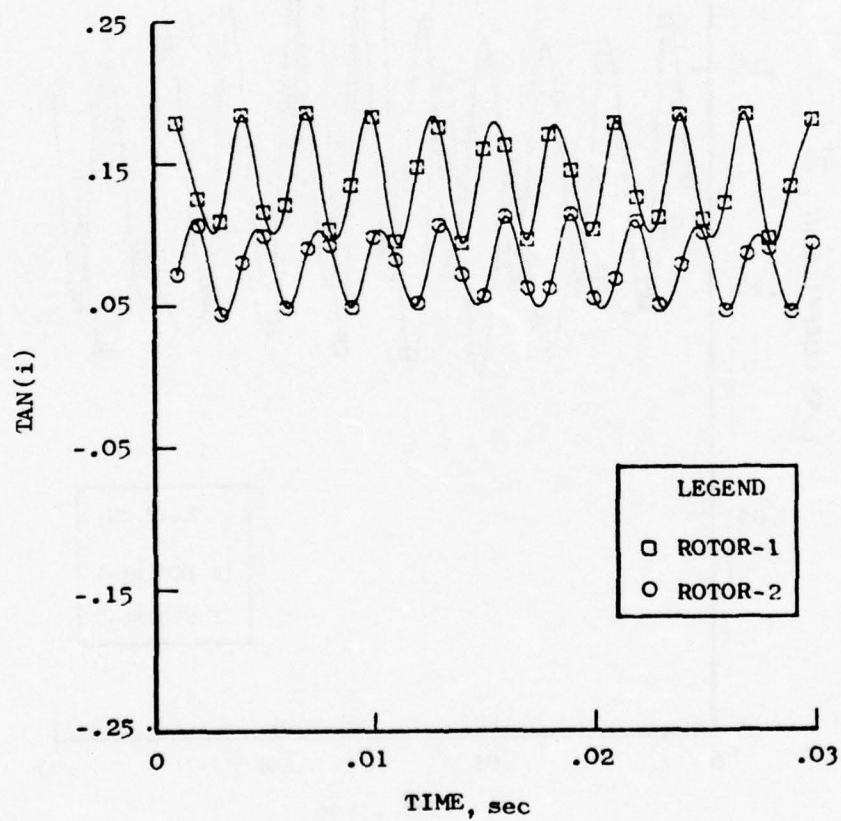


Figure 157. Tangent of Incidence Angle Vs. Time, 80% $N/\sqrt{\theta}$, 350 Hz.

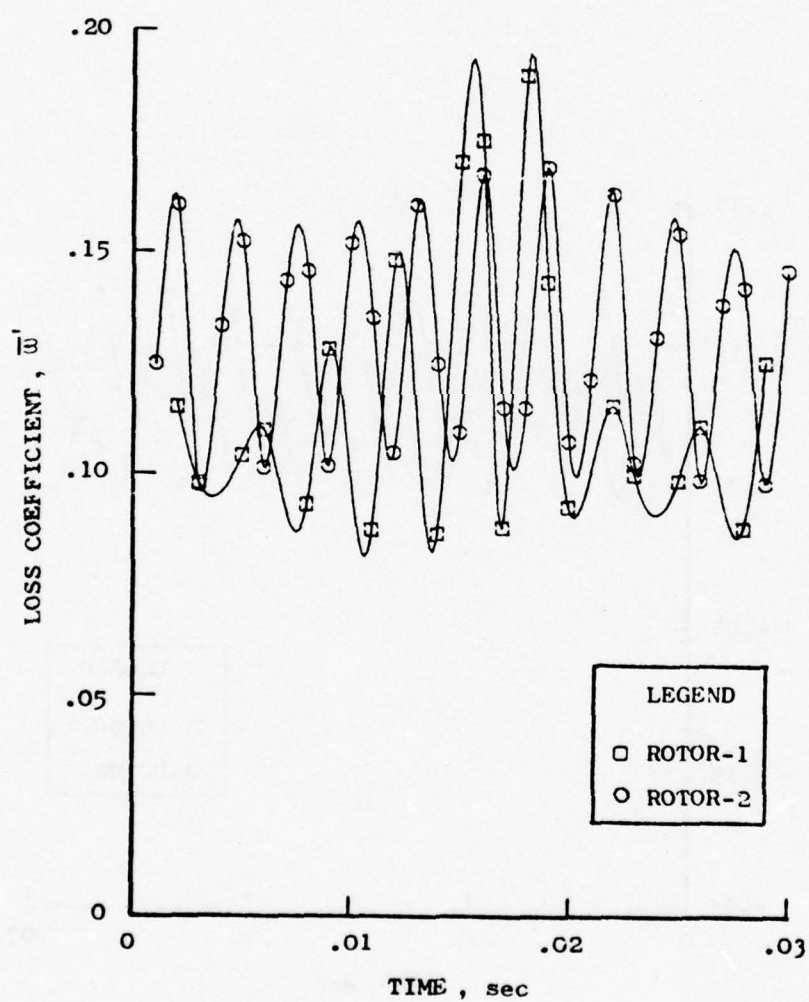


Figure 158. Loss Coefficient Vs. Time, $80\% N/\sqrt{\theta}$, 350 Hz.

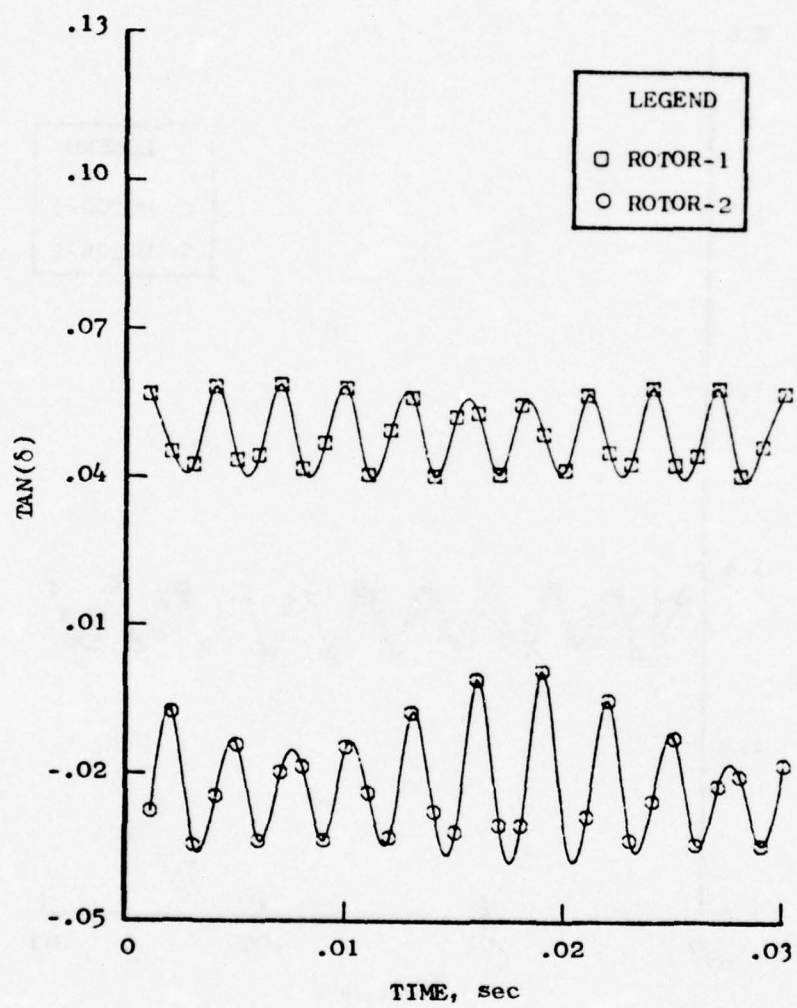


Figure 159. Tangent of Deviation Angle Vs. Time, 80% $N/\sqrt{\theta}$, 350 Hz.

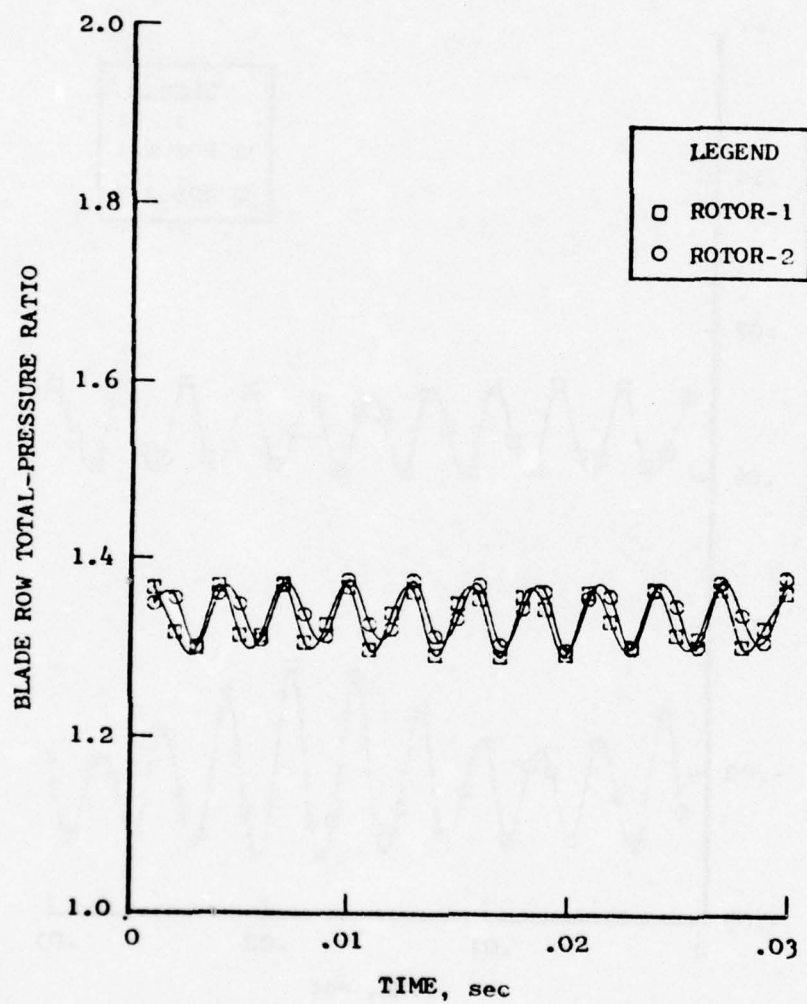


Figure 160. Blade Row Total-Pressure Ratio Vs. Time, 80% $N/\sqrt{\theta}$, 350 Hz.

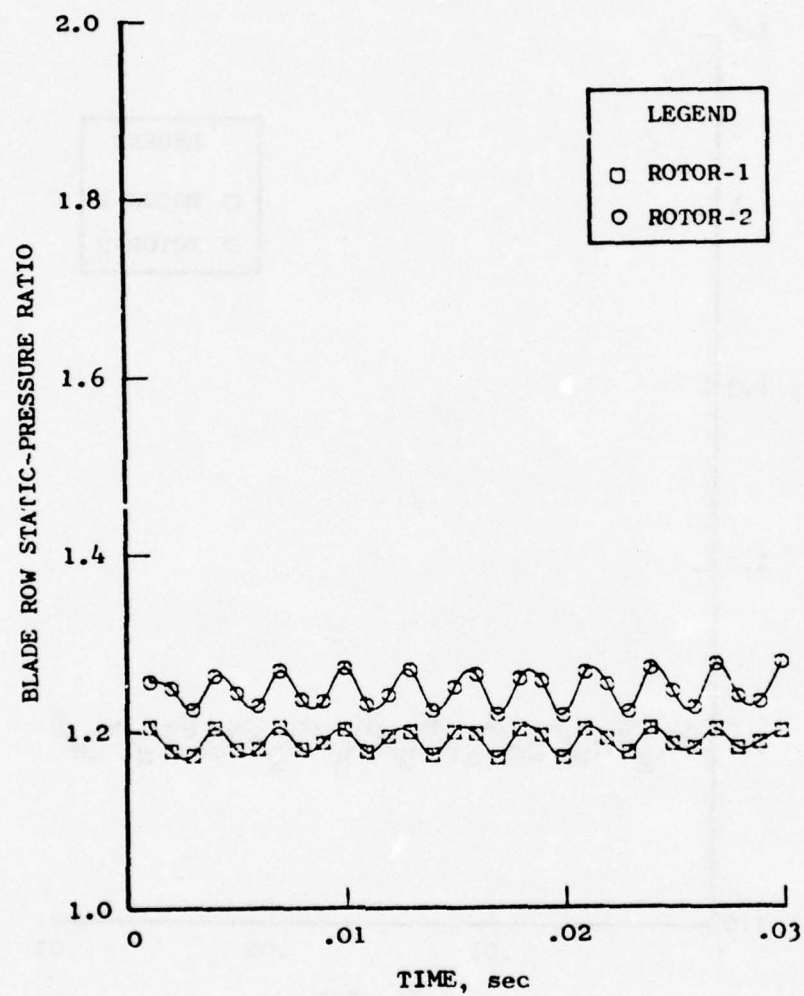


Figure 161. Blade Row Static-Pressure Ratio Vs. Time, 80% N/\sqrt{h} , 350 Hz.

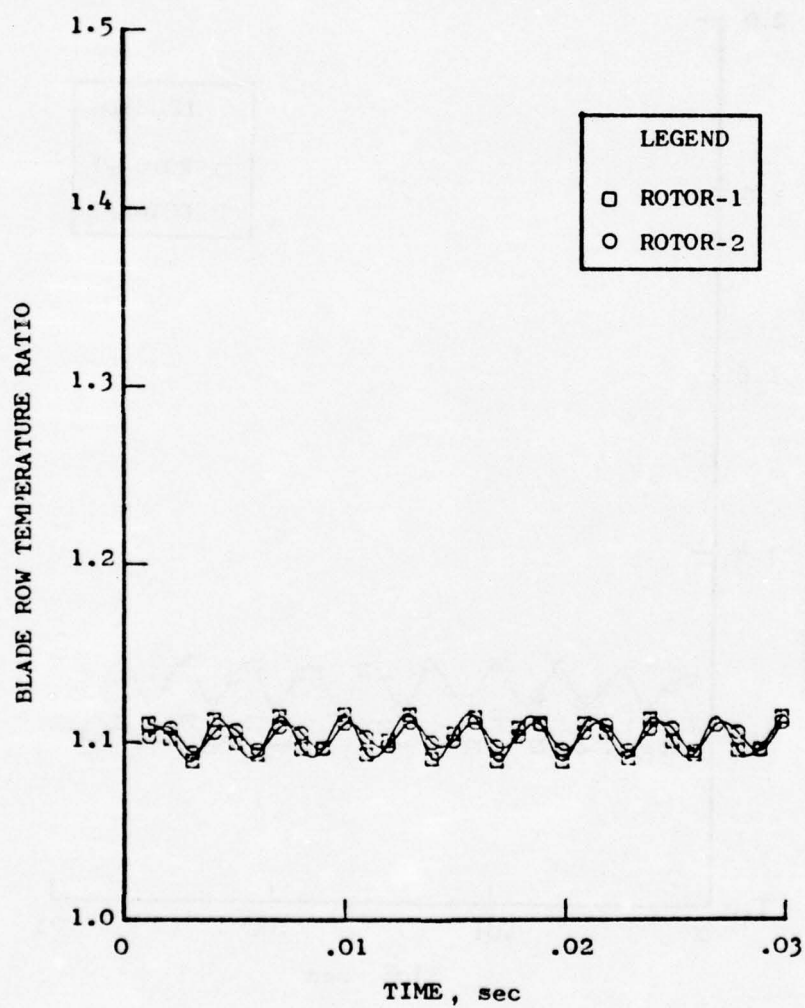


Figure 162. Blade Row Total-Temperature Ratio Vs. Time, 80% $N/\sqrt{\theta}$, 350 Hz.

APPENDIX D

AMPLITUDE TRANSMISSION CHARACTERISTICS

The IGV, Stage 1, Stage 2, and overall amplitude transmission characteristics are given for each frequency in Figures 163-169 for 100% corrected speed and in Figures 170-174 for 80% corrected speed.

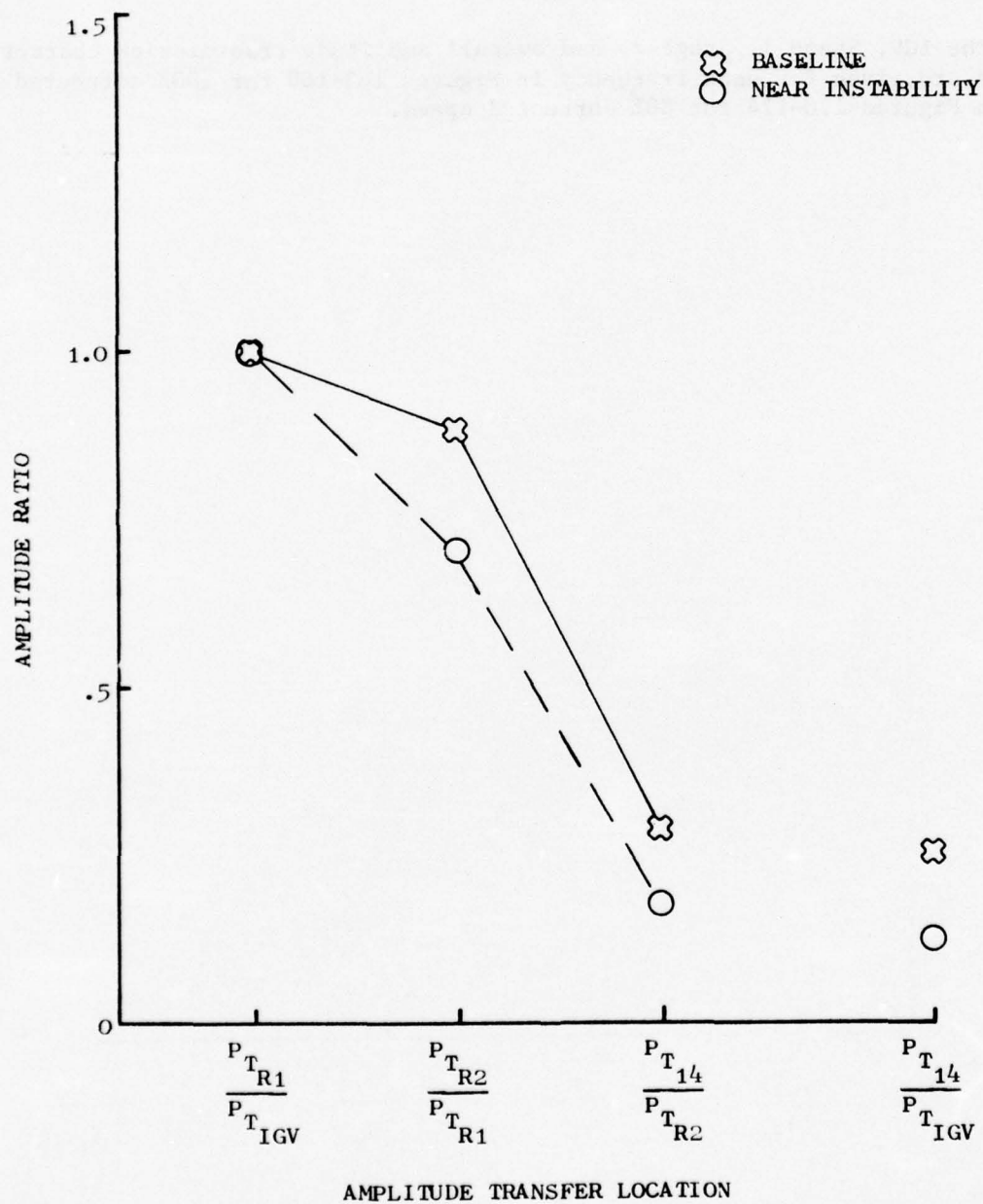


Figure 163. Amplitude Transmission Characteristics, 100% $N/\sqrt{\theta}$, 25 Hz.

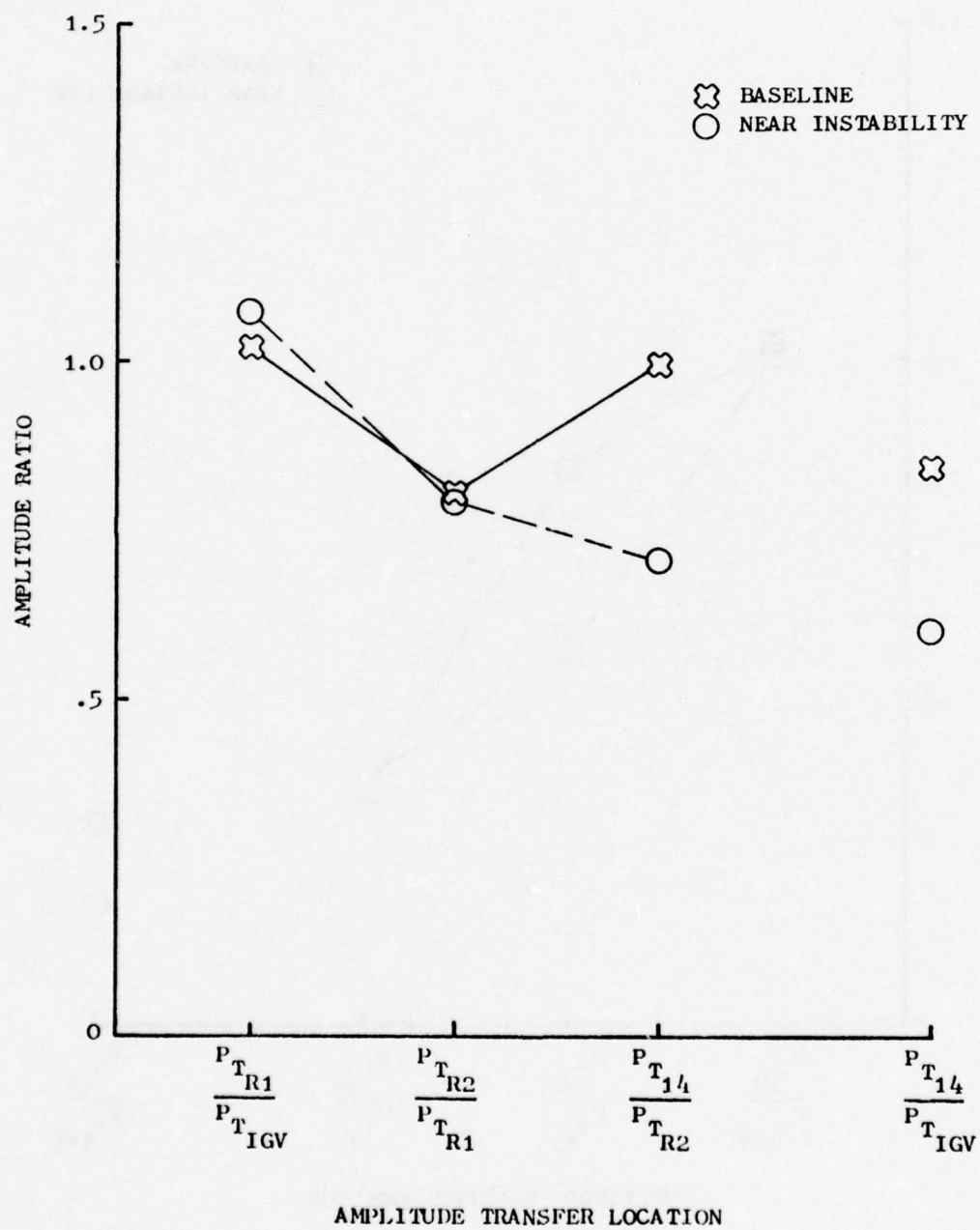


Figure 164. Amplitude Transmission Characteristics, 100% $N/\sqrt{\theta}$, 42 Hz.

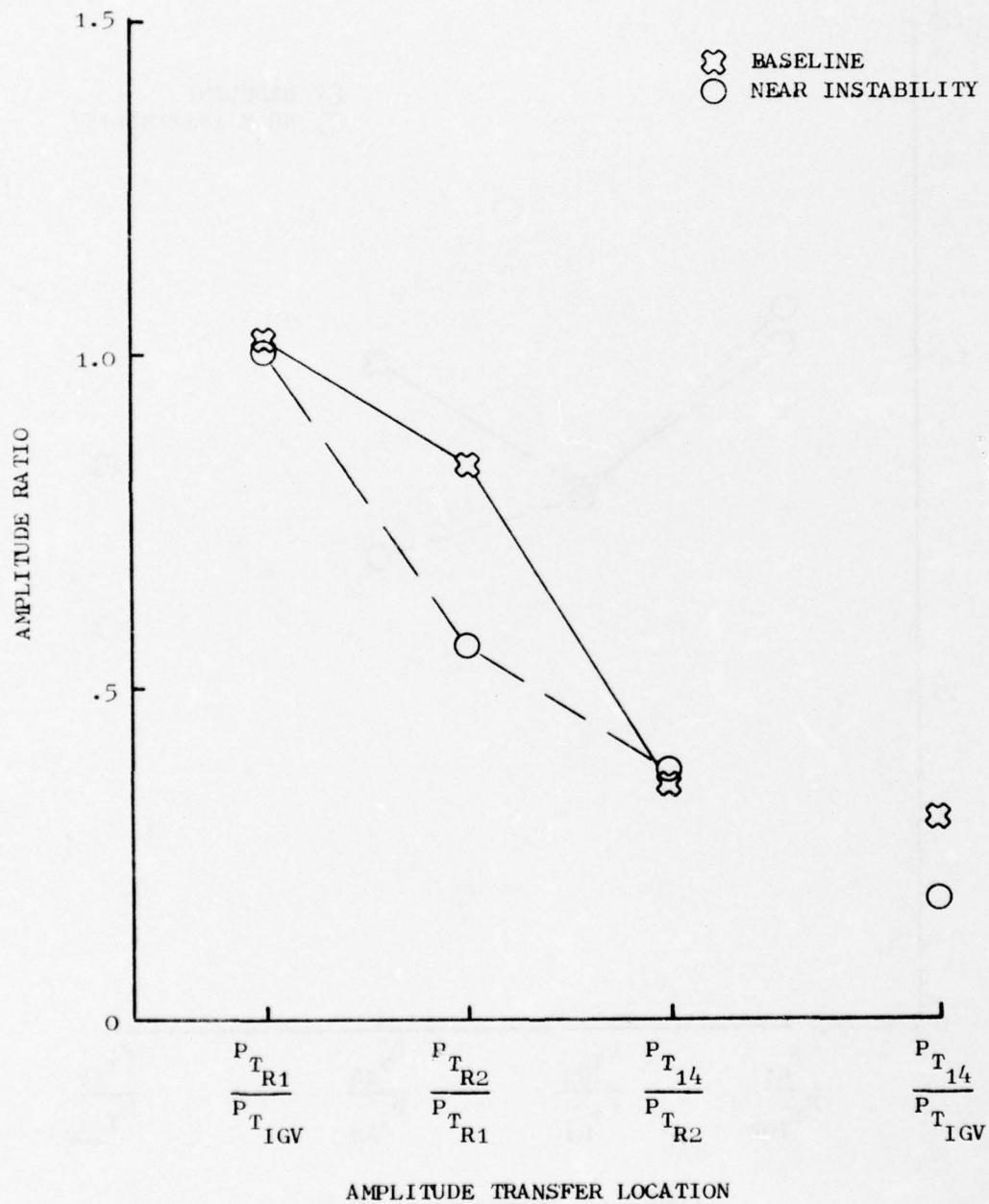


Figure 165. Amplitude Transmission Characteristics, 100% $N/\sqrt{\theta}$, 60 Hz.

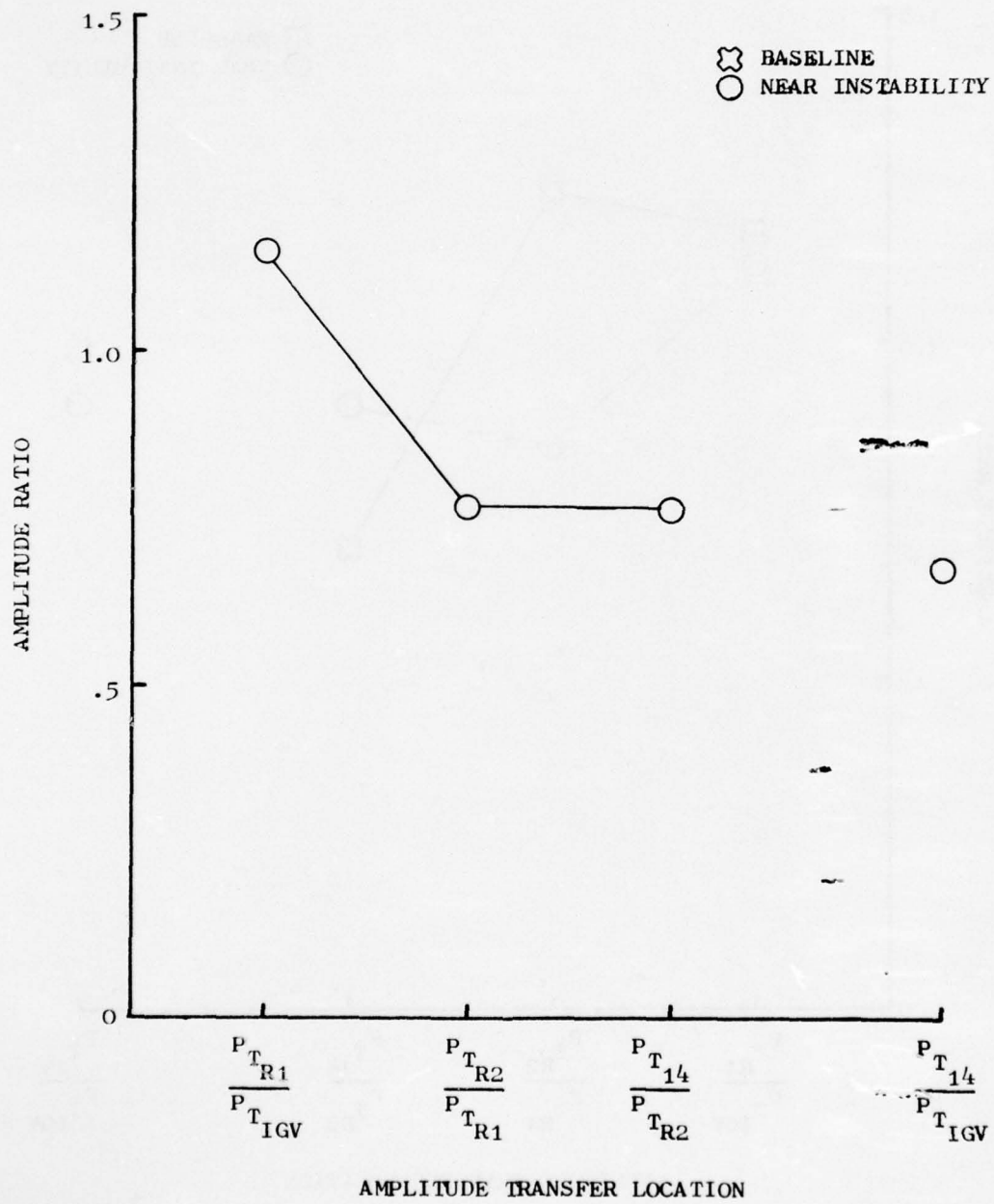


Figure 166 . Amplitude Transmission Characteristics, 100% $N/\sqrt{\theta}$, 80 Hz.

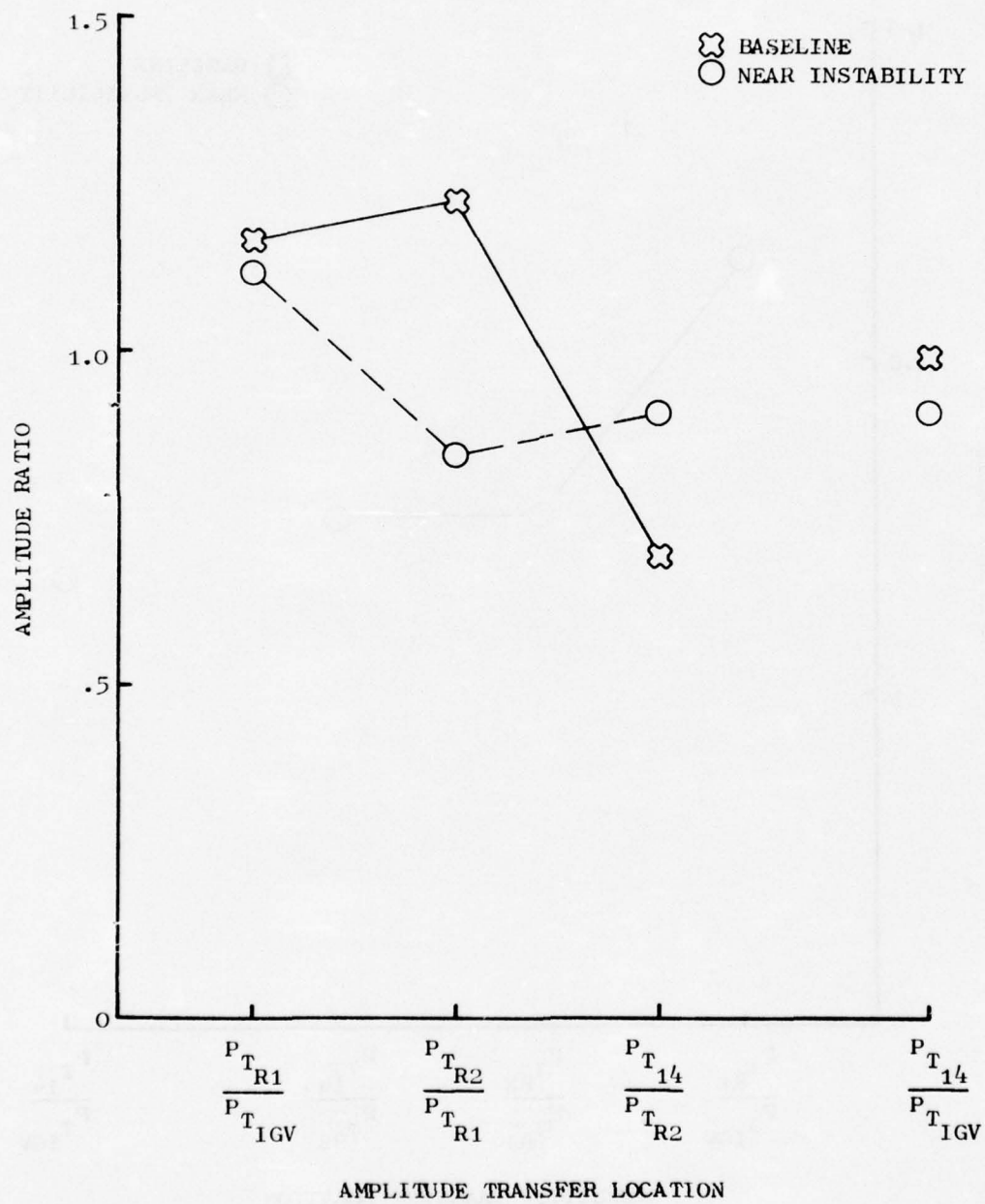


Figure 167. Amplitude Transmission Characteristics, 100% $N/\sqrt{\theta}$, 118 Hz.

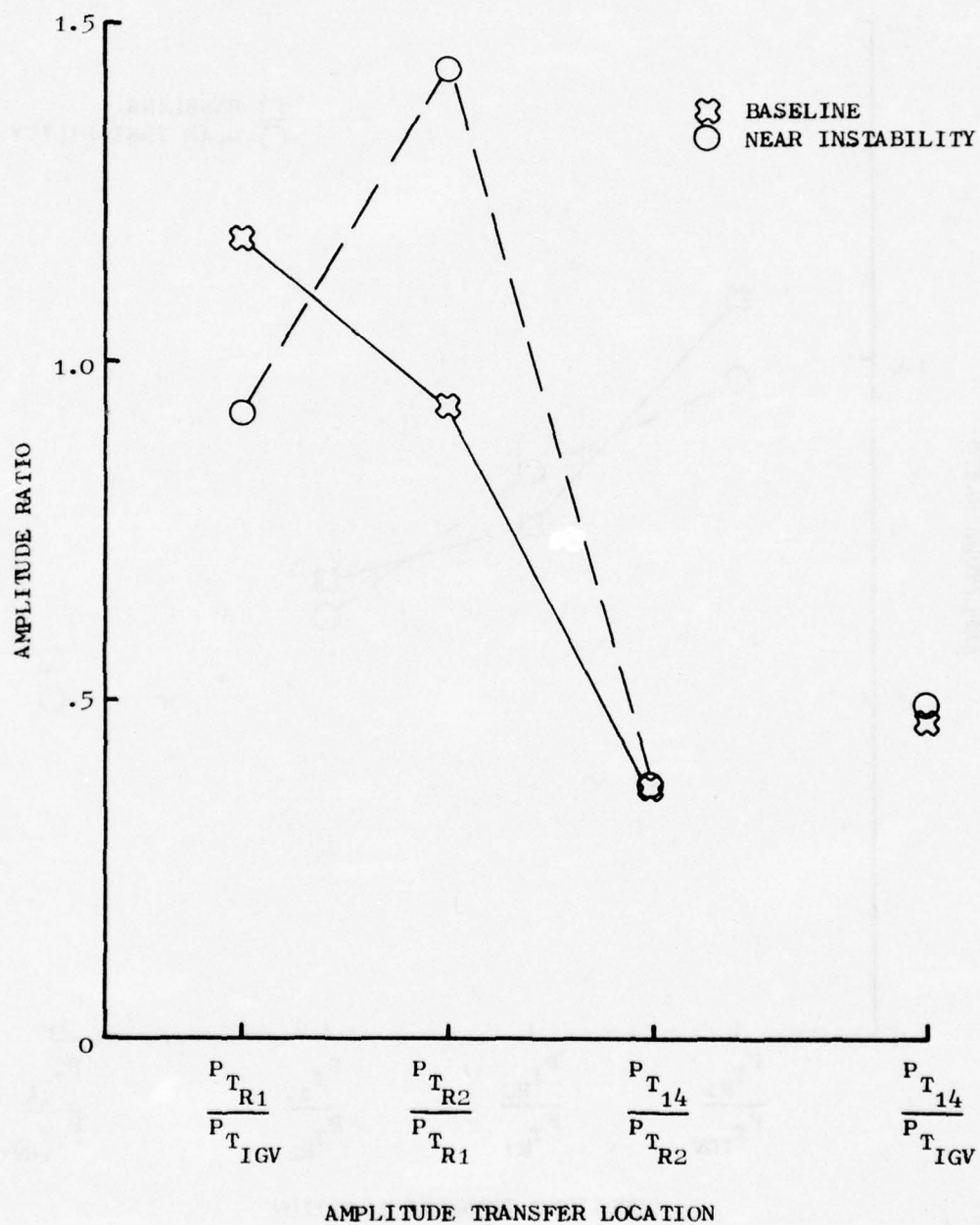


Figure 168 Amplitude Transmission Characteristics, 100% $N/\sqrt{\theta}$, 220 Hz.

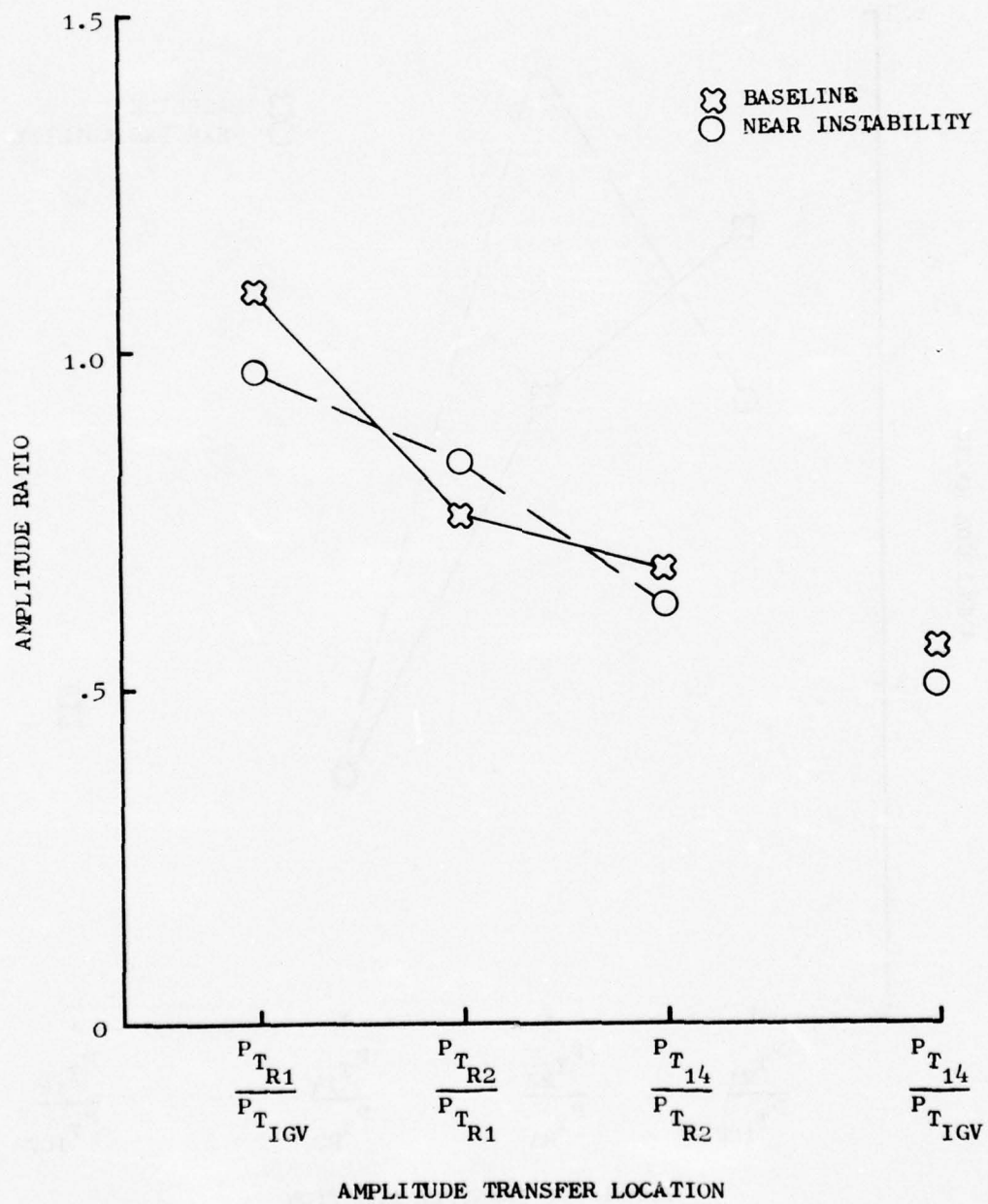


Figure 169. Amplitude Transmission Characteristics, 100% $N/\sqrt{\theta}$, 350 Hz.

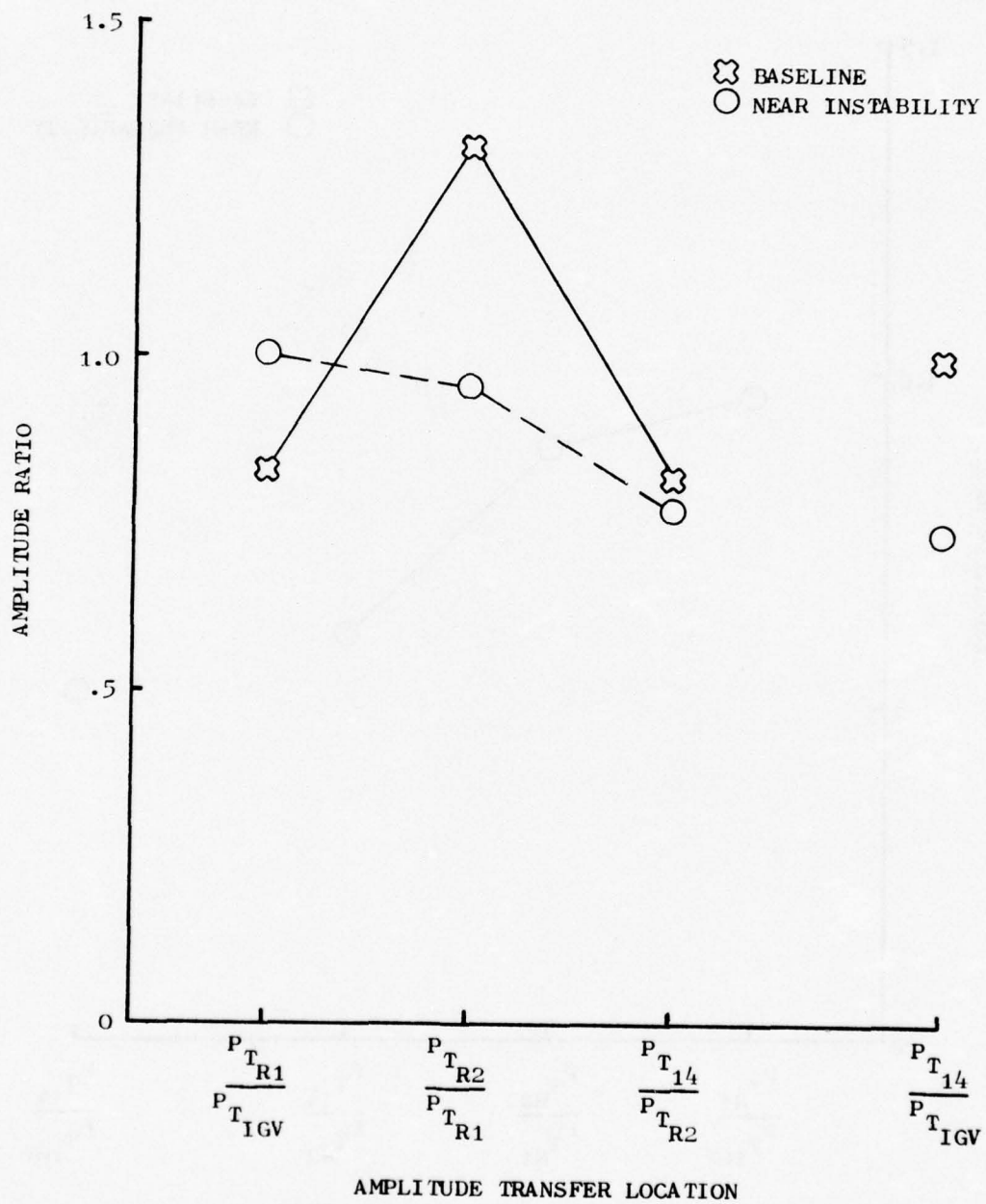


Figure 170. Amplitude Transmission Characteristics, 80% $N/\sqrt{\theta}$, 42 Hz.

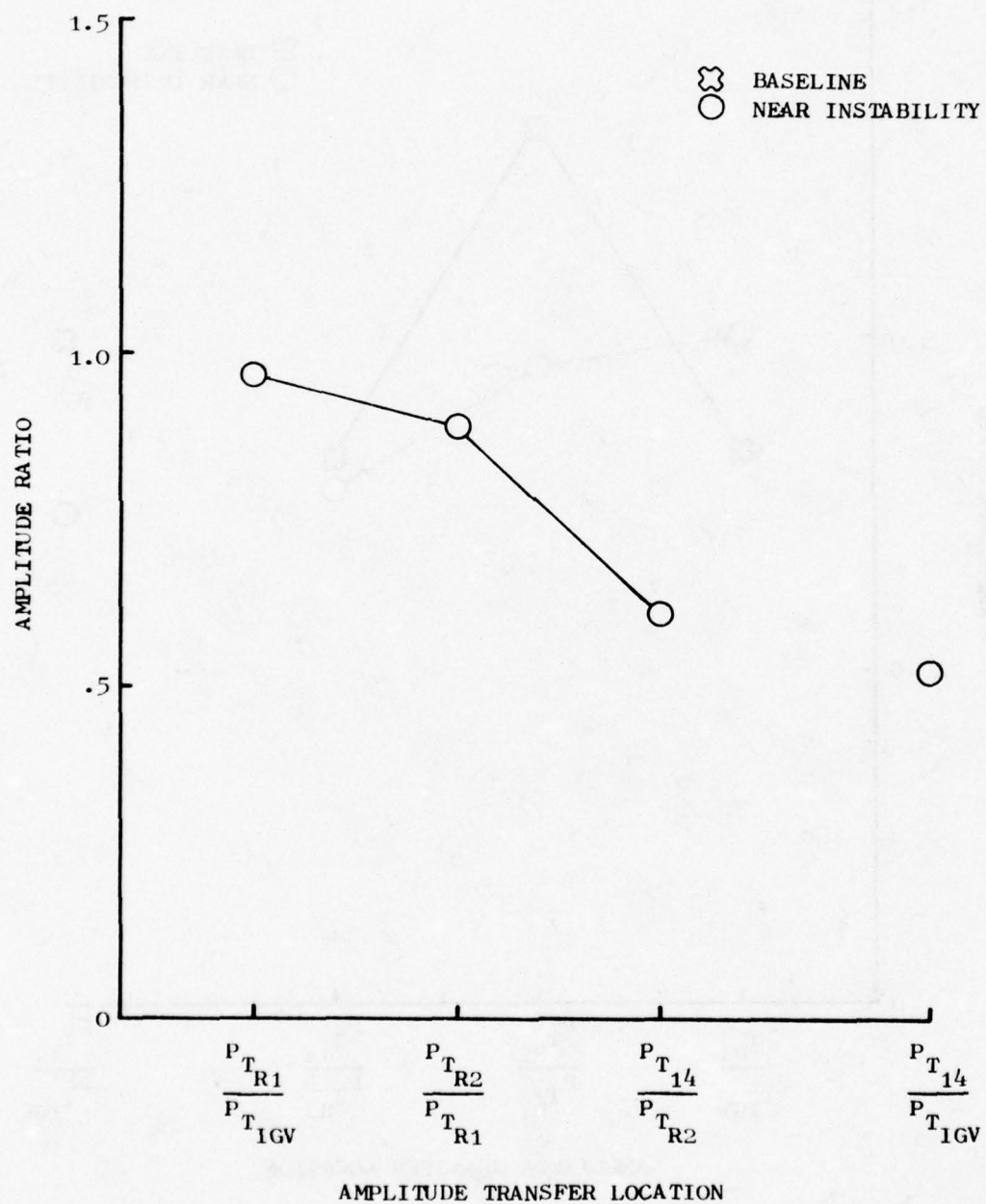


Figure 171. Amplitude Transmission Characteristics, 80% $N/\sqrt{\theta}$, 75 Hz.

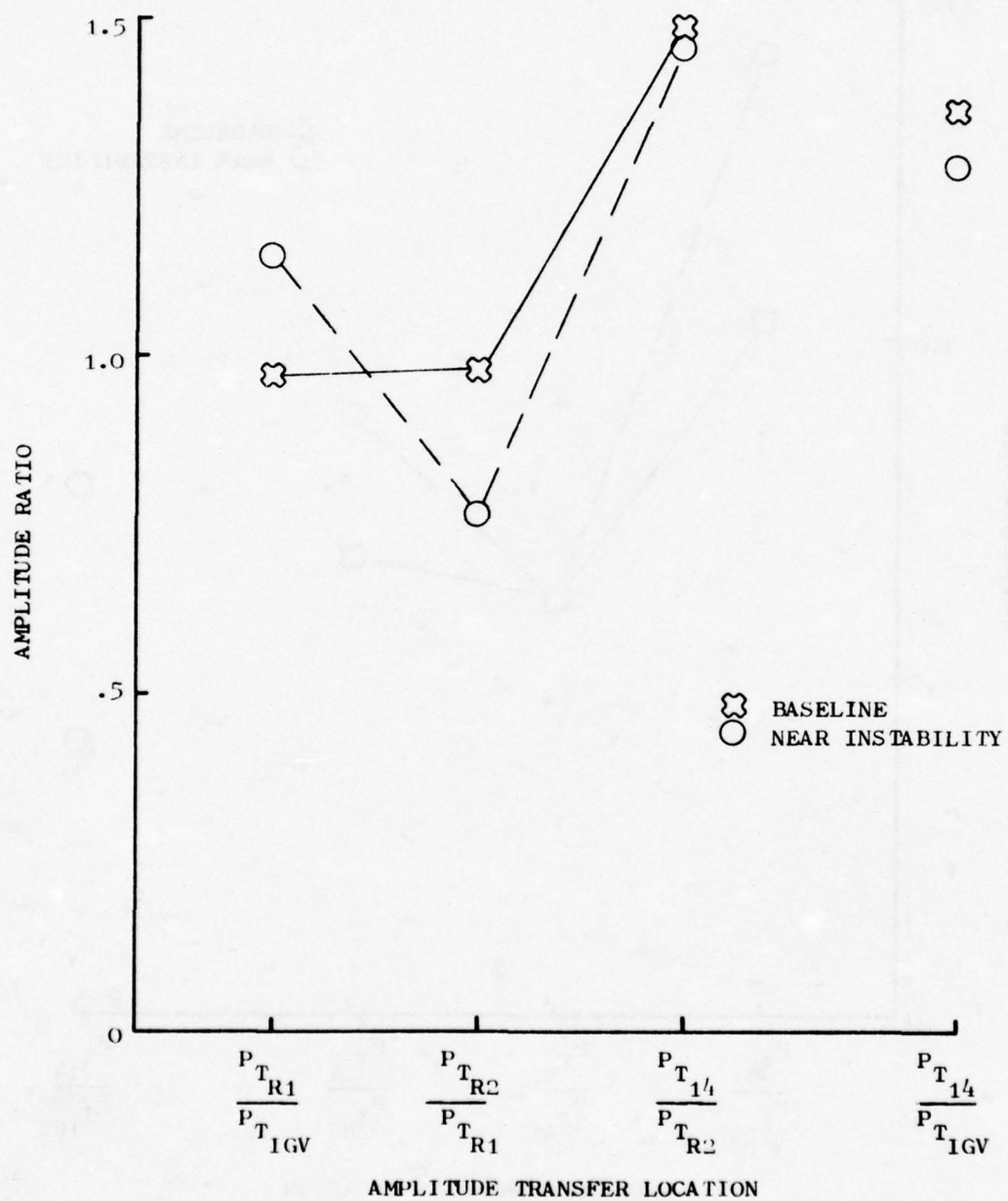


Figure 172. Amplitude Transmission Characteristics, 80% $N/\sqrt{\theta}$, 118 Hz.

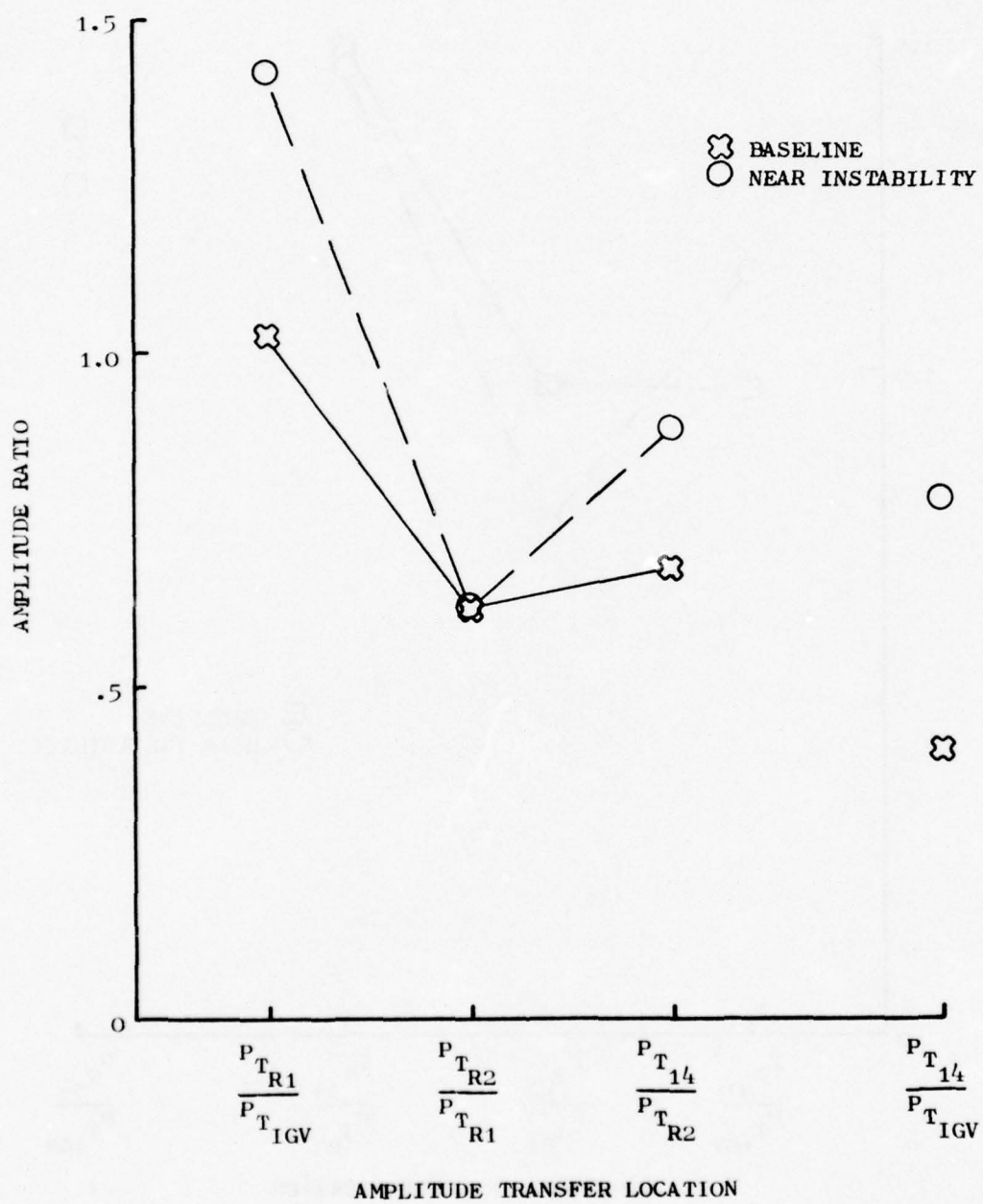


Figure 173. Amplitude Transmission Characteristics, 80% $N/\sqrt{\theta}$, 240 Hz.

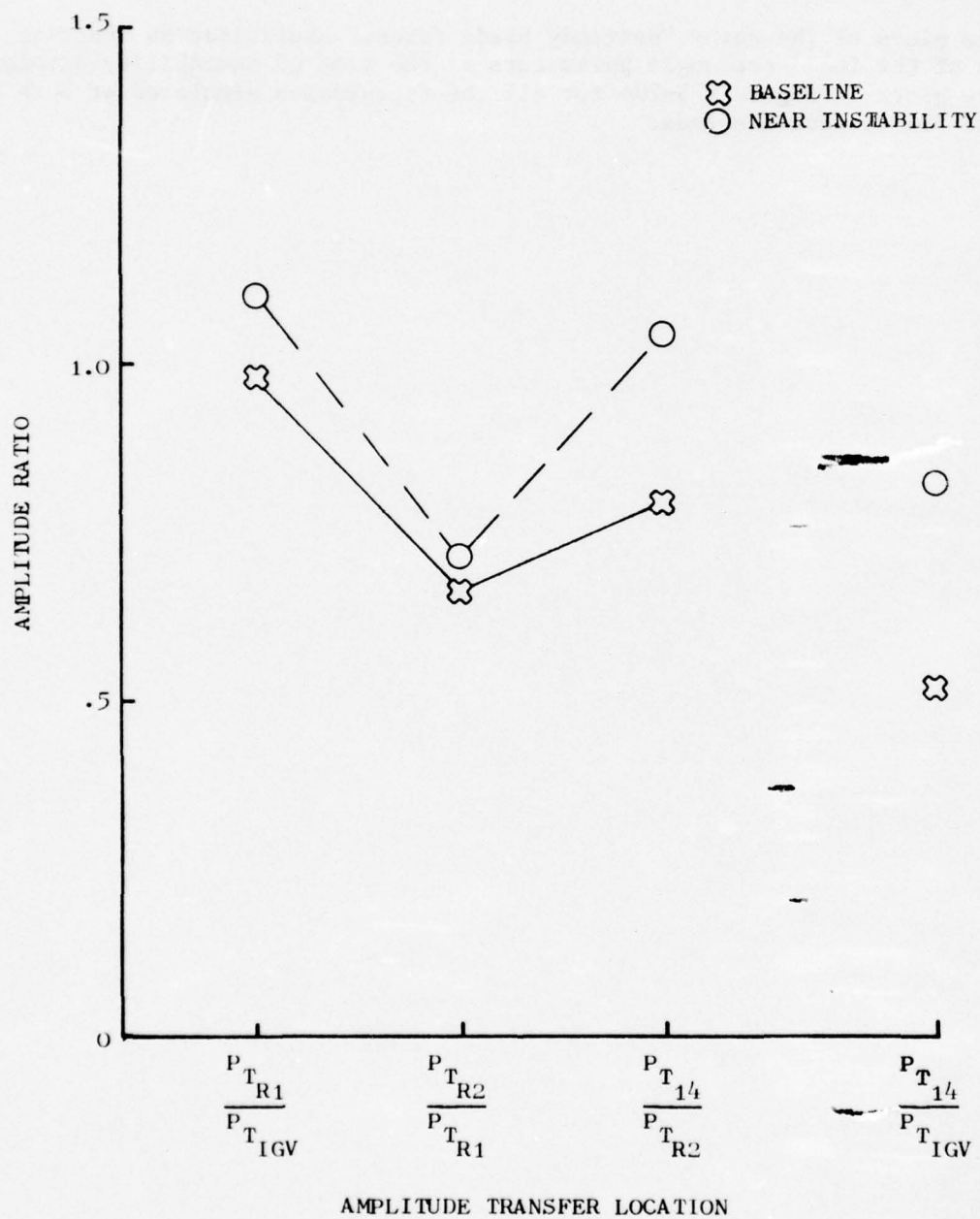


Figure 174 . Amplitude Transmission Characteristics, $20\% N/\sqrt{\theta}$, 350 Hz.

APPENDIX E

INSTABILITY IDENTIFICATION PARAMETERS

The plots of the rotor "unsteady blade force," amplification function, and tangent of the incidence angle parameters at the time of instability development are given in Figure 175-204 for all the frequencies simulated at both 100% and 80% corrected speeds.

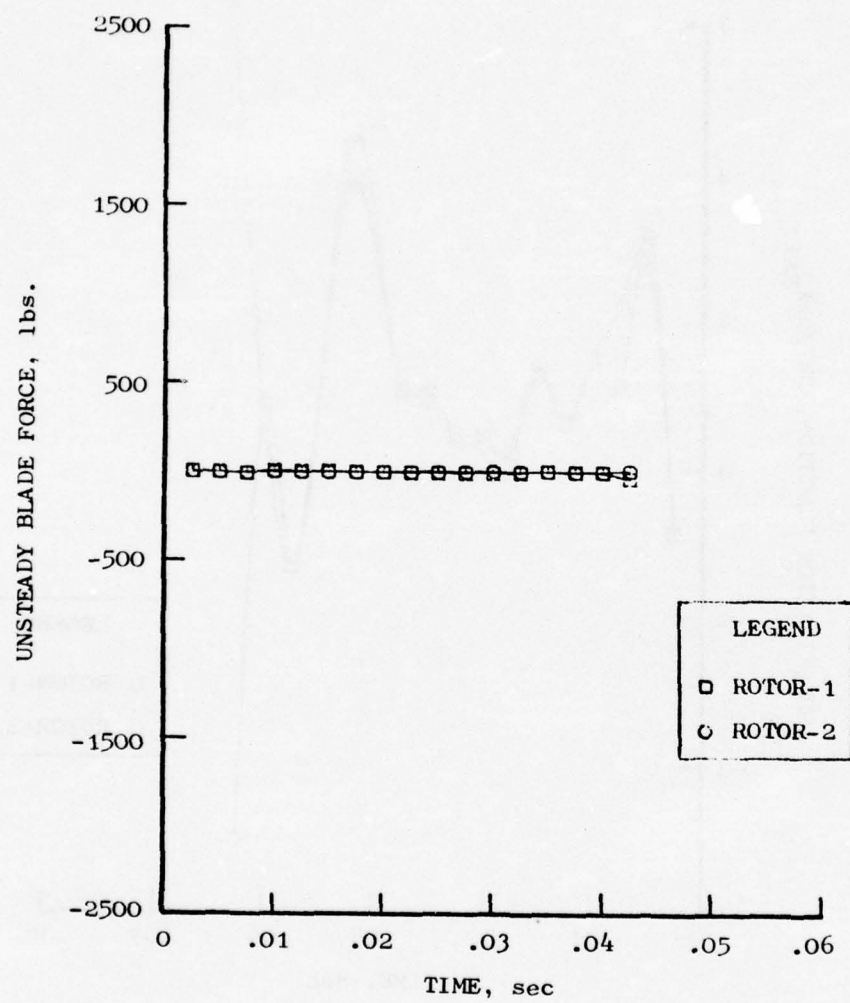


Figure 175. Unsteady Blade Force Vs. Time, $100\% N/\sqrt{\theta}$, 25 Hz.

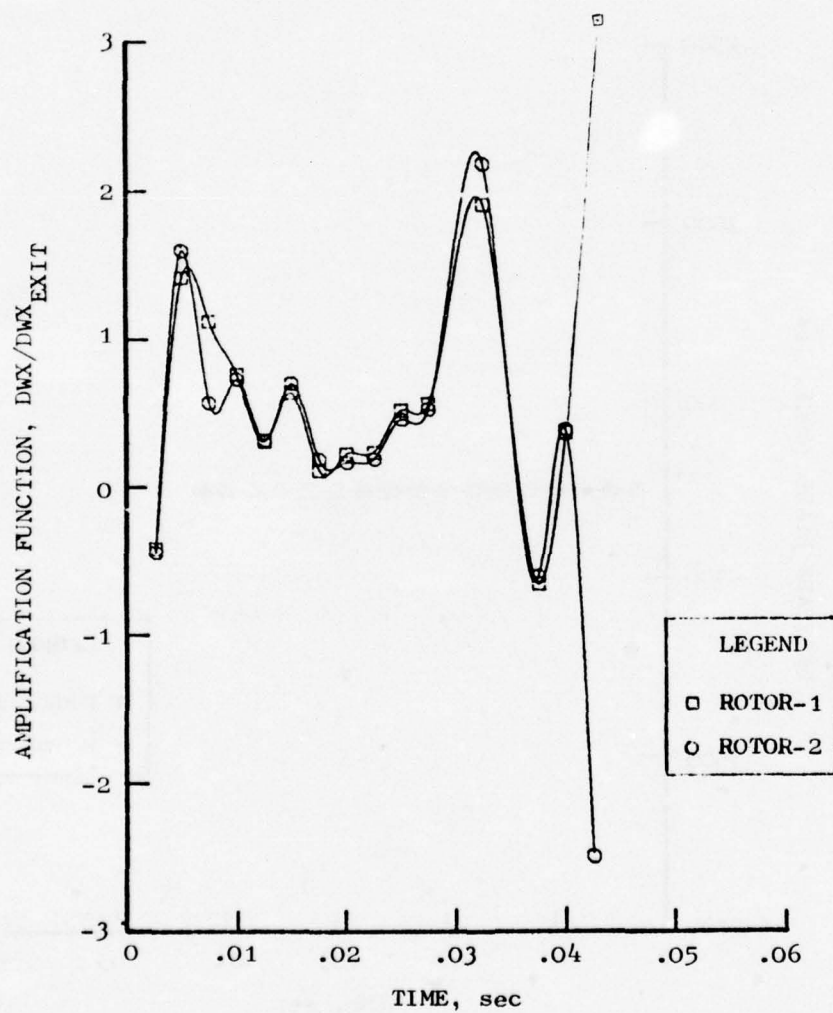


Figure 176. Amplification Function Vs. Time, $100\% N/\sqrt{\theta}$, 25 Hz.

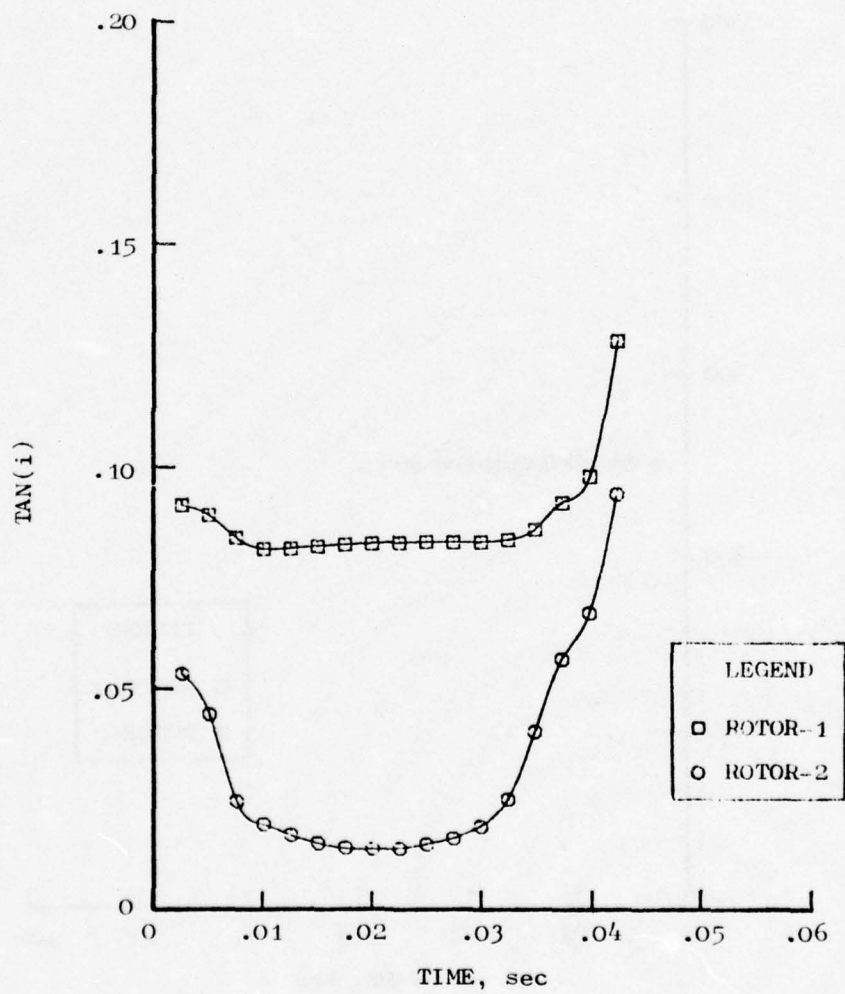


Figure 177. Tangent of Incidence Angle Vs. Time, 100% $N/\sqrt{\theta}$, 25 Hz.

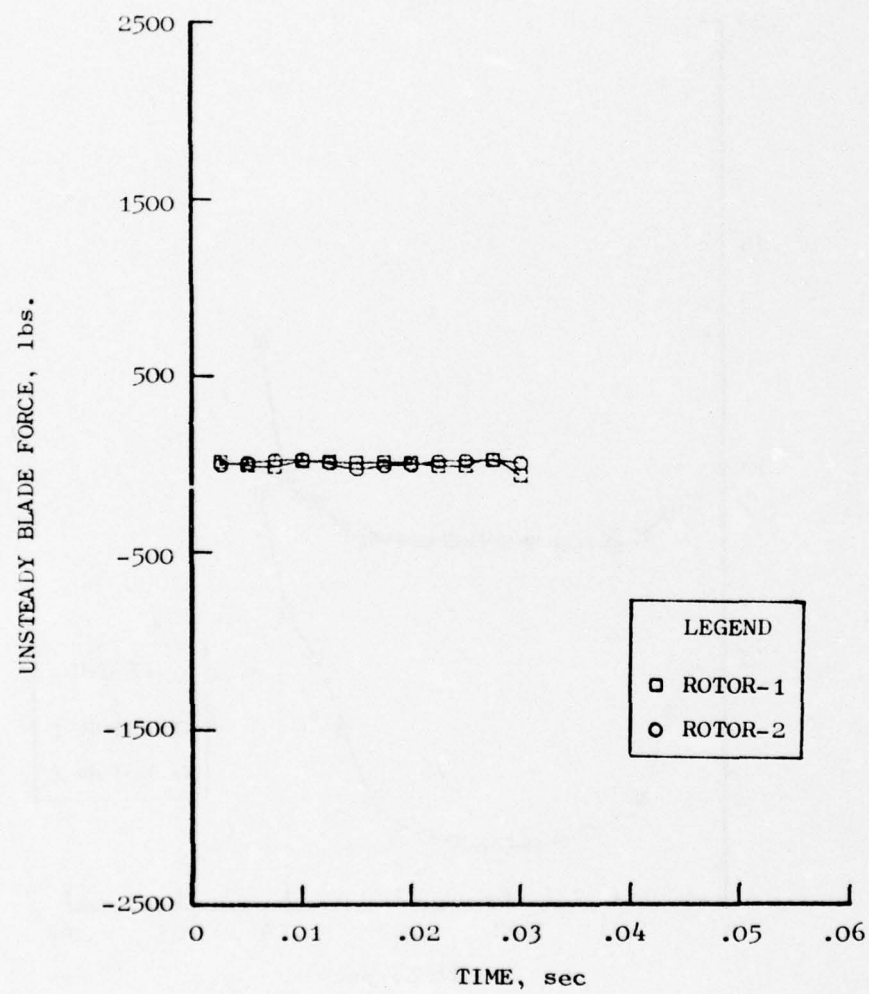


Figure 178. Unsteady Blade Force Vs. Time, $100\% N/\sqrt{\theta}$, 60 Hz.

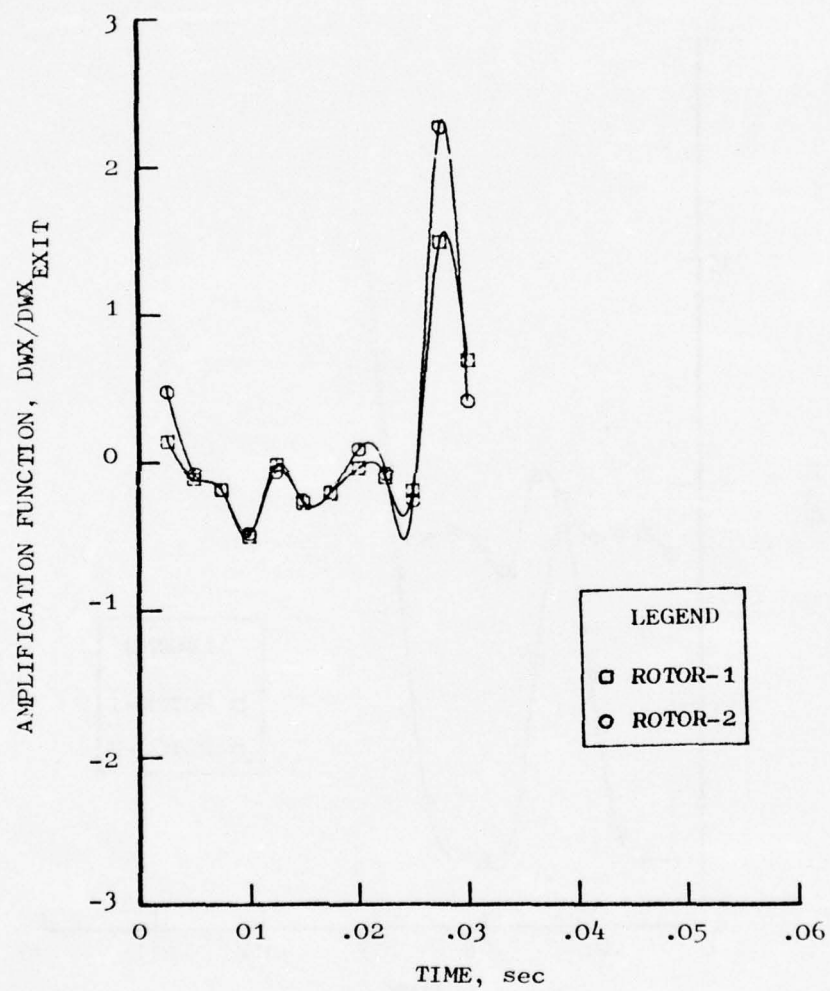


Figure 179. Amplification Function Vs. Time, $100\% N/\sqrt{\theta}$, 60 Hz.

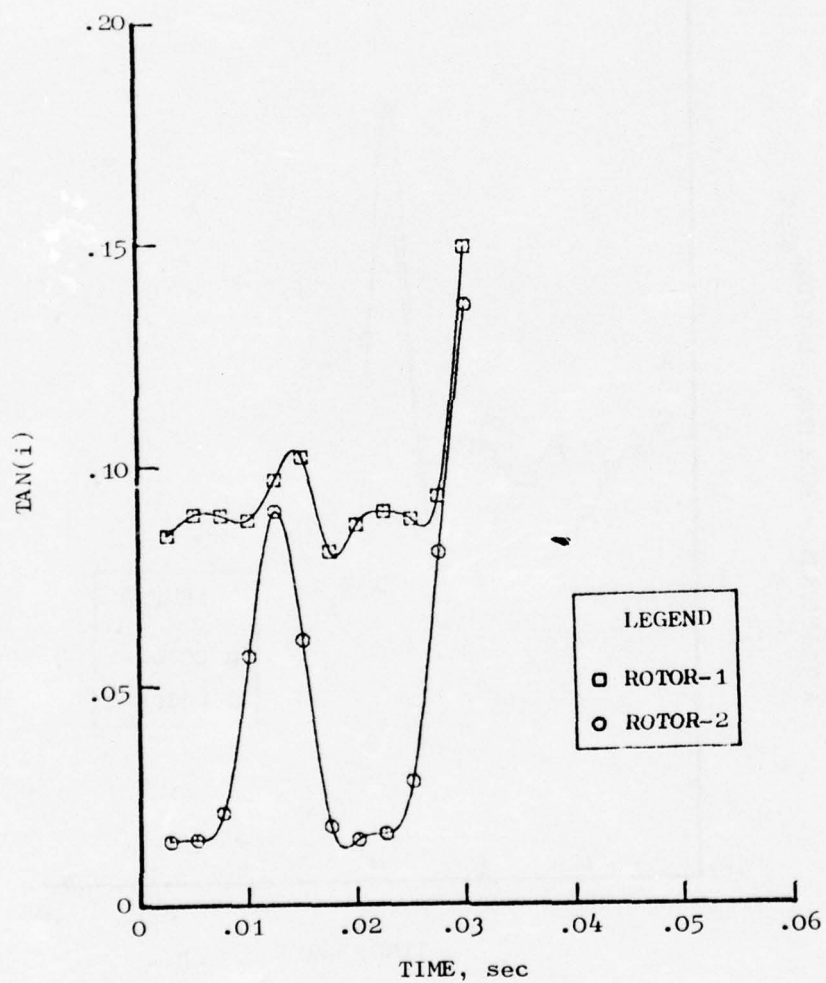


Figure 180. Tangent of Incidence Angle Vs. Time,
 $100\% N/\sqrt{\theta}$, 50 Hz.

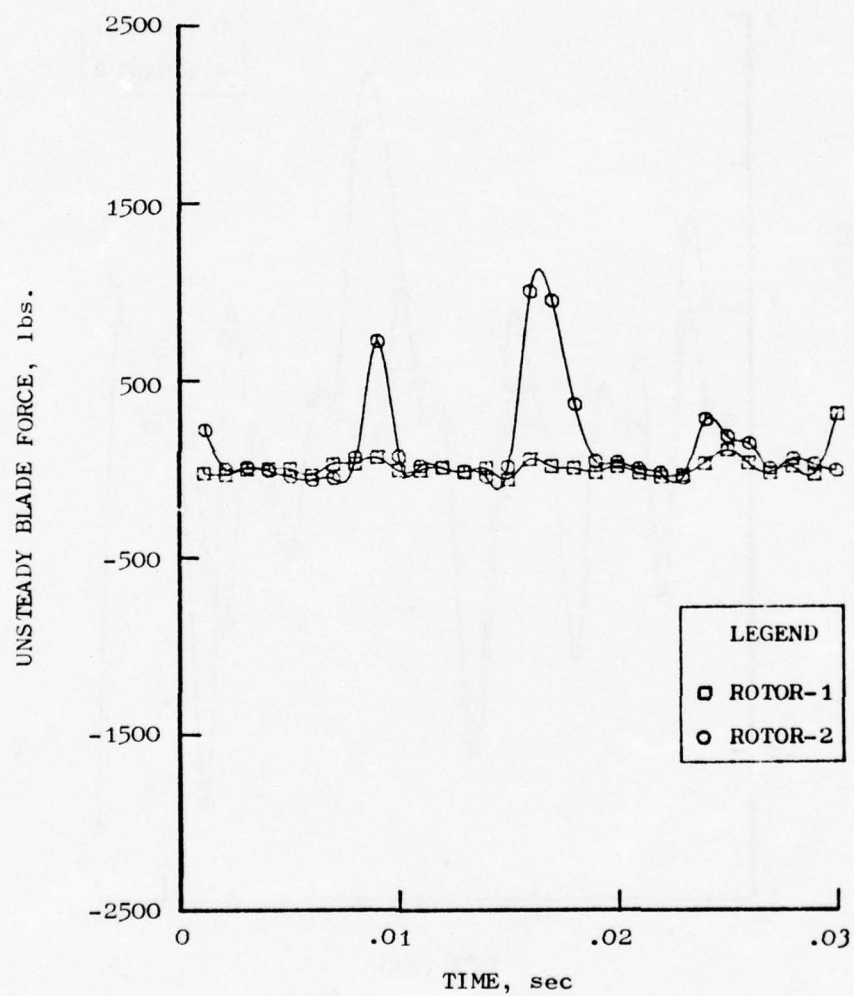


Figure 181. Unsteady Blade Force Vs. Time , 100% $N/\sqrt{\theta}$, 118 Hz.

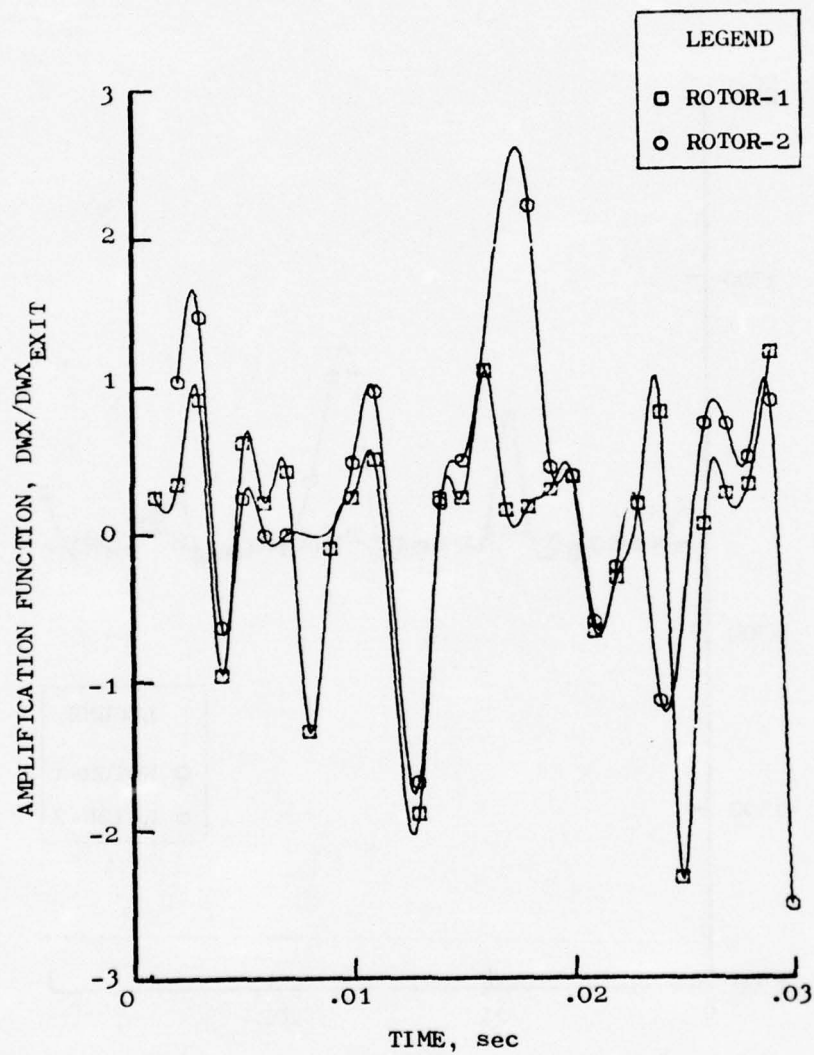


Figure 182. Amplification Function Vs. Time , $100\% N/\sqrt{\theta}$, 118 Hz.

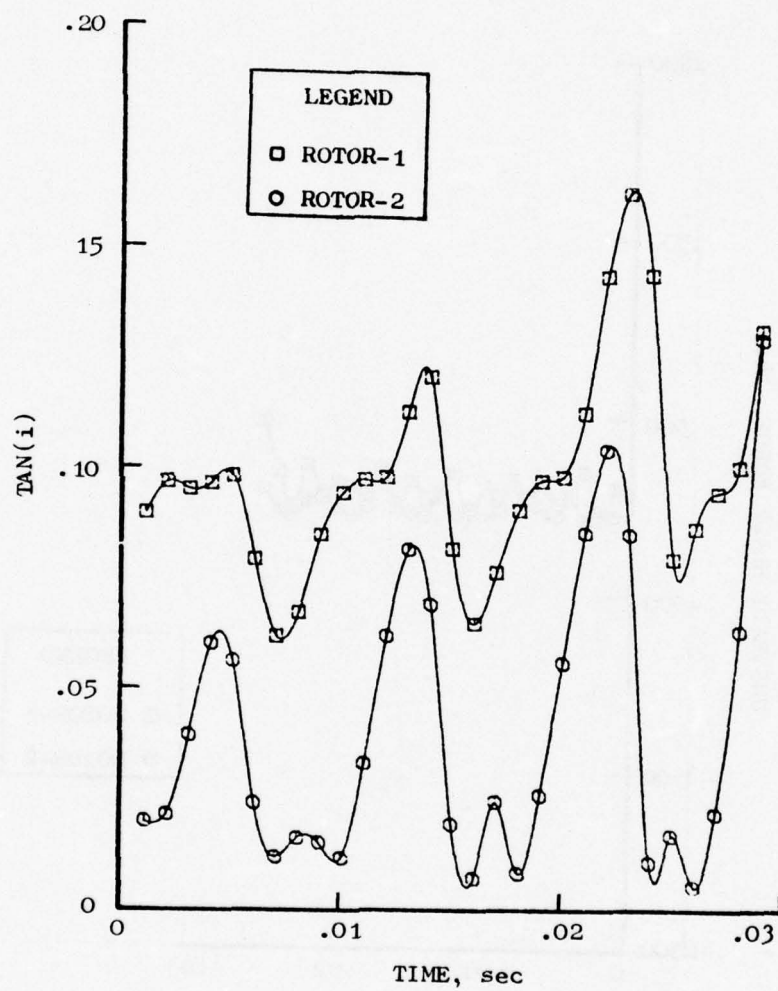


Figure 183. Tangent of Incidence Angle Vs. Time, 100% $N/\sqrt{\theta}$, 118 Hz.

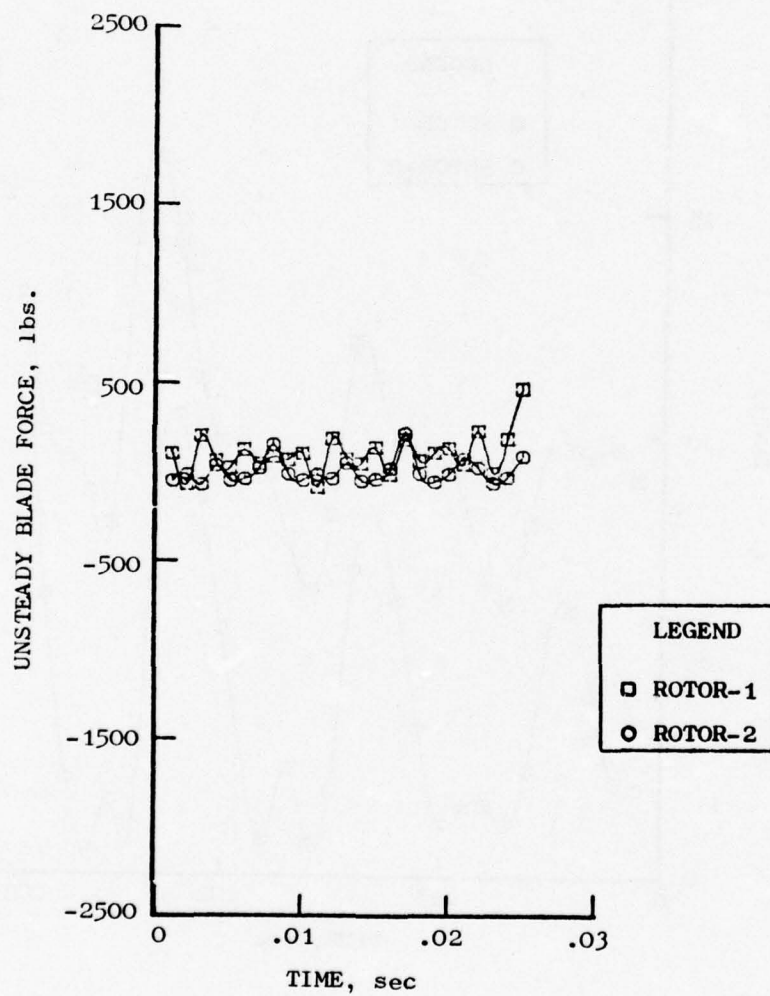


Figure 184. Unsteady Blade Force Vs. Time,
 $100\% N/\sqrt{\theta}$, 220 Hz.

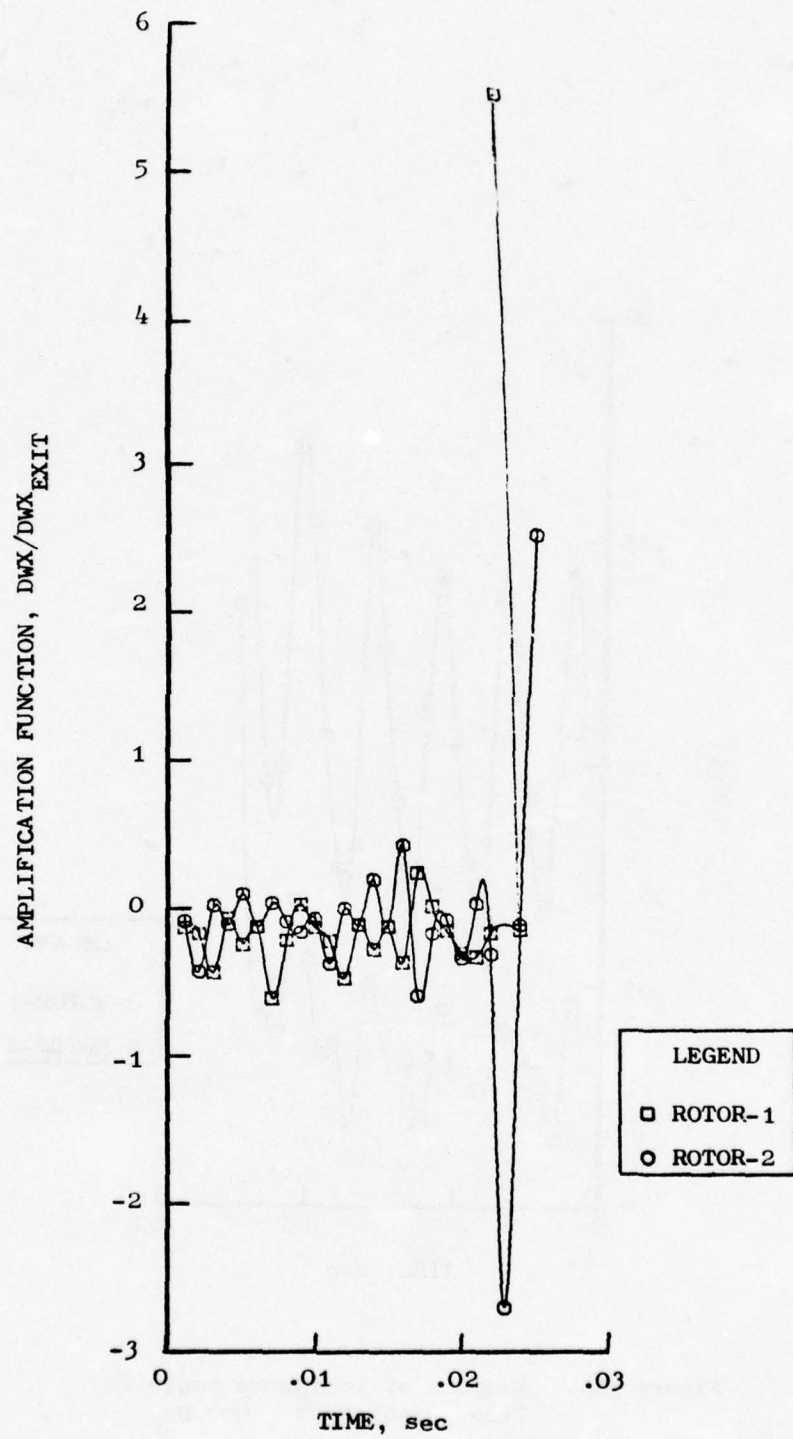


Figure 185. Amplification Function Vs. Time ,
100% $N/\sqrt{\theta}$, 220 Hz.

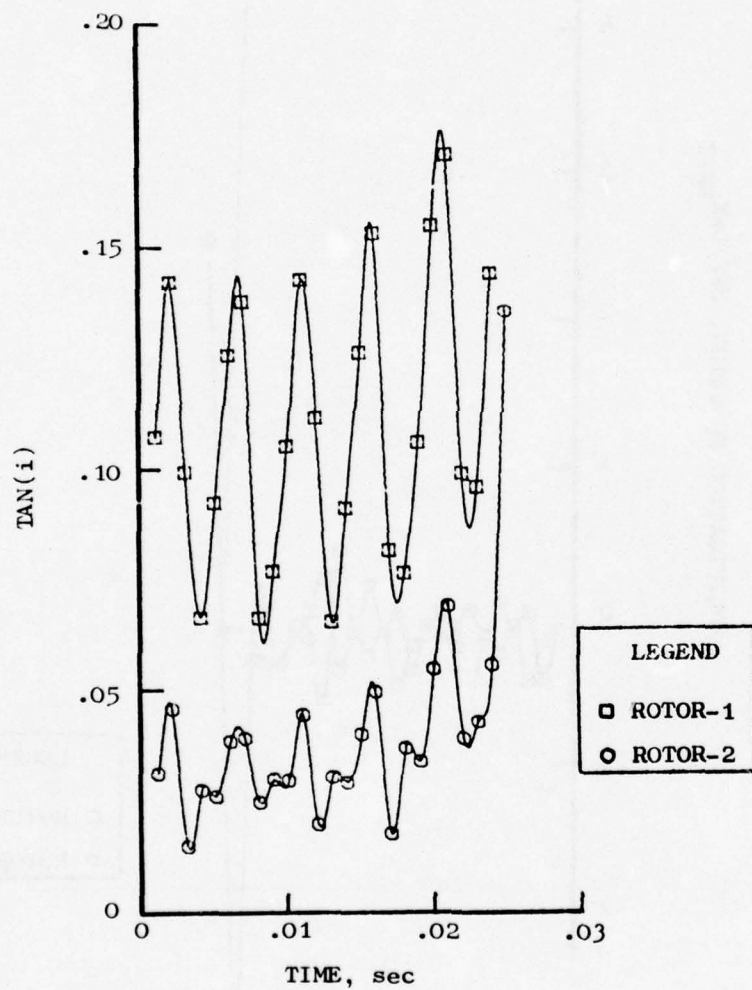


Figure 186. Tangent of Incidence Angle Vs. Time, $100\% N/\sqrt{\theta}$, 220 Hz.

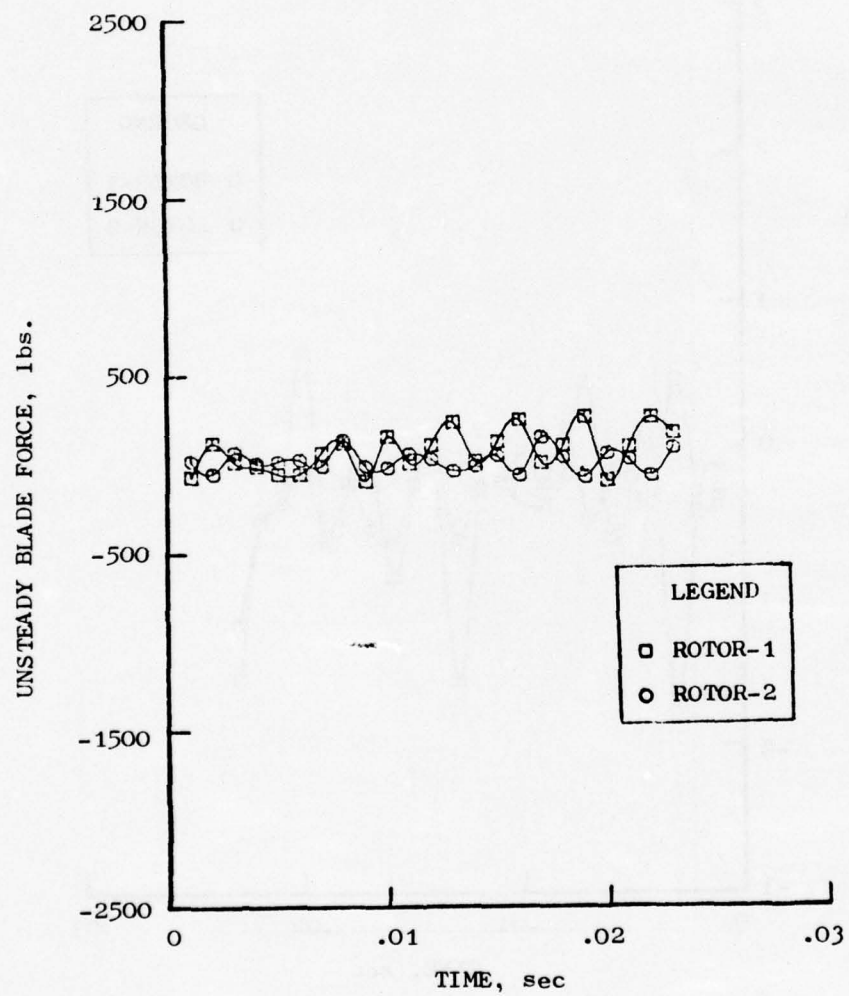


Figure 187. Unsteady Blade Force Vs. Time , $100\% N/\sqrt{\theta}$, 350 Hz.

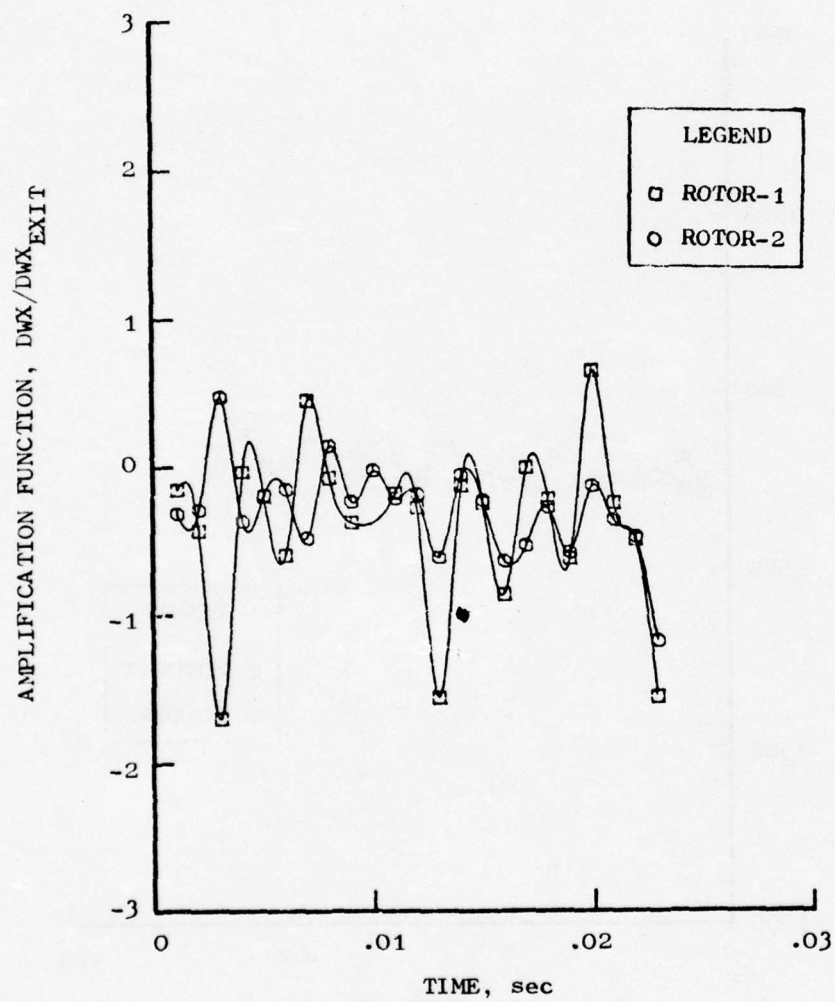


Figure 188. Amplification Function Vs. Time, $100\% N/\sqrt{\theta}$, 350 Hz.

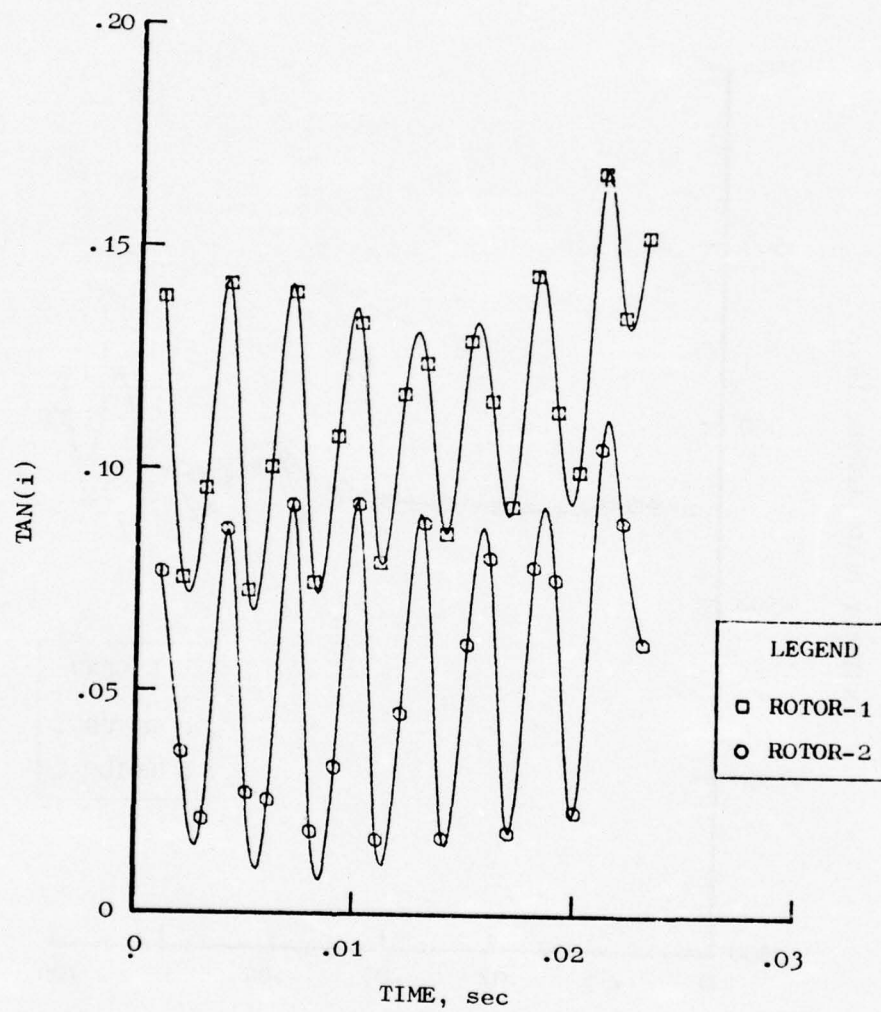


Figure 189. Tangent of Incidence Angle Vs. Time, $100\% N/\sqrt{\theta}$, 350 Hz.

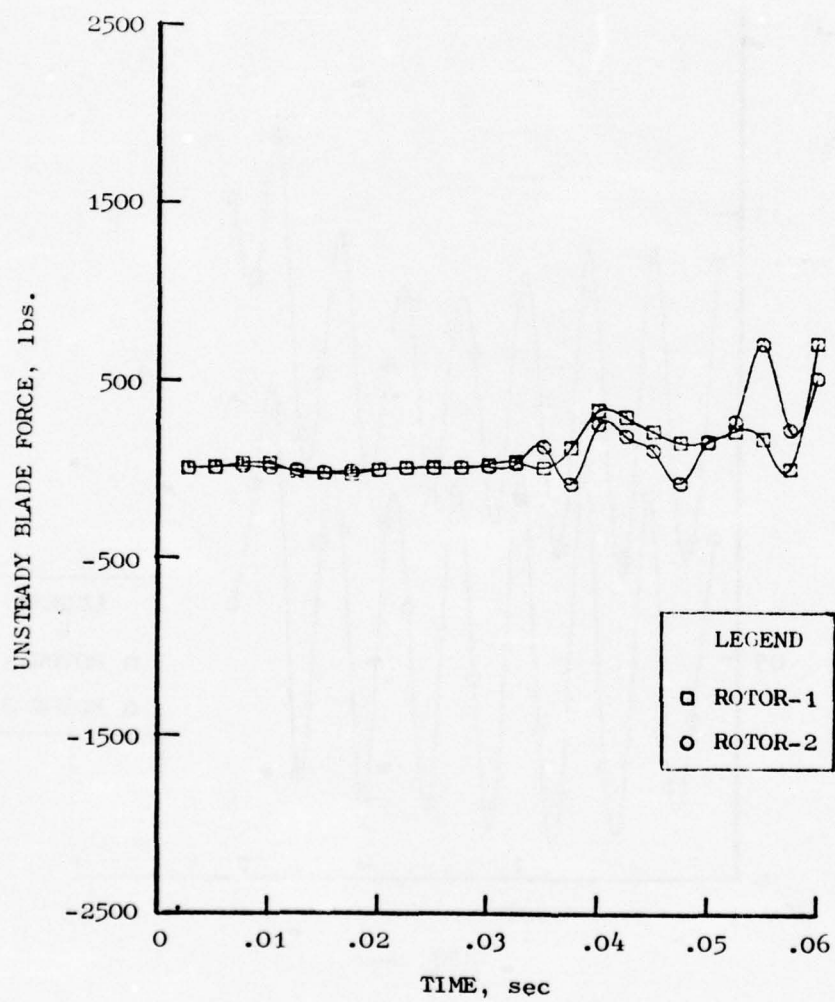


Figure 190. Unsteady Blade Force Vs. Time , $80\% N/\sqrt{\theta}$, 42 Hz.

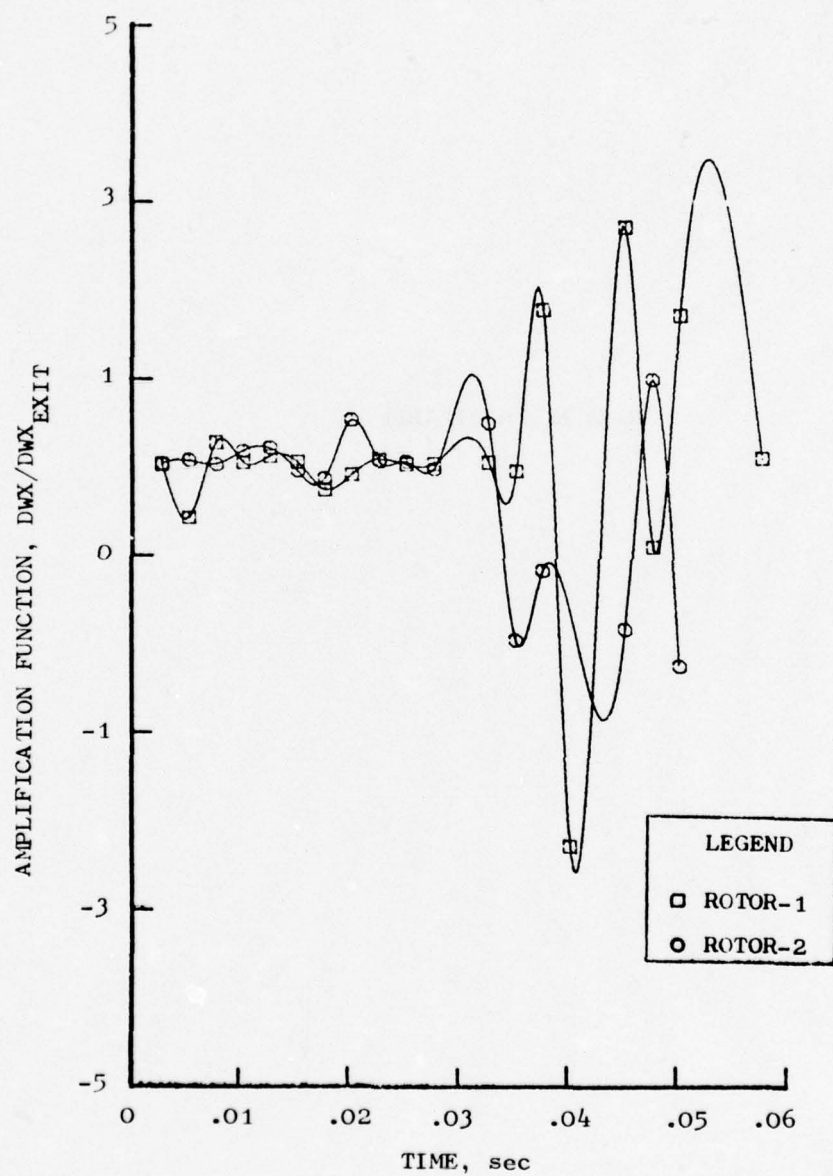


Figure 191. Amplification Function Vs. Time , $80\% N/\sqrt{\theta}$, 42 Hz.

DATA NOT AVAILABLE

Figure 192. Tangent of Incidence Angle Vs. Time, $80\% N/\sqrt{\theta}$, 42 Hz.

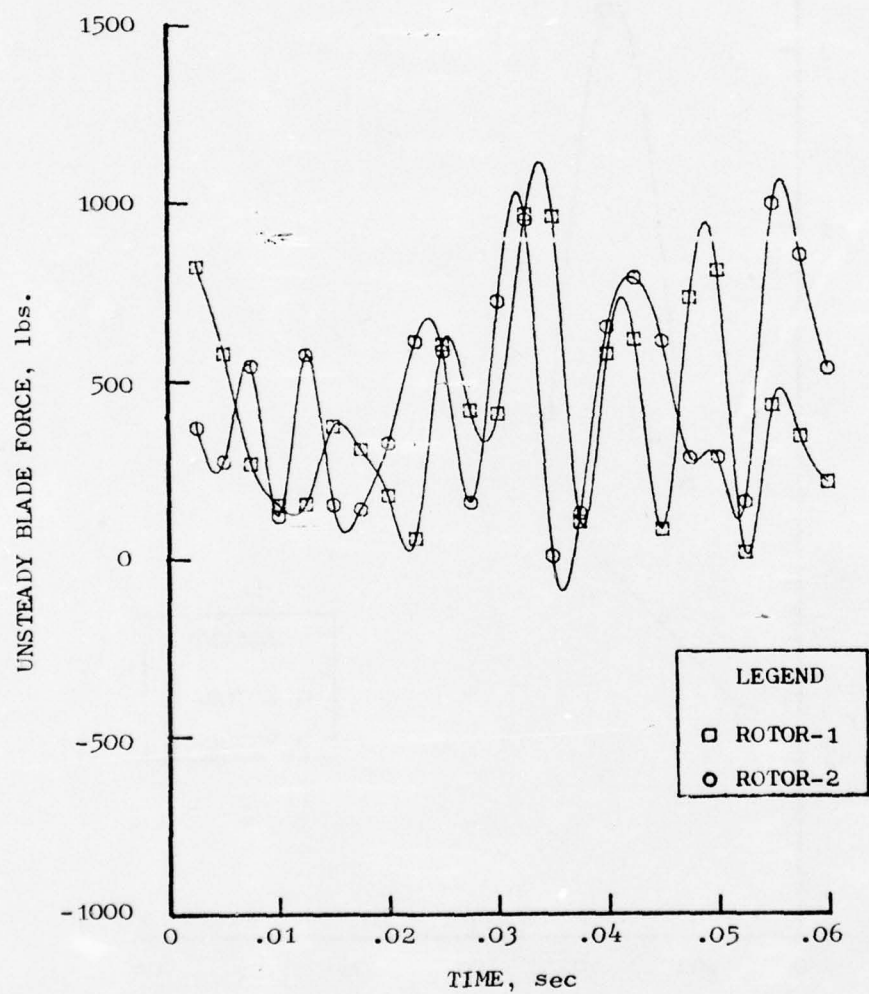


Figure 193. Unsteady Blade Force Vs. Time, $80\% N/\sqrt{\theta}$, 75 Hz.

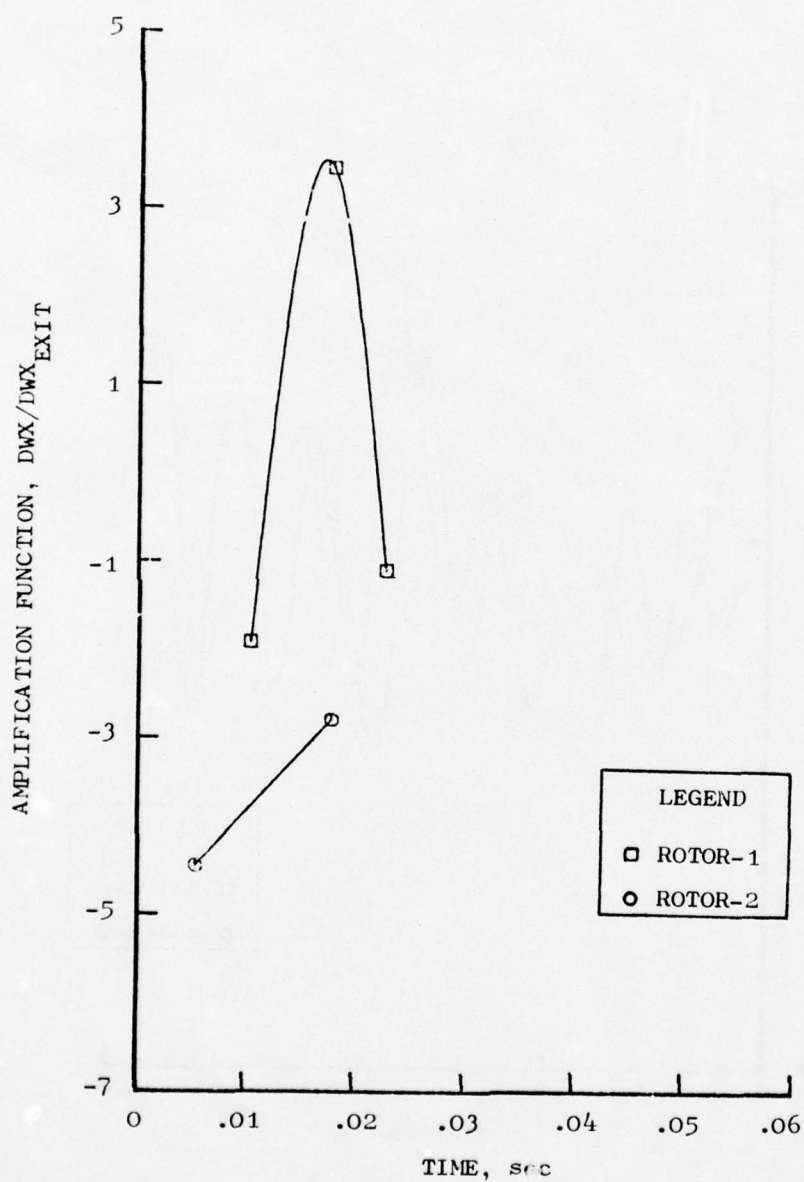


Figure 194. Amplification Function Vs. Time , $80\% N/\sqrt{\theta}$, 75 Hz.

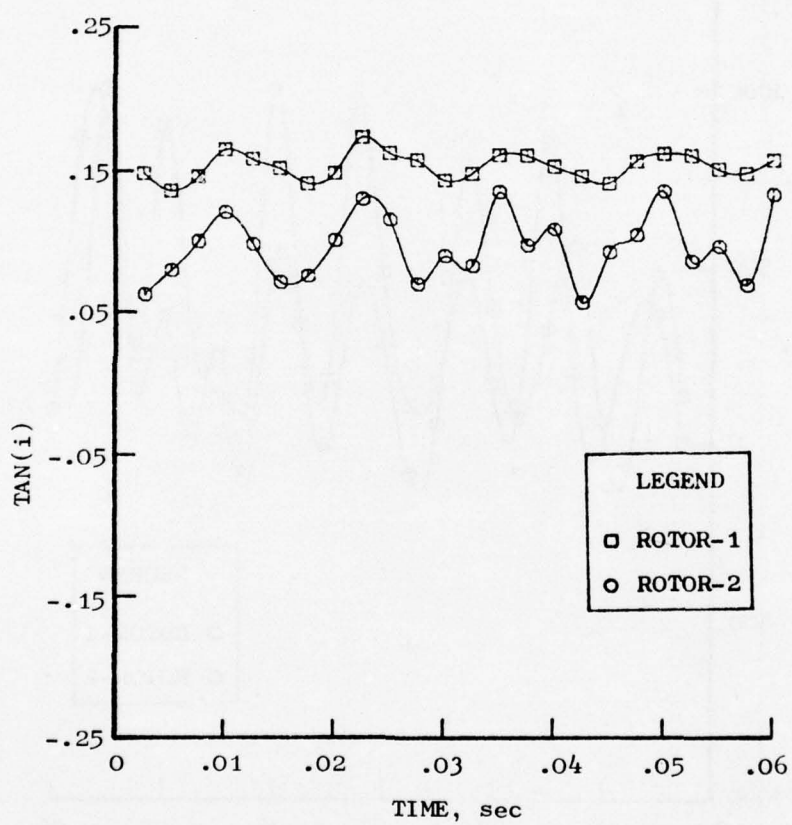


Figure 195. Tangent of Incidence Angle Vs. Time, 80% $N/\sqrt{\theta}$, 75 Hz.

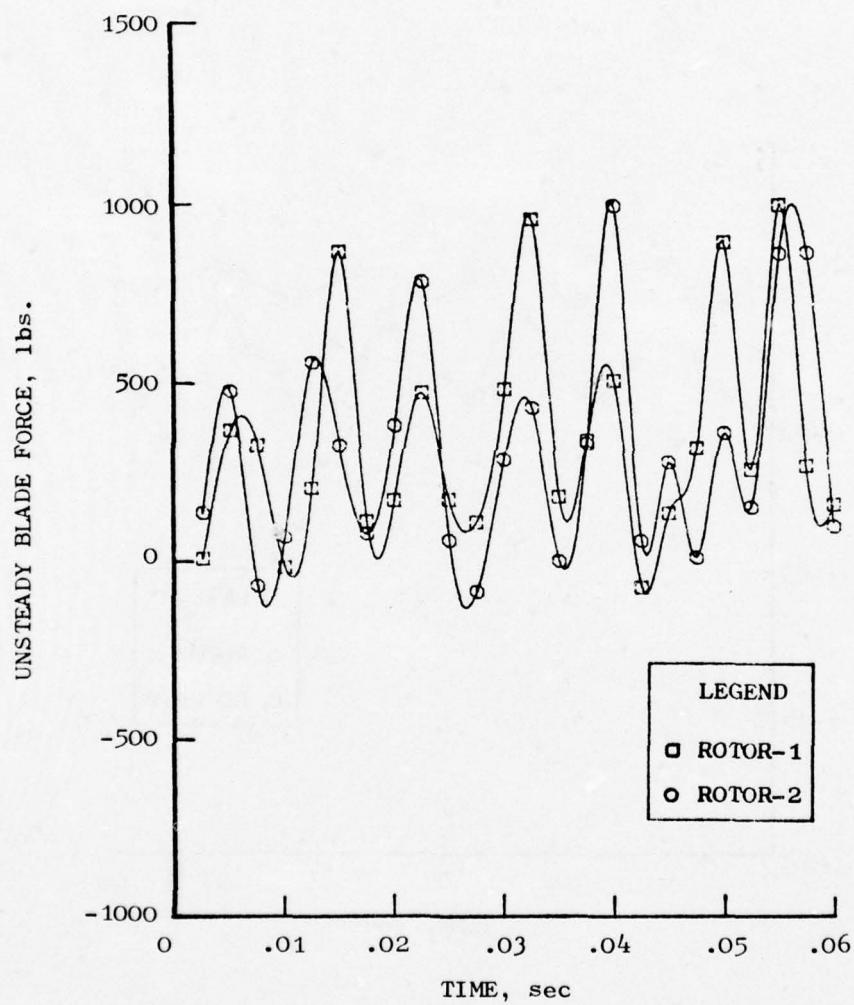


Figure 196. Unsteady Blade Force Vs. Time, $80\% N/\sqrt{\theta}$, 118 Hz.

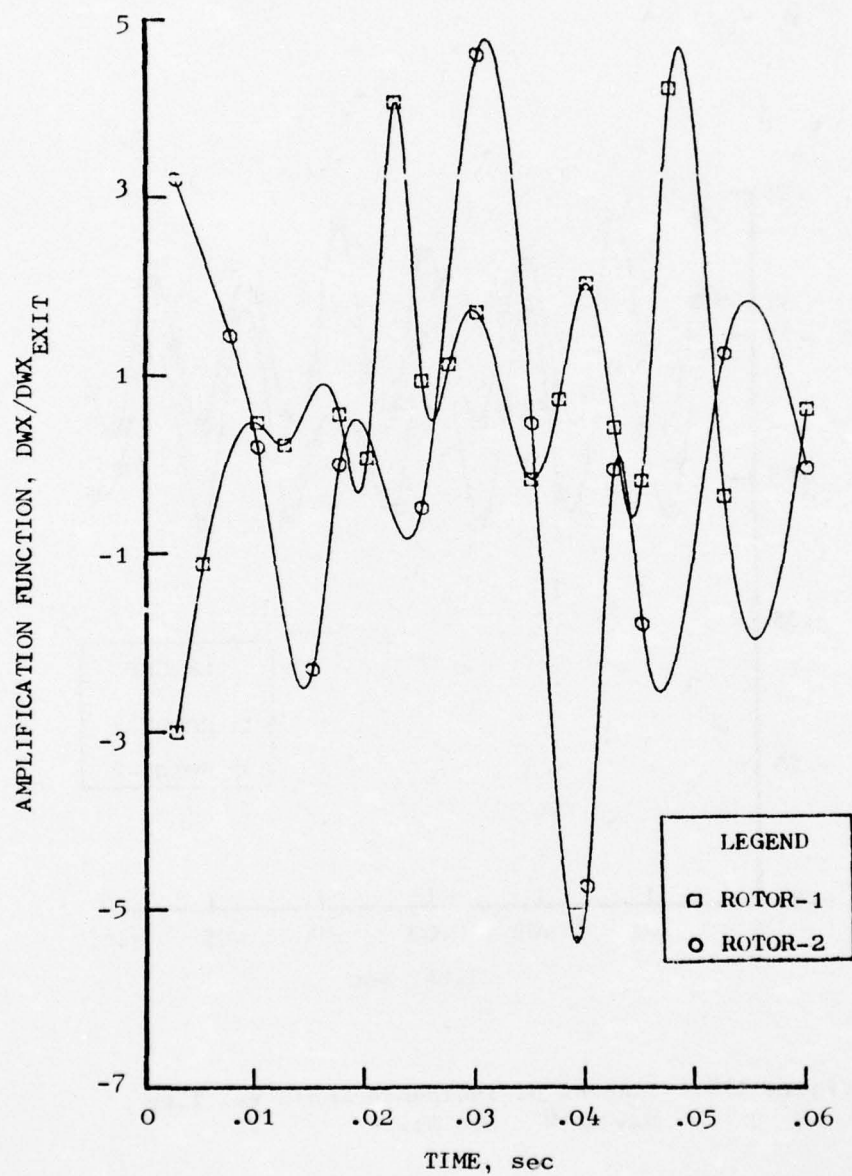


Figure 197. Amplification Function Vs. Time , $80\% N/\sqrt{\theta}$, 118 Hz.

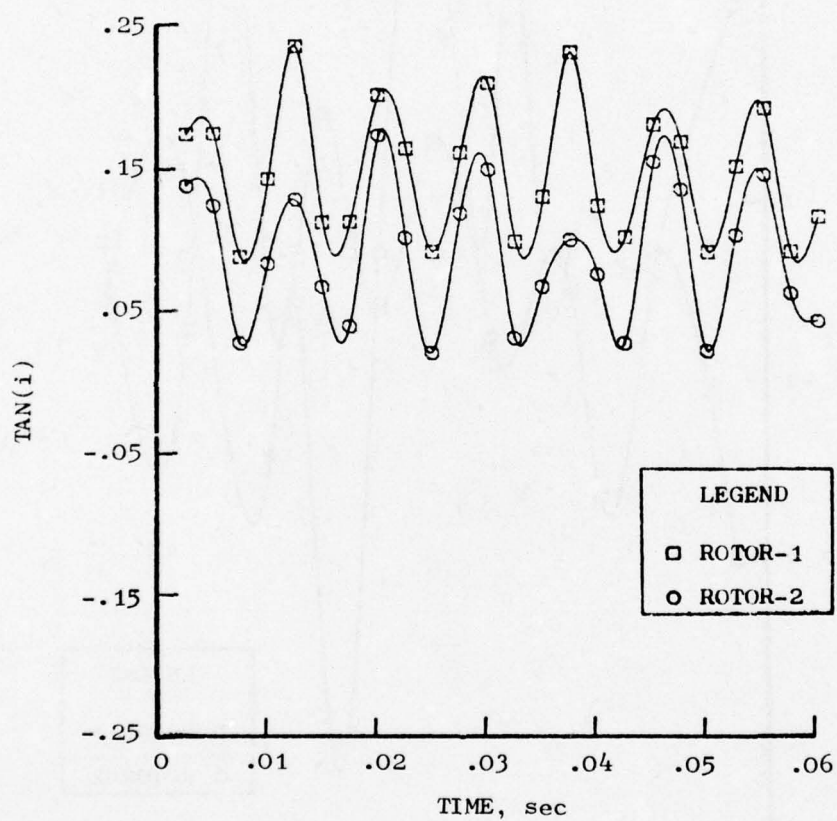


Figure 198. Tangent of Incidence Angle Vs. Time ,
80% $N/\sqrt{\theta}$, 118 Hz.

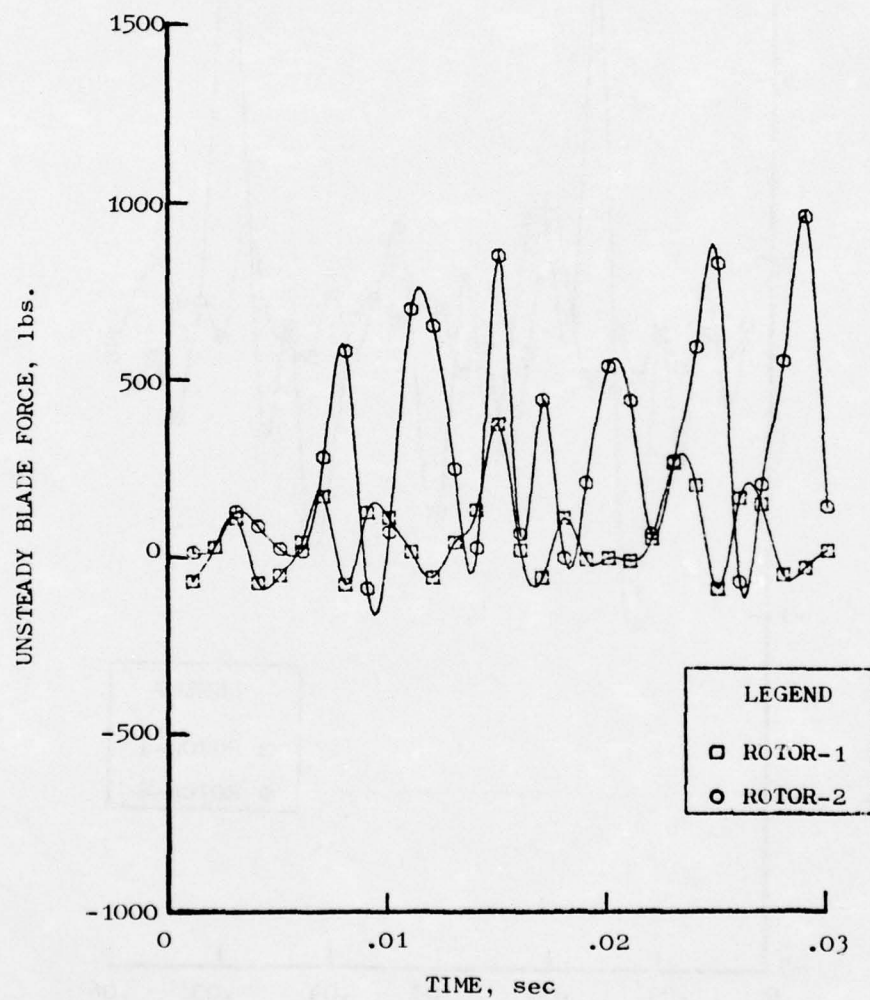


Figure 199. Unsteady Blade Force Vs. Time , $80\% N/\sqrt{\theta}$, 240 Hz.

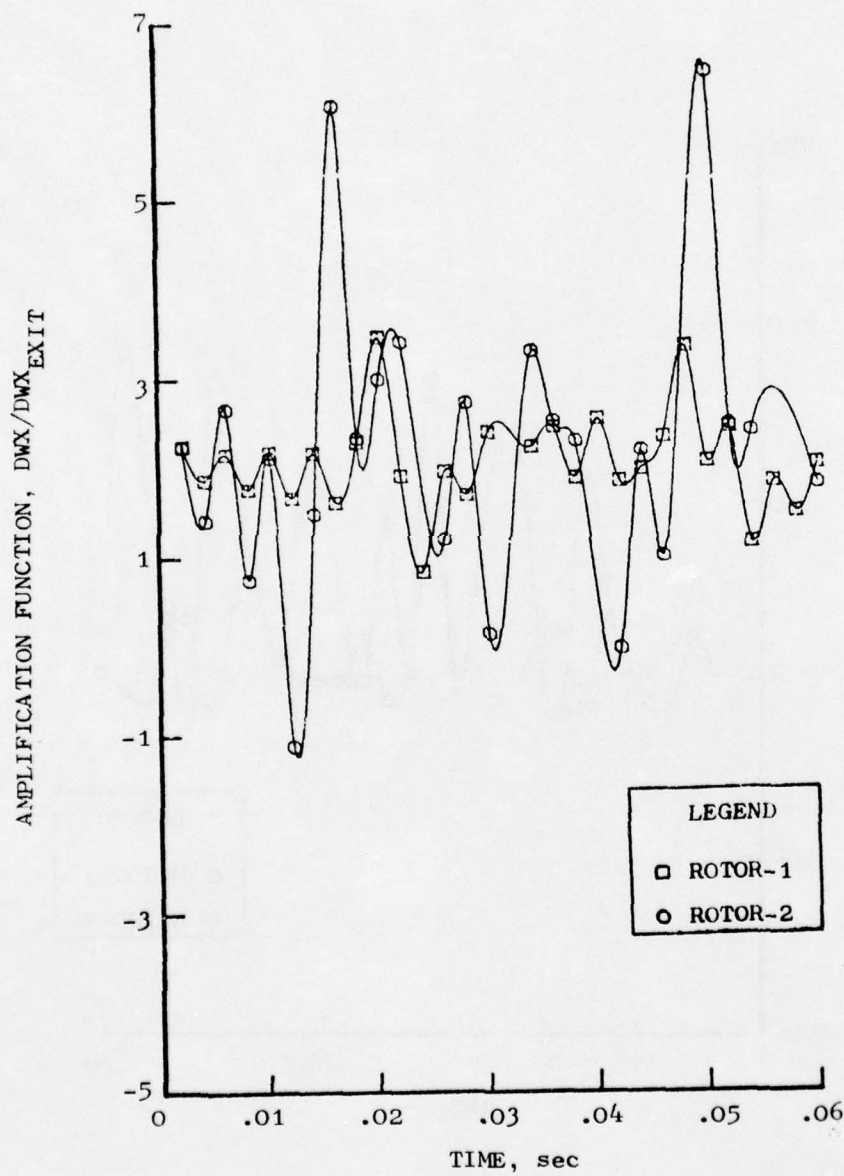


Figure 200. Amplification Function Vs. Time , $80\% N/\sqrt{\theta}$, 240 Hz.

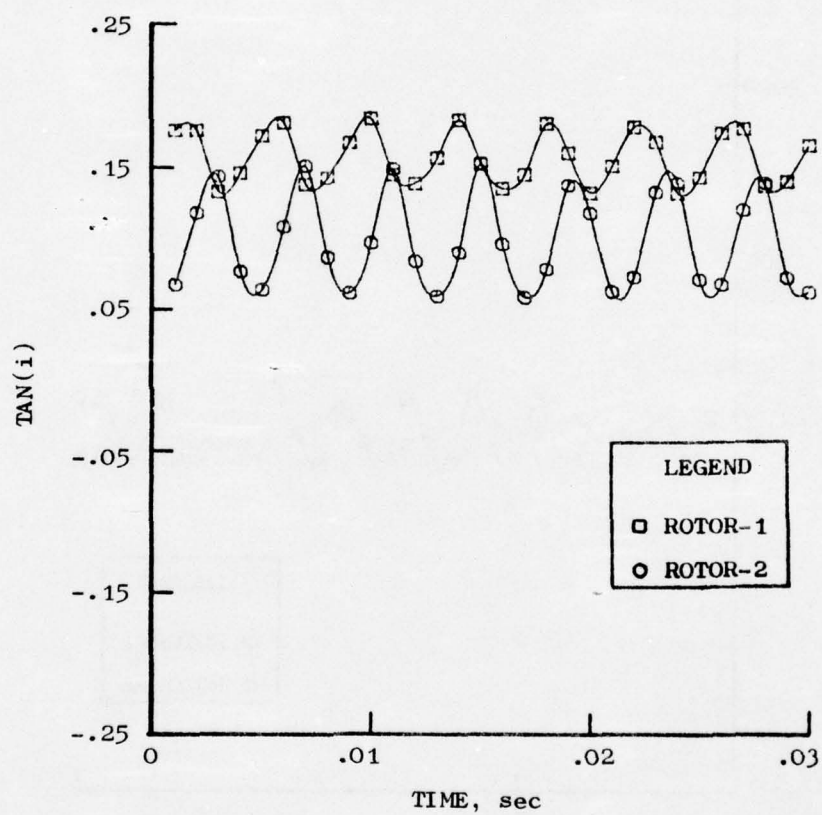


Figure 201. Tangent of Incidence Angle Vs. Time, $80\% N/\sqrt{\theta}$, 240 Hz.

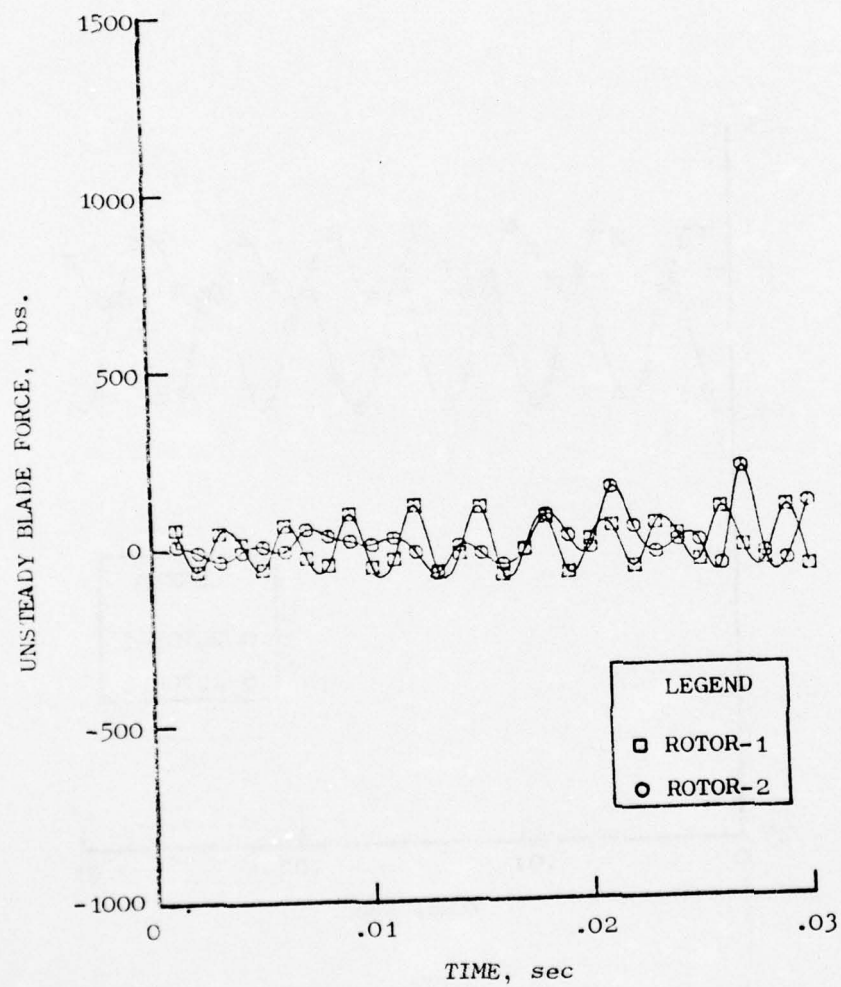


Figure 202. Unsteady Blade Force Vs. Time , $80\% N/\sqrt{\theta}$, 350 Hz.

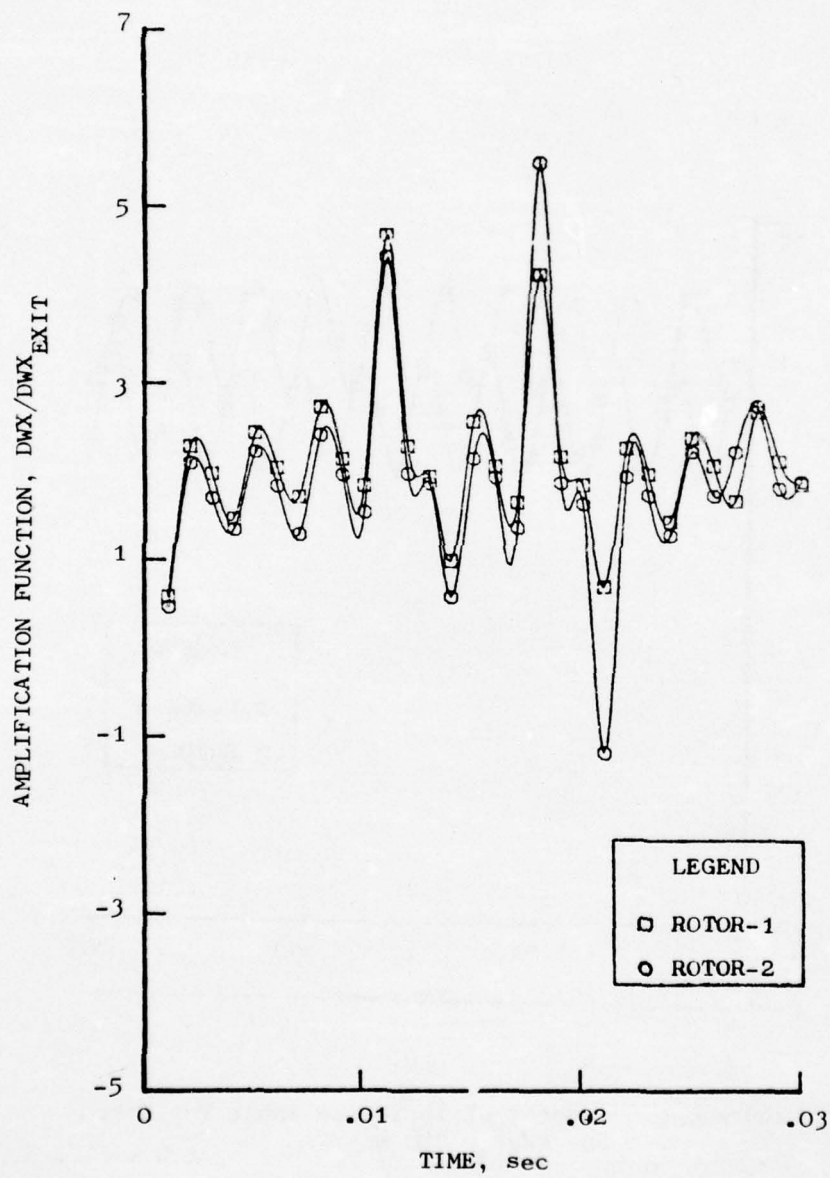


Figure 203. Amplification Function Vs. Time , $80\% N/\sqrt{\theta}$, 350 Hz.

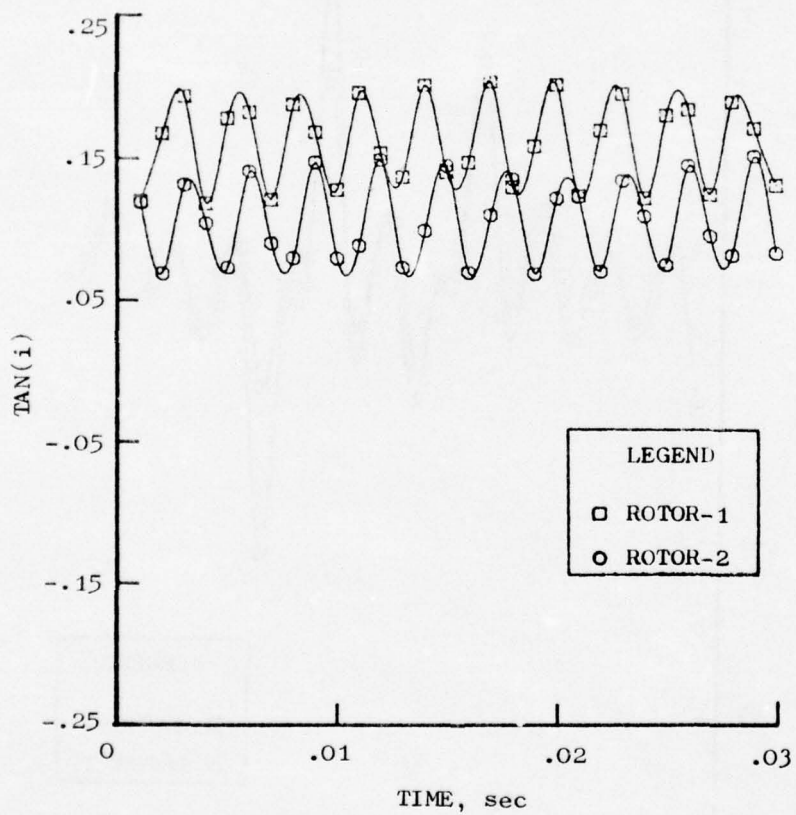


Figure 204. Tangent of Incidence Angle Vs. Time, $80\% N/\sqrt{\theta}$, 350 Hz.

REFERENCES

1. Plourde, G.A. and Brimelow, B., "Pressure Fluctuations Cause Compressor Instability," proceedings of the Air Force Airframe-Propulsion Compatibility Symposium, Air Force Aero Propulsion Laboratory Technical Report AFAPL-TR-69-103, June 1970.
2. Brimelow, B., Collins, T.P., and Pfefferkorn, G.A., "Engine Testing in a Dynamic Environment," presented at the AIAA/SAE 10th Propulsion Conference held at San Diego, California during October 21-23, 1974, AIAA Paper No. 74-1198.
3. Reynolds, G.G., Vier, W.F., and Collins, T.P., "An Experimental Evaluation of Unsteady Flow Effects on an Axial Compressor - P3 Generator Program," Air Force Aero Propulsion Laboratory Technical Report AFAPL-TR-73-43, July 1973.
4. Tesch, W.A. and Steenken, W.G., "Blade Row Dynamic Digital Compressor Program, Volume 1, J85 Clean Inlet Flow and Parallel Compressor Models," National Aeronautics and Space Administration Report NASA CR-134978, March 1976.
5. Gray, W.G., "Propulsion System Flow Stability Program (Dynamic) Phase 1 Technical Report, Part 5. Models for Predicting Compressor Response to Spatial and Time-variant Distortion - Basic Theory and Comparisons of Model and Test Data," Air Force Aero Propulsion Laboratory Technical Report AFAPL-TR-68-142, Part V, December 1968.
6. Jansen, W., Swarden, M.C., and Carlson, A.W., "Compressor Sensitivity to Transient and Distorted Transient Flows," Naval Air Systems Command Report 1149-1, September 1970.
7. Willoh, R.G. and Seldner, K., "Multistage Compressor Simulation Applied to the Prediction of Axial Flow Instabilities," National and Aeronautic Space Administration NASA TM X-1880, September 1969.
8. Schorr, B., and Reddy, K.C., "Inviscid Flow Through Cascades in Oscillatory and Distorted Flow," AIAA 8th Aerospace Sciences Meeting, AIAA Paper No. 70-131, January, 1970.
9. Tesch, W.A., and Steenken, W.G., "Dynamic Blade Row Compression Component Model for Stability Studies," presented at the AIAA 14th Aerospace Sciences Meeting, Washington, D.C., January 26-28, 1976, AIAA Paper No. 76-203.
10. Bird, R.B., Stewart, W.E., and Lightfoot, E.N., Transport Phenomena, Wiley, New York, 1960.

REFERENCES (Concluded)

11. Sokolnikoff, I.S., and Redheffer, R.M., Mathematics of Physics and Modern Engineering, McGraw-Hill, 1958.
12. Shepherd, D.G., Elements of Fluid Mechanics, Harcourt, New York, 1965.
13. Bisplinghoff, R.L., R.L., Ashley, H., and Halfman, R.L., Aeroelasticity, Addison-Wesley, Cambridge, 1955.
14. Melick, H.C., "Analysis of Inlet Flow Distortion and Turbulence Effects on Compressor Stability," National Aeronautics and Space Administration Report NASA CR-114577, March 1973.
15. Kimzey, W.F., "An Analysis of the Influence of Unsteady Cascaded Airfoil Behavior on Axial Flow Compressors With Unsteady and Distorted Inflow," Paper Prepared for Tennessee Section AIAA Colloquium and Festschrift Honoring Dr. B.H. Goethert, November 1975.
16. Jansen, W., and Smith, G.E., "Propulsion System Flow Stability Program (Dynamic) Phase I Final Technical Report Part X. Explicit Stall Prediction Model - Theory and Comparison of Computed and Experimental Results," Air Force Aero Propulsion Laboratory Technical Report AFAPL-68-142, Part X, December 1968.
17. Goethert, B.H. and Staff of University of Tennessee Space Institute, "Research and Engineering Studies and Analysis of Fan Engine Stall, Dynamic Interaction with other Subsystems, and Systems Performance," Air Force Aero Propulsion Laboratory Technical Report AFAPL TR-70-51, July 1970.

AD-A032 079

GENERAL ELECTRIC CO CINCINNATI OHIO AIRCRAFT ENGINE GROUP F/G 1/3
DYNAMIC DIGITAL BLADE ROW COMPRESSION COMPONENT STABILITY MODEL--ETC(U)
AUG 76 G G REYNOLDS, W G STEENKEN F33615-75-C-2029

UNCLASSIFIED

R76AEG299

AFAPL-TR-76-76

NL

4 OF 4
ADA032079



END

DATE
FILMED

1 - 77

GLOSSARY

- Nondimensional Amplitude - One-half of the difference between the wave maximum and wave minimum divided by the average value of the wave.
- Amplitude Ratio - Ratio of nondimensional total-pressure amplitude at exit to the nondimensional total-pressure amplitude at entrance taken across the IGV, Rotor 1, or Rotor 2.
- Planar Wave Distortion Transfer Coefficient - Ratio of the fan discharge nondimensional total-pressure amplitude to the fan entrance nondimensional total-pressure amplitude.
- Planar Wave Distortion Sensitivity - The loss in surge pressure ratio at given frequency measured from the clean surge line to the mean operating point at surge with planar wave distortion divided by the nondimensional amplitude of the inlet total-pressure fluctuations.

NOMENCLATURE

A	-	Area
$A_{1\beta}$	-	Area Normal to Flow Direction
A^*	-	Choked Area at $M = 1$
B	-	Y-Axis Intercept of Lift Direction Correction Angle
C	-	Absolute Velocity
$C(k)$	-	Theodorsen's Function
C_i	-	Coefficients for Relative Total-Pressure Loss Coefficient Polynomials
C_L	-	Lift Coefficient
C_z	-	Axial Velocity
C_u	-	Absolute Tangential Velocity
C_3	-	Time Constant Coefficient
D_i	-	Coefficients for Deviation Angle Polynomials
F_B	-	Blade Force
F_D	-	Drag Force in Direction of Blade Entrance Flow
F_{DZ}	-	Axial Component of Drag Force
F_L	-	Blade Lift Force
F_T	-	Blade Tangential Force
IGV	-	Inlet Guide Vane
L	-	Volume Length
L	-	Lift Force
M	-	Mach Number
M	-	Slope of Lift Direction Correction Angle
N	-	Rotor Speed in Revolutions per Minute
$N/\sqrt{\theta}$	-	Corrected Speed

NOMENCLATURE (Continued)

P	-	Static Pressure
P _d	-	Dynamic Pressure ($P_T - P$)
P _M	-	Mean Static Pressure
P _n	-	Polynomial of Degree n
P ³ _G	-	Planar Pressure Pulse Generator
P _T	-	Total Pressure
ΔPRS	-	Loss in Surge Pressure Ratio
R	-	Specific Gas Constant
R	-	Region
S	-	Blade Spacing in Definition of Solidity
S	-	Surface
S _F	-	Entropy Production Term
T _T	-	Total Temperature
U	-	Pitch Line Wheel Speed
U	-	Freestream Velocity
U _R	-	Relative Velocity
V	-	Volume
W	-	Flow Rate
W _C	-	Corrected Flow
WCA	-	Approximate Corrected Airflow (See Section 5.2.1)
W	-	Relative Velocity
a _T	-	Stagnation Velocity of Sound
c	-	Blade Chord
f	-	Frequency

NOMENCLATURE (Continued)

g_0	-	Gravitational Constant
i	-	Incidence Angle
q	-	Kinetic Pressure, $1/2 \rho (W')^2$
r	-	Pitch-line Radius
s	-	Specific Entropy
t	-	Time
α	-	Angle of Attack
α, β	-	Blade Inlet Air Angles (Stator and Rotor, Respectively)
α^*, β^*	-	Blade Inlet Metal Angles (Stator and Rotor, Respectively)
β_c	-	Lift Direction Vector Correction Angle
β_∞	-	Lift Direction Vector
γ	-	Ratio of Specific Heats for Air
δ	-	Deviation Angle
ϵ	-	Small Quantity
η	-	Efficiency (ψ_m/ψ'_m)
θ	-	T_T/T_{STD}
λ	-	Wavelength
ξ	-	Dummy Variable
ρ	-	Density
σ	-	Solidity
τ	-	Blade Row Time Constant
ϕ	-	Blade Camber
ϕ	-	Flow Coefficient $(\frac{C_{z_i}}{2\pi N r_i})$

NOMENCLATURE (Continued)

ψ_m	-	Work Coefficient $\frac{\gamma}{\gamma-1} g_o R \frac{(T_{T_{i+1}} - T_{T_i})}{[2\pi N(r_i)]^2/2}$
ψ'_m	-	Pressure Coefficient $\frac{\gamma}{\gamma-1} g_o R T_{T_i} \left[\frac{P_{T_{i+1}}}{P_{T_i}} \frac{(\gamma-1)/\gamma}{-1} \right] \frac{1}{[2\pi N(r_i)]^2/2}$
\bar{w}	-	Relative Total-Pressure Loss Coefficient
ω^*	-	Reduced Frequency ($2\pi fc/W'$)
ω	-	Circular Frequency
Underline	-	Vector Quantity
.	-	Scalar Product
x	-	Vector Product

SUBSCRIPTS

0	-	Mean
1	-	Compressor Entrance Station; also Blade Row Entrance Station
2	-	Compressor Discharge Station; also Blade Row and Exit Station
E	-	Effective
I	-	Instantaneous
M	-	Mean
S	-	Standing
T	-	Total
T	-	Traveling
i	-	i-th Station
k	-	K-th Volume
m	-	M-th Stage
n	-	N-th Blade Row

NOMENCLATURE (Concluded)

SUPERSCRIPTS

- Volume Average
- ' - Relative Frame of Reference
- . - Derivative with Respect to Time